University of Zagreb

Faculty of Mechanical Engineering and Naval Architecture

Luka Balatinec

Numerical Model of Lubricated Wear in Rotating Machinery

DOCTORAL THESIS

Zagreb, 2025.

University of Zagreb

Faculty of Mechanical Engineering and Naval Architecture

Luka Balatinec

Numerical Model of Lubricated Wear in Rotating Machinery

DOCTORAL THESIS

Supervisor: prof. Hrvoje Jasak, PhD

Zagreb, 2025.

Sveučilište u Zagrebu

Fakultet strojarstva i brodogradnje

Luka Balatinec

Numerički model trošenja uz podmazivanje u strojevima s rotirajućim komponentama

DOKTORSKI RAD

Mentor: prof. dr. sc. Hrvoje Jasak

Zagreb, 2025.

Acknowledgements

First and foremost, I would like to express my deepest gratitude to my supervisor and mentor, Professor Hrvoje Jasak, who not only provided assistance and guidance during my PhD studies but also continued to do so even after starting his tenure at the University of Cambridge. Working with Professor Jasak has always been a great source of motivation. I am especially grateful to Professor Jasak for selflessly supporting his group in Zagreb during the many months of the Faculty's renovation.

Special thanks must be given to Tessa Uroić and Vanja Škurić, who have been there for me from day one. Tessa has been a great motivator and showed great willingness to help with the turmoil of bureaucracy, while Vanja has always managed to find time to talk about my work and to help with any struggles along the way. Thank you both.

I am very grateful to my dear friend and colleague Matej Čorak, who was always ready to lend an ear and offer help. Matej was there for me through many hardships, providing constant support, without which I would not have been able to make it. Matej, you are a true friend indeed–thank you.

I would like to thank Robert Keser for always finding time for a chat, offering kind words and counsel on so many different subjects, from work and research to personal matters.

In addition, I would like to express my sincere gratitude to my family, who were always by my side and gave me endless love, patience, and support throughout my PhD and through all the struggles of daily life. I would not have been able to go through it all without you–thank you.

Dedicated to all who stood by my side, through every challenge and every success.

"We do what we must because we can."
— GLaDOS, *Portal*

Abstract

This research presents a comprehensive numerical framework for wear analysis of rough surface contacts under lubricated contact conditions, integrating wear, a deterministic contact and lubrication models. The framework was implemented within the `foam-extend` software and relies on the Finite Area Method. It uses a wear model together with a lubricated contact model, enabling accurate predictions of contact pressures, surface changes and wear depth across different lubrication regimes. The model captures surface evolution by iteratively updating surface geometries based on wear and other calculated contact parameters.

The key features of the framework include the application of a wear model based on Archard's Wear Law, a deterministic asperity contact model which allows the use of measured surface data as input, and a modified Reynolds equation used to govern lubricant flow with cavitation effects. The developed wear algorithm combines the aforementioned models and is validated on several test cases, chosen to closely mimic different tribological scenarios. Single–surface wear was validated against numerical data from then literature in a Pin–On–Disc test case showing excellent agreement for contact pressure and surface profile evolution. Bilateral surface wear was validated using the same test case, with the numerical results closely matching the numerical data from the literature, demonstrating the capability of the model to calculate wear for surfaces with different wear coefficients. Wear of initially line contacts was validated on a Ring–On–Block case, closely agreeing with numerical data from the literature and following the trends seen in experiments. The quasi–steady–state wear model was validated on a reciprocating Ball–On–Flat case, accurately predicting the surface profile and contact pressure evolution. A Ring–On–Ring test case was used in combination with surface scans of a real rough surface, validating the ability of the algorithm to preform wear simulations using direct surface measurements. Finally, the wear algorithm was used for wear analysis of rough surfaces under lubricated contact conditions in a lubricated Ball–On–Disc test case using the Shell Turbo T68 oil as lubricant. The results were analysed for two cases under mixed and near-

boundary lubrication regimes, confirming the ability of the algorithm to predict contact pressure and surface profile evolution due to wear throughout lubrication regime transitions.

The implemented wear algorithm was validated against available numerical, analytical and experimental data for different tribological test cases, confirming the robustness and applicability of the developed framework for wear analysis across various tribological scenarios and lubrication regimes.

Prošireni sažetak

Ovaj rad predstavlja razvoj i validaciju numeričkog modela trošenja površina u podmazanom kontaktu s relativnim gibanjem, razvijenog u okviru metode kontrolnih volumena (površina) u svrhu analize trošenja u numeričkim simulacijama s rotirajućim komponentama.

I   Uvod

Provođenje adekvatne analize trošenja hrapavih površina u kontaktu uz podmazivanje ključno je za razumijevanje triboloških procesa i optimizaciju kontakta uz prisutnost trošenja u inženjerskim primjenama. Tradicionalni pristup ispitivanju trošenja oslanja se na primjenu, često financijski zahtjevnih i dugotrajnih, eksperimentalnih mjerenja. Sve većom dostupnošću računalnih resursa te napretkom računalnih metoda, numeričko modeliranje postaje sve više prisutan alat za predviđanje trošenja površina, pružajući mogućnost uvida u fenomene povezane s trošenjem te ponašanjem maziva u kontaktu.

Analiza triboloških procesa uključuje istraživanje složenih interakcija između hrapavih površine, režima podmazivanja te mehanizama trošenja. Trenje i trošenje hrapavih površina u najvećoj mjeri ovise o kontaktnim tlakovima, debljini tankog sloja maziva (filma) te materijalnim svojstvima površina između kojih je ostvaren kontakt. Numeričko modeliranje podmazanih kontakata zahtijeva rješavanje spregnutog sustava jednadžbi koji opisuju deformaciju površine, strujanje maziva i evoluciju površine uslijed trošenja.

Ovo istraživanje predstavlja razvoj numeričkog okvira primjenjivog za analizu trošenja podmazanih hrapavih površina, integrirajući model trošenja površina, deterministički model površinskog kontakta i model podmazivanja. Numerički je okvir implementiran u sklopu računalnog paketa `foam-extend` uz primjenu metode kontrolnih površina (eng. *Finite Area Method*). Glavni je cilj istraživanja točno predvidjeti kontaktne tlakove, visinu trošenja (dubinu potrošenog materijala) i evoluciju površine u različitim režimima podmazivanja.

II   Numerički modeli i implementacija

Razvijeni okvir za analizu trošenja sastoji se od tri međusobno povezana numerička modela. Model trošenja razvijen je na temelju Archardovog zakona trošenja te omogućava proračun visine trošenja (dubine potrošenog materijala) i volumena trošenja tijekom vremena. Model omogućava analizu utjecaja trošenja kod nominalno glatkih, ali i hrapavih površine, a razvijen je tako da omogućava analizu trošenja za slučaj jednostranog i obostranog trošenja površina u kontaktu. Model je također razvijen kako bi omogućio korištenje snimki topografije površine (eng. *surface scans*) kao ulaznih podataka za izračun trošenja i analizu promjene geometrije kontakta.

Deterministički model kontakta precizno opisuje interakcije topografije hrapavih površina, uzimajući u obzir učinke površinske hrapavosti na mikroskali. Ova metoda omogućava precizno određivanje kontaktnih parametara, uključujući kontaktne tlakove, kontaktne površine i deformacije, a čime se osigurava veća točnost u odnosu na statističke modele.

Model podmazivanja temelji se na modificiranoj Reynoldsovoj jednadžbi koja uzima u obzir efekte kavitacije i opisuje strujanje tankog sloja maziva između hrapavih površina. Reynoldsova jednadžba diskretizirana je primjenom metode kontrolnih površina (dvodimenzionalne inačice metode kontrolnih volumena), čime je osigurano očuvanje mase prilikom modeliranja tankih filmova maziva u mješovitom ii hidrodinamičkom režimu podmazivanja.

Ova su tri modela međusobno povezana, omogućujući iterativno ažuriranje topografije površine na temelju varijabli izračunatih analizom trošenja. Okvir je razvijen kako bi omogućio korištenje eksperimentalnih podataka o hrapavosti površina kao ulaznih podataka za numeričke simulacije stvarnih površina u uvjetima podmazanog kontakta.

III   Validacija i verifikacija

Provedena je detaljna validacija i verifikacija kako bi se osigurala točnost i robusnost implementiranog modela. Numerički rezultati su uspoređeni sa postojećim analitičkim, numeričkim i eksperimentalnim podacima pronađenim u literaturi.

Testni slučajevi na kojima je provedena validacija, razvijeni su kako bi što vjernije reproducirali različite tribološke eksperimente.

Model trošenja jedne površine validiran je na testnom slučaju u kojem valjčić kruži po disku („valjčić po disku“, eng. *Pin–on–disc*) pomoću numeričkih te analitičkih podataka iz literature. Predviđeni kontaktni tlakovi, promjena površine uslijed trošenja te dubina i volumen potrošenog materijala, pokazali su izvrsno podudaranje s analitičkim i numeričkim rezultatima iz literature. Korištenjem istog testnog slučaja „valjčić po disku“, također je ispitan model bilateralnog trošenja, potvrđujući sposobnost modela da točno predvidi trošenje obje kontaktne površine. Testni slučaj prstena koji rotira oslonjen o ravan blok („prsten po bloku“, eng. *Ring–On–Block*) korišten je kako bi se analiziralo trošenje u uvjetima linijskog kontakta, gdje su numerički rezultati pokazali izvrsno poklapanje s numeričkim rezultatima iz literature te vrlo dobro poklapanje s trendovima vidljivim iz eksperimentalnih podataka. Kvazistacionarni model trošenja validiran je pomoću testnog slučaja kuglice koja se linearno pomiče po ploči („kuglica po ploči“, eng. *Reciprocating Ball–On–Flat*), potvrđujući sposobnost modela da predvidi trošenje kod cikličkih gibanja površina u kontaktu uz izvrsno poklapanje s numeričkim rezultatima iz literature. Validacija trošenja hrapavih površina provedena je pomoću testnog slučaja glatkog prstena koji rotira prislonjen uz hrapavi prsten („prsten po prstenu“, eng. *Ring–On–Ring*), gdje su korišteni eksperimentalno izmjereni profili površina. Numerički model uspješno je predvidio trošenje na temelju stvarnih snimki topografije površine. Dodatno, analiza trošenja u podmazanom kontaktu provedena je koristeći testni slučaj hrapave kuglice koja rotira po glatkom disku („kuglica po disku “, eng. *Ball–On–Disc*) uz korištenje maziva Shell Turbo T68, čime je pokazano kako je razvijeni okvira za analizu trošenja moguće koristiti i za proračun trošenja u mješovitom i graničnom režimu podmazivanja. Pokazano je kako različiti režimi podmazivanja značajno utječu na raspodjelu kontaktnih tlakova, pri čemu prelaskom u hidrodinamički režim dolazi do smanjenja izravnog kontakta površina i tako smanjenja trošenja. Analizirajući rezultate navedenih testnih slučajeva, pokazano je kako razvijeni okvir za proračun trošenja materijala pokazuje vrlo dobro slaganje s podacima dostupnim u literaturi, potvrđujući primjenjivost modela u stvarnim triboloških sustavima.

IV Zaključak

Ovo istraživanje predstavlja razvoj i implementaciju numeričkog okvira namijenjenog za analizu trošenja, koji se temelji na sprezi model trošenja, determinističkog model kontakta i modela podmazivanja za kontakt hrapavih površina. Numerički je okvir implementiran unutar programskog paketa otvorenog koda `foam-extend`, a temelji se na metodi kontrolnih površina. Razvijeni numerički okvir omogućava predviđanja visine trošenja (dubine potrošenog materijala), evolucije površine uslijed trošenja te kontaktnih tlakova i drugih veličina značajnih za analizu trošenja u različitim režimima podmazivanja, kao i u suhom kontaktu.

Ključne riječi

Tribologija, Numerička analiza trošenja, Podmazani kontakt, Hrapave površine, Reynoldsova jednadžba, Archardov zakon trošenja, Deterministički model kontakta, Metoda kontrolnih površina, OpenFOAM.

Contents

Contents

List of Figures

List of Tables

Nomenclature

Calligraphy letters

$\nabla_s \bullet$	Surface divergence operator	–
∇_s	Surface gradient operator	–
$\top$	Transpose operator	–

Greek letters

α	Cavitation switch function	–
α	Non–orthogonality angle of finite area edge	–
α	Pressure–viscosity coefficient	–
α^*	Pressure–viscosity coefficient	–
α_A	Fraction of plastic contacts in real contact area	–
β	Fluid bulk modulus	Pa
β^*	Temperature–viscosity coefficient	–
β_f	Thermal expansion coefficient of the lubricant film	K^{-1}
β_K	Thermal expansion coefficient	–
$\dot{\boldsymbol{\gamma}}$	Shear rate vector	s^{-1}
$\dot{\gamma}$	Total shear strain rate	s^{-1}
$\dot{\gamma}_\mathrm{e}$	Elastic strain rate	s^{-1}
$\dot{\gamma}_\mathrm{v}$	Viscous shear strain rate	s^{-1}
γ	Peklenik surface parameter	–

Γ_ρ	Diffusion coefficient of property ρ	–
$\mathbf{\Delta}_e$	Vector of orthogonal contribution to normal surface gradient	–
δ	Elastic deflection	m
δ_e	Elastic deformation	m
η	High–shear dynamic viscosity	Pa s
η'	Jacobson–Vinet parameter	–
η_C	Carreau shear–thinning dynamic viscosity	Pa s
η_RE	Ree–Eyring shear–thinning dynamic viscosity	Pa s
θ	Fractional film content	–
θ_form	Fractional film content next to the formation boundary	kg/m^3
λ	Characteristic time	s
λ	Correlation length	m
$\lambda_{0.5}$	Half–correlation length	m
K_D1	Wear coefficient of surface 1	–
K_D2	Wear coefficient of surface 2	–
μ	Dynamic viscosity	Pa s
μ_0	Dynamic viscosity at ambient pressure and temperature	Pa s
μ_B	Dynamic viscosity calculated using Barus' law	Pa s
μ_g	Dynamic glass viscosity	Pa s
μ_H	Dynamic viscosity calculated using Houpert's equation	Pa s
μ_R	Dynamic viscosity at reference state	Pa s
μ_R	Dynamic viscosity calculated using Roelands' equation	Pa s

NOMENCLATURE

μ_f	Film dynamic viscosity	$\mathrm{Pa\,s}$
$\overline{\mu}$	Dimensionless dynamic viscosity	–
μ	Coefficient of friction	–
μ_a	Coefficient of adhesive friction	–
ν	Limiting shear stress parameter	–
ν	Poisson's ratio	–
ν_d	Poisson's ratio of disc	–
ν_p	Poisson's ratio of pin	–
$\overline{\rho}$	Dimensionless density	–
ρ	Density	$\mathrm{kg/m^3}$
ρ_0	Density at ambient pressure	$\mathrm{kg/m^3}$
ρ_cav	Density at cavitation pressure	$\mathrm{kg/m^3}$
ρ_form	Density of gas–liquid mixture next to the formation boundary	$\mathrm{kg/m^3}$
ρ_ref	Reference density	$\mathrm{kg/m^3}$
σ_s	Squeeze number	–
τ	Shear stress	Pa
τ_E	Eyring stress	Pa
τ_f	Film shear stress	Pa
τ_L	Limiting shear stress	Pa
τ_m	Mean shear stress across the film thickness	Pa
τ_tot	Total traction	Pa
τ_s	Average shear strength of junctions	Pa

ϕ_η	Viscosity flow factor	–
ϕ_s	Shear flow factor	–
ϕ_{xy}	Pressure flow factor	–
ψ	Calculated property	–
ψ^{ref}	Reference property	–
Ω	Full–film region	–
Ω_{cav}	Cavitating region	–

Latin letters

ΔA	Max. contribution of contact area per asperity contact	m^2
A	Real contact area	m^2
a	Asperity contact radius	m
a	Yasuda parameter	–
A_1	Yasutomi parameter	°C
A_2	Yasutomi parameter	GPa^{-1}
A_n	Nominal (apparent) contact area	m^2
A_{pl}	Plastic contact area	m^2
A_r	Contact area ratio	–
B	Lubricant–dependent constant in Doolittle viscosity relation	–
B_0	Jacobson–Vinet parameter	Pa
b_1	Improved Yasutomi parameter	GPa^{-1}
b_2	Improved Yasutomi parameter	–
B_{form}	Formation boundary	–

NOMENCLATURE

B_{rup}	Rupture boundary	–
$\mathbf{C}$	Transformation tensor	–
C	Critical yield coefficient	–
C_1	Coefficient for pressure–density relation	–
C_1	Dowson–Higginson coefficient	Pa
C_1	WLF parameter	–
C_2	Coefficient for pressure–density relation	–
C_2	Dowson–Higginson coefficient	–
C_2	WLF parameter	°C
D_{k}	Normal surface gradient corrector due to curvature	–
E'	Equivalent elastic modulus	Pa
E_{d}	Elastic modulus of disc	GPa
E_{p}	Elastic modulus of pin	GPa
E_{r}	Reduced elastic modulus	Pa
F	Applied force/load	N
f	Rotational speed	rpm
F_{a}	Force needed to break the bonds between junctions	N
F_{f}	Friction force	N
F_{target}	Target contact force	N
F_{total}	Total contact force	N
$\mathbf{g}$	Vector of gravitational acceleration	m/s^2
G	Effective shear modulus	Pa

G	Surface gap	m
g	Cavitation switch function	–
G_0	Initial gap	m
g_x	Gravitational acceleration component in x–direction	m/s^2
g_y	Gravitational acceleration component in y–direction	m/s^2
g_z	Gravitational acceleration component in z–direction	m/s^2
$\dfrac{\mathrm{d}h_\mathrm{w}}{\mathrm{d}L}$	Rate of wear depth per sliding distance	m/m
$\dfrac{\mathrm{d}h_\mathrm{w}}{\mathrm{d}t}$	Rate of wear depth per unit time	m/s
$\dot{h}_\mathrm{w}$	Wear rate	m/s
H	Material hardness	Pa
h	Film thickness	m
h_0	Initial average height of the surface	m
h_l	Local film thickness	m
h_w	Wear depth	m
h_w1	Wear depth of surface 1	m
h_w2	Wear depth of surface 2	m
$\mathbf{k}_e$	Vector of non–orthogonal correction	–
K	Wear coefficient	–
k	Bulk maximum shear stress of the softer material	Pa
K_0'	Rate of change of the bulk modulus	–
K_0	Bulk modulus at ambient pressure	Pa
K_1	Probability factor for creation of a worn particle	–

NOMENCLATURE

K_{D}	Dimensional wear coefficient	Pa^{-1}
$K_{0,0}$	Rate of change of bulk modulus	Pa^{-1}
ΔL	Sliding distance of an asperity contact	m
L	Sliding distance	m
L_{tot}	Total sliding distance	m
L_e	Length of finite area edge	m
$\mathbf{m}_e$	Unit binormal vector of finite area edge	–
$\mathbf{n}_e$	Unit normal vector of finite area edge	–
$\mathbf{n}_P$	Unit normal vector of finite area face P	–
n	Carreau power law exponent	–
n	Number of asperity contact spots	–
p	Pressure	Pa
p_{cav}	Cavitation pressure	Pa
p_{c}	Contact pressure	Pa
p_{m}	Mean contact pressure	Pa
p_{n}	Normal contact pressure	Pa
p_{ref}	Reference pressure	Pa
q'_x	Flow rate in x–direction	m^2/s
q'_y	Flow rate in y–direction	m^2/s
R	Asperity radius	m
R	Radius of pin, disc, or ring	mm
r	Pressure flow factor constant	–

R_0	Lubricant–dependent constant in Doolittle viscosity relation	–
R_{G}	Gap residual	–
$R_{\mathrm{q_a}}$	Root mean squared roughness of surface a	m
$R_{\mathrm{q_b}}$	Root mean squared roughness of surface b	m
R_{q}	Combined root mean squared surface roughness	m
Re	Reynolds number	–
$\dot{s}$	Flux through finite area edge	m^3/s
$\mathbf{S}$	Boundary face area vector	m^2
S	Sliding path length per cycle	m
S_P	Surface area of finite area face P	m
Δt	Timestep	s
$\mathbf{T}$	Second rank tensor variable	–
T	Total time interval	s
T	temperature	K
t	Time	s
T_0	ambient temperature	K
T_{g}	Glass transition temperature	°C
T_{g}	Glass transition temperature	°C
T_{ref}	Reference temperature	K, °C
T_{tot}	Total simulation time	s
$\overline{\mathbf{U}}$	Mean velocity of two surfaces	–
$\mathbf{U}$	Velocity vector	m/s

NOMENCLATURE

$\mathbf{U}_{\mathrm{a}}$	Velocity vector of surface a	m/s
$\mathbf{U}_{\mathrm{b}}$	Velocity vector of surface b	m/s
U_{e}	Entrainment speed	m/s
U_{s}	Slip velocity magnitude	m/s
U_x	Velocity component in x–direction	m/s
U_y	Velocity component in y–direction	m/s
U_z	Velocity component in z–direction	m/s
ΔV	Volume of an individual worn particle	m^3
$\mathbf{V}$	Vector variable	–
V	Total worn volume	m^3
v	Sliding velocity	m/s
V_{r}	Variance ratio of a surface	–
v_{s}	Slip velocity	m/s
ΔW	Max. contribution of load per asperity contact	N
W	Normal component of the load	N
Y	Material yield strenght	Pa
y_{s}	Distance between mean surface plane and mean asperity height plane	m
z	Surface height	m
z_0	Initial surface height	m
Z_{T}	Target contact plane	m

Superscripts

q^n	New timestep or iteration	–

q^{oo} Timestep or iteration before old timestep or iteration   –

q^{o} Old timestep or iteration   –

Subscripts

q_{a} Value at surface a –

q_{b} Value at surface b –

q_{e} Edge interpolated value   –

q_{in} Value at the inlet   –

$\mathbf{q}_{n}$ Normal component of the vector   –

q_{N} Neighbouring finite area face–centred value   –

q_{out} Value at the outlet   –

q_{P} Current finite area face–centred value   –

$\mathbf{q}_{t}$ Tangential component of the vector   –

1. Introduction

1.1. Background

The Jost Report, commissioned by the UK government in 1966, revealed that major financial losses in the UK's industry, amounting to 1% of the UK's GDP, may be attributed to inefficiencies and equipment breakdown caused by excessive wear, friction and poor lubrication [6]. This investigation revealed that such significant economic loses may be avoided by improving practices related to lubrication and by reducing friction. As a result of this report, a new term encompassing issues related to lubrication, friction and wear was coined – tribology. The term "tribology" was accepted globally as a formal discipline, while also becoming an important field of study in material science and engineering. This lead to the formation of research groups, national centres and academic courses dedicated solely to the investigation of the field of tribology.

While the Jost Report lead to the wide acceptance and recognition of tribology as a singular filed, specific concepts which we toady associate with tribolgy, can be dated to earlier times. An overview of how tribology developed along with the development of modern industry [7] recognises four stages in which the field of tribology advanced, coinciding with industrial revolutions. Early in the First Industrial Revolution (18$^{\text{th}}$ century) tribological concepts became important with the development of bearings and lubricants in steam-powered machines. During this period, first attempts at quantifying friction (Coulomb's Law of Friction) and early concepts regarding hydrodynamic lubrication emerged. With the introduction of electricity during the Second Industrial Revolution (19$^{\text{th}}$ century), the focus shifted towards mass production of machine elements (e.g. bearings) and leading to first analytical solutions for hydrodynamic lubrication being used. Moreover, the foundation for computational models was laid out in 1886 with the development of the Reynolds Equation for hydrodynamic lubrication [8]. During a wave of automation and digitization of the Third Industrial Revolution (20$^{\text{th}}$ century) tribology shifted towards computational methods. For the first

1. Introduction

time investigators employed numerical methods to investigate different problems associated with friction, lubrication and wear. During this time, Elastohydrodynamic Lubrication Theory (EHL) was developed and for the first time elastic deformation of surfaces was incorporated into hydrodynamic calculations. With the development of computers and higher availability of computational resources, first numerical solutions for problems regarding friction and lubrication emerged. First numerical solutions for EHL contacts were given by Dowson and Higginson in 1966 [9]. During the 1970s, Finite Element Analysis (FEA) became widely adopted in the field of tribology, allowing researchers to model strain, stress and wear in machine components. The next step in the evolution of tribology involved studies of friction and wear on the atomic level. This became possible with the development of Molecular Dynamics (MD) during the 1990s and its more widespread use in nano–tribology. More recently, the focus of the Fourth Industrial Revolution (Industry 4.0) shifted towards improving efficiency, flexibility and productivity of manufacturing processes by incorporating advanced digital technologies, such as artificial intelligence, virtual reality, digital twins, cloud and computing. The technologies introduced in Industry 4.0 also had a great impact on tribology. The advancement of computational resources meant that more complex computational models may be developed, giving way to mixed lubrication and micro–EHL simulations, which can handle mixed and boundary lubrication regimes, as well as thin film lubrication and asperity contact. In recent times, advanced numerical techniques are extensively used in modern tribological applications to simulate the behaviour of lubricants under various conditions. On of these techniques if Computational Fluid Dynamics CFD, a numerical approach which is used in both industrial applications and academic research.

One of the main goals of Industry 4.0 is the advancement of green technologies by optimising efficiency in mechanical systems and by reducing energy losses [10]. CFD is one of the most extensively used tools in modern tribological research, giving invaluable insight into lubricant flow and various phenomena associated with friction and wear. The goal of CFD analyses in modern tribology is the improvement of surface interactions and lubrication in renewable energy systems, such as electric vehicles and wind turbines. These tribological improvements, which are central to "green tribology", are focused on reducing energy consumption,

2

waste and emissions [10]. By enhancing the efficiency of mechanical components, improvements brought on by the use of modern numerical techniques (e.g. CFD), play a pivotal role in the advancement of ecologically informed and sustainable practices of Industry 4.0.

Friction and wear are one of the main areas of concern in the field of tribology. Wear, which may be considered as the visible consequence of friction [11], is the main focus of investigation in thesis. Generally, wear is considered as the progressive loss of surface material at the area of contact between two solid bodies due to relative tangential motion of the contacting surfaces [11].

Due to a global shift towards clean and sustainable energy systems, modern industrial progresses are faced with new challenges regarding ecological sustainability, pollution and climate change [7]. This means that tribology has a pivotal role in achieving greater efficiency, adhering to stringent demands for lowering wear and friction. Tribology also plays a vital role in the ongoing electrification of transportation. Electric motors used in electric vehicles should be sealed once produced and should require minimal maintenance, thus relying on modern tribological practices to reduce or minimise the need for lubrication. Generally, modern tribology aims at minimising friction and wear through the use of self–lubricating elements, dry lubrication, sustainable and biodegradable coatings and new lubrication additives [12]. More specifically, heavily loaded contact pairs, such as sliding or rolling contact bearings, may be found in most rotating machinery. Rolling contact bearings and other heavily loaded contact pairs are common in modern engineering devices (e.g. power transmission systems of wind turbines, drivetrains of electric vehicles, etc.) and some older devices, such as Vickers pumps. These machines are subject to a high number of start–stop cycles and are usually operated in part–load conditions, shifting the focus of the investigation of contact, friction and wear away from nominal load conditions. At the same time, equipment and lubricant manufacturers, driven by the increased efficiency demands, are decreasing friction losses in the lubricant by reducing its viscosity, thus trying to minimise wear. Correctly assessing lubrication, friction and wear is of great importance in various industries (e.g. bearing design), as unoptimized conditions can reduce productivity and product quality.

Numerical modelling emerged as a valid and cost–effective alternative to ex-

perimental methods in contact analysis [13]. With the advancement of computational resources, greater accuracy of numerical methods was achieved. These advancements made numerical methods a viable design tool in contact analysis, capable of taking into account microscopic contact and friction. Numerical procedures for the assessment of lubrication and wear continue to be of interest, due to their great importance for the development of novel lubrication mixtures for highly loaded structures and their use in assessing wear in heavily loaded contact pairs. Numerical modelling greatly reduces the time needed for analysis of lubricant and device performance, ranging from the molecular (computational chemistry) to the macro level (continuum mechanics and fluid-solid interaction).

This thesis focuses on the development of a numerical framework, deigned to be used as a viable tool for simulating wear of lubricated rough surfaces. To better contextualise the research presented in this thesis, a review of previous studies is given next. This overview aims to highlight key findings and recent contributions, while presenting gaps in existing research, which the research presented in this thesis aims to address.

1.2. Previous and Related Studies

Wear modelling was studied experimentally and theoretically for years, but recent advancements in theoretical approaches regarding wear, together with swiftly advancing numerical capabilities, resulted in a more pronounced use of numerical simulations in understanding phenomena fundamental to wear [14]. The first examples of numerical simulations in wear analysis started during the late 1990s, as computational resources began to develop rapidly. During this time, researchers began using computational methods to investigate wear phenomena in engineering and manufacturing. Boukas et al. [15] used a probabilistic approach based on Markov chains and dynamic programming to develop a numerical wear model. The authors used the developed model to optimise wear–related costs in manufacturing systems. Stalin–Muller and Dang Van [16] employed Finite Element Analysis (FEA) to simulate sliding wear under steady–state conditions. They developed a wear model based on an elasto–plastic framework, which estimates the mechanical state of the material in the wear region using plastic strain ten-

sors and a ratchetting mechanism and then applies FEA analysis to calculate changes in stress and strain under varying loading conditions. This method does not rely on any empirical wear laws, but analyses the evolution and dissipation of strain in the area of contact. Another study dealing with unlubricated sliding wear was performed by Rice and Moslehy [17]. Their approach defines the area of contact (contact interface) as a dynamic zone in which the interacting asperities and debris transmit forces and displacement between the contacting surfaces. The developed model integrates energy dissipation and damping, determining wear based on the coupling between normal and frictional forces. Furthermore, the authors validated their approach by performing experimental tests using a pin–on–disc apparatus.

Meng and Ludema [18] performed a survey of journal and conference papers relevant to the analysis of wear and found that most models used to describe wear are developed for specific problems, which makes them inappropriate for general application. The authors identified the Archard wear model as the only model with relatively high general applicability and wide use in wear research. Archard proposed a simple wear model based on experimental observations [19]. The author concluded that, for steady–state conditions, wear may be modelled as being proportional to the applied load. The simplicity and general applicability of this model are the main reason why most numerical approaches to studying wear rely on the Archard wear model. Põdra and Andersson [20] developed a procedure in which contact resolution is performed using the Finite Element Method (FEM) and the calculated contact parameters are fed to Archard's wear model to calculate wear for a sliding contact. Williams [21] combined computational with analytical methods to model wear, using wear maps to classify asperity interactions based on load, speed and hardness, categorising them into mild and sever wear. The author builds on Archard's wear model by introducing wear maps as visual representations of the dominant wear mechanism according to specific parameters such as load, speed and temperature. Öqvist [22] used a similar approach to calculating wear, but introduces a procedure to update the initial surface geometry using the calculated wear depth. Molinari et al. [23] formulated a wear model which is capable of taking in account temperature dependence of the material hardness. Hegadekatte et al. [24] presented a

1. Introduction

procedure for calculating wear based on the combination of Archard's law and FEM analysis, validating the results with experimental data. Da Silva et al. [25] demonstrated an approach where Archard's Wear Law may be treated as an initial value problem. The authors used the sliding distance, defined by the geometry of the contact, and an experimentally determined wear coefficient to calculate the height of the worn material, i.e. wear depth. Rodríguez-Tembleque et al. [2] presented a three–dimensional Boundary Element Method BEM model for analysing wear in different contact problems, such as a sliding pin–on–disc case and a twin disc tribometer.

The majority of authors use a combination of FEM and simple wear models for the numerical investigation of wear phenomena, mostly dealing only with dry contact conditions [26]. Andersson et al. [27] performed numerical simulations using Archard's wear model and a FFT-based deterministic contact model to investigate a ball–on–disc case, comparing their findings with experimental data. Bortoleto et al. [28] combine Archard's wear law with FEM contact analysis to model wear transition between mild and severe wear in a pin–on–disc setup. A combined FEM–BEM approach was used by Ilincic et al. [29] study wear in reciprocating contacts, validating their findings against experimental data. Similarly, Lengiewicz and Stupkiewicz [30] studied periodic sliding contacts by introducing a quasi–steady–state wear model and verified the results against a three–dimensional FEM model. Furustig et al. [3] performed wear simulations using measured surface topography as input, comparing the results to surface scans of worn surfaces. Bose and Ramkumar used a FEM–based model to predict unlubricated (dry) wear for contact between a metal ball and disc in a tribometer [31], introducing an extrapolation technique to reduce computational costs. Similarly, Curelli et al. [32, 33] use a FEM model which relies on a combination of a local and a global contact model to predict wear. Zhan and Huang [34] developed a time–varying wear model for elastic line contacts and comapred their findings against experimental data from a ring–on–ring apparatus. More recently, some authors focused on developing FEM–based model which would be able to consider the effects of a lubricated contact in wear analysis. Winkler et al. [35] investigated wear in thrust roller bearings under mixed lubrication conditions by introducing a numerical wear model based on a three–dimensional FEM model

6

for elastohydrodynamic (EHL) lubrication and a modification of Archard's wear model. In their wear analysis, the authors assume that wear occurs only on asperity contact points, where the surfaces are not separated by the lubricant film. Maier et al. [36] performed wear analysis in textured contacts under lubricated contact conditions, using a multiscale numerical wear model, showing how surface texture influences lubrication and wear.

Recent studies, while still based on Archard's wear model, further extend the model for unsteady conditions and tribofilm formation. Ghanbarzadeh et al. [37] presented and validated a tribochemical wear model based on thermodynamics of interfaces and kinematics of tribochemical reactions. They used the developed model to analyse tribofilm formation on the contact surface and validated their findings using experimental data [38]. Azam et al. [39] developed a tribochemical model which considers the interaction of wear particles and the lubricant in the formation of the tribofilm. The evolution of the contact parameters of the contacting surfaces due wear is well–documented [40]. Thus, Zhan and Hang [34] proposed a numerical wear model which takes into account changes to the contact parameters due to wear. Ciavarella et al. [41] formulated a similar model which considers changes in contact pressure and temporal evolution of wear.

The crucial part in numerical wear analysis is the correct resolution of contact, while most authors resort to using FEM for dry contact resolution, it can be argued that the Finite Volume Method (FVM) presents a valid alternative when dealing with lubricated contact. Škurić [42] presented a modelling framework based on the Finite Area method (FAM, a two–dimensional variant of FVM) to model lubricated contact between rough surfaces in metal forming. The author implemented a deterministic elastic–perfectly–plastic contact model, based on the procedure presented by Stanley and Kato [43] and Sahin et al. [44, 45]. The framework uses a modified Reynolds equation with a cavitation algorithm and can use surface data from a deterministic or statistical contact model as input. The same author validated the framework with the penalty method [46] and presented results from wire and sheet rolling simulations [47].

The development of a wear model applicable to contacts involving lubricated rough surfaces, may be divided into several essential parts, each dealing with one of the challenges associated with modelling such phenomena:

- predicting wear of nominally smooth surface,

- predicting wear of rough surfaces,

- predicting wear under lubricated contact conditions.

The development of such a wear model includes the modelling of wear for a single or both surfaces in contact, special treatment of rough surfaces (involving either statistical or deterministic contact models) and liquid film modelling for different lubrication regimes. Review of the previous relevant work directly related to each of the challenges listed above is given in Chapter 2..

1.3. Present Contributions

The present research contributes to the field of numerical contact analysis by providing a framework for wear analysis of rough surfaces under lubricated contact conditions. During this study, a unique method, which combines wear calculation with lubricated contact calculations, was developed and implemented. The framework was developed to be able to describe several complex phenomena associated with wear analysis of lubricated rough surfaces: resolution of surface contact, inclusion of the effects of lubricant in the area of contact and wear calculation. Thus, the wear analysis framework was developed as a unique implementation of three models: a wear model, a deterministic contact model and a lubrication model.

The wear model used in the framework was implemented as a numerical model based on the Archard wear equation [19], capable of predicting wear of nominally smooth surfaces, while also being able to take into account the evolution of the surface topology due to wear. The framework uses experimental data (the wear coefficient) for different pairs of materials to calculate the wear depth and wear volume for a single or both surfaces in contact.

As one of the key aspects in wear resolution is accurate modelling of the topography of the surfaces in contact, the wear calculation framework was expanded to include an asperity contact model. As the mechanism behind adhesive wear directly depends on the interaction of surface asperities [19], the contact model

needs to be able to describe asperity interaction as accurately as possible. The asperity contact model allows the wear model to take into account the surface roughness of real rough surfaces, moving away from nominally flat surfaces. The wear model was implemented to be compatible with both deterministic and statistical contact models, with the main focus of the research being a deterministic contact model, as such a model is capable of taking into account the microscale topology of surface asperities. The implemented deterministic contact model enables the use of surface scans and measured surface roughness profiles as input for calculating the information necessary for the wear and lubrication models.

The presence of lubricants greatly influences the parameters of contact. Thus, a separate numerical model was implemented to resolve lubricated contacts, following the procedure presented by Škuriš [42]. The initial lubricated contact model was modified and implemented as a new model, compatible with the surface wear model. Thus, the wear analysis framework was extended by implementing a lubricated contact model capable of calculating hydrodynamic properties of lubricant and their effect on the analysis of wear for contacts under different lubrication conditions.

The wear model, deterministic contact model and the lubricated contact model are coupled together, allowing for the calculation of contact pressures, wear depth and wear volume, area ratios and film thickness, in lubricated and dry contact conditions, for the contact of both smooth and rough surfaces. The framework allows for numerical wear analysis of machine elements or various tribological apparatuses used in experimental procedures, e.g. ball–on–disc or pin–on–disc tribometers.

The numerical implementation of the wear model was realised within the framework of the Finite Area Method (FAM) [1], a two–dimensional counterpart to the Finite Volume Method (FVM), as opposed to the majority of the previous studies which rely on the Finite Element Method (FEM). The flow of the lubricant was modelled using a modified Reynolds equation [48], which was discretised using the Finite Area Method. Using the Finite Area Method to discrtetise the Reynolds equation and model lubricant flow is a novel approach used by only a few authors [47, 48].

A combined numerical model, incorporating the aforementioned wear, deter-

ministic contact and lubrication models, makes the core of the wear analysis framework. A detailed overview of each model and its implementation is given. As far as the author is aware, the combination of the aforementioned models has, to this date, not been implemented. Several utilities were also developed as part of the framework, which are used for pre– and post–processing procedures. The numerical models and procedures were implemented in `foam-extend`, an open-source numerical toolbox developed using the C++ programming language. The `foam-extend` package is an object–oriented software library, developed as community driven fork of the general computational continuum mechanics software OpenFOAM [49]. The entirety of the code produced during this research was developed to be as efficient as possible, while still being written cleanly and in accordance with object–oriented programming patterns, enabling easier continuation of development and straightforward code maintenance.

Validation of the wear analysis framework was performed. Each model was validated separately for different wear conditions. Firstly, the framework was validated for single surface wear of a nominally flat surface, then validation for wear of both surfaces in contact was performed. After validation of the wear model for point contacts, a separate validation for line contacts was performed. The framework was then validated for rough surface wear analysis based on real rough surface data. Lastly, a cumulative validation of the complete wear framework was performed on a point contact case under different lubrication conditions. Verification and validation was carried for each of the described cases, comparing the numerical results from the current research with available experimental data or numerical data available in the literature.

1.4.   Thesis Outline

The rest of the text is organised in the following chapters.

Chapter 2. examines friction and wear, discussing the fundamental concepts behind these phenomena. A review of adhesive wear theory is given, culminating in the introduction of the Archard wear model. The fundamental equations of the model are introduced, setting the basis for later numerical implementation.

Chapter 3. focuses on the modelling of lubrication and rough surface contacts.

The modified Reynolds equation is introduced, governing thin film flows. An overview of cavitation and asperity contact models is given together with different relations governing the properties of the lubricant.

Chapter 4. introduces the Finite Area Method, a numerical approach used to discrtetise the Reynolds equation. This method reduces the Finite Volume Method to two dimensions by performing discretisation over a curved surface. Details on spatial domain and transport equation discretisation are provided.

Chapter 5. focuses on the numerical modelling and implementation of the various models which, coupled together, make the wear algorithm developed in this study. The implementation of a deterministic asperity contact model is discussed first. Then, the Finite area discretisation of the Reynolds equation, incorporating a cavitation model and flow factors to enable calculation of thin flows between rough surfaces, is given. Furthermore, the implementation of different relations used to govern the properties of the lubricant was discussed. Lastly, the implementation of the Archard wear model was given in the form of an incremental wear model and a quasi–steady–state wear model.

Chapter 6. presents numerical cases used to validate different aspects of the wear algorithm. Single surface wear is validated first using a pin–on–disc test case, with the same test case used for validation of bilateral wear analysis. After validation of initially point contact cases, validation of the wear model for line contacts in a ring–on–block setup was performed, comparing the results to both numerical and experimental data from the literature. A reciprocating ball–on–flat case was used to analyse wear using the quasi–steady–state approach. Next, the wear algorithm was used with direct surface profile measurements to analyse wear in a ring–on–ring apparatus, comparing the results with experimental scans of the worn surfaces found in the literature. Lastly, after separate validation of different aspects of the wear algorithm for dry contact conditions, wear analysis was performed on a ball–on–disc apparatus, using a measured surfaces profile and under lubricated contact conditions. The Shell Turbo T68 oil was used as lubricant to analyse wear under mixed and near–boundary lubrication regimes.

Chapter 7. concludes the thesis by offering a summary of the work performed during this research and presenting the resulting conclusions. A brief discussion on future research is given last.

2. Modelling Wear

2.1. Introduction

In this chapter an examination of friction, wear and related phenomena is provided. The fundamental concepts regarding friction are examined first. Adhesion and deformation phenomena are introduced as the main mechanisms causing resistance in then contact between surfaces. An overview of the fundamental works by Amontons and Coulomb is given, together with an overview of Bowden and Tabor's adhesive friction theory. This sets the framework for understanding how friction contributes to wear throughout engineering applications. The four main types of wear are presented, and adhesive wear is investigated in detail as it is the basis for the numerical model developed in this thesis. The Archard wear model is presented, followed by a discussion on the model's assumptions. The chapter offers an overview of the fundamental equations used by the model, providing a basis for the model's numerical implementation.

2.2. Friction and Wear

To understand the phenomena behind wear, one must first discuss friction. Friction is essential for understanding wear, as frictional forces directly contribute to the mechanisms causing wear. When two solid bodies are in contact, the tangential resistance to motion between the contacting bodies is defined as friction [50]. If the bodies are in relative motion, the resulting friction follows the same direction as the vector of the relative tangential velocity of the two bodies in contact. When there is no film of liquid or gas lubricant present in the area of contact, the type of friction that occurs is called dry friction. Thus, dry friction may be defined as the resistance between two solid surfaces without lubrication. According to Gohar [50], two laws of friction were introduced by Amontons in 1699:

(1) friction is independent of the apparent (nominal) area of contact,

(2) friction is directly proportional to the nominal component of the load.

The second law was expressed mathematically as:

$$F = \mu W, \tag{2.1}$$

where W represents the normal component of the load and μ the constant of proportionality, which is called the coefficient of friction. A third law of friction was proposed by Coulomb in 1785:

(3) friction is largely independent of sliding speed.

Coulomb experimentally determined that the same relationship, as given by Eq. 2.1, may be assumed for sliding bodies under relative motion. Coloumb's experiments helped us distinguish between static and kinematic friction. Static friction can be thought of as the resistance to initial motion, while the resistance to ongoing movement is called kinetic friction. As less force is required to keep an object in motion than to start the motion, kinetic friction is typically somewhat lower then static friction.

Gohar [50] recognises two main mechanisms behind friction: adhesion and deformation. Adhesive friction is the result of the resistance occurring when two surfaces are pressed together, due to the formation of small cold–welded areas, which are the results of atomic interactions. On the other hand, the deformation mechanism involves the ploughing effect of the harder material against the softer material in contact.

During the 1950s, Bowden and Tabor [51] developed their theory of adhesive friction. Based on their experimental and theoretical research, the authors reported several key findings on the mechanism of adhesive friction:

- The authors analysed the formation of microscopic asperities when two surfaces come into contact under sufficient load. They determined that on the microscopic level, the surfaces stick together due to atomic forces (adhesive force) and form cold–welded junctions.

2. Modelling Wear

- A distinction is made between the apparent and real areas of contact. The apparent area of contact is the total visible projected area that seems to be in contact between two surfaces and depends solely on the geometry of the contacting surfaces. The real area of contact is defined as the total sum of asperity contact points and is much smaller than the apparent area of contact. The real area of contact is directly proportional to the frictional force, which is not the case for the apparent area of contact.

- Adhesive friction between contacting surfaces is dependent on material properties, specifically shear strength and the hardness of the softer material.

- The authors determined that, as the load increases, so does the number of asperities that come in contact between the two surfaces, expanding the real contact area, which in turn leads to an increase in friction.

- The authors noticed that the contact area between two surfaces increases under tangential or shear forces in high–load conditions. This "junction growth" was attributed to the deformation of asperities due to additional plastic growth under combined normal and tangential loads.

With these findings in mind, the following equation may be written:

$$W = A p_m, \tag{2.2}$$

where A represents the real contact area, p_m the mean contact pressure and W the load supported by the asperities in contact. These cold–welded asperities are close to fully plastic conditions, thus p_m is assumed to be equal to H, the hardness of the softer material in contact:

$$W \approx AH. \tag{2.3}$$

If we introduce F_a as the force needed to break the bonds between junctions over the real contact area A, with an average shear strength of the junctions defined as τ_s, the following expression is given:

$$F_a = A \tau_s. \tag{2.4}$$

If we consider F_a as the force needed to break the bonds between junctions, then τ_s can be considered very close to k, the bulk maximum shear stress of the softer material. τ_s approaches the value of k due to plastic yielding at the junctions, which is caused by the combined effect of bulk (normal) and shear stresses. This is why the following condition is valid:

$$F_a = Ak. \tag{2.5}$$

From Eqs. 2.4 and 2.5, it follows that

$$\mu_a = \frac{F_a}{W} \approx \frac{k}{H}. \tag{2.6}$$

By taking a look at the equation derived above, we can determine that the coefficient of adhesive friction μ_a between two rubbing surfaces depends solely on their material properties: the maximum bulk shear stress and hardness. Eq. 2.6 also shows that μ_a does not depend on either load or sliding speed. Eq. 2.6 confirms the findings reported by Amontons, but does not fully explain friction behaviours in some real–word environments. For instance, Bowden and Tabor [51] found that the coefficient of friction is higher in real–word conditions then initially predicted. To explain such behaviour, the authors introduced the aforementioned junction growth model. For more information on the effects of junction growth and the influence of contaminant films, the reader is referred to [50].

The short overview of friction and the underlying phenomena presented in this section was given because it is essential for understanding wear and wear related phenomena. Adhesive friction theory is of great importance for understanding wear, as it describes how microscopic interactions between surfaces result in material transfer and degradation.

2.3. Wear

Wear is considered as the visible consequence of friction on surfaces [50]. Bhushan [52] defines wear as the removal of material from one, or both solid surfaces, when those surfaces are in relative contact, i.e. the surfaces are in sliding, rolling or impaction motion. Wear that is usually considered in engineering applications is

caused by progressive loss of material on a surface of contact between two solid bodies due to relative tangential motion. This type of wear arises from friction, which is in turn cause by the roughness features of the contacting surfaces.

For most engineering applications, when talking about wear, we consider the wear of metals, as the most commonly used engineering material. Other materials are also subject to wear. Several researchers investigated wear when one or both surfaces in contact are non–metallic, such as weld metals with non–metallic inclusions [53], polymers and composites [54, 55] and even bone structures [56]. Wear can be considered a very complex subject that depends on experimental investigation. Some simple theories exist which, depending of the type of wear discussed, try and analyse the physics behind wear.

Khonsari and Booser [57] recognise four main types of wear:

- **adhesive wear** caused by shearing along the interface or within asperities due to formation and rupture of asperity junctions during sliding;

- **abrasive wear** attributed to hard abrasive particles in the system and, in its simplest form, it may happen as the transition of sliding wear as it progresses in time;

- **corrosive wear** caused by sliding contact in a chemically reactive environment;

- **surface fatigue** which can be considered as life–limiting wear due to repeated stressing of machine elements, dirt, insufficient lubrication, etc.

All four main types of wear are related to friction and are important in engineering applications. Special attention will be given to adhesive wear, as it is closely related to the adhesive theory of friction presented in the previous section and forms the basis of the wear model developed by Archard, which is used as the foundations for this study.

2.3.1. Adhesive Wear Theory

Khonsari and Booser [57] describe adhesive wear as the most common type of wear. The theory of adhesive wear was originally proposed by Bowden and Tabor [51] as a logical continuation of the theory of adhesive friction (discussed in

Sec. 2.2.) and was further developed by Archard [19]. If the contact area between two bodies is thought of as being composed of hemispherical asperities and the normal load that is carried by those asperities is sufficiently high for some of the asperities (on the side of the softer material) to become plastic, they will be cold–welded onto the surface of the harder material [50]. Sliding contact between the surfaces of the bodies in contact results in the formation of cold welds at some asperity junctions. Shearing action, when the junction strength becomes greater than the bulk strength of one of the materials in contact, leads to breaking of the cold welds and formation of fragments. These fragments may be transferred to the original surface or may form loose wear particles. Typically, the material is transferred from the soft material body to the harder material body (Fig. 2.1a), with the opposite being possible if local weaker spots or regions exist in the harder material (Fig. 2.1b).

(a) Contact between harder and softer, resulting in creation of a wear fragment.

(b) Formation of small wear fragment from the harder body.
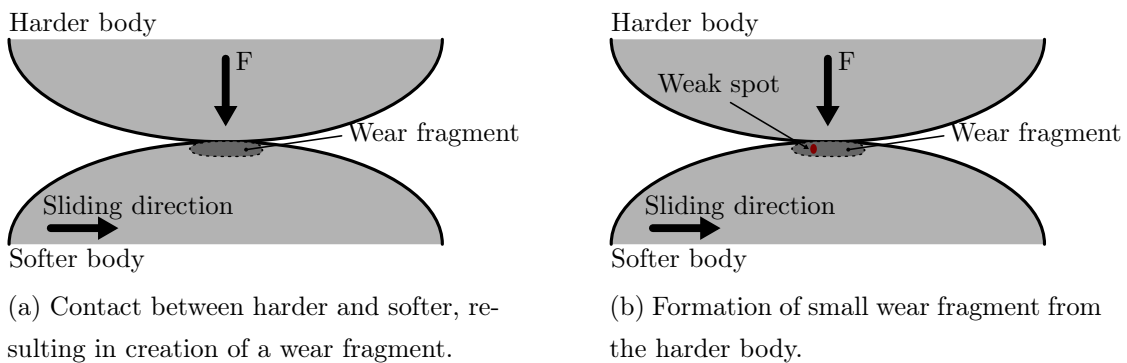
Figure 2.1: Formation of wear fragments at junctions between a soft and a hard body

The initial wear during the running–in of machine parts (e.g. bearings) involves higher wear rates, due to different factors such as surface finish, misalignment, contaminants, etc. When the wear rate reaches a steady–state, this steady wear may be described by the relatively simple formulation of the Archard Wear Model, which will be discussed next.

2.4.   Archard Wear Model

The Archard Wear Model is a widely used empirical model used to describe sliding wear based on asperity contacts and presented by Archard in the 1950s. As noted

by Villaggio [58], Reye proposed a very similar law, much earlier, in 1860. Reye's energy dissipative hypothesis stated that the volume removed due to wear is proportional to the work done by friction forces [59]. According to Villaggio, Reye's work is recognised in Europe, but English and American literature mostly refer to Archard's theory. This is probably due to the facet that Reye's work was only published in German and was missing the experimental work needed to support the hypothesis, which was performed by Archard for his theory. A similar model was also presented by Khrushchov and Babichev in 1960, in which the authors describe wear as a surface–driven process dependent on factors such as material hardness, surface pressure and material properties [60]. This is why some modern literature refers to a joint wear model as the Reye—Archard—Khrushchov wear law, noting the work done by all of the aforementioned authors [61]. For simplicity, and as this thesis focuses on the work done by Archard using his interpretation as the basis for implementing a numerical wear model, the Reye—Archard—Khrushchov model will simply be referred to as the Archard model.

2.4.1. Archard's Wear Law

Archard proposed a simple wear model based on experimental observations [19]. The author concluded that, by assuming the removal of lumps at contact areas formed by plastic deformation, wear may be modelled as being proportional to the load. Several assumptions were made by the author while developing the model [19, 62]:

1. **Assumed contact area** is based on a multiple contacts model. One event in the contact is defined as the contact of two asperities. At each event the contact between the asperities is modelled as a circular spot of radius a.

   The maximum contribution of the contact area δA for each asperity contact event, to the total area of contact A, may be modelled as:

$$\delta A = a^2 \pi. \tag{2.7}$$

   Similarly, the maximum contribution of load of the asperity contact to the

total load W is denoted by δW. If the complete contact area between the contacting surfaces is said to consist of n circular spots of radius a. The total area of contact A and the total load W may be expressed as follows:

$$A = \sum \delta A = n\, \delta A, \tag{2.8}$$

$$W = \sum \delta W = n\, \delta W. \tag{2.9}$$

The relationship between the contact area and load may be expressed using the hardness of the material H, taking note that the hardness used here is the hardness of the softer material in the material pair:

$$H = \frac{W}{A} = \frac{n\, \delta W}{n\, \delta A} = \frac{\delta W}{\delta A}, \tag{2.10}$$

thus load per contact event may be expressed as:

$$\delta A = \frac{\delta W}{H}. \tag{2.11}$$

2. **Duration of asperity contact**, from the moment two circular spots (of radius a) come into contact, until they part again, is assumed to be a sliding distance equal to $2a$ (Fig. 2.2).
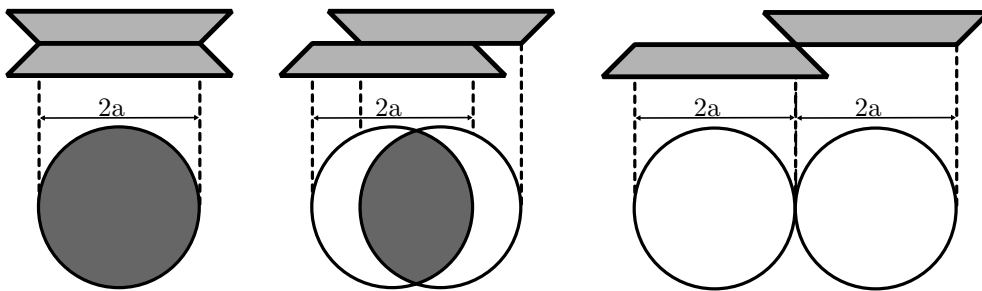
Figure 2.2: Representation of the contact area.

Archard assumed the duration of the contact (sliding distance δL) between asperities at each contact event is proportional to the size of the contact (radius a of the contact spot). He also assumed that a new contact point

is formed after a previous contact point passes the distance of δL. The duration of the contact, i.e. the sliding distance, may be expressed thusly:

$$\delta L = 2a. \tag{2.12}$$

3. **The shape of worn particles** is assumed to be that of equi–axial lumps, meaning that the worn particles resemble spheres.

   According to [63] the volume of a worn particle (denoted by δV) is expected to be proportional to the size of the contact point (radius a). Archard reported that experimental data showed the wear particles are equi–axed, meaning that they are lumps of material roughly equal all three dimensions [63]. That is why the volume of wear lumps is assumed to be proportional to a^3, i.e. the worn particles (lumps) are expected to be hemispherical:

$$\delta V = \frac{1}{2}\frac{4}{3}a^3\pi,$$
$$\delta V = \frac{2}{3}a^3\pi. \tag{2.13}$$

4. **Probability of the creation of a worn particle** is expressed as probability factor K_1. It depends on the properties of material pairs and is measured experimentally. Not every contact event results in a wear particle, that is why the probability factor K_1 is introduced. K_1 represents the probability that a contact event will produce a wear particle. If each contact event produced a wear particle, the probability factor K_1 would be equal to 1.

Taking note of the assumptions above, the derivation of Archard's law of wear is presented next. The contribution of a single asperity contact, sliding the distance of δL and producing a hemispherical wear particle of volume δV, to the total wear rate, may be expressed as the worn volume per unit sliding [57]. The expression for the contribution to the worn volume δV per sliding distance δL may be given using Eqs. 2.12 and 2.13:

$$\frac{\delta V}{\delta L} = \frac{\frac{2}{3}a^3\pi}{\frac{2a}{1}} = \frac{1}{3}\underbrace{a^2\pi}_{\delta A} = \frac{1}{3}\delta A. \tag{2.14}$$

The relation between contact area and load given by Eq. 2.11 may be used next:

$$\frac{\delta V}{\delta L} = \frac{1}{3}\frac{\delta W}{H}. \tag{2.15}$$

Eq. 2.15 assumes that every contact event results in the formation of a worn particle, as that is not the case, the probability factor K_1 must be introduced:

$$\frac{\delta V}{\delta L} = \frac{1}{3}K_1\frac{\delta W}{H}. \tag{2.16}$$

The total wear rate, taking note of the conservation of the contact area (Eq. 2.8) and load (Eq. 2.9), may be given as follows:

$$\frac{V}{L} = \sum \frac{\delta V}{\delta L} = \sum \frac{1}{3}K_1\frac{\delta W}{H} = \sum \frac{1}{3}K_1\,\delta A, \tag{2.17}$$

$$\frac{V}{L} = \frac{1}{3}K_1\,A = \frac{1}{3}K_1\frac{W}{H}. \tag{2.18}$$

Equation 2.18 represents a general form of Archard's Wear Law, derived from theoretical assumptions which will be discussed next. The same law was supported by the analysis of experimental data and the, relatively simple, linear relation between load and wear was confirmed by a number of experiments found in the literature [19, 62, 63].

2.4.2. Analysis of Archard's Assumptions

The **assumed area of contact** used in the derivation of Eq. 2.18 was further investigated by Archard and Hirst [62]. The authors analysed data from a large number of experiments and concluded that, when equilibrium surface conditions are attained, the wear rate becomes **independent of the apparent area of contact**.

Archard argues [63] that the factor of $\frac{1}{3}$ in Eq. 2.18 is the result of the geometrical assumptions regarding **contact duration** (i.e. sliding distance) of an asperity contact event and **shape (volume) of a worn particle**. Other assumptions may be made regarding the shape of worn particles and contact duration, as long as the expected dimensions of the worn volume and sliding distance are proportional to the size of the contact, i.e.:

$$\delta V \propto a^3 \quad \text{and} \quad \delta L \propto a. \tag{2.19}$$

As long as the essential assumption of proportionality to contact size given by Eq. 2.19 is true, the only effect of assuming different worn particle shapes or different durations of contact, is a different value of the factor in Eq. 2.18, i.e. the value of $\frac{1}{3}$ will change to some other constant factor. That is why a new variable $K = \frac{1}{3}K_1$ may be introduced. The coefficient of wear K incorporates the value of the constant ($\frac{1}{3}$ or other value) and the probability factor K_1, transforming Eq. 2.18 into a more general form:

$$\frac{V}{L} = K A = K \frac{W}{H}. \tag{2.20}$$

The wear coefficient K, as defined in Eq. 2.20, was obtained from a wide range of experiments performed by Archard [63]. An example of Archard's wear coefficient is given in Table 2.1 for different pairs of materials. The wear coefficient K is a dimensionless parameter and can be thought of as the resistance of a pair of materials in contact to wear. The wear coefficient is highly dependent on several factors: material properties, surface roughness and surface finish, contact pressure, sliding velocity and the environment in which the wear process occurs (e.g. existence of lubricants, temperature, humidity). This is why the wear coefficient K is usually determined experimentally for pairs of materials and under specified contact conditions.

2.4.3. Plastic and Apparent Contact Area

The contact area used in the development of the essential equations of Archard's Wear Law, describes the area of contact during an asperity contact event. Since

Table 2.1: Experimental data reported by Archard [5] for tests with 3.9 N load at 1.8 m/s.

Wearing Surface	Counter Surface	Friction Coefficient	Hardness (kg/mm^2)	Wear Coefficient
Mild Steel	Mild Steel	0.62	186	7×10^{-5}
60/40 Lead Brass	Tool Steel	0.24	96	6×10^{-4}
PTFE	Tool Steel	0.18	5	2.4×10^{-3}
Stellite	Tool Steel	0.60	690	5.5×10^{-5}
Ferritic Stainless Steel	Tool Steel	0.53	250	1.7×10^{-5}
Polyethylene	Tool Steel	0.53	17	1.3×10^{-3}
Tungsten Carbide	Tungsten Carbide	0.35	1300	1×10^{-4}

plastic deformation of the asperities in contact is expected from such contact events, the contribution to the contact area δA and the contact area A represents the plastically deformed area of contact. The theory of adhesive friction, analysed in Sec. 2.2., recognises the difference between the apparent and real areas of contact. The real area of contact is defined as the total sum of asperity contact points, while the apparent area of contact is the total visible projected area of contact between two surfaces. Archard's theory assumes the stress at asperity contacts to exceed the yield strength of the softer material, i.e. it assumes that most or all asperities deform plastically. Thus, making the real area of contact approximately the same as the plastic contact area.

The two variables referencing the area of contact may be rewritten as to more clearly reflect the plastically deformed contact area they denote:

$$\delta A \rightarrow \delta A_{pl},$$
$$A \rightarrow A_{pl}. \tag{2.21}$$

Thus, Eq. 2.20 may be rewritten as:

$$\frac{V}{L} = K \, A_{pl} = K \, \frac{W}{H}. \tag{2.22}$$

If we divide Eq. 2.22 by the nominal (apparent) contact area A_n, the following expression is obtained:

$$\frac{h_w}{L} = K \, \frac{A_{pl}}{A_n} = K \, \frac{W}{H \, A_n} = K \, \frac{p_n}{H}. \tag{2.23}$$

23

The left term of Eq. 2.23 the represents the height of the worn volume (wear depth) h_w per sliding distance L. The load W divided by nominal contact area A_n, results in the average normal contact pressure or normal stress on the contact surface p_n.

In an approach similar to the one used by da Silva et al. [25], a variable may be chosen to represent the quotient of the plastic deformation area A_{pl} and the nominal surface area A_n:

$$\frac{h_w}{L} = K \frac{A_{pl}}{A_n} = K \alpha_A. \tag{2.24}$$

The factor α_A in Eq. 2.24 may be used with the wear coefficient K for the appropriate material pair from Table 2.1, to determine the wear depth per unit sliding. α_A may be thought of as a measure of the fraction of plastic contacts belonging to the real contact area [25].

Knowing the exact value of α_A from the contact model and choosing the right coefficient of wear K makes it possible to calculate the wear depth h_w for sliding distance L.

2.4.4. Wear as an Initial Value Problem

An approach will be demonstrated where Archard's Wear Law may be treated as an initial value problem. Similarly to the approach used by da Silva et al. [25], Eq. 2.24 may be used to give the following expression:

$$\frac{\mathrm{d}\, h_w}{\mathrm{d}\, L} = K \alpha_A, \tag{2.25}$$

and applying the chain rule to the left-hand term of Eq. 2.25 results in:

$$\frac{\mathrm{d}\, h_w}{\mathrm{d}\, t} = \frac{\mathrm{d}\, h_w}{\mathrm{d}\, L} \underbrace{\frac{\mathrm{d}\, L}{\mathrm{d}\, t}}_{v}. \tag{2.26}$$

Using Eq. 2.25 and keeping in mind that the sliding velocity v may be expressed as $v = \frac{\mathrm{d} L}{\mathrm{d} t}$, Eq. 2.26 takes the following form:

$$\frac{\mathrm{d}\,h_w}{\mathrm{d}\,t} = K\,\alpha_A\,v, \tag{2.27}$$

allowing for the initial value problem to be formulated as:

$$\begin{cases} \dfrac{\mathrm{d}\,h_w}{\mathrm{d}\,t}\,(t) = (K\,\alpha_A\,v)\,(t), & \forall t \in (0,T), \\ h_w(0) = h_0. \end{cases} \tag{2.28}$$

Eq. 2.28 represents the change in depth of the worn material, in the form of an initial value problem, where T represents the total time interval of the process and h_0 the initial average height of the surface. Similarly, the rightmost term of Eq. 2.23 may be used as the starting point for reformulating Archard's wear equation:

$$\frac{h_w}{L} = K\,\frac{p_n}{H}. \tag{2.29}$$

The wear coefficient K used in Eq. 2.29 (and previous equation)i is the dimensionless wear coefficient. Since both K and the hardness H (softer material) are properties of a material, they may be expressed as a single material–dependant coefficient. After introducing $K_D = \frac{K}{H}$ as the **dimensional wear coefficient**, Eq. 2.29 may be transformed to:

$$\frac{h_w}{L} = K_D\,p_n, \tag{2.30}$$

$$h_w = K_D\,p_n\,L. \tag{2.31}$$

Eq. 2.31 may be disctretised over time in order to derive an equation which could be used to calculate the wear depth for each point on the surface:

$$\frac{\mathrm{d}\,h_w}{\mathrm{d}\,t} = \frac{\mathrm{d}}{\mathrm{d}\,t}\left(K_D\,p_n\,L\right),$$

$$\frac{\mathrm{d}\,h_w}{\mathrm{d}\,t} = K_D\left(p_n\,\underbrace{\frac{d\,L}{\mathrm{d}\,t}}_{v} + L\,\frac{\mathrm{d}\,p_n}{\mathrm{d}\,t}\right),$$

$$\frac{\mathrm{d}\,h_w}{\mathrm{d}\,t} = K_D\left(p_n\,v + L\,\frac{\mathrm{d}\,p_n}{\mathrm{d}\,t}\right). \tag{2.32}$$

The normal contact pressure p_n is directly connected to the applied load W. As the load is kept constant for a certain time increment (during one time–step), the normal contact pressure p_n should also stay constant. Thus, Eq. 2.32 is reduced to:

$$\frac{\mathrm{d}\,h_w}{\mathrm{d}\,t} = K_D\,p_n\,v, \tag{2.33}$$

or expressed as an initial value problem:

$$\begin{cases} \dfrac{\mathrm{d}\,h_w}{\mathrm{d}\,t}(t) = (K_D\,p_n\,v)(t), & \forall t \in (0, T), \\ h_w(0) = h_0. \end{cases} \tag{2.34}$$

The wear depth h_w may be calculated by integrating Eq. 2.33 over time:

$$\Delta h_w = \int K_D\,p_n\,v\,\mathrm{d}\,t. \tag{2.35}$$

Alternatively, one could start from Eqs. 2.24 and 2.30, and integrate over the sliding distance:

$$\frac{\mathrm{d}\,h_w}{\mathrm{d}\,L} = K_D\,p_n \quad \rightarrow \quad \Delta h_w = \int K_D\,p_n\,v\,\mathrm{d}\,L. \tag{2.36}$$

2.4.5. Combined Wear Coefficient

As noted by Mattei and Di Puccio [64], Archard's equations, such as Eq. 2.36, are generally applied to the coupling of the surfaces in contact, meaning that h_w

represents the combined wear depth of the two surfaces in the contact, and that the wear coefficient (K or K_D) represents the combined wear coefficient for the two surfaces. The authors also note that for wear of each of the surfaces to be analysed separately, experimental measurements for the wear coefficient of each surface need to be available, thus volume–loss measurements for each surface need to be performed.

As the wear coefficient K is crucial for the calculation of the wear depth or volume, a good understanding of the origin of the provided coefficient is necessary. Generally, the value of the wear coefficient K is determined experimentally and should be provided as an input for numerical wear models.

2.5. Conclusion

This chapter offered an exploration of the fundamental concepts behind friction and wear. An analysis of friction was given first, focusing on the adhesion and deformation as the primary mechanisms of resistance between contacting surfaces. The work done by Amontons, Coloumb, together with Bowden and Tabor's adhesive friction theory, was presented. Thus, establishing the important role of friction in wear related related phenomena.

An overview of the four main types of wear was given next, with a greater focus placed on adhesive wear as the basis for this research. The work done by Archard on understanding wear was presented, culminating in the formation of Archard's Wear Law. An examination of Archard's assumptions is given together with the fundamental equations of the model. This sets the basis for the numerical implementation of the model, which will be presented later.

3. Modelling Lubricated Contact of Rough Surfaces

3.1. Introduction

To successfully describe wear and calculate the evolution of pressure and wear depth of rough surfaces under lubricated conditions, the implemented wear algorithm relies on three separate models: a lubrication model, a contact model and a wear model. While the details regarding the wear model were given in Chapter 2., this chapter will focus on modelling of the lubricant and contacts under different conditions lubrication regimes. Firstly, a survey focusing on the derivation of a modified Reynolds equation for calculating thin film flows is given together with an overview of cavitation modelling. The Averaged Reynolds equation, which uses flow factors to take into account the effect of surface roughness, is presented next. Different asperity contact models are analysed, with a greater focus on FFT–based deterministic contact models. An overview of different relations for the density and the rheological properties of lubricants is given.

3.2. Modified Reynolds Equation

This section offers an overview of the derivation of a modified variant of the Reynolds equation [8], which was initially introduced in 1886 by Osborne Reynolds. The modified Reynolds equation governs the lubricant flow throughout different lubrication regimes. It is used to calculate shear stress and the hydrodynamic pressure of the lubricant film between two (rough) surfaces, which are in relative motion.

According to Wang and Qian [65], the Reynolds equation is a partial differential equation derived from the well–known Navier–Stokes equations, taking into account several assumptions: Newtonian fluid is assumed, viscous forces of the fluid are considered to be dominant (ignoring surface tension, inertia and fluid

body forces), film curvature is neglected (i.e. fluid film thickness is considerably smaller when compared to its length orr width), pressure variations across the film are disregard. The original form of the Reynolds equation was changed to mitigate the need for assumptions, e.g. for the Newtonian fluid assumption [65]. Up to the 1990s, the models which relied on the Reynolds equation used the steady–state form of the equation and constant fluid properties to analyse various engineering problems, such as: journal and thrust bearings [66, 67], elastohydrodynamic lubrication [68, 69], seal design [70] and fluid flow between rough surfaces [71]. With the sudden development of computational resources in the 2000s, more researchers focused on computational models based on the Reynolds equation. An overview of numerical models based on the Reynolds equation and applied to modelling of thin film flows, was given by Škurić [42]. It concludes that, more modern models consider pressure and temperature dependent fluid density [72, 73, 74], effects of surface roughness [44, 45, 75], non–Newtonian viscosity [76, 77] and thermal effects [78, 79, 75]. The focus of some of the most recent studies shifted to different numerical approaches which use the Reynolds equation to understand complex phenomena such as: improved finite difference algorithms for solving the Reynolds equation [80], advanced numerical [81, 82] and neural network–based approaches for investigating journal bearings [83], computationally less demanding models for thin–film lubrication [84].

The continuity equation (Eq. 3.1) and the Navier—Stokes momentum equation for compressible fluids (Eq. 3.2) [85] represent the starting point for the derivation of the Reynolds equation:

$$\frac{\partial \rho}{\partial t} + \nabla_\bullet(\rho \mathbf{U}) = 0, \tag{3.1}$$

$$\frac{\partial \rho \mathbf{U}}{\partial t} + \nabla_\bullet(\rho \mathbf{U}\mathbf{U}) = \rho \mathbf{g} - \nabla\left(p + \frac{2}{3}\mu \nabla_\bullet \mathbf{U}\right) + \nabla_\bullet\left[\mu\left(\nabla \mathbf{U} + (\nabla \mathbf{U})^\top\right)\right]. \tag{3.2}$$

Following the procedure outlined in [42] and order–of–magnitude analysis of the Reynolds equation needs to be performed to rewrite the equation in a more convenient form [86]. After some reorganisation and using the Cartesian component notation, the Navier–Stokes momentum equations for compressible viscous flows with varying viscosity are given as:

$$\rho\frac{\partial U_x}{\partial t} + \rho\left(U_x\frac{\partial U_x}{\partial x} + U_y\frac{\partial U_x}{\partial y} + U_z\frac{\partial U_x}{\partial z}\right) =$$
$$\rho g_x - \frac{\partial p}{\partial x} - \frac{2}{3}\frac{\partial}{\partial x}\left[\mu\left(\frac{\partial U_x}{\partial x} + \frac{\partial U_y}{\partial y} + \frac{\partial U_z}{\partial z}\right)\right]$$
$$+ 2\frac{\partial}{\partial x}\left(\mu\frac{\partial U_x}{\partial x}\right) + \frac{\partial}{\partial y}\left[\mu\left(\frac{\partial U_y}{\partial x} + \frac{\partial U_x}{\partial y}\right)\right] + \frac{\partial}{\partial z}\left[\mu\left(\frac{\partial U_z}{\partial x} + \frac{\partial U_x}{\partial z}\right)\right],$$

$$\tag{3.3}$$

$$\rho\frac{\partial U_y}{\partial t} + \rho\left(U_x\frac{\partial U_y}{\partial x} + U_y\frac{\partial U_y}{\partial y} + U_z\frac{\partial U_y}{\partial z}\right) =$$
$$\rho g_y - \frac{\partial p}{\partial y} - \frac{2}{3}\frac{\partial}{\partial y}\left[\mu\left(\frac{\partial U_x}{\partial x} + \frac{\partial U_y}{\partial y} + \frac{\partial U_z}{\partial z}\right)\right]$$
$$+ \frac{\partial}{\partial x}\left[\mu\left(\frac{\partial U_y}{\partial x} + \frac{\partial U_x}{\partial y}\right)\right] + 2\frac{\partial}{\partial y}\left(\mu\frac{\partial U_y}{\partial y}\right) + \frac{\partial}{\partial z}\left[\mu\left(\frac{\partial U_z}{\partial y} + \frac{\partial U_y}{\partial z}\right)\right],$$

$$\tag{3.4}$$

$$\rho\frac{\partial U_z}{\partial t} + \rho\left(U_x\frac{\partial U_z}{\partial x} + U_y\frac{\partial U_z}{\partial y} + U_z\frac{\partial U_z}{\partial z}\right) =$$
$$\rho g_z - \frac{\partial p}{\partial z} - \frac{2}{3}\frac{\partial}{\partial z}\left[\mu\left(\frac{\partial U_x}{\partial x} + \frac{\partial U_y}{\partial y} + \frac{\partial U_z}{\partial z}\right)\right]$$
$$+ \frac{\partial}{\partial x}\left[\mu\left(\frac{\partial U_z}{\partial x} + \frac{\partial U_x}{\partial z}\right)\right] + \frac{\partial}{\partial y}\left[\mu\left(\frac{\partial U_z}{\partial y} + \frac{\partial U_y}{\partial z}\right)\right] + 2\frac{\partial}{\partial z}\left(\mu\frac{\partial U_z}{\partial z}\right).$$

$$\tag{3.5}$$

The left–hand side terms of Eqs. 3.3-3.5 represent the inertia effects and convective transport terms, while the right–hand side terms represent the body forces, the pressure gradient and the viscous term. The continuity equation in the Cartesian component notation is given as:

$$\frac{\partial \rho}{\partial t} + \frac{\partial(\rho U_x)}{\partial x} + \frac{\partial(\rho U_y)}{\partial y} + \frac{\partial(\rho U_z)}{\partial z} = 0. \tag{3.6}$$

Hamrock et al. [86] performed an order–of–magnitude analysis of the Navier–Stokes momentum and continuity equations for fluid film lubrication problems. A summary of the analysis, together with further simplification used to derive the Reynolds equation, is reported by Škurić [42]. The resulting form of the Reynolds equations, written using vector notation, is given as:

$$\underbrace{\nabla_s \bullet \left(\frac{\rho h^3}{12\mu}\nabla_s p\right)}_{\text{Poiseuille}} = \underbrace{\nabla_s \bullet \left[\frac{\rho h \left(\mathbf{U}_\text{a} + \mathbf{U}_\text{b}\right)}{2}\right]}_{\text{Couette}} + \underbrace{\rho\frac{\partial h}{\partial t} + h\frac{\partial \rho}{\partial t}}_{\text{Squeeze and local expansion}},$$

$$(3.7)$$

Eq. 3.7 represents the modified Reynolds equation, which governs the distribution of pressure in viscous thin film flows. This is the pressure–based form of the equation and is discretised using the Finite Area Method (FAM), thus ∇_s represents a two–dimensional surface gradient and $\nabla_s\bullet$ represents a two–dimensional divergence operator. The variables denoted as ρ, μ and p represent the density, fluid viscosity and pressure. The vectors $\mathbf{U}_a$ and $\mathbf{U}_b$ represent the velocities of the two surfaces which are in contact and the variable h represents the thickness of the lubricant film.

3.3.   Modelling Cavitation

Cavitation needs to be taken into account when thin film flows are studied. The possibility of cavitation may be localised to areas between surface asperities (microscale cavitation) or cavitation may occur globally in divergent areas of contact (macroscale cavitation) [87]. Divergent parts of the contact are areas where the gap between the two surfaces in contact widens, thus leading to a sudden decrease in the lubricant pressure, potentially leading to cavitation. On the other hand, cavitation occurs locally when the lubrication film fills the pockets between asperities. This causes the film to become thin or even break apart and leads to the creation of small gaps in the lubricant film. This, in turn, causes pressure drops which result in cavitation. According to Gropper et al. [87], cavitation may occur multiple times in a single contact. This means that special attention needs to be given to the conversation of mass of the fluid (lubricant), when it passes through the rupture and reformation boundaries. The rupture boundary represents the area where the lubricant film breaks down and the onset of cavitation begins, while the reformation boundary refers to the area where cavitation stops (vapour bubbles collapse) and the continuity of the lubricant film is established.

3. Modelling Lubricated Contact of Rough Surfaces

Škurić [42] performed a review of different cavitation models. The author concluded that, while a significant number of different approaches to modelling cavitation exist, most models are developed for specific types of problems. There are some more general models, nevertheless, there is no single universal cavitation model, which would be computationally efficient and easy to implement. The Swift-Stieber [88, 89] cavitation model was one of the earliest developed models for the Reynolds equation. It assumed a zero pressure gradient at the rupture boundary, but does not take into account mass conversation in the zone of cavitation. Thus the model isb unable to correctly predict the location of the reformation boundary. To address the problems with mass conservation, the Jakobsson–Floberg–Olson (JFO) boundary conditions are used [90, 91]. The introduction of the JFO boundary conditions satisfied the mass conservation between the cavitating region and the non–cavitating (full–film) region, Fig. 3.1. According to the JFO boundary condition, a zero gradient boundary condition is applied to the pressure at the rupture boundary B_{rup}, with a constant value of the pressure set to the cavitation pressure of the fluid p_{cav} in the cavitating region, Eq. 3.8. On the other hand, at the formation boundary B_{form}, the boundary condition is set to non–zero gradient for pressure in Eq. 3.9, which represents the feeding of the full–film zone by the cavitating region. The feeding of the full–film zone is depicted in Fig. 3.2. The boundary conditions applied to the rupture B_{rup} and formation B_{form} boundaries are given below:

$$B_{\mathrm{rup}} \quad \rightarrow \quad \nabla_s\, p = 0 \qquad p = p_{\mathrm{cav}}, \qquad (3.8)$$

$$B_{\mathrm{form}} \quad \rightarrow \quad \frac{h^2}{12\mu}\nabla_s p = \frac{\mathbf{U}_{\mathrm{a}} + \mathbf{U}_{\mathrm{b}}}{2}\left(1 - \theta_{\mathrm{form}}\right), \qquad (3.9)$$

where the variable ρ_{form} represents the density of the gas–liquid mixture at the formation boundary B_{form}, looking in the upwind direction. The fraction $\theta_{\mathrm{form}} = \rho_{\mathrm{form}}/\rho_{\mathrm{cav}}$ represents fractional film content inside the cavitating region.
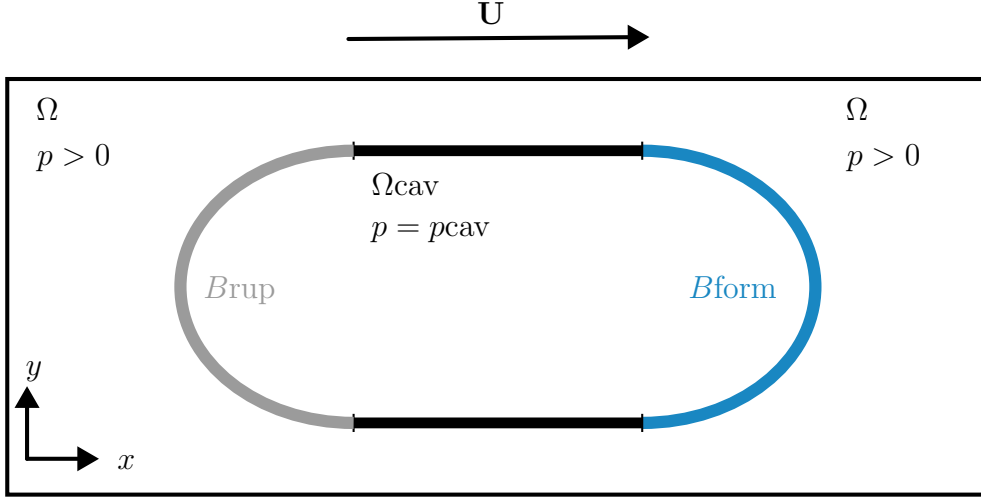
Figure 3.1: Cavitating and non–cavitating (full–film) regions.
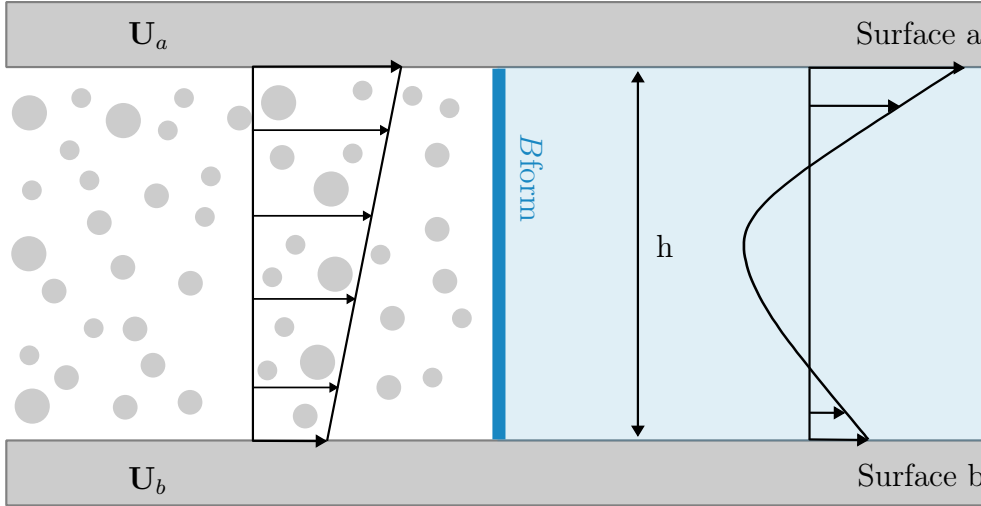
Figure 3.2: Representation of the formation boundary B_{form}

Elrod and Adams [92] built upon the JFO boundary conditions and incorporated them into their cavitation algorithm. The cavitation algorithm is developed using the Finite Difference Method and dividing the computational domain iteratively into cavitating and full–film regions. The authors proposed the following form of the Reynolds equation:

$$\nabla_s \bullet \left(g \frac{\beta h^3}{12\mu} \nabla_s \theta \right) = \nabla_s \bullet \left[\frac{\theta h \left(\mathbf{U}_a + \mathbf{U}_b \right)}{2} \right], \tag{3.10}$$

33

where β represents the bulk modulus of the fluid and is calculated as $\beta = \rho\left(\partial p/\partial\rho\right)$. The authors also introduced a switch function to terminate the pressure term of Eq. 3.10 inside the cavitating zone. The switch function g is given as:

$$
\begin{aligned}
\theta < 1 &\longrightarrow \quad \text{cavitating} \quad \longrightarrow \quad g = 0 \\
\theta \geq 1 &\longrightarrow \quad \text{full-film} \quad \longrightarrow \quad g = 1,
\end{aligned}
\tag{3.11}
$$

The approach used by Elrod and Adams treats the flow of the lubricant in the cavitating region as a two–phase flow, consisting of the liquid lubricant and a gas with a homogeneous density. In the full–film region, the liquid lubricant is treated as a compressible flow with a constant bulk modulus. The value of θ in Eq. 3.11 represents the fractional film content, which governs the treatment of the lubricant flow, switching between compressible flow in the full–film region and the lubricant–gas mixture in the cavitating region. According to Škurić [42], the approach proposed by Elrod and Adams can be successfully applied to hydrodynamic lubrication, but instabilities caused by the switch function g may cause convergence problems. The instabilities occur due to sudden changes between the elliptic nature of the Eq. 3.10 in the non–cavitating (full–film) region and the hyperbolic nature in the cavitating region..

Many different authors tried to improve upon the Elrod–Adams cavitation model to achieve better stability [93], improve convergence [94, 95] and implement the model in the FEM [96, 97] or FVM [98] frameworks. Other authors focused on expanding the model to include changes to lubricant properties. More specifically, Sahlin et al. [99], expanded the algorithm to considering arbitrary density–pressure relations by using a switch function that terminates the pressure gradients in regions where cavitaion occurs. Bayada and Chupin [73] proposed a mixture model which can incorporate viscosity and incompressibility changes. Almqvist and Wall [100] introduced a model which also consideres piezoviscosity and non–Newtonian effects of the lubricant. The large number of cavitation models which were developed based on the Elrod–Adams algorithm, leads to the conclusion that choice of the model to be used should be based on specific type of application and that no single general model can be applied.

3.4. Averaged Reynolds Equation

The modified Reynolds equation (Eq. 3.7) presented in Section 3.2. governs the distribution of pressure in viscous thin film flows between smooth surfaces in contact. To be able to calculate hydrodynamic flow of lubricant between real surfaces, Eq. 3.7 needs to be modified to take into account the effect of micro–asperities on the lubricant flow.

In contrast to smooth surfaces, which have minimal irregularities or roughness on both the macroscopic and microscopic level, real surfaces may seem smooth on the macroscopic level, but have a large number of asperities on the microscopic level. These micro–asperities are characterised as surface roughness and influence lubricant flow [11]. The height of the micro–asperities influences the flow of the lubricant, depending on the height of the asperities and the thickness of the lubricant film. Depending on the interaction of the surface asperities and the lubricant film, Wilson [101] differentiates between four distinct lubrication regimes: hydrodynamic thick film, hydrodynamic thin film, mixed and boundary lubrication. A graphical representation of the aforementioned regimes is given in Fig. 3.3. During hydrodynamic lubrication, the two surfaces are not in direct contact, but are separated by a fluid (lubricant) film. If the thickness of the lubricant film is such that the surfaces are sufficiently separated, so that the surface roughness does not influence the flow, the lubricant flow is in the hydrodynamic thick film regime [102]. As the lubricant film is thick enough, we can consider the surfaces smooth. On the other hand, in the thin film hydrodynamic regime, the surfaces are still completely separated by the lubricant film, but surface roughness heavily influences the flow on the lubricant. In the boundary lubrication regime, the entirety of the contact pressure between the surfaces is carried by the asperities in contact, while the lubricant film is reduced to only small amounts of lubricant separated into valleys by the asperities [102]. In the mixed lubrication regime, the surface asperities are in contact, but they do not carry the entirety of the contact pressure. The contact pressure is shared between the lubricant film and the asperities which are in contact [102].

HYDRODYNAMIC THICK FILM REGIME

HYDRODYNAMIC THIN FILM REGIME

MIXED REGIME

BOUNDARY REGIME
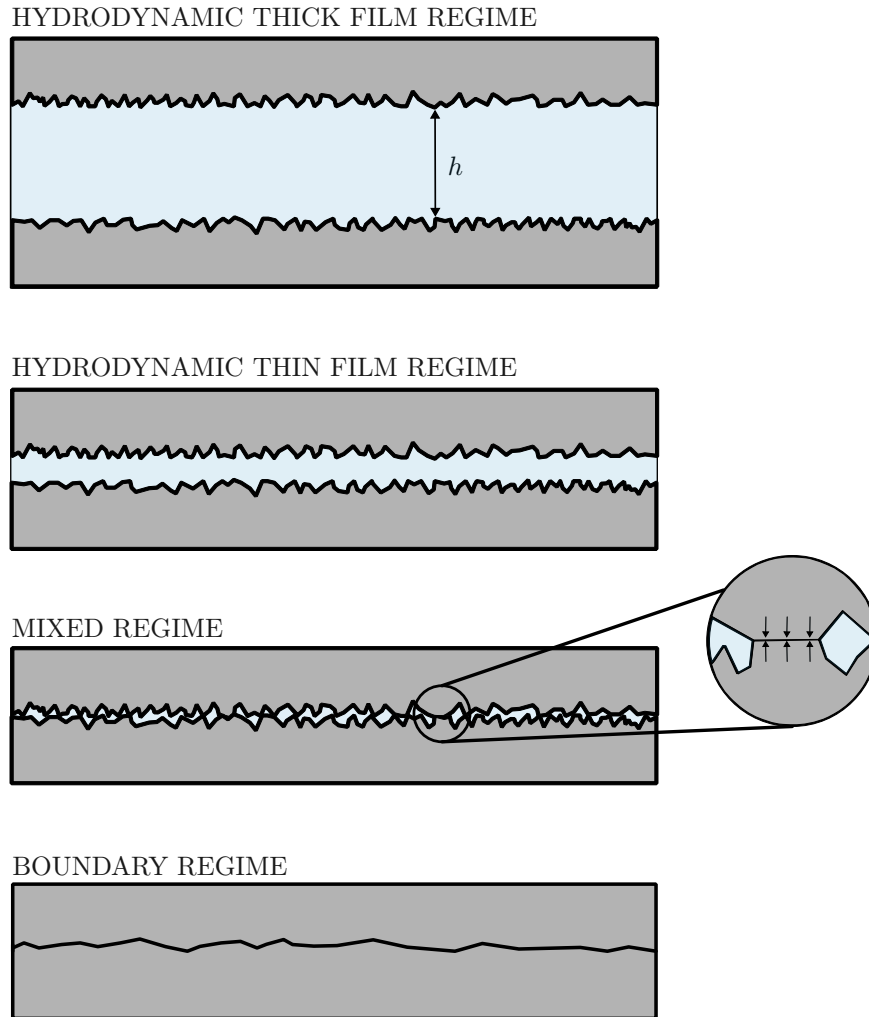
Figure 3.3: Different lubrication regimes.

Almqvist investigated the influence of surface roughness on thin film flows, in order to enable efficient numerical analysis of contacts under different lubrication regimes [103]. The author concluded that the Reynolds equation, as given in Eq. 3.7, is not appropriate for calculating lubricant flow for regimes where surface roughness influences the flow. Using this form of the Reynolds equation would require a very dense computational mesh, capable of accurately representing the surface roughness, which would lead to significant computational demands. Almqvist suggested an alternative approach that introduces modifications to the Reynolds equation, which would allow the surface roughness to influence the lubricant flow, without the need to preform the calculation on the

microscopic level [103]. This approach uses a statistical representation of the surface topography, thus making it computationally less demanding than relying on a dense computational mesh. As such, this approach is only slightly more computationally demanding than calculating hydrodynamic flow between smooth surfaces [103].

A similar approach was proposed by Patir and Cheng [104, 105]. The authors introduced a modification to the Reynolds equation by employing correction factors. By including these correction factors, which the authors defined as flow factors, in Eq. 3.7, thin film flow between rough surfaces may be considered:

$$
\nabla_s \bullet \left(\phi_{xy} \frac{\rho h^3}{12\mu} \nabla_s p \right) = \nabla_s \bullet \left[\frac{\rho h \left(\mathbf{U}_a + \mathbf{U}_b \right)}{2} \right] - \nabla_s \bullet \left[\frac{\phi_s \rho \left(\mathbf{U}_a - \mathbf{U}_b \right)}{2} \right] R_q + \frac{\partial(\rho h)}{\partial t}.
$$
(3.12)

Eq. 3.12, is the **averaged** Reynolds equation and contains flow factors: the pressure flow factor ϕ_{xy} and the shear flow factor ϕ_s. Eq. 3.12 also includes the combined root mean squared (RMS) surface roughness R_q of the surfaces in contact (denoted as a and b): $R_q = \sqrt{R_{q_a}^2 + R_{q_b}^2}$. The approach in question has the advantage that it is applicable to the thick hydrodynamic, thin hydrodynamic and the mixed lubrication regimes, relying on a single equation. For the near–boundary lubrication regime, where the film thickness is small compared to the surface roughness ($h_q < 1$), i.e. asperities in contact occupy a large portion of the total area, the flow factors given by Patir and Cheng [104, 105] do not apply. Wilson and Marsault [106] presented semi–empirical equations for calculating flow factors, which would allow for the averaged Reynolds equation to be applicable for the full range of lubrication regimes, including the near–boundary regime.

Škurić [42] performed an analysis of Eq. 3.12 and the assumptions necessary for the use of flow factors. As flow factors rely on statistical analysis of the surface, the distance between calculation points must include a large enough number of asperities for the statistical representation to be representative, on the other hand the chosen distance must remain small when compared to the whole geometry in question. Once the flow factors are determined, they can be included in Eq. 3.12 and have a minimal effect on the computational performance. Any additional computation, when compared to a hydrodynamic case, is attributed only to the

calculation of flow factors using analytical equations, based on the film thickness for a certain computational point. Škurić [42] also reported some drawbacks of this approach: no theoretical explanation was found regarding the number of deterministic calculations needed to acquire statistically relevant results for flow factor calculation and uncertainty on how to truncate results in order to reduce the influence of boundary conditions [42].

3.5. Modelling Contact

In order to analyse wear using Archard's wear model presented in Ch. 2., information regarding surface contact needs to be provided. To calculate the value of the normal contact pressure, needed for the wear model, an appropriate contact model needs to used. For wear to occur under lubricated contact conditions, the lubricant film thickness needs to be insufficient to fully separate the surfaces or the lubricant film needs to be disrupted. Thus, wear is predicted to occur under conditions where direct surface–to–surface contact may occur, i.e. under mixed and boundary lubrication conditions.

The previous section (Sec. 3.4.) offered an overview of different lubrication regimes. It was shown that in the mixed and boundary lubrication regimes, the contact pressure is shared between the lubricant film and the asperities in contact. This is why, when analysing lubricated contact conditions, we also need to be able to model direct solid–to–solid contact conditions, i.e. dry contact conditions. Under direct solid–to–solid contact between surface asperities, depending on the applied load, the asperities are flattened and undergo elastic or plastic deformations.

If the surfaces in contact are not smooth and surface roughness needs to be considered, the contact model needs to be able to take into account surface topographies in one if two ways: using statistical or deterministic modelling [42].

Statistical contact models consider the statistical distribution of surface asperities to predict the behaviour of rough surfaces in contact. They are used when dealing with complex surface topographies which cannot be modelled explicitly. One of the earliest statistical contact models is the model derived by Greenwood and Williamson (GW) [107]. The GW model used Hertzian contact

theory for asperity deformations. The model introduced elastic contact of asperities and relied on Gaussian height distribution. Due to limitations of the model, most notably that fact that only elastic deformations were considered, many authors tried to improve upon the original GW model [108]. Jackson [109] introduced closed–form solutions to integrals, which were calculated numerically in the GW model. The GW model was expanded to be applicable to asperities with non–uniform radii [110], curved surfaces [111], anisotropic surfaces [112] and misaligned rough surfaces [113]. Pullen and Williamson [114] used the GW model to investigate plastic contact between rough surfaces, while Chang, Etsion and Bogy [115] expanded the GW model by incorporating elastic–plastic deformation, accounting for the transition between elastic and plastic deformation. Zhao, Maietta and Chang [116] improved the accuracy of the GW model in different contact regimes. Jackson and Green (JG) [117, 118] presented a statistical model based on finite element simulations of a hemisphere deforming against a flat. They used the GW model to determine elastic deformations, while adding analytical equations for plastic deformation, which they derived from their finite element simulations. Wadwalkar et al. [119] used finite element simulations to extend the JG model for larger plastic deformations, while Peng et al. [120] used finite element simulations of single–asperity contact to derive a contact model for elastic—perfectly—plastic rough surfaces.

The statistical contact models presented earlier rely on different surface properties as input data. The surface data required for these models include: asperity density, mean asperity curvature and RMS surface roughness. These variables are usually derived from surface roughness measurements [112] or using spectral moments [109]. Statistical contact models may be computation very efficient and easy to implement, but as they rely on only a few parameters to describe surfaces, the same parameters may be calculated for very different topographies [42]. Furthermore, the models use a mean value of the asperity curvature, which usually varies between individual asperities [103].

While statistical contact models provide easy implementation and computational efficiency, they introduce uncertainties due to simplifications used during their derivation. For more accurate results, deterministic models should be used, which account for surface topographies explicitly and without statistical averag-

ing. Deterministic models enable the direct use of surface measurements (precise topography measurements) to calculate contact parameters such as the contact area, contact pressure and deformations [42]. Megalingam and Ramji [108] reported a number of authors using FEM analysis together with deterministic contact models. Yastrebov et al. [121] used FEM to resolve normal contact between real rough surfaces. The authors concluded that for surface topographies of rough surfaces, which have fine–scale, rapidly varying features, the computational domain necessary for accurately describing high frequency spatial variations of the surface heights increases rapidly, leading to very high computational efforts. Alternatively, deterministic models can be based on closed–form analytical solutions for specific topographies [122, 123] or may employ the Fast Fourier Transformation (FFT) [43, 124, 44, 45].

Focusing on FTT–based methods due to faster calculation time, the model developed by Stanley and Kato [43] will be introduced first. Stanley and Kato [43] developed a three–dimensional elastic contact model and analysed interactions between a rough half–space and a rigid plane. The authors used a combination of linear elasticity and FFT to calculate contact pressures and surface normal displacements, while also accounting for multiscale topography and asperity interactions. The model was extended by Almqvist et al. [124] as to include elastic–perfectly–plastic deformations. A more detailed implementation and its application was given by Sahlin et al. [44, 45].

FFT–based deterministic contact models enable fast calculation of contact pressures, surface deformations, and contact areas, based on real rough surface measurements. Wear analysis of real rough surfaces requires the surface topographies to be as accurate as possible, deterministic models have an obvious advantage over statistical model. Statistical contact models may demand fewer computational resources, but do not provide accurate results. On the other hand, FFT–based deterministic models provide the required accuracy, without being computationally too expensive.

3.6. Properties of Lubricants

In lubricated contact analysis, the properties of the lubricant film change due to changes in pressure and temperature. In an analysis of the Reynolds equation [42] changes in lubricant density and viscosity were identified as the most important changes in lubricant properties. Proper treatment of these changes is necessary in order to accurately capture lubricant film characteristics, such as pressure, film thickness and traction.

3.6.1. Pressure and Temperature Dependence of Viscosity

According to Habchi [125] lubricant viscosity is highly sensitive to changes in pressure. Furthermore, it is also dependent on temperature and, for non–Newtonian lubricants, on shear stress. Three commonly used pressure–viscosity relations for numerical analysis of lubricated contacts are given [125]:

Barus law:
$$\mu_\mathrm{B} = \mu_0 \exp\left(\alpha p\right), \tag{3.13}$$

Roelands-Houpert model:
$$\mu_\mathrm{H} = \mu_\mathrm{R} \exp\left(-\beta^*(T - T_0)\right), \tag{3.14}$$

$$\mu_\mathrm{R} = \mu_0 \exp\left(\alpha^* p\right), \tag{3.15}$$

Doolittle model:
$$\mu(p, T) = \mu_\mathrm{R} \exp\left[BR_0\left(\frac{\frac{V_\infty}{V_{\infty\mathrm{R}}}}{\frac{V}{V_\mathrm{R}} - R_0 \frac{V_\infty}{V_{\infty\mathrm{R}}}} - \frac{1}{1 - R_0}\right)\right]. \tag{3.16}$$

The relation given in Eq. 3.13 is the Barus law, one of the most commonly used relations describing the pressure dependence of viscosity. The Barus law defines viscosity μ_B as function of pressure by relying on a constant pressure–viscosity coefficient α. Due to the face that the coefficient α is kept constant, the applicability of this model is limited to pressures under 0.5 GPa, loosing accuracy at higher pressures [11]. Roelands [126] and Houpert [127] improved upon Barus' model by adding coefficient for both the temperature (α^*) and pressure (β^*) dependence, as can be noted in Eqs. 3.14 and 3.15. The Roelands–Houpert model has been routinely applied for viscosity calculations [11], but has limited

accuracy under high pressures [128, 129]. Doolittle [130] presented a free volume model 3.16, which uses the relative volume of molecules per unit of free volume V/V_{R}. This model is more accurate at high pressures than the Roelands–Houpert model, but due to the fact that it relies on detailed experimental data and due to its complex implementation, the model is rarely used. More recently, due to the availability of detailed experimental data on the behaviour of lubricants, the Roelands–Houpert model, in combination with Tait's equation of state [125], has seen wider use in modelling of lubricant behaviour [5, 76].

3.6.2. Shear Stress Dependence of Viscosity

When lubricants are put under extreme conditions, like high pressures (up to 3 GPa) and high entrainment speeds, they exhibit non–Newtonian behaviour and they loose the linear stress–strain relationship [125]. To capture the non–Newtonian behaviour, shear–thinning and limiting–shear–stress models are used [131]. When lubricants are considered viscoelastic, i.e. they do not exhibit a linear stress–strain relationship, their total shear strain rate can be expressed as the sum of elastic and viscous strain rates [132]:

$$\dot{\gamma} = \dot{\gamma}_{\mathrm{e}} + \dot{\gamma}_{\mathrm{v}}. \tag{3.17}$$

The two most commonly used models are the Ree–Eyring and the Carreau Model [42]. Introduced by Johnson and Tevaarwerk [133], the Ree–Eyring model is a shear–thinning model, which describes the shear–thinning behaviour of the lubricant using a hyperbolic sine law. The model was later expanded to include limiting shear stress [134]. Bair et al. [129] performed experimental measurements which lead to the conclusion that viscous response for elastohydrodynamic contacts is not likely and that the elastic strain rate can be disregarded, resulting in a expression for Ree–Eyring shear–thinning viscosity of the fluid:

$$\eta_{\mathrm{RE}} = \frac{\tau_{\mathrm{E}}}{\dot{\gamma}} \sinh^{-1}\left(\frac{\mu\dot{\gamma}}{\tau_{\mathrm{E}}}\right), \tag{3.18}$$

where τ_{E} is the Eyring stress, $\dot{\gamma}$ is the shear rate, μ is the low–shear viscosity

(described in Subsec. 3.6.1.) and ν_{RE} the Ree–Eyring shear–thinning viscosity of the lubricant.

Another widely used model is the Carreau [135] shear–thinning model. This model uses the power–law equation for shear–thinning and was modified by Bair et al. [136, 137] to account for shear stress distribution using the relaxation time $\lambda = \mu/G$ and to include the Yasuda parameter a, resulting in a more general expression with better experimental fit then the original Carreau equation [138]:

$$\eta_{\mathrm{CY}} = \mu \left[1 + \left(\frac{\tau}{G} \right)^a \right]^{\frac{n-1}{an}}. \tag{3.19}$$

Given in Eq. 3.19 is the expression for the Carreau–Yasuda equation used to calculate shear–thinning viscosity, where G is the effective shear modulus, a the Yasuda parameter and $\lambda = \mu/G$ the relaxation time.

The Ree–Eyring and Carreau–Yasuda models are not the only models used to describe the shear–thinning behaviour of lubricants under different conditions, but they are the well–suited for numerical analysis of lubricated contact, as they are able to effectively capture the non–Newtonian behaviour of lubricants at high shear rates [125].

3.6.3. Pressure and Temperature Dependence of Density

According to Hajishafiee [131], the lubricant density is significantly less sensitive to changes in pressure than viscosity, thus less research was aimed at predicting lubricant compressibility than at rheological properties (shearing and viscosity) of lubricants. One of the most widely used density–pressure relations is the one presented by Dowson and Higginson [139] for isothermal conditions:

$$\frac{\rho}{\rho_{\mathrm{ref}}} = \frac{C_1 + C_2(p - p_{\mathrm{ref}})}{C_1 + (p - p_{\mathrm{ref}})}, \tag{3.20}$$

where C_1 and C_2 are constants which depend on the lubricant, while ρ_{ref} is the reference density at reference pressure p_{ref}. Dowson and Higginson [139] initially proposed coefficients ($C_1 = 0.59\mathrm{x}10^9$,$C_2 = 1.34$ for mineral oils under pressures up to 400 MPa. Sahlin et al. [99] provided modified coefficients for better accuracy

under pressure up to 3 GPa. Two more density–pressure relations are widely used for calculating density changes in numerical analyses of lubricated contacts [42]:

Murnaghan model:
$$\frac{\rho_0}{\rho} = \left(1 + \frac{K_0'}{K_0}p\right)^{(-1/K_0')}, \tag{3.21}$$

Tait equation of state:
$$\frac{\rho_0}{\rho} = 1 - \frac{1}{1 + K_0'}\ln\left[1 + \frac{p}{K_0}\left(1 + K_0'\right)\right]. \tag{3.22}$$

The Murnaghan model [76, 140] is a popular density–pressure relation given in Eq. 3.21, where K_0' denotes the rate of change of the bulk modulus at initial pressure and K_0 is the bulk modulus at ambient pressure. Expressed by Eq. 3.22 is the Tait equation of state [125], another density–pressure relation which uses the same parameters as the Murnaghan model to calculate density. While the Murnaghan and the Tait models provide more physically informed results, they remain more complicated than the Dowson–Higginson model and require specific experimental data, which may not always be available [42].

As temperature variations influence compressibility, several authors expanded the aforementioned equations to model the influence of both the temperature and pressure changes on the density of lubricants. Linear temperature corrections were added to the Murnaghan equation (Eq. 3.21) [76], to the Tait equation (Eq. 3.22) [125] and to the Dowson–Higginson equation (Eq. 3.20) [141, 142, 143].

3.7. Conclusion

This chapter offered a detailed overview of numerical models necessary for contact analysis of lubricated rough surfaces. The modified Reynolds equation (Eq. 3.7), which governs the lubricant pressure in thin film flows, was presented together with its derivation from the Navier–Stokes and continuity equations. The problem of including cavitation was discussed next. The boundary conditions necessary for ensuring mass conservation for both the cavitating and full–film regions were introduced: the zero–gradient pressure boundary condition at the rupture boundary and the non–zero pressure gradient at the formation boundary (Eq. 3.8, Eq. 3.9).

To include the effects of surface roughness on thin film flows, the averaged Reynolds equation was introduced (Eq. 3.12). The averaged form of the Reynolds equation uses flow factors (the pressure flow factor ϕ_{xy} and the shear flow factor ϕ_s) to account for the influence of surface asperities without leading to a large increase in computational requirements. The flow factors are calculated analytically based on surface parameters.

A review of contact models was given next. Contact models are used to calculate contact parameters (e.g. contact pressure and area of contact) for direct solid–to–solid contacts. Statistical contact models, such as the Greenwood–Williamson model, were discussed along deterministic contact models, such as the Stanley and Kato model. In contrast to statistical models, deterministic contact models directly use surface topography data to calculate the required contact parameters (contact pressure, area, deformations), providing higher accuracy whit an acceptable increase in computational requirements.

Lastly, a review was given of relations describing the changes in density and rheological properties of lubricant due to variations in pressure, temperature and shear stress. These relations include models for viscosity–pressure dependence, such as the Barus (Eq. 3.13) and Roelands–Houpert (Eq. 3.14) model, and density–pressure models, like the Dowson–Higginson model (Eq. 3.20).

Together, these models enable the formation of a framework for understanding and predicting the behaviour of contact of rough surfaces under different lubrication regimes, forming the foundation for the development of a numerical algorithm for the analysis of surface wear under lubricated contact conditions.

4. Finite Area Method

4.1. Introduction

This chapter offers an overview of the Finite Area Method (FAM), a numerical
discretisation technique related to the Finite Volume Method (FVM), and con-
sidered as a two–dimensional counterpart to the Finite Volume Method. The
computational mesh employed in the FAM is created by discretisation of spatial
curved surfaces using polygonal finite areas of arbitrary shape. In accordance
with the FVM principles, the computational point is located at the face centroid.

Originally developed and implemented in `foam-extend` by Tuković [1], an
overview of the FAM, the principles for the discretisation of the computational
domain and transport equations, and a discussion regarding the treatment of
boundary conditions was given by in [42], however a brief review of the method
is given for sake of completeness. The discretisation of the spatial domain is
discussed first, continuing with a discussion on the discretisation of the transport
equation. Lastly, an discussion on the treatment of boundary conditions is given.

4.2. Spatial Domain Discretisation

Figure 4.1 shows a curved surface with a time–dependent position and shape. If
we consider the depicted surface as a computational domain, it can be discretised
spatially using a finite number of finite area faces. The resulting computational
domain consists of said number of non–overlapping finite area faces. Each finite
area face is a convex polygon that can have an arbitrary number of straight edges,
where the centroid of the polygon is considered as the computational point of the
finite area face. Two such faces are shown in Fig. 4.2, representing neighbouring
faces P and N, where: S_P is the surface area of face P and $\mathbf{n}_\mathrm{P}$ is the unit normal
vector placed at the centroid of face P. The two faces are connected by edge
e with a length of L_e, and a unit normal vector $\mathbf{n}_\mathrm{e}$ placed in the centroid of

edge e. The unit normal vector $\mathbf{n}_e$ can be calculated as the mean value between the two unit normal vectors located at the endpoints of edge e, while the vector perpendicular to the unit vector $\mathbf{n}_e$ and edge e, which points to the neighbouring face N, is called the unit binormal vector $\mathbf{m}_e$. The equations for calculating the vectors $\mathbf{n}_e$ and $\mathbf{m}_e$ are:

$$\mathbf{n}_e = \frac{\mathbf{n}_i + \mathbf{n}_j}{|\mathbf{n}_i + \mathbf{n}_j|}, \tag{4.1}$$

$$\mathbf{m}_e = \hat{\mathbf{e}} \times \mathbf{n}_e, \tag{4.2}$$

where the unit vector $\hat{\mathbf{e}}$ is parallel to the edge e. For the calcualtion of a unit normal vector located at an arbitrary point of the mesh, the reader is referred to [1]. The line connecting the face centres of the two neighbouring finite area faces P and N is the geodesic line $Pe'N$. If there is zero–skewness between the neighbouring faces P and N at the edge e, the point e', defined as the point where the geodesic line intersects the edge e, is located at the centroid of the edge e. If skewness between the faces exists, the position of the intersection point e' can be determined as:

$$\mathbf{r}'_e = \mathbf{r}_i + \beta_e \mathbf{e}. \tag{4.3}$$

The vector $\mathbf{e} = \mathbf{r}_j - \mathbf{r}_j$ is parallel to the edge e and its length is equal to the length of the edge L_e. The vectors $\mathbf{r}_i$ and $\mathbf{r}_j$ are position vectors of points i and j, while β_e is a coefficient calculates using:

$$\beta_e = \frac{[\mathbf{d}_e \times (\mathbf{r}_i - \mathbf{r}_P)] \bullet (\mathbf{d}_e \times \mathbf{e})}{|\mathbf{d}_e \times \mathbf{e}|^2}, \tag{4.4}$$

where vector $\mathbf{d}_e$ is defined as $\mathbf{d}_e = \overline{PN}$ and $\mathbf{r}_P$ is the position vector of point P. Eq. 4.4 is used to calculate β_e, in a way that the triangle defined by the vectors $\overline{PN}$, $\overline{Pe'}$ and $\overline{e'N}$ has minimal surface area [1].

To calculate the geometric properties of finite area faces, the same approach is used as for finite volume cells. The definition of finite area faces is based on edge addressing, relying on a list of points, a list of edges, a list of faces and a list of boundaries. The criteria used for ensuring topological and geometrical validity of finite volume meshes [85] are also applied to finite area meshes.
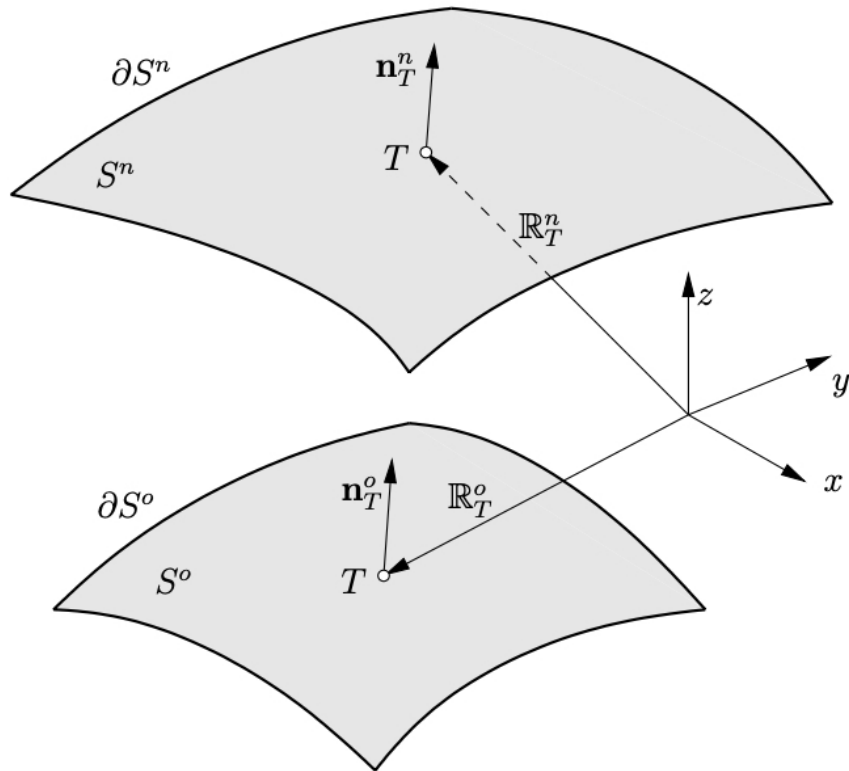
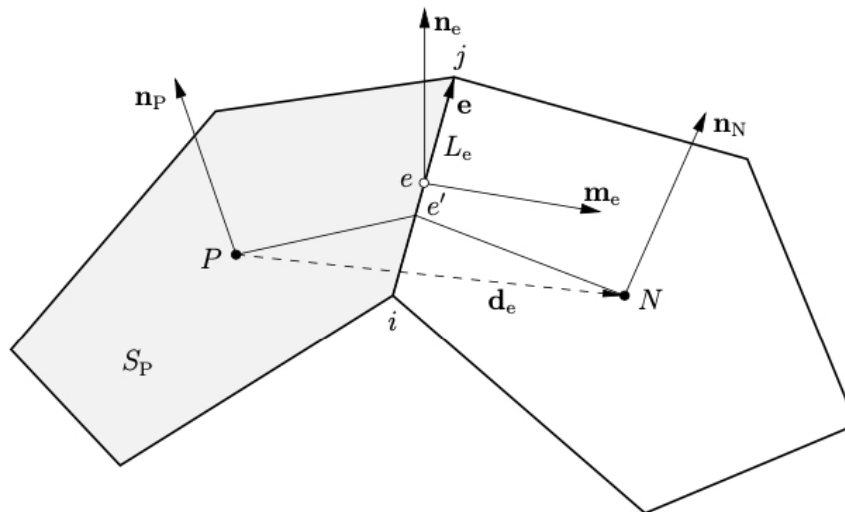Figure 4.1: Time–dependent shape of curved smooth surface [1].

Figure 4.2: Neighbouring finite area faces (P and N) [1].

4.3.   Transport Equation Discretisation

Tukuvić [1] provided the integral from of the differential equation for the surface transport of property ρ along a deformable surface:

$$\frac{\mathrm{d}}{\mathrm{d}t} \int_S \rho \, \mathrm{d}S + \oint_{\partial S} \mathbf{m} \bullet (\mathbf{v}_t - \mathbf{b}_t) \rho \, \mathrm{d}L = \oint_{\partial S} \mathbf{m} \bullet (\Gamma_\rho \nabla_s \rho) \, \mathrm{d}L + \int_S s_\rho \, \mathrm{d}S. \qquad (4.5)$$

Looking at the expression given by Eq. 4.5, ∂S denotes a curve enclosing an arbitrary movable surface S and $\mathbf{m}$ is a unit binormal vector. The material surface velocity vector and the arbitrary surface velocity vector have tangential components, denoted as $\mathbf{v}_t$ and $\mathbf{b}_t$, respectively. The following expression, provided by Tuković [1], is used to limit the movement of these two surfaces:

$$\mathbf{n} \bullet \mathbf{b} = \mathbf{n} \bullet \mathbf{v}. \qquad (4.6)$$

After performing the finite area discretisation of Eq. 4.5, assuming normal movement of the finite are faces ($\mathbf{b}_t = 0$), and integrating the equation over the finite area S_P, the resulting equation is given:

$$\underbrace{\frac{\mathrm{d}}{\mathrm{d}t} \int_{S_P} \rho \, \mathrm{d}S}_{\text{Temporal term}} + \underbrace{\oint_{\partial S_P} \mathbf{m} \bullet \mathbf{v}_t \rho \, \mathrm{d}L}_{\text{Convection term}} = \underbrace{\oint_{\partial S_P} \mathbf{m} \bullet (\Gamma_\rho \nabla_s \rho) \, \mathrm{d}L}_{\text{Diffusion term}} + \underbrace{\int_S s_\rho \, \mathrm{d}S}_{\text{Source term}} \;, \quad (4.7)$$

where the boundary of finite area S_P is denoted as ∂S_P and contains a finite number of straight lines.

For the discretisation of the convection and diffusion spatial terms in Eq. 4.7, linear distribution of variable ρ over finite area P is assumed [1]:

$$\rho(\mathbf{r}) = \rho_P + (\mathbf{r} - \mathbf{r}_P) \bullet (\nabla_s \rho)_P, \qquad (4.8)$$

where the surface gradient of variable ρ at the face centroid is denoted as $(\nabla_s \rho)_P$, while the position vector of point P is given as $\mathbf{r}_P$. Furthermore, the temporal distribution of variable ρ over a defined interval $[t^o, t^n]$ is given as:

$$\rho(t^o + \Delta t) = \rho(t^o) + \Delta t \left(\frac{\partial \rho}{\partial t} \right)^o. \qquad (4.9)$$

For the spatial term discretisation, all tensor variables located at the face area centres and edge centres are assumed to be defined in the global Cartesian coordinate system.

4.3.1. Spatial Terms

For the finite area discretisation of surface integrals, the central point rule is adopted [1]:

$$\int_{S_P} \rho(\mathbf{r}) \, \mathrm{d}S = \rho_P S_P. \tag{4.10}$$

The line integral over the surface boundary can be expressed as the sum of line integrals per every edge (central point rule), as each finite area is bounded by a finite number of straight edges. The line integral, in which the value of variable ρ at the edge centroid e is defined as $\rho_e = \rho(\mathbf{r}_e)$ and the edge length defined as L_e, can be expressed as:

$$\oint_{\partial S_P} \rho(\mathbf{r}) \, \mathrm{d}L = \sum_e \int_{L_e} \rho(\mathbf{r}) \, \mathrm{d}L = \sum_e \rho_e L_e. \tag{4.11}$$

Convection Term

By using Eq. 4.11, discretisation of the convection term results in:

$$\begin{aligned}
\oint_{\partial S_P} \mathbf{m} \bullet \mathbf{v}_t \rho \, \mathrm{d}L &= \sum_e \mathbf{m}_e \bullet (\mathbf{v}_t)_e L_e \rho_e \\
&= \sum_e \dot{s}_e \rho_e,
\end{aligned} \tag{4.12}$$

where the edge flux of the material surface is defined as $\dot{s}_e = \mathbf{m}_e \bullet (\mathbf{v}_t)_e L_e$.

An appropriate convection discretisation scheme must be applied for the calculation of the value of variable ρ on the edge e using the values stored in the centroids of the neighbouring face areas. According to Tuković [1], if the variable ρ is a scalar variable, conventional finite volume schemes may be applied, but the Euclidean distance between neighbouring finite volume should be replaced by the geodesic distance between neighbouring finite areas.

To calculate the scalar variable ρ on the edge e by using the central differencing scheme, the following equation is used:

$$\rho_e = e_x \rho_P + (1 - e_x)\rho_N, \tag{4.13}$$

where e_x represents an interpolation defined as a ratio of geodesic distances depicted in Fig. 4.2:

$$e_x = \frac{\overline{eN}}{\overline{PN}}.$$

If the variable ρ is a vector variable $\mathbf{V}$, it should be defined in the global Cartesian coordinate system. The edge value of the vector variable can be interpolated using the central differencing scheme as follows [1]:

$$\mathbf{V}_e = (\mathbf{C}_e)^T \bullet [e_x \mathbf{C}_P \bullet \mathbf{V}_P + (1 - e_x)\mathbf{C}_N \bullet \mathbf{V}_N]. \tag{4.14}$$

If the variable ρ is a second rank tensor variable $\mathbf{T}_e$, the interpolation using the central differencing scheme is performed as:

$$\mathbf{T}_e = (\mathbf{C}_e)^T \bullet [e_x \mathbf{C}_P \bullet \mathbf{T}_P \bullet (\mathbf{C}_P)^T + (1 - e_x)\mathbf{C}_N \bullet \mathbf{T}_N \bullet (\mathbf{C}_N)^T] \bullet \mathbf{C}_e, \tag{4.15}$$

where $\mathbf{T}_P$, $\mathbf{T}_N$ and $\mathbf{T}_e$ are transformed from the global Cartesian to the local orthogonal curvilinear coordinate system using transformation tensors $\mathbf{C}_P$, $\mathbf{C}_N$ and $\mathbf{C}_e$.

Diffusion Term

By using Eq. 4.11, the diffusion term can be discretised as:

$$
\begin{aligned}
\oint_{\partial S_P} \mathbf{m} \bullet (\Gamma_\rho \nabla_s \rho) \, \mathrm{d}L &= \sum_e \mathbf{m}_e \bullet (\Gamma_\rho \nabla_s \rho)_e L_e \\
&= \sum_e (\Gamma_\rho)_e L_e \mathbf{m}_e \bullet (\nabla_s \rho)_e,
\end{aligned}
\tag{4.16}
$$

where the normal surface gradient of variable ρ on the edge e is given as $\mathbf{m}_e \bullet (\nabla_s \rho)_e$.

The orthogonality of the computational mesh determines the discretisation of the normal surface gradient. For every edge on a non–structured finite area mesh (Fig. 4.3), a non–orthogonality angle α_e is defined [1]:

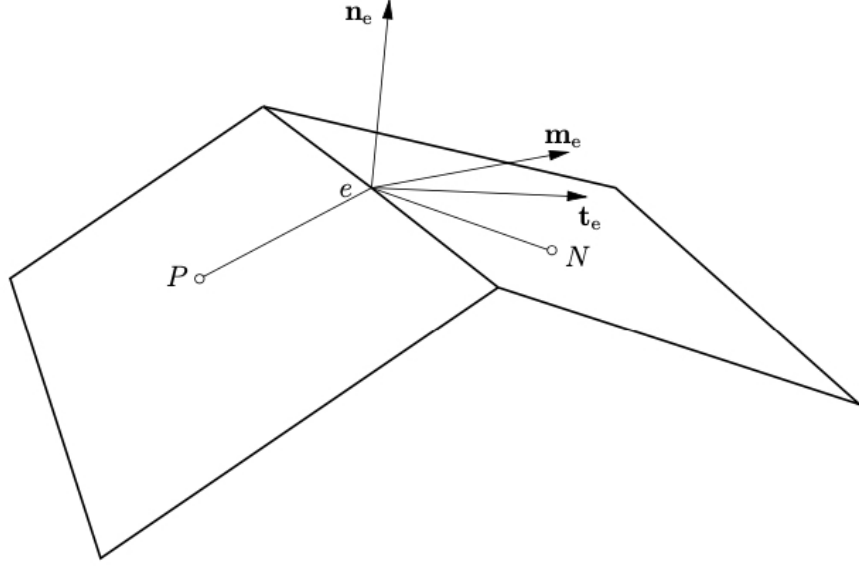$$\alpha_e = \arccos(\mathbf{t}_e \bullet \mathbf{m}_e). \tag{4.17}$$

Figure 4.3: Definition of non–orthogonality for a finite area mesh [1].

The definition of mesh orthogonality at edge e when $\alpha_e = 0$ is given as:

$$\mathbf{t}_e \boldsymbol{\cdot} \mathbf{m}_e = 1,$$

while the expression for calculating the normal surface gradient of variable ρ on edge e for an orthogonal finite area mesh, is given as:

$$\mathbf{m}_e \boldsymbol{\cdot} (\nabla_s \rho)_e = \frac{\rho_N - \rho_P}{L_{PN}}, \tag{4.18}$$

where the geodesic distance L_{PN} is the distance between centroids of neighbouring faces P and N. For non–orthogonal meshes, a correction is introduced when calculating the normal surface:

$$\mathbf{m}_e \boldsymbol{\cdot} (\nabla_s \rho)_e = \underbrace{|\boldsymbol{\Delta}_e| \frac{\rho_N - \rho_P}{L_{PN}}}_{\text{Ortho. contribution}} + \underbrace{\mathbf{k}_e \boldsymbol{\cdot} (\nabla_s \rho)_e}_{\text{Non-ortho. correction}} . \tag{4.19}$$

The vectors $\boldsymbol{\Delta}_e$ and $\mathbf{k}_e$ in Eq. 4.19 are calculated using over–relaxed non–orthogonal correction [1, 85]:

$$\boldsymbol{\Delta}_e = \frac{\mathbf{t}_e}{\mathbf{t}_e \boldsymbol{\cdot} \mathbf{m}_e}, \tag{4.20}$$

$$\mathbf{k}_e = \mathbf{m}_e - \boldsymbol{\Delta}_e. \tag{4.21}$$

Tuković [1] notes that the non–orthogonal correction used in Eq. 4.19 should be treated explicitly. The edge surface gradient $(\nabla_s \rho)_e$ should interpolated with the central differencing scheme using the surface gradients from the centroids of neighbouring finite areas. Gauss's theorem for a curved surface can be applied for the surface gradient calculation in a finite area centroid [1]:

$$(\nabla_s \rho)_P = \frac{1}{S_P}(\mathbf{I} - \mathbf{n}_P \mathbf{n}_P) \boldsymbol{\cdot} \sum_e \mathbf{m}_e \rho_e L_e, \tag{4.22}$$

where ρ_e is the value of variable ρ on a finite area edge from the previous iteration.

When a real curved surface is discretised using finite area faces, it is bounded by straight lines. Thus, the geodesic distance between two neighbouring areas is shorter than the length of the geodesic line between two corresponding points on a real curved surface. This difference is accounted for when calculating normal surface gradients as an explicit correction [1, 85] added to the right hand side of Eq. 4.19:

$$D_k = \frac{1}{15}\left[|\boldsymbol{\Delta}_e|\frac{\rho_N - \rho_P}{L_{PN}} - \boldsymbol{\Delta}_e \boldsymbol{\cdot} (\nabla_s \rho)_e\right]. \tag{4.23}$$

4.3.2. Temporal Discretisation

After discretisation of spatial integrals, Eq. 4.7 gains a new form [1]:

$$\frac{\mathrm{d}}{\mathrm{d}t}(\rho_P S_P) = -\sum_e \dot{s}_e \rho_e + \sum_e (\Gamma_\rho)_e L_e \mathbf{m}_e \boldsymbol{\cdot} (\nabla_s \rho)_e + s_{\rho u} S_P + s_{\rho p} S_P \rho_P, \tag{4.24}$$

where $s_{\rho p} S_P \rho_P$ is the implicit part and $s_{\rho u} S_P$ is the explicit part of the source term defined in Eq. 4.7.

The completely discretised form of the transport equation for a finite area face S_P depends on the choice of temporal discretisation:

- Implicit Euler method,

$$
\begin{aligned}
&\frac{\rho_P^n S_P^n - \rho_P^o S_P^o}{\Delta t} + \sum_e \dot{s}_e^n \rho_e^n \\
&= \sum_e (\Gamma_\rho)_e^n L_e^n \mathbf{m}_e^n \boldsymbol{\cdot} (\nabla_s \rho)_e^n + s_{\rho u}^n S_P^n + s_{\rho p}^n S_P^n \rho_P^n,
\end{aligned} \tag{4.25}
$$

- Second order backward implicit method,

$$
\frac{3\rho_P^n S_P^n - 4\rho_P^o S_P^o + \rho_P^{oo} S_P^{oo}}{2\Delta t} + \sum_e \dot{s}_e^n \rho_e^n
$$
$$
= \sum_e (\Gamma_\rho)_e^n L_e^n \mathbf{m}_e^n \bullet (\nabla_s \rho)_e^n + s_{\rho u}^n S_P^n + s_{\rho p}^n S_P^n \rho_P^n,
\tag{4.26}
$$

- Crank–Nicolson method,

$$
\frac{\rho_P^n S_P^n - \rho_P^o S_P^o}{\Delta t} + \frac{1}{2}\sum_e \dot{s}_e^n \rho_e^n + \frac{1}{2}\sum_e \dot{s}_e^o \rho_e^o
$$
$$
= \frac{1}{2}\sum_e (\Gamma_\rho)_e^n L_e^n \mathbf{m}_e^n \bullet (\nabla_s \rho)_e^n + \frac{1}{2}\sum_e (\Gamma_\rho)_e^o L_e^o \mathbf{m}_e^o \bullet (\nabla_s \rho)_e^o
\tag{4.27}
$$
$$
+ \frac{1}{2}\left(s_{\rho u}^n S_P^n + s_{\rho p}^n S_P^n \rho_P^n \right) + \frac{1}{2}\left(s_{\rho u}^o S_P^o + s_{\rho p}^o S_P^o \rho_P^o \right).
$$

The discretisation procedure presented above considers the motion of the mesh in the surface normal direction, where the finite area face S_P, binormal unit vector $\mathbf{m}_e$ and edge length L_e change with time.

4.3.3.   Boundary Conditions

Figure 4.4 depicts a finite area face P with an edge b placed at the edge of the spatial domain. The centroid of the finite area P is the starting point of vector $\mathbf{d}_b$ and the end point is the centroid of the edge $\mathbf{b}$. Having that in mined, the length of vector, denoted as $\mathbf{d}_m$, can be calculated as:

$$
|\mathbf{d}_m| = \frac{(\mathbf{I} - \mathbf{n}_P \mathbf{n}_P) \bullet \mathbf{m}_b}{|(\mathbf{I} - \mathbf{n}_P \mathbf{n}_P) \bullet \mathbf{m}_b|} \bullet \mathbf{d}_b.
\tag{4.28}
$$

Using the defined geometrical parameters of the boundary edges b, values for ρ_e and $\mathbf{m}_e \bullet (\nabla_s \rho)_e$ can be calculated using the same principles as for the Finite Volume Method [1].

4.4.   Conclusion

This chapter provided an overview of the Finite Area Method and its fundamental principles: spatial discretisation, discretisation of the transport equation,
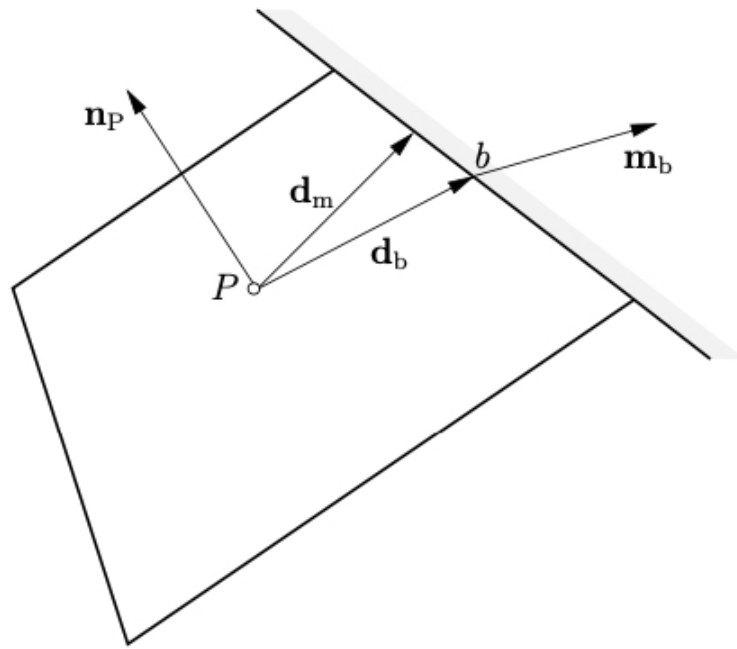
Figure 4.4: Definition of the geometrical parameters of a boundary edge [1].

temporal discretisation and treatment of mesh boundaries. A finite number of finite area faces is used for spatial discretisation of curved surfaces. Each finite area face is a convex polygon bounded by an arbitrary number of straight edges. The principles of the Finite Volume Method are applied for the discretisation of the spatial terms of the transport equation, replacing volume integrals and face fluxes with face integrals and edge fluxes. Temporal discretisationg using the implicit Euler, second order backward and Crank–Nicolson temporal schemes is discussed, Lastly, treatment of boundary edges is presented.

5. Numerical Modelling and Implementation

5.1. Introduction

This chapter provides an overview of the implementation of the numerical models used for predicting wear in contacts between lubricated rough surfaces. A deterministic asperity contact model is presented first. The model uses the Fast Fourier Transform to calculate plastic and elastic deformations without using the ambiguous approach of statistical models, which rely on the Gaussian distribution of asperities. A modified Reynolds equation, which employs a cavitation model and flow factors, is used to govern the fluid flow of thin films between rough surfaces. A cavitation model with special treatment of the boundaries between the active and cavitating regions is used to ensure smooth transitions between the regions. Lastly, the chapter offers an overview of the implementation of a numerical wear model based on Archard's Wear Law. The models uses an incremental approach to calculate wear using time or sliding distance increments, while incorporating a quasi–steady–state approach to describe the surface evolution due to wear. The described models are integrated into a wear algorithm, designed to be a viable tool simulating wear in mechanical systems under different tribological conditions.

5.2. Lubricated Contact Model

This section provides an overview of the different models and lubricant property relations which were implemented as part of the lubricated asperity contact model. An overview of the deterministic asperity contact model is given first, followed by the implementation of the modified Reynolds equation, the cavitation algorithm and flow factors. Lastly, an overview of the implemented relations governing the properties of the lubricant is discussed.

5.2.1. Asperity Contact Model

Section 3.4. discussed four distinct lubrication regimes, which included the mixed and boundary lubrication regimes, where contact between surface asperities is achieved. Under such conditions, the contact pressure between two surfaces in contact is shared between the remnants of the lubricant film and the contacting asperities. The surface asperities which come into contact are deformed due to pressure. The resulting deformation can be elastic or plastic, depending on the applied load. To be able to address asperity deformation, an algorithm for calculating solid–to–solid contact was implemented.

Statistical contact models, which were discussed in Sec. 3.5., are usually based on the assumption of a single hemispherical asperity with Gaussian asperity height distribution and a single average radius. In most cases, these models do not taking into account the interaction of surface asperities [109, 144]. Thus, the use of statistical contact models may introduce ambiguity, as different surface topographies used as input, may produce the same output parameters [103].

To avoid the uncertainty which may be introduced with the use of a statistical contact model, a deterministic model capable of calculating elastic–perfectly–plastic contact is used. The algorithm, on which the model is based, uses the Fast Fourier Transform (FFT) method for calculating elastic deflection of a rough surface following the procedure presented by Stanley and Kato [43], while also being capable of calculating plastic deformation following the procedure presented by Sahlin et al. [44, 45]. As discussed in Section 3.5., FFT–based deterministic contact models provide a fast calculation of contact pressures, surface deformations, and contact areas, based on real rough surface measurements, without being computationally too expensive.

A depiction how pressure p is acting on element E_Q, resulting in elastic deflection δ at a point (x, y) is given in Fig. 5.1. From the perspective of the FAM, the deflection δ at a point (x, y) can be regarded as the value of deflection $\delta(x, y)$ of a finite area face P with a centre located at (x, y), which is the result of pressure p acting on the finite area face Q.

Thorough the use of the Boussinesq–Cerruti theory [145, 146], which describes the distribution of stress and displacement due to external forces acting on a half–
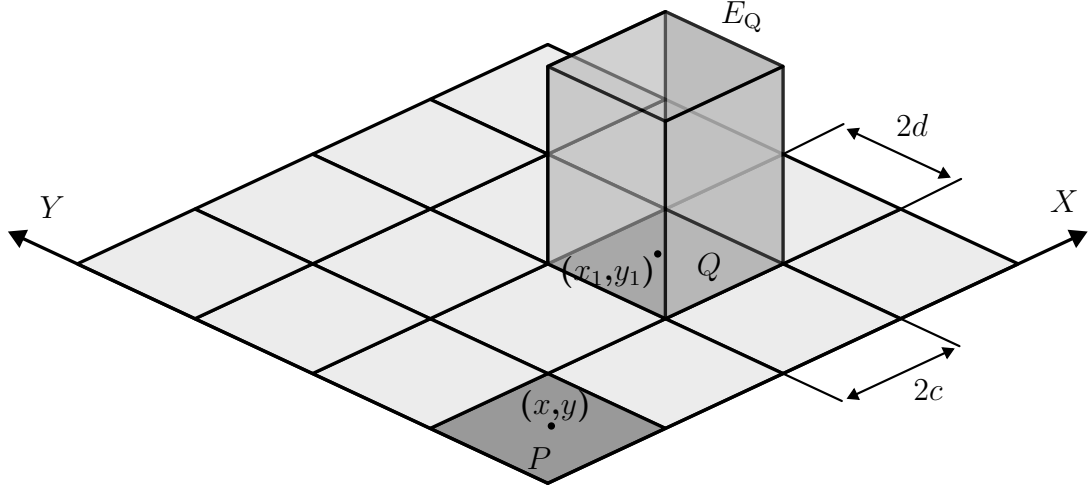
Figure 5.1: Surface element E_Q and its elastic deflection.

space, the deflection of element E_Q at point (x, y) due to pressure p acting on that element, can be expressed as:

$$\delta(x, y) = \frac{1}{E_r} \int_{-d}^{d} \int_{-c}^{c} \frac{p \, dx_1 \, dy_1}{\sqrt{(x - x_1)^2 + (y - y_1)^2}}. \tag{5.1}$$

As per Fig. 5.1, the element E_Q has a rectangular base Q with its centroid located at (x_1, y_1). As such, it is considered a flat–roofed element and the pressure p acting upon the it is considered to be constant over the entire element. Under these assumptions, Eq. 5.1 can be integrated, resulting in the expression [146]:

$$\delta(x, y) = \frac{p}{E_r} D(x', y'), \tag{5.2}$$

where the terms x' and y' are expressed as $x' = x - x_1$ and $y' = y - y_1$, while $E_r = \pi E'$ describes the reduced elastic modulus and $D(x', y')$ the flexibility coefficient. The flexibility coefficient $D(x', y')$ may be defined as:

$$D(x', y') = \quad (y' - d) \ln \left[\frac{(x' - c) + \sqrt{(y' - d)^2 + (x' - c)^2}}{(x' + c) + \sqrt{(y' - d)^2 + (x' + c)^2}} \right]$$
$$+ (y' + d) \ln \left[\frac{(x' + c) + \sqrt{(y' + d)^2 + (x' + c)^2}}{(x' - c) + \sqrt{(y' + d)^2 + (x' - c)^2}} \right]$$
$$+ (x' + c) \ln \left[\frac{(y' + d) + \sqrt{(y' + d)^2 + (x' + c)^2}}{(y' - d) + \sqrt{(y' - d)^2 + (x' + c)^2}} \right] \quad (5.3)$$
$$+ (x' - c) \ln \left[\frac{(y' - d) + \sqrt{(y' - d)^2 + (x' - c)^2}}{(y' + d) + \sqrt{(y' + d)^2 + (x' - c)^2}} \right].$$

Eq. 5.3 is applied to contacts with such geometries that point contact is achieved, e.g. ball bearings [146]. The same equation may be modified to be applicable to line contacts. The pressure element from Fig. 5.1 may be transformed to have a long strip as its base, as shown in Fig. 5.2. If only the middle of the strip is being considered, i.e. $y = 0$, and by making $d = b$, where b is assumed to be much greater than both x and c, Eq. 5.3 may be simplified for line contacts. After simplification ($y = 0$) and some manipulation, the equation for the flexibility coefficient in line contacts may be given as:

$$D(x') = \quad 4c \ln 2b$$
$$+ (x' + c) \ln(x' + c)^2 \quad (5.4)$$
$$+ (x' - c) \ln(x - c)^2.$$

Remaining within the FAM framework, the influence of pressure p on every finite area face P needs to be accounted for. Accounting for the influence of pressure on other finite area faces, the deflection δ_P at finite are face P, may be calculated using circular convolution, leading to the following expression:

$$\delta_P = \frac{1}{E_{\rm r}} \sum_{i=0}^{i=n-1} p_i \times D_i^P$$
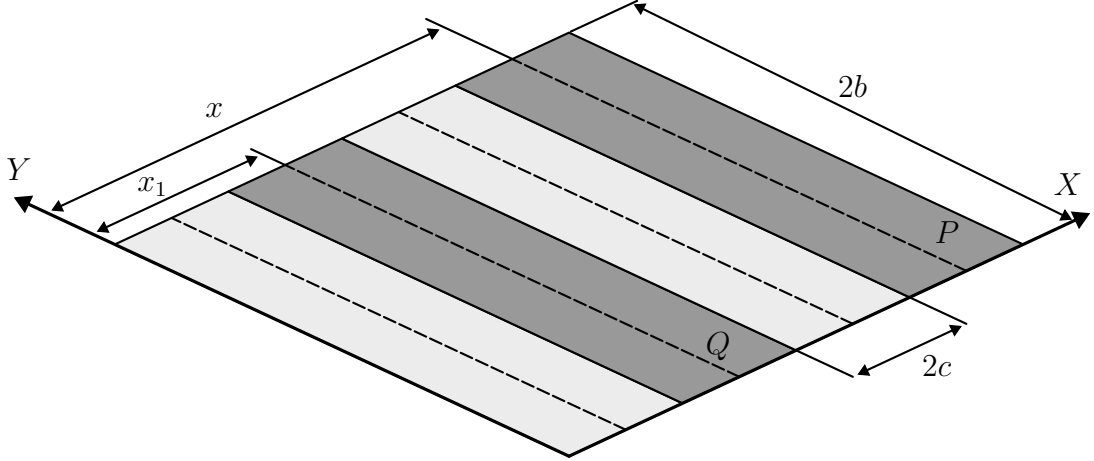$$= \frac{1}{E_{\rm r}} \left(p \otimes D^P \right). \quad (5.5)$$

Figure 5.2: Strip element considered for a line contact.

Looking at Eq. 5.5, the variable n represents the total number of finite area faces and i represents the index of a specific finite area face. For efficient calculation of the circular convolution over all finite area faces, the Fast Fourier Transform (FFT) is applied. The FFT approach requires significantly less operations when compared to direct integration [42]. By employing circular convolution, Direct Fourier Transform (DFT) may be applied, allowing numerical calculation of Eq. 5.5. As noted by Škurić [42], due to the fact that the computational domain is only a periodically–repeating part of a larger domain, special care must be taken to re–introduce periodicity of the pressure, This is achieved by mirroring the values of the pressure matrix, as described by Chen et al. [147].

The complete procedure for calculating elastic–perfectly–plastic deformations and the contact pressure between two real rough surfaces is presented next. The procedure is based on the procedure presented in [44, 45] and later implemented by Škurić [42] in the FAM framework. The procedure is outlined by the steps given below:

1. An initial position of the target contact plane Z_t is set and an initial value for contact pressure p is assumed.

2. The initial surface height z_0 is determined and the initial gap G_0 between the undeformed surface and contact plane is calculated:

$$G_0 = Z_T - z_0. \tag{5.6}$$

3. The current gap G is used to calculate the contact pressure:

$$p = \left(\frac{p}{E'} - \frac{G}{R_{q0}} \right) E'. \tag{5.7}$$

4. Negative values of pressure need to be truncated: $p = max(p, 0)$.

5. Faces with plastic deformation are identified. If the pressure p is higher than the material hardness H, the faces is identified as undergoing plastic deformation.

6. Pressure values greater than the value of hardness H are truncated:
$p = min(p, H)$.

7. FFT is used to calculate surface deformation δ_e based on pressure p and using Eq. 5.5. Due to the fact that pressures greater than the hardness of the material were truncated, the calculated deformations are considered elastic only.

8. Elastic deformations δ_e are used to calculate elastically deformed surface height. This is done by subtracting elastic deformations from the initial surface heights:

$$z = z_0 - \delta_e. \tag{5.8}$$

9. The elastic surface gap G between the elastically deformed surface heights z and the target plane Z_T is calculated:

$$G = Z_T - z. \tag{5.9}$$

10. Only the faces for which the non–truncated value of pressure is smaller than the material hardness are considered and used to calculate:

$$\begin{aligned}
\text{maximum height of surface} \quad &\rightarrow \quad max(\, z(p < H)\,), \\
\text{minimum height of surface} \quad &\rightarrow \quad min(\, z(p < H)\,), \\
\text{maximum gap in contact} \quad &\rightarrow \quad max(\, G(p < H)\,).
\end{aligned} \tag{5.10}$$

11. New vales of the surface heights are calculated, taking into account elastic and perfectly–plastic deformations:

$$G = Z_\mathrm{T} - z; \qquad (5.11)$$

12. The maximum contact gap residual is calculated using:

$$\max(R_\mathrm{G}) = \left| \frac{\max(G(p < H))}{\max(z(p < H)) - \min(z(p < H))} \right|; \qquad (5.12)$$

13. If the residual calculated via Eq. 5.12 is smaller than the predetermined threshold, the procedure is finished. Otherwise, the procedure goes back to step 3 and continues.

The procedure outlined in this section allows for the calculation of parameters necessary for lubricated rough surface analysis and wear calculation for an arbitrary distance between the contact plane and the mean of the surface heights. More specifically, the deterministic elastic–perfectly–plastic contact model enables direct calculation of contact pressures, area ratios and film thickness for two surfaces in contact via available measurements of surface topography.

5.2.2. Lubricant Flow Model

This section offers an overview of the implementation of the models which govern the fluid flow of the lubricant, discussed in Ch. 3.. The modification of the Reynolds equation to include the effects of cavitation is discussed, together with its discretisation within the framework of the Finite Area Method. The addition of flow factors into the Reynolds equation is presented, allowing for the inclusion of the effects of surface roughness in the mixed and thin film lubrication regimes, together with analytical equations used to calculated the aforementioned flow factors.

The thickness of the lubricant film between the surfaces in contact directly influences the properties of the lubricant flow. As discussed in Sec. 3.4., four main regimes of lubricant flow may be recognised: the hydrodynamic thick film regime in which the surfaces are fully separated by the lubricant and surface roughness does not affect fluid flow (i.e. smooth surfaces may be assumed), hydrodynamic

thin film regime in which the surfaces are still fully separated, but surface roughness significantly affects fluid flow, mixed regime in which the surfaces remain in partial contact and the contact pressure is shared by lubricant and the contacting asperities, and the boundary lubrication regime, where the entirety of the contact pressure is carried by the asperities. The modified Reynolds equation (Eq. 3.7) was introduced in Sec. 3.2. and governs the distribution of pressure in thin film flows. By modifying Eq. 3.7 to take into account the effects of surface roughness, the averaged form of the Reynolds equation is introduced (Eq. 3.12).

Modified Reynolds Equation

The lubricant flow throughout different lubrication regimes is governed by a modified Reynolds equation. The compressible form of the modified Reynolds equation is used to calculate the hydrodynamic pressure and the shear stress of the lubricant film bounded by two rough surfaces in relative motion. The equation governs the distribution of pressure in viscous thin film flows and is a partial differential equation derived from the Navier–Stokes equations, taking into account several assumptions [65], which were discussed in Sec. 3.2..

A pressure–based from of the Reynolds equation is presented as the starting point for the derivation of the modified Reynolds equation:

$$\nabla_s \bullet \left[\frac{\rho h \left(\mathbf{U}_\mathrm{a} + \mathbf{U}_\mathrm{b} \right)}{2} \right] + \frac{\partial \left(\rho h \right)}{\partial t} = \nabla_s \bullet \left(\frac{\rho h^3}{12 \mu} \nabla_s p \right). \tag{5.13}$$

The Eq. 5.13 is given in vector notation and is discretised on a contact patch using the FAM, thus ∇_s represents a two–dimensional surface gradient and $\nabla_s \bullet$ represents a two–dimensional divergence operator. The density, pressure and viscosity of the fluid (lubricant) are given as variables p, ρ and μ, respectively. The vectors $\mathbf{U}_\mathrm{a}$ and $\mathbf{U}_\mathrm{b}$ represent velocities of the two surfaces in contact, while the variable h denotes the thickness of the film [86].

The possibility of cavitation in thin film flows should be considered. To account for the occurrence of cavitation in the lubricant flow, a cavitation algorithm was developed using the method proposed by Elord and Adams [92]. The method calls for dividing the computational domain into two regions: a cavitating region

and a full-film region. The cavitation algorithm introduces a switch function to distinguish between the cavitating and the full-film regions:

$$
\begin{aligned}
\rho^o \geq \rho_{\text{cav}} &\longrightarrow \quad \text{full-film} \quad \longrightarrow \quad \alpha = 1 \\
\rho^o < \rho_{\text{cav}} &\longrightarrow \quad \text{cavitating} \quad \longrightarrow \quad \alpha = 0,
\end{aligned}
\tag{5.14}
$$

where the fluid density in the previous time step is denoted as ρ^o, while ρ_{cav} represents the fluid density at cavitation pressure p_{cav}. With the inclusion of the cavitation switch function α and the bulk modulus of the fluid ($\beta = \rho \frac{dp}{d\rho}$), a modified Reynolds equation, similar to the one described in [73], may be presented:

$$
\nabla_s \bullet \left(\alpha \, \frac{h^3 \beta}{12\eta} \nabla_s \rho \right) = \nabla_s \bullet \left[\frac{\rho h \left(\mathbf{U}_\text{a} + \mathbf{U}_\text{b} \right)}{2} \right] + \frac{\partial (\rho h)}{\partial t}.
\tag{5.15}
$$

Eq. 5.15 is a density–based form of the Reynolds equation and is solved numerically for the values of density ρ. The non–Newtonian viscosity needed for Eq. 5.15 may be calculated using one of the shear–thinning models discussed in Sec. 3.6.2., such as the Ree–Eyring [133], Carreau [135, 136] or the Carreau–Yasuda model [138]. The pressure–dependent values of the fluid bulk modulus β and pressure viscosity require known values of the lubricant pressure, thus the Dowson–Higginson pressure relation is used to calculate lubricant pressure from the values of density [139].

For the cavitating region, where the variable ρ represents the density of the liquid and gas mixture, the switch function evaluates to zero ($\alpha = 0$), thus the left–hand term of Eq. 5.15 (Poiseuille term) becomes zero. The right–hand terms, i.e. the Couette term (first term) and the squeeze and local expansion term (second term), remain as the only active terms. For the full–film region, where the switch function evaluates to unity ($\alpha = 1$), all of the terms in Eq. 5.15 remain active. The full–film and cavitation regions are separated by a either a rapture or formation boundary. As previously mentioned, the solution of Eq. 5.15 represents the values of lubricant density (full–film region) or the density values for a liquid and gas mixture (cavitating region).

Special care must be taken to satisfy the condition for mass conservation between the cavitating and full–film regions. More precisely, at the boundaries

between these regions: the rupture boundary, where cavitation is initiated, and formation boundary, where the two–phase mixture of gas and liquid turns fully back into a film. The Jakobsson–Floberg–Olson (JFO) boundary conditions were discussed in Sec. 3.5. and are used to handle mass conservation at the rupture and formation boundaries [90, 91]. At the rupture boundary, which is formed at the boundary moving from a full film (active) to the cavitating zone, the pressure is treated by applying a zero gradient condition with a constant value of the cavitation pressure p_{cav} [148]:

$$\nabla_s\, p = 0 \qquad\qquad p = p_{\mathrm{cav}}, \tag{5.16}$$

on the other hand, the pressure gradient at the formation boundary, which is formed as the boundary between the cavitating and active zone, is calculated as [148]:

$$\frac{h^2}{12\mu}\nabla_s p = (1 - \theta_{\mathrm{form}})\, \frac{\mathbf{U}_{\mathrm{a}} + \mathbf{U}_{\mathrm{b}}}{2}, \tag{5.17}$$

The non–zero pressure gradient in Eq. 5.17 governs the feeding of the active (full–film) zone. The variable ρ_{form} is the density of the mixture of the gas and the liquid at the formation boundary in the upwind direction and $\theta_{\mathrm{form}} = \rho_{\mathrm{form}}/\rho_{\mathrm{cav}}$ is the fractional film content for the cavitating zone.

Eq. 5.15 is discretised on an orthogonal finite area mesh and the discretisation procedure needs to take into account the cavitation boundaries. Special care must be taken to satisfy the condition for mass conservation between the cavitating and full–film regions, i.e. to satisfy the boundary conditions specified by Eqs. 5.16 and 5.17. According to Škurić [42] different treatment of the Poiseuille and Couette terms is required. Treatment of the terms depends on whether a finite area face is completely in the active region, completely in the cavitating region or at the rupture or formation boundary. The discretisation procedure for Eq. 5.15 and a description of the treatment of different terms from the equation is provided in the Appendix A.

Averaged Reynolds Equation

Eq. 5.15 allows for the calculation of hydrodynamic properties of the lubricant flow between two smooth surfaces in contact. For the Reynolds equation to be

applicable to calculate thin film flows between real rough surfaces, the roughness of the surfaces (surface asperities) needs to be considered. The thickness of the lubricant film between the surfaces in contact directly influences the properties of the lubricant flow. As previously mentioned, four different regimes of lubricant flow may be recognised [101]: hydrodynamic thick film, hydrodynamic thin film, mixed and boundary lubrication regimes.

For geometries which are of interest in this study, the surface roughness affects the flow of the lubricant. Furthermore, the surface texture, i.e. geometry of the surface roughness, is significantly smaller when compared to the entirety of the geometry. A computational domain with a sufficiently high resolution, which would allow for the surface roughness to be captured correctly, would result in a significant increase in the required computational resources. An alternative approach would involve a modification of the Reynolds equation, which would allow the equation to take into account the effects of surface roughness on the fluid pressure in thin film flows. Such an approach involves including a statistical representation of the surface topography (surface asperities) in the Reynolds equation, thus enabling computationally inexpensive calculations of hydrodynamic flow between rough surfaces with acceptable loss of information regarding the topography of asperities on the microscopic level [103]. This involves using a set of correction factors for the Reynolds equation called flow factors, which were first introduced by Patir and Cheng [104, 105]. Using flow factors, Eq. 5.15 may be reformulated as:

$$
\begin{aligned}
\nabla_{s}\bullet\left(\alpha\,\phi_{\mathrm{xy}}\,\frac{h^{3}\beta}{12\mu}\nabla_{s}\rho\right) &= \nabla_{s}\bullet\left[\frac{\rho h\left(\mathbf{U}_{\mathrm{a}}+\mathbf{U}_{\mathrm{b}}\right)}{2}\right] \\
&\quad -\nabla_{s}\bullet\left[\frac{\phi_{s}\rho\left(\mathbf{U}_{\mathrm{a}}-\mathbf{U}_{\mathrm{b}}\right)}{2}\right]R_{\mathrm{q}} \\
&\quad +\frac{\partial(\rho h)}{\partial t}.
\end{aligned}
\tag{5.18}
$$

The compressible form of the Reynolds equation given by Eq. 5.18 uses flow factors to enable computationally efficient calculation of a thin film flow between two rough surfaces a and b. The new terms introduced by Eq. 5.18 are the pressure flow factor ϕ_{xy}, the shear flow factor ϕ_{s} and the combined RMS roughness of surfaces a and b, calculated as $R_{\mathrm{q}} = \sqrt{R_{\mathrm{qa}}^{2}+R_{\mathrm{qb}}^{2}}$.

The flow factors introduced by Patir and Chang [104, 105] are not applicable for film flows with a small film thickness when compared to the RMS surface roughness, i.e. flows which are near the boundary regime. Thus, for Eq. 5.18 to be applicable in the near–boundary lubrication regime, semi–empirical equations for flow factors, developed by Wilson and Marsault [106], are used, This makes Eq. 5.18 applicable for the full range of lubricated contact conditions. Furthermore, as the use of flow factors is not restricted to a certain direction (longitudinal or transversal), Eq. 5.18 is applicable to three–dimensional surfaces. The use of flow factors requires their calculation via additional analytical equations. Once calculated, flow factors do not cause a significant strain on computational performance.

The choice whether to use the flow factors by Wilson and Marsault [106] or the ones by Patir and Chang [104, 105] depends on the lubrication regime. More practically, the choice between the flow factors depends on the value of the non–dimensional film thickness H, which is calculated as:

$$H = \frac{h}{R_{\mathrm{q}}}. \tag{5.19}$$

The analytical equations derived by Wilson and Marsault [106] are used to calculated the flow factors for contact conditions with large fractional contact areas. The analytical equations for calculating the pressure flow factor ϕ_{x} and the shear flow factor ϕ_{s} according to [106] are given as:

$$\text{Pressure } (H < 3): \qquad \phi_{\mathrm{x}} = \left[a_2(H - H_{\mathrm{c}})^2 + a_3(H - H_{\mathrm{c}})^3\right]/H^3, \tag{5.20}$$

$$\text{Shear } (H < 5): \qquad \phi_{\mathrm{s}} = b_0 + b_1 H + b_2 H^2 + b_3 H^3 + b_4 H^4 + b_5 H^5, \tag{5.21}$$

where H_{c} is the value of the non–dimensional film thickness H corresponding to the percolation threshold, a_2 and a_3 are functions of the correlation length, i.e of the Peklenik surface parameter γ. The expressions for calculating the aforementioned parameters, including parameters b_0, b_1, b_2, b_3, b_4, b_5 from Eq. 5.21, are discussed in the Appendix B.

Škurić [42] performed an analysis of the shear flow factors provided by Wilson and Marsault [106] and determined that (Eq. 5.21) results in inconsistent results for

some values of γ. More specifically, under–prediction for $\gamma = 1/9$, over–prediction for $\gamma = 1/3$ and notable deviation from results given by [106] for $\gamma = 1/6$. In order to achieve better agreement between shear flow factors, Škurić [42] proposed a new analytical equation derived by curve–fitting:

$$
\begin{aligned}
\phi_{\rm s} =& p_{00} + H \left\{ p_{10} + H \left[p_{20} + H \left(p_{30} + H \left(p_{40} + p_{50}H \right) \right) \right] \right\} \\
&+ H\gamma \{ \\
&\qquad\qquad p_{11} + H \left[p_{21} + H \left(p_{31} + p_{41}H \right) \right] \\
&\qquad\qquad + \gamma \left[p_{12} + \gamma \left(p_{13} + p_{14}\gamma \right) \right] \\
&\qquad\qquad + H\gamma \left(p_{22} + p_{32}H + p_{23}\gamma \right) \\
&\qquad \} \\
&+ \gamma \left\{ p_{01} + \gamma \left[p_{02} + \gamma \left(p_{03} + \gamma \left(p_{04} + p_{05}\gamma \right) \right) \right] \right\} ,
\end{aligned}
\tag{5.22}
$$

where the constants $p_{\rm xy}$ depend on the value of γ and are provided in the Appenix B as Equations B10 and B11.

The flow factors derived by Patir and Cheng [104, 105] are used for mixed lubrication and hydrodynamic lubrication regimes, i.e. for contact conditions with small fractional contact areas. According to [105], the pressure flow factor ϕ_x and the shear flow factor ϕ_s may be expressed as:

Pressure $(H \geq 3)$:

$$
\phi_{\rm x} = 1 - C \exp(-rH) \qquad \text{for} \qquad \gamma \leq 1, \tag{5.23}
$$

$$
\phi_{\rm x} = 1 - CH \exp(-r) \qquad \text{for} \qquad \gamma > 1, \tag{5.24}
$$

Shear :

$$
\phi_{\rm s} = V_{\rm r_a} \Phi_{\rm s} \left(H, \gamma_{\rm a} \right) - V_{\rm r_b} \Phi_{\rm s} \left(H, \gamma_{\rm b} \right) \quad \text{with:} \tag{5.25}
$$

$$
\Phi_{\rm s} = A_1 H^{\alpha_1} \exp \left(-\alpha_2 H + \alpha_3 H^2 \right) \qquad\qquad \text{for} \quad H \leq 5, \tag{5.26}
$$

$$
\Phi_{\rm s} = A_2 \exp \left(-0.25H \right) \qquad\qquad \text{for} \quad H > 5. \tag{5.27}
$$

Looking at Eq. 5.25, the variables $V_{\rm r_a}$ and $V_{\rm r_b}$ represent the variance ratios of surfaces a and b, which are calculated as follows:

$$V_{r_a} = \left(\frac{R_{q_a}}{R_q} \right)^2$$
$$V_{r_b} = \left(\frac{R_{q_b}}{R_q} \right)^2 = 1 - V_{r_a}.$$

$$(5.28)$$

The constants C and r, used in Eqs. 5.21 and 5.23, are defined for different values of the Peklenik parameter γ in Table B1 of the Appendix B. Furthermore, the coefficients $A_1, A_2, \alpha_1, \alpha_2, \alpha_3$ used in Eqs. 5.26 and 5.27 are also functions of γ (Peklenik parameter) and are given in Table B2 of the Appendix B.

As previously mentioned, the choice of flow factors depends on the value of the non–dimensional film thickness H, i.e. it depends on the lubrication regime. For values of $H \geq 3$, ϕ_x, the pressure flow factor ϕ_x is calculated using Eqs. 5.23 ($\gamma \leq 1$) and 5.24 ($\gamma > 1$), while for values of $H < 3$, Eq. 5.20 is used. Similarly, for the shear flow factor ϕ_s, and values of $H \geq 5$, Eqs. 5.25 and 5.27 are used, while for $H < 5$, ϕ_s is calculated using Eq. 5.22.

5.2.3. Lubricant Properties

Section 3.6. explored different relations which govern the properties of the lubricant. Different models are used to describe the dependence of lubricant properties on changes in pressure and temperature. The choice of the exact model which should be applied depends on the particular case which is studied. More specifically, the choice of the model depends on the lubricant used in the contact analysis and the available experimental data pertaining to lubricant characteristics. Different pressure–temperature–density relations and high–shear and low–shear viscosity equations described in Sec. 3.6. are compatible with the lubrication model used in this study The most suitable relations are implemented based on the selected lubricant and validation case conditions. In the lubricated wear case, which will be presented later, the Shell Turbo T68 oil [149, 5] is used as lubricant. Thus, the implementation of the most suitable relations based on the selected lubricant and validation case conditions is given next.

Density

The Dowson–Higginson pressure–density relation was implemented for use with the Shell Trubo T68 oil. Using this pressure-density relation, given by Eq. 3.20, the bulk modulus β can be calculated as:

$$\beta = \rho\frac{\mathrm{d}p}{\mathrm{d}\rho} = \rho\frac{C_1(C_2-1)\rho_{\mathrm{ref}}}{(\rho - \rho_{\mathrm{ref}}C_2)^2}, \tag{5.29}$$

where the values of the reference density ρ_{ref} and the coefficients C_1, C_2 are determined on a case–specific basis.

Viscosity–Pressure and Temperature Dependence

The most commonly used pressure–viscosity relations discussed in Sec. 3.6.1. were: the Barus law, the Roelands–Houpert model and the Doolittle model. While these models are the most commonly applied in general, for use under lubricated contact conditions where the Shell T68 oil is applied as lubricant, an improved version of the Yasutomi model, introduced by Bair et al. [5, 150] is implemented as:

$$\mu = \mu_{\mathrm{g}}\exp\left[\frac{-2.303\,C_1\,(1+b_1p)^{b_2}\,(T-T_{\mathrm{g}})}{C_2+(1+b_1p)^{b_2}\,(T-T_{\mathrm{g}})}\right], \tag{5.30}$$

$$T_{\mathrm{g}} = T_{\mathrm{g0}} + A_1\ln(1+A_2p),$$

where T_{g} is the transition temperature of glass and μ_{g} is the glass viscosity. Additional parameter are required in Eq. 5.30: the Yasutomi model parameters A_1, A_2, the improved Yasutomi model parameters b_1, b_2 and the Williams–Landel–Ferry parameters (WLF) C_1, C_2. All of the aforementioned parameters, including glass viscosity μ_{g}, are dependent on the lubricant used. The parameters needed in Eq. 5.30 for use in cases with the T68 oil as lubricant were proposed by Bair [5]. The parameters are provided in Table 5.1.

Viscosity–Shear Dependence

The model implemented in order to calculate the shear–dependent viscosity of the Shell Turbo T68 oil is the Ree–Eyring model [133]. Additionally, an approach

Table 5.1: Improved Yasutomi model parameters for Eq. 5.30 [5].

μ_g	10^{12}	Pa s
T_g0	-127.88	°C
A_1	1180.0	°C
A_2	0.1362	GPa^{-1}
b_1	17.26	GPa^{-1}
b_2	-0.1453	-
C_1	17.75	-
C_2	56.98	°C

for calculating viscosity flow factors by Ehret et al. [151] was implemented. The expression for the shear–thinning function using the Ree–Eyring model and the resulting expressions for the viscosity flow factor ϕ_ν, is given next:

$$\text{Ree–Eyring:} \quad f(\tau)_\mathrm{RE} = \frac{\tau_\mathrm{E}}{\tau}\sinh\left(\frac{\tau}{\tau_\mathrm{E}}\right) \quad \rightarrow \quad \begin{aligned} \phi_{\eta_\mathrm{x}} &= \cosh\left(\frac{\tau}{\tau_\mathrm{E}}\right), \\ \phi_{\eta_\mathrm{y}} &= \frac{\tau_\mathrm{E}}{\tau}\sinh\left(\frac{\tau}{\tau_\mathrm{E}}\right), \end{aligned} \tag{5.31}$$

where the viscosity flow factor in the direction of the shear stress τ is expressed as ϕ_{η_yx}, while the viscosity flow factor in the direction orthogonal to the shear stress is expressed as ϕ_{η_y} [76]. The Eyring stress parameter τ_E needed in the shear–thinning function and needed for calculating the viscosity flow factors, is given as $\tau_\mathrm{E} = 4.70$ MPa for the Shell Turbo T68 oil. Lastly, shear stress τ may be calculated using the magnitude of the slip velocity U_s [73]:

$$\frac{U_\mathrm{s}\mu}{h} = \tau f(\tau)_\mathrm{RE}. \tag{5.32}$$

5.3. Wear Model

Chapter 2. offered an overview of the theory behind friction and wear, focusing on adhesive wear. Also, the work done by Archard on the field of wear modelling was discussed and Archard's Wear Law was presented. In this section, the numerical

implementation of the Archard's equations is presented for different wear analysis scenarios.

First, let us consider one of formulation of Archard's wear equations presented in Chapter 2.:

$$\frac{h_{\mathrm{w}}}{L} = p_n \underbrace{\frac{K}{H}}_{\mathrm{K_D}} \quad \rightarrow \quad h_{\mathrm{w}} = K_D \, p_n \, L, \qquad (5.33)$$

where h_{w} is the wear depth or, more precisely the height of the worn volume, L is the sliding distance, p_n the normal contact pressure, K the non–dimensional wear coefficient and H the hardness of the softer material. The quotient of the non–dimensional wear coefficient K and the material hardness H may also be expressed as the dimensional wear coefficient K_D. Looking at Eq. 5.33, the expression allows us to calculate the height of the worn volume or wear depth h_{w} per sliding distance L, for a material of known parameters (K and H or K_D) under normal contact pressure p_n. Further treatment of Eq. 5.33 and calculation of required input variables, are highly case–specific and depend on the modelling approach.

The numerical procedure which involves the simulation of the surface wear evolution is usually based on the idea of solving the initial contact problem for a fixed geometry, updating the geometry and re–evaluating the contact conditions in an incremental manner.

5.3.1. Incremental Wear Model

For the wear equations to be applicable in the wear algorithm developed in this study, an incremental wear model was adopted. The incremental wear model was implemented in a way that allows us to calculate the wear increment $\Delta h_{\mathrm{w,i}}$ for each solution step i. The incremental modelling approach may be used to calculate a wear increment $\Delta h_{\mathrm{w,i}}$ for constant time increments Δt [152, 24] or constant slide increments ΔL [20].

Archard's wear law, given by Eq. 5.33, may be discretised with respect to the sliding distance, resulting in the expression:

$$\frac{\mathrm{d}h_{\mathrm{w}}}{\mathrm{d}L} = p_n \, K_D. \tag{5.34}$$

After some modification as per Sec. 2.4.4., the equation may be discretised with respect to the sliding time:

$$\frac{\mathrm{d}h_{\mathrm{w}}}{\mathrm{d}t} = p_n \, K_D \, v, \tag{5.35}$$

where v represent the sliding velocity. Furthermore, Eq. 5.34 and 5.35 can be expressed in discrete localized forms:

$$\Delta h_{\mathrm{w}} = p_n \, K_D \, \Delta L, \tag{5.36}$$

$$\Delta h_{\mathrm{w}} = p_n \, K_D \, v \, \Delta t. \tag{5.37}$$

The relation given by Eq. 5.36 can be used to calculate the wear depth contribution Δh_{w} at a point which is subjected to the normal pressure p_n over a sliding distance ΔL. While Eq. 5.37, allows for the calculation of the same wear depth contribution Δh_{w} for a material point moving at a sliding velocity v, while subjected to the same normal pressure p_n for a sliding time increment Δt. By definition, the value of the wear coefficient remains constant during each increment. During each solution step, the sliding distance increment ΔL and time increment Δt are constant, and determine the size of the solution step. The value of the pressure p_n is determined for each increment and the calculated value is kept constant for the duration of step. The calculation of the pressure, including any averaging of the pressure over time or sliding direction, should be performed in a way which is most appropriate for the specific use case, considering the geometry of the contact and whether the contacting surfaces are both affected by wear, thus changing the contact pressure between the surfaces.

For each solution step i, the contribution to the total wear depth $h_{\mathrm{w,i}}$, expressed as the wear increment $\Delta h_{\mathrm{w,i}}$, is calculated using Eq. 5.36 or Eq. 5.37. The total wear depth for the current solution step i can be expressed using the Euler integration scheme, using the total wear depth up to the previous solution step $h_{\mathrm{w,i-1}}$ and the wear depth contribution (wear increment) calculated for the current solution step i:

$$h_{\text{w}}^{\text{i}} = h_{\text{w}}^{\text{i}-1} + \Delta h_{\text{w}}^{\text{i}}. \tag{5.38}$$

If a fixed sliding distance increment ΔL is determined as the relative sliding distance between the two surface for solution step i of the calculation procedure, the contribution to the total of the surfaces in contact may be expressed as:

$$\Delta h_{\text{w}}^{\text{i}} = p_n \, K_D \, \Delta L, \tag{5.39}$$

transforming Eq. 5.38 into:

$$h_{\text{w}}^{\text{i}} = h_{\text{w}}^{\text{i}-1} + p_n \, K_D \, \Delta L. \tag{5.40}$$

The term $h_{\text{w,i}}$ in Eq. 5.40 signifies the cumulative wear depth occurring for two surfaces in contact. This means that the dimensional wear coefficient from Eq. 5.40 represents the combined wear coefficient of the surface pair, which can be expressed as the sum of the wear coefficients for each of the two surfaces (denoted as 1 and 2) [64]:

$$K_{\text{D}} = K_{\text{D,1}} + K_{\text{D,2}}. \tag{5.41}$$

and the total combined wear depth for the surface pair may be expressed as the sum of the wear depths for each of the two surfaces:

$$h_{\text{w}}^{\text{i}} = h_{\text{w,1}}^{\text{i}} + h_{\text{w,2}}^{\text{i}}. \tag{5.42}$$

The wear depth contribution of each surface to the total combined wear depth of the surface contact pair, may thus be expressed as [2]:

$$h_{\text{w,1}}^{\text{i}} = \frac{h_{\text{w}}^{\text{i}}}{1 + K_{\text{D,2}}/K_{\text{D,1}}}, \tag{5.43}$$

$$h_{\text{w,2}}^{\text{i}} = \frac{h_{\text{w}}^{\text{i}}}{1 + K_{\text{D,1}}/K_{\text{D,2}}}. \tag{5.44}$$

As was noted in Sec. 2.4.5., in most cases the provided dimensional wear coefficient K_D represents the combined wear coefficient for the pair of surfaces in

contact. K_D is determined experimentally through measurements of the combined volume of the worn material produced during the experiment. To be able to determined the exact contribution of each surface to the total wear depth, the wear coefficient for each of the surface needs to be available. This means that separate experimental measurements of the worn volume need to be performed for each of the two surfaces in contact.

5.3.2. Quasi–Steady–State Wear Model

The wear model presented in this thesis should be applicable to rotating machinery, or more specifically, to mechanical components which undergo reciprocating or periodic motion. Such mechanical components are best represented by the standard tribological tests: the pin–on–disc, pin–on–cylinder, reciprocating pin–on–flat, etc. According to Lengiewicz and Stupkiewicz [30] these standard tribological configurations, representative for wear phenomena occurring due to frictional sliding in most tribological pairs, may be analysed as a representative **periodic pin–on–flat** wear problem, Fig. 5.3.
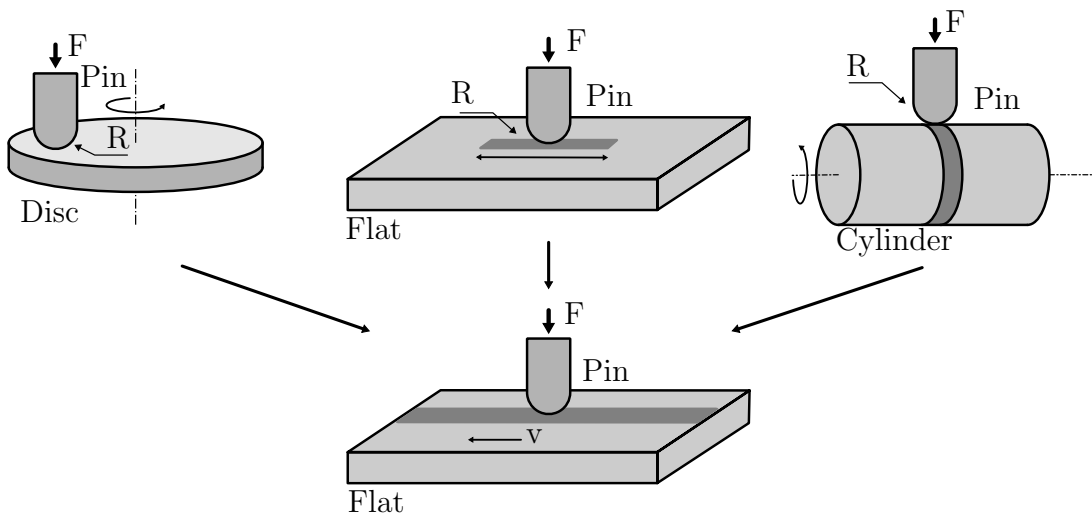
Figure 5.3: Tribological tests simplified as a periodic pin–on–flat problem.

Let us consider a pin–on–disc case as depicted in Fig. 5.3. The wear process develops slowly over time, thus two different time scales need to be introduced [30]: the slow time scale at which total wear accumulates over several revolutions of the disc, and a fast time scale which corresponds to a single rotation of the

disc. The quasi–steady–state model proposed by Lengiewicz and Stupkiewicz [30], allows us to decouple the periodic contact problem and the surface evolution problem (due to wear) on the two time scales. More specifically, in quasi–steady–state wear model, the contact pressure is considered constant in the fast time scale, meaning that the evolution of pressure due to wear is temporary ignored during a single increment of the fast time scale. In the slow time scale, the evolution of the surface shape and that of the contact pressure due to wear are considered, and the surface shape is updated to reflect changes due to wear accumulated during several increments of the fast time scale. The inherently transient process of wear may thus be reduced to a quasi–steady–state process, by assuming steady–state contact conditions (i.e. constant pressure) during the fast time scale and taking into account surface and contact pressure evolution in the slow time scale.

The assumption of the quasi–steady–state wear modelling approach include

- the bodies in contact are considered rigid (most metals), meaning that the elastic deformations are considered small when compared to the surface changes caused by wear,

- the model considers bilateral surface wear, thus both surfaces are affected and evolve due to wear.

The rigid body assumption of the quasi–steady–state wear model does not limit the applicability of the model developed in this research, as most contacts between metallic bodies **can be considered rigid body contacts**. Similarly, the case of bilateral wear is considered a more complex case than unilateral wear of a single surface. The calculation of single surface wear, with the assumption that the other surface is sufficiently harder and does not wear, is a special case where the contact pressure evolution is easier to calculate and usually depends on trivial geometrical evolution of a single surface.

As previously mentioned, the quasi–steady–state wear model involves the separation of two time scales: the fast time scale τ and the slow time scale t. This means that different wear rates, depending on the time scale, are introduced [30]: the instantaneous wear rate $\dot{\tilde{h}}_\mathrm{w}$ at the fast time scale τ and the cumulative (av-

eraged) wear rate $\dot{h}_{\mathrm{w}}$ at the slow time scale t. The instantaneous wear rate is determined by a suitable formulation of Archard's wear law, e.g. using Eq. 5.35:

$$\dot{\tilde{h}}_{\mathrm{w}} = p\,K_D\,v, \tag{5.45}$$

where p represents the local contact pressure, v the sliding velocity and K_D the dimensional wear coefficient. To obtain the cumulative wear rate $\dot{h}_{\mathrm{w}}$ at the slow time scale t, averaging of the instantaneous wear rate $\dot{\tilde{h}}_{\mathrm{w}}$ over the time interval $\Delta\tau$ needs to be performed:

$$\dot{h}_{\mathrm{w}} = \frac{1}{\Delta\tau}\int_{t}^{t+\Delta\tau}\dot{\tilde{h}}_{\mathrm{w}}\,\mathrm{d}\tau = \frac{1}{\Delta\tau}\int_{0}^{S}\dot{\tilde{h}}_{\mathrm{w}}\frac{\mathrm{d}x}{v} = \frac{1}{S}\int_{0}^{S}\dot{\tilde{h}}_{\mathrm{w}}\,\mathrm{d}x. \tag{5.46}$$

In Eq. 5.46 the averaging of the instantaneous wear rate is performed over the time interval $\Delta\tau$, under the assumption that the contact pressure p is constant along the direction of sliding x. This allows us to replace the temporal integration with integration along the sliding path, where the time interval $\Delta\tau$ is replaced with the characteristic sliding path per cycle of the periodic motion S.

For a general use case, the Eq. 5.46 is used to calculate the wear rate (wear depth increment) for each surface in contact. The geometrical averaging along the sliding path, the contact pressure, alculation of the characteristic slide distance S and the time increment $\Delta\tau$, depend on the geometry of each of the surface (e.g. flat pin, spherically tipped pin, ball, flat, etc.) and on the contact motion achieved in the particular setup.

If a pin–on–disc case is considered, where a spherically tipped pin with a tip radius R is pressed down on the disc with a constant force F, while the disc rotates with a constant angular velocity ω, the case may be translated into the periodic pin–on–flat case. Fig. 5.4a shows the contact between a spherically tipped pin in contact with a flat, thus depicting the representative periodic pin–on–flat case. The length of the flat is chosen to be equal to the length of the circular sliding path from the pin–on–disc case, and can be expressed as $S = 2\,R\,\pi$. Similarly, the pin slides across the flat with a constant sliding velocity v, calculated for a fixed time increment Δt as $v = S/\Delta\tau$. The sliding path S represents the sliding path length per one cycle, i.e. the sliding distance of the pin per one cycle of a periodic motion. In this case, the distance of the repeated sliding contact between
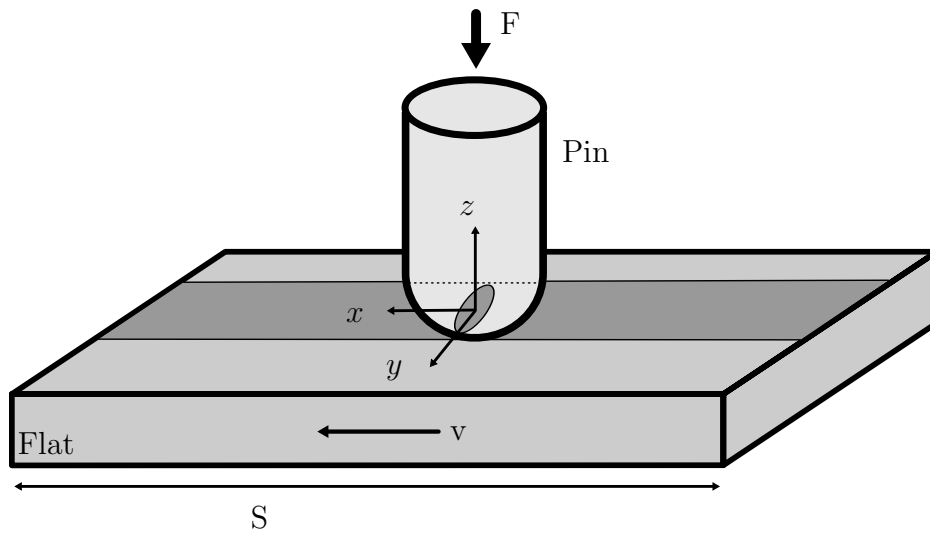
(a) Wear groove and elliptical contact zone.
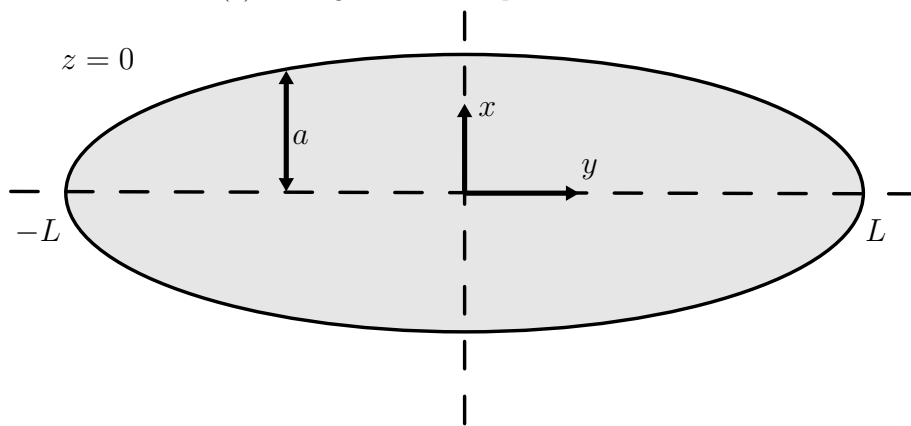
(b) Contact zone in the xy-plane

Figure 5.4: Formation of wear fragments at junction between a soft and a hard body

the pin and the disc is $2\,R\,\pi$,, but may diff in other cases. Fig. 5.4b shows the contact zone between the ball and the flat. The contact zone originally started as a point contact, but evolved due to wear into an elliptical shape shown in Fig. 5.4b. The length of the contact zone in the direction of sliding is $2a(y,t)$, where the semi–width $a(y,t)$ evolves through time as the contact zone changes through the wear process.

The calculation of the cumulative (averaged) wear rate needs to be performed separately for the pin and the disc, as the effect of the periodic variations of the contact pressures affect the pin and the disc differently. This means that the wear calculation needs to be treated differently for each of the two surfaces. As the surface of the pin is in constant contact with the disc, for every rotation (cycle) of the disc, the instantaneous wear rate calculated on the fast time scale can be directly used in the slow time scale. Thus, the calculation of the cumulative (averaged) wear rate for a point on the surface of the pin is performed as follows:

$$\dot{h}_{\mathrm{w,p}}(x,y,t) = \frac{1}{\Delta\tau} \int_{t}^{t+\Delta\tau} \dot{\tilde{h}}_{\mathrm{w,p}}(x,y,t)\,\mathrm{d}\tau = \dot{\tilde{h}}_{\mathrm{w,p}}(x,y,t)\,\mathrm{d}\tau, \tag{5.47}$$

and by using Eq. 5.45 another expression is given as:

$$\dot{h}_{\mathrm{w,p}}(x,y,t) = p(x,y,t)\,K_{\mathrm{D,p}}\,v. \tag{5.48}$$

By examining the geometry of the contact between the spherically tipped pin and the wear groove of the flat, depicted in Fig. 5.4b, we can see that the geometry of the wear groove does not change in the direction of sliding, during one cycle. Thus the local contact pressure $p(x,y,t)$ may be considered constant in the sliding direction (denoted as $p(y,t)$). Looking at Eq. 5.45, we can see that the instantaneous wear rate depends only on the pressure changes, as K_{D} and v are kept constant, and as the contact pressure is constant in the sliding direction, so is the instantaneous wear rate. Thus, the averaged wear rate for the surface of the pin may be expressed as:

$$\dot{h}_{\mathrm{w,p}}(y,t) = p(y,t)\,K_{\mathrm{D,p}}\,v, \tag{5.49}$$

where both the local contact pressure $p(y,t)$ and the cumulative wear rate $\dot{h}_{\mathrm{w,p}}(y,t)$ are constant in the sliding direction.

5. Numerical Modelling and Implementation

The cumulative wear rate of the disc (flat) is calculated in a different manner. In this case, the circular motion of the pin sliding over the disc is transformed into a linear sliding motion of the pin sliding over a flat, following a sliding path S (Fig. 5.4a). The wear groove is considered uniform in the sliding direction during at fast time scale, i.e. the local contact pressure and the wear rate can also be considered as constant in the sliding direction. The wear rate is *smeared out* over the sliding distance S, more precisely, the wear rate of the surface of the disc is geometrically averaged as:

$$\dot{h}_{\mathrm{w,d}}(y,t) = \frac{1}{S} \int_0^S \dot{\tilde{h}}_{\mathrm{w,d}}(y,t) \, \mathrm{d}x, \tag{5.50}$$

if we consider that the contact pressure, and thus the wear rate, outside of the contact area shown in Fig. 5.4b are reduced to zero, i.e. $\dot{\tilde{h}}_{\mathrm{w,d}}(x,y,t) = 0$ for $|x| > a(y,t)$. According to Fig. 5.4b, the integration is performed for the length of the contact zone $2a(y,t)$:

$$\dot{h}_{\mathrm{w,d}}(y,t) = \frac{1}{S} \int_{-a(y,t)}^{a(y,t)} \dot{\tilde{h}}_{\mathrm{w,d}}(y,t) \, \mathrm{d}x, \tag{5.51}$$

thus, the temporal averaging may be simplified to:

$$\dot{h}_{\mathrm{w,d}}(y,t) = \frac{2a(y,t)}{S} p(y,t) \, K_{\mathrm{D,d}} \, v, \tag{5.52}$$

where $a(y,t)$ is the semi–width of the elliptical contact zone, $K_{\mathrm{D,d}}$ the dimensional wear coefficient of the disc and v the sliding velocity.

The wear depths for the surfaces of the pin and the disc are calculated using an incremental solution procedure. Following the theory of the incremental wear modelling approach, the numerical solution procedure involves discretisation into distinct time increments Δt, for each step of the solution procedure i [30]: $t_i = t_i + \Delta t_i$. Thus, the wear depths of the pin and the disc may be calculated using the Euler integration scheme:

$$h_{\mathrm{w,p}}^{\mathrm{i}} = h_{\mathrm{w,p}}^{\mathrm{i-1}} + \dot{h}_{\mathrm{w,p}}^{\mathrm{i}} \Delta t, \tag{5.53}$$

$$h_{\mathrm{w,d}}^{\mathrm{i}} = h_{\mathrm{w,d}}^{\mathrm{i-1}} + \dot{h}_{\mathrm{w,d}}^{\mathrm{i}} \Delta t. \tag{5.54}$$

80

Using Eqs. 5.48 and 5.52 in combination with Eqs. 5.53 and 5.54, the wear depth for each point on the surfaces in contact may be calculated, thus determining the surface evolution in a representative pin–on–disc case. By decoupling the wear calculation at the fast and slow time scales, the surface and pressure evolution at the fast scale, i.e. for the duration of one numerical iteration step determined by the length of the time increment Δt, can be neglected. The decoupling procedure still allows us to consider the cumulative changes due to surface wear, which lead to the surface and pressure evolution on the slow time scale. The same procedure may be applied to different use cases, taking into account the specifics of the contact geometries between the surfaces, modifying the averaging procedure in accordance with the movement between the surfaces and determining the cyclic sliding path S.

5.4.   Wear Algorithm

The aim of this research was to develop and implement a numerical procedure in the form of a wear algorithm, which may be applied to wear analysis of lubricated rough surfaces chosen to represent simplified contacts between mechanical components of rotating machinery. Several numerical models were implemented as the building blocks of the wear algorithm: the asperity contact model, the lubrication model and the wear model.

Initially implemented by Škurić [42] for numerical simulations of wire drawing and wire rolling, the lubricated contact model was modified and re–implemented to be compatible with the wear algorithm.

The wear algorithm relies on the combination of the wear model discussed in Sec. 5.3. with either the deterministic point contact or line contact models, discussed in Subsection 5.2.1., to calculate wear under dry (unlubricated) contact conditions. To be applicable for cases when a lubricant is used in the contact zone between rough surfaces, the wear algorithm needs to be able to predict wear depending on the lubrication regime. Thus, the wear model and the asperity contact model need to be used together with the lubricant flow model discussed in Subsection 5.2.2. and various lubricant property relations given in Subsection 5.2.3.. Through the use of the aforementioned models, proper assessment of

contact pressures, area ratios and the height of lubricant film is possible, allowing the wear algorithm to be applicable even in the mixed and boundary lubrication regimes.

A flowchart outlining a simplified version of the wear algorithm is given in Fig. 5.5. The outline depicts the main functions of the algorithm, used for wear analysis of two surfaces. Thus, let us consider the contact between two rough surfaces, denoted as 1 and 2. Each of the surfaces has a specific surface geometry defined as the distance between the surface and a flat plane, i.e. surface separation or surface height. What is more, each of the surfaces is described by a number of properties, the most important of them being the wear coefficients k_{D1}, k_{D2}, Young's moduli E_1, E_2 and Poisson's ratios ν_1, ν_2. Those two initial surfaces are considered as the input parameters for the wear algorithm.

The next step involves the creation of an equivalent surface, i.e. the contact between the two initial surfaces is reimagined as the contact between an equivalent surface and a flat rigid plane. The equivalent surface is created to consider the geometries of both of the initial surfaces by calculation of a combined surface separation and using combined surface properties (k_D, E_R). The contact model is applied to resolve the initial contact as the contact between the equivalent surface and a rigid plane. In simplified terms, the contact model moves the equivalent surface closer to the rigid plane and calculates the contact pressure, elastic and plastic deformations and the total resulting load. The contact model may be used together with the lubrication model, slightly altering the iteration procedure, to calculate the contact pressure when a lubricant is present in the contact area. Once the target load between the surfaces is achieved, i.e. the total load F_{total} calculated thorough the contact model is within the predetermined tolerances of the set target load F_{target}, the contact model calculates the final values of the contact pressure, elastic and plastic deformations, surface separation, lubricant pressure, lubricant film height, etc.

Once the contact iterations are finished for the initial contact conditions, the required variables from the contact, most importantly the contact pressure p_c, are used within the wear model to determine the combined wear depth (volume) for the contact of the equivalent surface and a rigid plane h_w. The wear coefficients of the initial surfaces K_{D1} and K_{D2} may be used to determine the contribution

of each surface to the total combined wear depth (volume). Using the calculated wear depths, the geometry of the surfaces is updated. The surface separation of the new updated geometry is now used as input for the contact model. For each simulation step (e.g. slide increment ΔL) the contact is re–evaluated, wear of the new surface is calculated and the geometry is updated. This is repeated until total sliding distance is reached.

The outline of the wear algorithm given in Fig. 5.5 represents a basic use case, while slight modifications to the algorithm are necessary depending on the specifics of the surfaces in contact, the application of lubricant, the roughness of the surfaces and whether we are using time Δt or sliding distance ΔL increments in the wear model, the general steps used in the procedure remain the same.

5.5.   Conclusion

This chapter offered an overview of the numerical models implemented for predicting wear of lubricated rough surface contacts.

A deterministic asperity contact model was introduced first. The deterministic models are employed when the assumption of the Gaussian distribution of the surface asperities used in statistical models does not provide the required accuracy. Relying on the Fast Fourier Transform, the deterministic contact model can accurately predict plastic and elastic deformations of real rough surfaces, while maintaining computational efficiency and without the ambiguity of the statistical models.

The lubricant flow model was discussed next. The model is based on a modification to the Reynolds equation, incorporating the effects of cavitation. This was achieved by discretising the computational domain into active and cavitating regions. Following the procedure by Elrod and Adams, the Poiseuille coefficient is reduced to zero inside the cavitating region and a zero–gradient condition is applied at the boundaries between the two regions to ensure a smooth transition (Appendix A). Flow factors were implemented for modelling thin film flows between rough surfaces and different analytical equations for flow factor calculation were provided based on lubricant film thickness values. A detailed implementation of which was provided in the Appendix B.

5. Numerical Modelling and Implementation
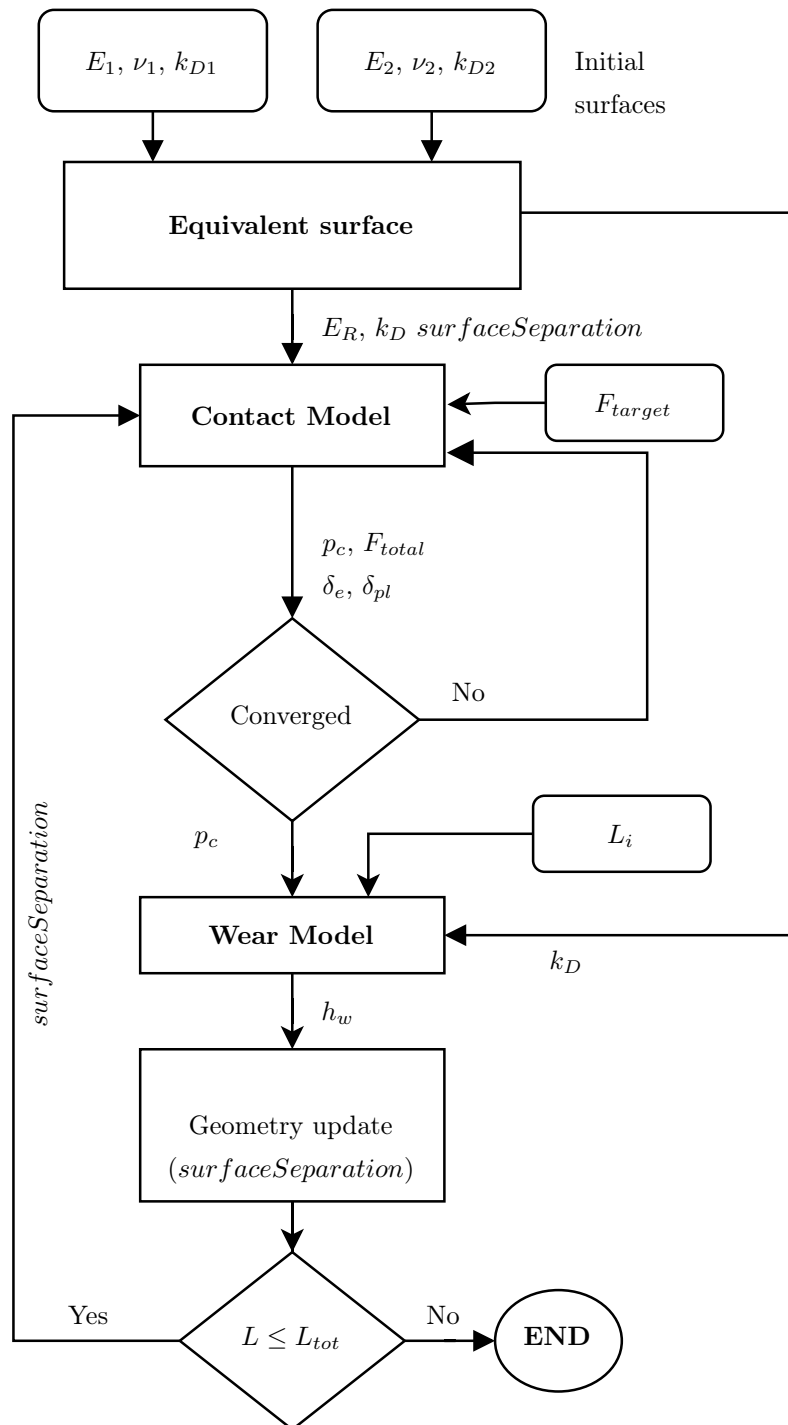
Figure 5.5: Flowchart outlining details of the wear algorithm.

The implementation of the wear model built on Archard's Wear Law was presented. The model employs an incremental and a quasi–steady–state approach, to predict wear for a single or both surfaces in contact. If the contact between surfaces follows a cyclic pattern (rotation, periodic sliding, etc.), a separation of the time scales is performed. By decoupling the calculation of wear on the fast time scale (e.g. a single rotation in a pin–on–disc setup) and the slow time scale (several rotations) the surface geometry and pressure evolution. due to the transient wear process, is captured effectively.

By integrating these model into a wear algorithm, an effective approach was developed for simulating wear under different lubrication regimes. The algorithm iteratively performs the calculation of contact parameters, calculates wear based on those parameters and updates the surface geometry accordingly, thus capturing the surface evolution due to wear. The algorithm may be used for a wide range of tribological conditions, including mixed and boundary lubrication regimes.

By combining the deterministic asperity contact model, lubricant flow models and the incremental wear modelling approach, a viable tool for wear analysis of lubricated rough surfaces in mechanical systems was developed.

6. Numerical Results

6.1. Introduction

In this chapter a number of numerical cases, designed to validate different aspects of the wear algorithm, are presented. Single surface wear is validated first, demonstrated on a pin–on–disc test case. This same test case is further extended to validate bilateral (two-surface) wear analysis. Following the validation of cases with initially point contact, the use of the model for assessing scenarios with initially line contacts. This is performed using a ring–on–block test case, with the results compared to both numerical and experimental data available in the literature. A reciprocating ball–on–flat analysed next, determining wear using the quasi-steady-state approach. Furthermore, the wear algorithm is applied to direct surface profile measurements, in a ring–on–ring case. The wear analysis results from the ring–on–ring case are compared to experimental scans of worn surfaces reported in the literature. Finally, after validating different aspects of the wear algorithm for dry contact conditions, wear analysis is performed on a ball–on–disc apparatus. This analysis incorporates measured surface profiles and considers lubricated contact conditions using the Shell Turbo T68 oil is as the lubricant to evaluate wear under **mixed and near–boundary** lubrication regimes.

6.2. Pin–On–Disc Sliding Wear

In this section, the wear algorithm will be used to analyse wear on a Pin–On–Disc (PoD) test case. The Pin–On–Disc setup is a classic tribological experiment used to measure friction and wear. The numerical results from the wear algorithm are validated against the numerical results provided by Rodríguez-Tembleque et al. [2].

A setup depicting a pin sliding over a rotating disc is shown in Fig. 6.1, while

a cross–section of the contact between the pin and the flat disc is given in Fig. 6.2. As seen in Fig. 6.2, the pin is spherically tipped with a radius $R = 50$ mm. The contact between the pin and the disc is achieved at a point which is sufficiently far away from the axis of rotation and the contact zone is small enough, so that the tangential slip velocity may be considered constant. Thus, all of the points in the contact zone have the same velocity and travel the same distance during one increment of the simulation.

The contact zone is a rectangular domain, discretised using the same number of finite area faces in each direction. The length and the width of the domain are determined following the recommendation regarding the size of the computational domain by Wu et al. [153]. Using Hertzian contact theory, the diameter of the area of contact is calculated for a predetermined load. The width and depth of the computational domain are set as twice the value of the Hertzian contact diameter. The discretised contact plane is given in Fig. 6.3.

The numerical representation of the Pin–On–Disc case was used to simulate two different scenarios. In the first scenario, only the surface of the pin is worn and the surface of the disc is considered sufficiently harder than the surface of the pin, while in the second scenario both the surface of pin and the disc are worn.
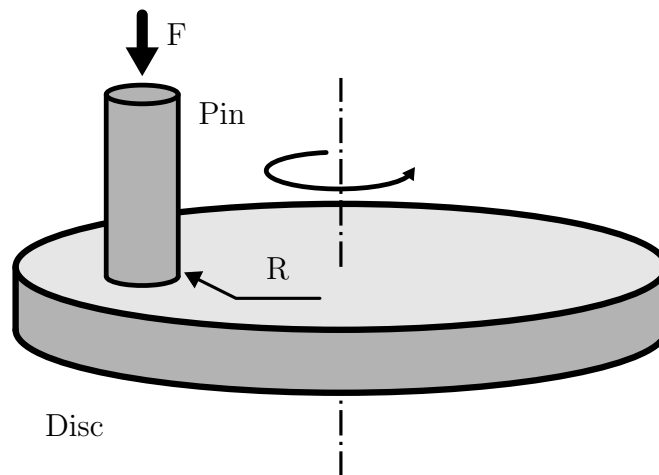
Figure 6.1: Representation of the Pin–On–Disc setup.
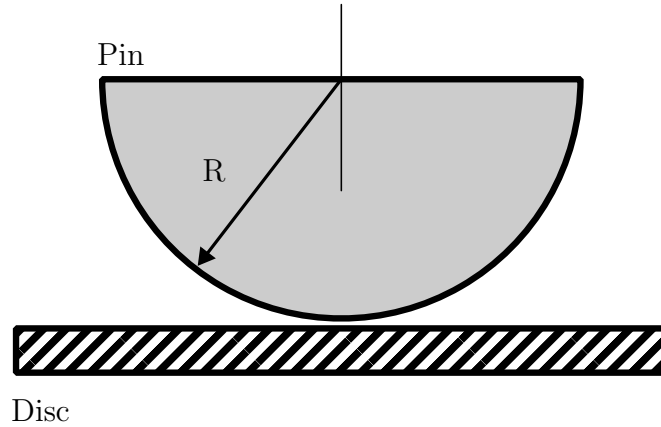
Figure 6.2: Spherical tip of the pin in PoD setup
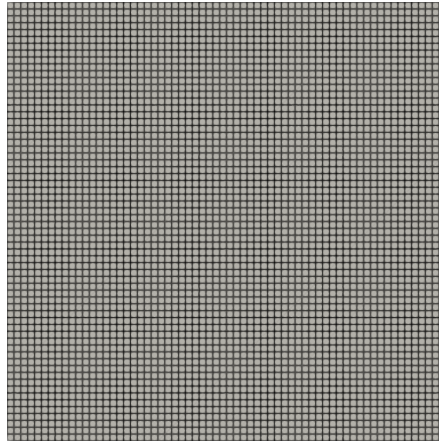
Figure 6.3: Contact zone discretised using 64x64 FA faces.

6.2.1.   Unilateral Surface Wear

For the investigation of unilateral wear, i.e. single surface wear, only wear on the surface of the pin is analysed. The solver `1SurfRodriguezWearFoam` was developed for this purposes and relies on the incremental wear model with a fixed sliding distance increment. The disc is considered sufficiently harder than the pin, thus no wear occurs on the surface of the disc. The material properties of the pin and the disc are considered to be the same, thus the Young's moduli of the pin and the disc are 210 GPa, while their Poisson's ratios are 0.3. (Table 6.1). The normal load between the pin in the disc is set to 10.2 N. Any friction between the pin and the disc is neglected, thus $\mu = 0.0$. The dimensional wear coefficient of the pin is $k_\mathrm{D} = 1.0 \times 10^{-13}$ Pa^{-1}.

Table 6.1: Parameters and material properties for the Pin-on-Disk (PoD) case.

Parameter	Symbol	Value
Load	F	10.2 N
Elastic modulus	E	210 GPa
Poisson's ratio	ν	0.3
Wear coefficient	$k_{\mathrm{D,pin}}$	1.0×10^{-13} Pa^{-1}
Radius of pin	R	50 mm

The simulation is carried out using a fixed sliding distance increment ΔL. For each iteration of the wear calculation loop the total sliding distance is increased by the value of the slide increment ΔL, until the maximum sliding distance is reached. The value of the slide increment ΔL determines the total wear depth of a surface for a single simulation step, thus small values of the increment significantly increase the duration of the simulation, requiring a greater number of wear iteration, and consequently the number of geometry updates, until maximum sliding distance is reached. On the other hand, choosing a large value for the slide increment ΔL, leads to instability as the calculated wear per simulation step is too large and the geometry is worn too fast. Radical changes in the surface geometry between increments lead to instabilities in the contact pressure, causing pressures spikes which promote the creation of fictitious high wear rates, causing even more radical changes in the geometry. The value of the slide increment ΔL is determined by employing a trial–and–error approach, relying the value of the wear coefficient and the resulting incremental wear in order to better inform the process. In the Pin–On–Disc case the value of the sliding distance increment was chosen as $\Delta L = 1.0$ mm.

The simulation was initially performed using a contact zone discretsised with 64×64 finite area (FA) faces. The comparison of pressure evolution for the 64×64 FA faces case with the numerical data provided by Rodríguez-Tembleque et al. [2] is given in Fig 6.4, while the comparison of the pin surface evolution due to wear is given in Fig. 6.5. The figures show how the contact pressure and the surface of the pin change through wear for different values of the total sliding distance.

6. Numerical Results

Comparison of the contact pressure results from the current research (simulation using the `1SurfRodriguezWearFoam` solver) and the numerical data provided by Rodríguez-Tembleque et al. [2] given in Fig. 6.4, shows good agreement between the two. The figure shows the distribution of pressure across the radial distance of the contact area for different sliding distances. The initially point contact between the pin and the disc changes due to wear and as the surface is worn, the contact area becomes larger. The same load is spread across a larger contact area, resulting in lower contact pressures. The results from the current research and the numerical data from [2] show close agreement. Slight differences may be noticed depending on the radial distance and contact pressure values. For the initial contact, i.e. peak pressure, the result align closely, with only a slight deviation at the highest contact pressure at the centre of contact. As we move away from the centre of the contact, small differences may be noticed. The shape of the curves remains consistent, with minor deviations in the width and slope of the contact pressure curves. The differences diminish as the sliding distance increases. The minor differences noticeable in lower pressure regions and at larger radial distances are attributed to **the modelling difference between the Finite Area approach used in the current research and the Boundary Element Method approach used by the authors in [2]**.

The evolution of the surface of the pin, as compared to the numerical results from [2], is shown in Fig. 6.5. The results from the current research are in excellent agreement with the numerical data from the literature [2]. The results align very closely for all radial distances and across different total sliding distances. The only visible differences appear for larger sliding distances (e.g. 320 mm and 640 mm), but these do not significantly alter the overall trends. Overall, Fig. 6.5 depicts how the surface of the pin is worn away as the sliding distance increases, loosing its initial spherical shape. The surface flattens as it is worn, thus resulting in lower contact pressure at the, now larger, contact areas.

A different number of FA faces was used to discretised the contact area used for the simulations, the results of which are shown in Figures 6.6, 6.7, 6.8 and 6.9 As the authors in [2] used 30×30 quadrilateral elements to discretise the area of contact, a lower number of FA faces was chosen first. The result of the 32×32 FA faces case are given in Fig. 6.6a, showing that the general trend remained
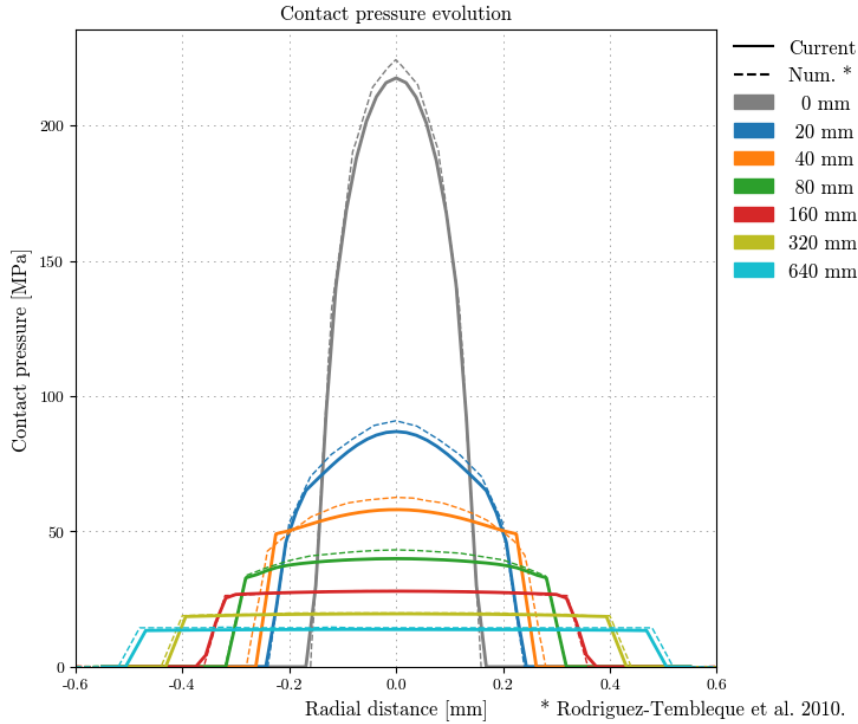
90

Figure 6.4: Contact pressure evolution, PoD case, 64×64 FA faces.

constant, but the discrepancies between the current numerical results and those from the literature appear near the edges, especially for higher sliding distances. Thus, higher mesh densities were used. Fig. 6.7 gives the same comparison of the pressure evolution, but for the 128×128 and 256×256 mesh densities respectively. For higher mesh densities, the contact pressure distribution becomes smoother, especially near the edges of the contact zone, when compared to the lower density meshes. Focusing the edges of the contact zone, the pressure curves given in Fig. 6.7a and 6.7b deviate from the results provided in [2], exhibiting steeper curves. Such deviations are attributed to the fact that for these cases much higher mesh densities were investigated than the one used by the authors in [2] (30×30 quadrilateral elements). It is possible that the pressure curves, shown here for higher density cases, represent a more realistic pressure distribution then the one presented by the authors in [2], as more elements (FA faces) were used to discretise the contact zone.

A similar comparison, but focusing on the surface evolution results for different mesh densities, was given in Fig. 6.8 and Fig. 6.9. The discrepancies between
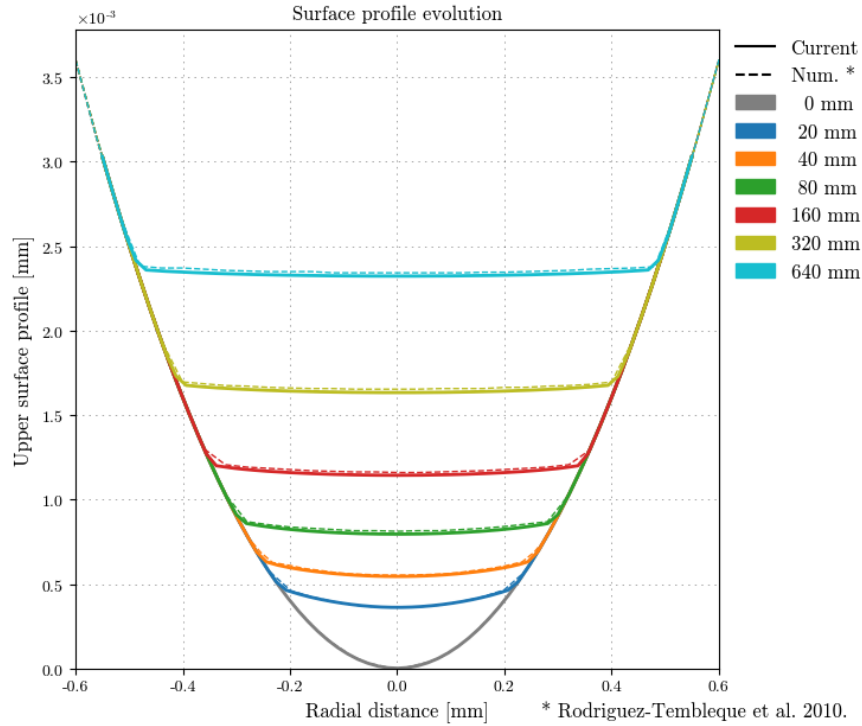
Figure 6.5: Pin surface evolution, PoD case, 64×64 FA faces.

the numerical results from the current research and the numerical data from the literature [2] can be considered very small and are localised at the edges of the contact zone. The surface profile evolution results remain in close agreement across all mesh densities. Increasing the mesh density results only in the improvement of the smoothness of the surface profile curve. Again, as with the contact pressure evolution shown in Fig. 6.6 and 6.7, the results given for higher density meshes are assumed to show a more accurate representation of the real surface evolution cause by wear.

The initial contact between the pin and the disc is a point contact, which evolves as the surface is worn away, increasing the initial contact area. Fig. 6.10 depicts the contact pressure field at the initial contact between the pin and the disc, prior to the surface of the pin being worn. On the other hand, the evolution of the contact pressure through wear is given in Fig. 6.11, depicting contact pressure fields for different sliding distances. As mentioned earlier, the contact area increases as the surface is worn, resulting in load being spread across a larger area, which leads to lower contact pressures.

As the contact pressure and surface profile evolution are not the only variables of interest when performing wear analysis for a specific case, an analysis of the calculated values of the maximum wear depth and total worn volume is performed for different sliding distances and mesh densities. Rodríquez-Tembleque et al. [2] used an analytical wear model to provide analytical data for the maximum wear depth and worn volume for different total sliding distances. These analytical results were compared to the numerical data calculated with data from the current numerical model. Fig. 6.12 shows the maximum wear depth results compared to analytical data from [2] for different mesh densities. The current numerical results show very good agreement with the provided analytical data. The finer mesh densities (128×128 and 256×256) show very slight deviation from the analytical result, while for the coarser mesh (64×64) the numerical results are still in very good agreement with the analytical data, but are slightly less precise. Regardless of the mesh density considered, the numerical result from the current research show that the wear depth grows non–linearly with the increase of the sliding distance, which is in agreement with the analytical data and can be explained as follows. The maximum calculated wear depth during a simulation increment, depends on the contact pressure, and thus on depends the geometry of the contact. the higher values of the contact pressure at the beginning of the simulation are concentrated at the initial point of contact, thus higher values of the wear depth are concentrated at the same location. As the sliding distance increases, and consequently the contact area, the initial load is spread throughout a larger contact area, thus changing the contact pressure distribution and decreasing the maximum values of the contact pressure. This, in turn, decreases the maximum value of the wear depth in the area of contact. This means that a higher contribution to the total wear depth is achieved at the beginning of the simulation, when higher contact pressures are dominant.

Fig. 6.13 depicts the comparison of the current numerical results for the worn volume and analytical data from the literature [2] for different sliding distances and different mesh densities. The numerical results show excellent agreement with the provided analytical data for all mesh densities. The results of the simulations using finer meshes (128×128 and 256×256) show no significant deviation from the analytical data, while the coarser mesh case (64×64) shows very slight

deviations, while remaining reasonably accurate. All of the numerical results in Fig. 6.13, regardless of the mesh density, follow the trend of a linear correlation between the worn volume and the sliding distance. This is expected as Archard's law dictates a linear relationship between these two variables under steady–state conditions. The worn volume represents the total material removed, which is an integral value measured over the area of contact.

Several different mesh densities were used for validating the results of the `1SurfRodriguezWearFoam` solver on the Pin–On–Disc case. While the finer meshes show better overall agreement with the numerical results from [2] and provide slightly better agreement with the analytical data from the same authors, the computational requirements increase considerably. On the other hand, the coarser mesh with 64×64 FA faces in the contact zone, showed very good agreement with the provided numerical and analytical data, with only small deviations when compared to the denser meshes, while remaining computationally inexpensive. Thus, the 64×64 mesh density case was chosen for the investigation of bilateral (dual surface) wear in the Pin–On–Disc case.
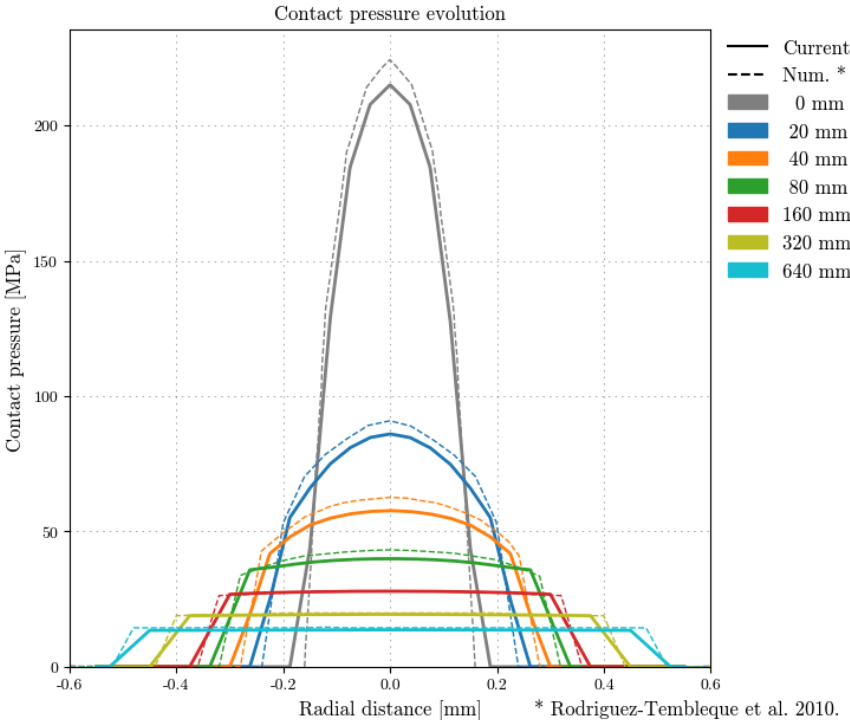
(a) 32×32 FA faces.
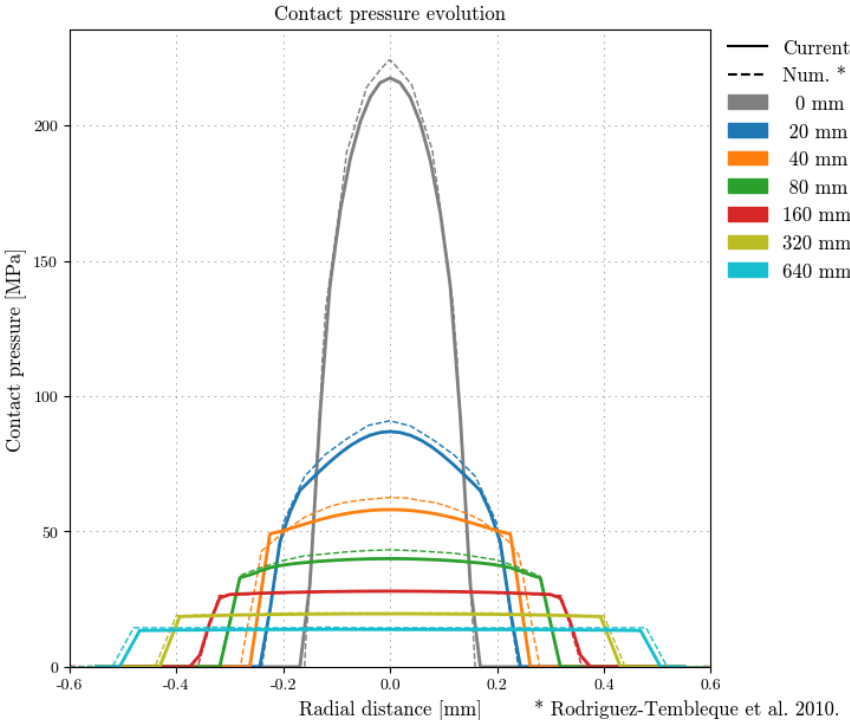
(b) 64×64 FA faces.

Figure 6.6: Contact pressure evolution for the PoD case, 32×32 and 64×64 mesh densities.

6. Numerical Results
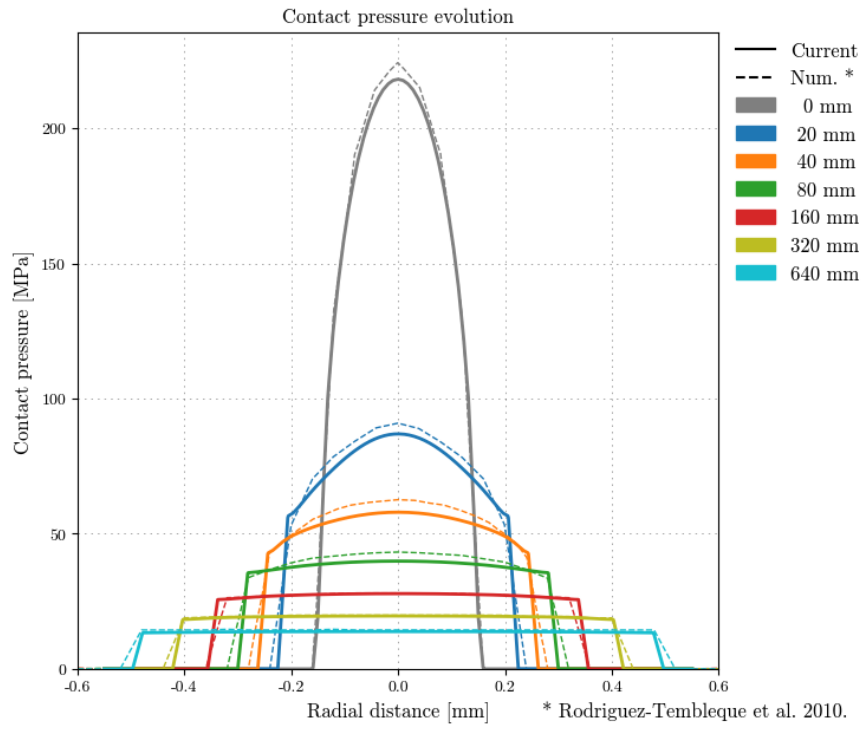
(a) 128×128 FA faces.
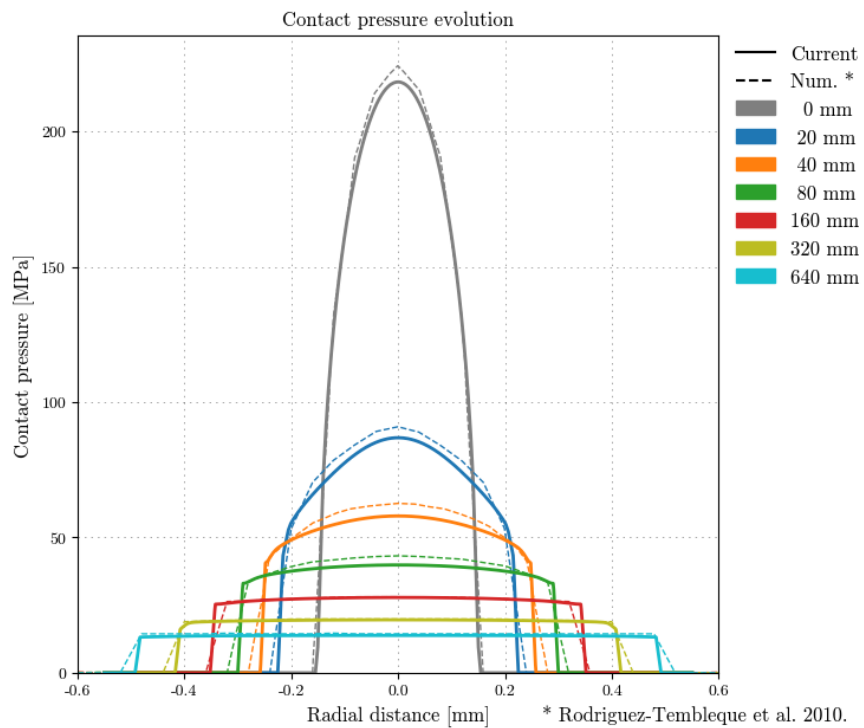
(b) 256×256 FA faces.

Figure 6.7: Contact pressure evolution for the PoD case, 128×128 and 256×256 mesh densities.
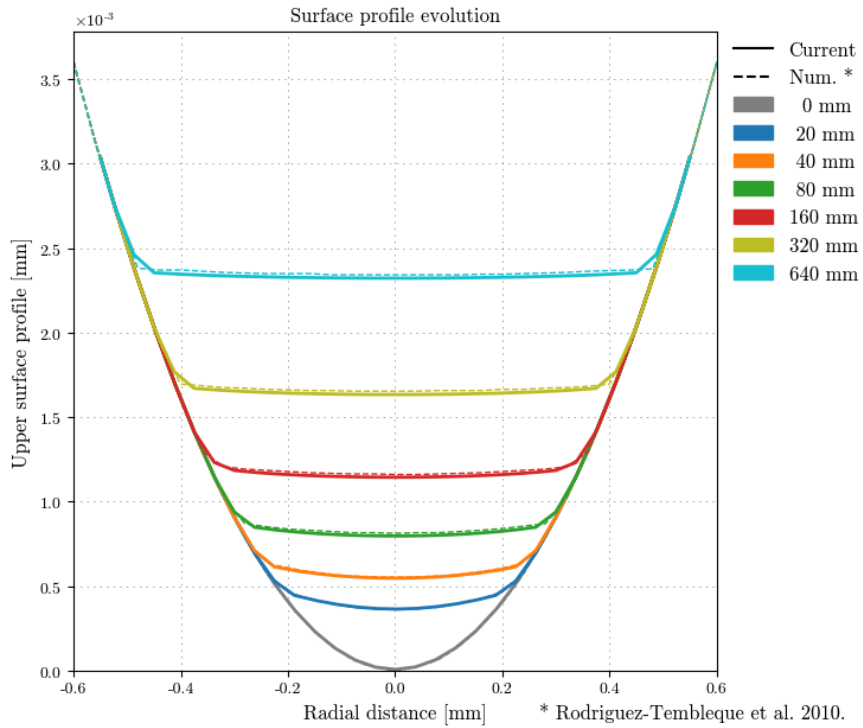
(a) 32×32 FA faces.
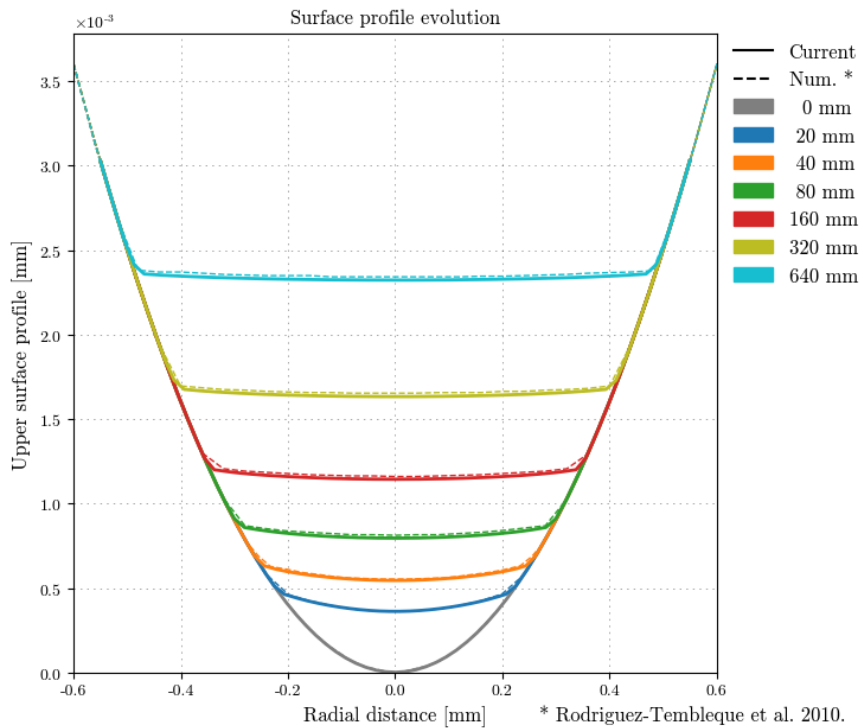
(b) 64×64 FA faces.

Figure 6.8: Pin surface evolution for the PoD case, 32×32 and 64×64 mesh densities.
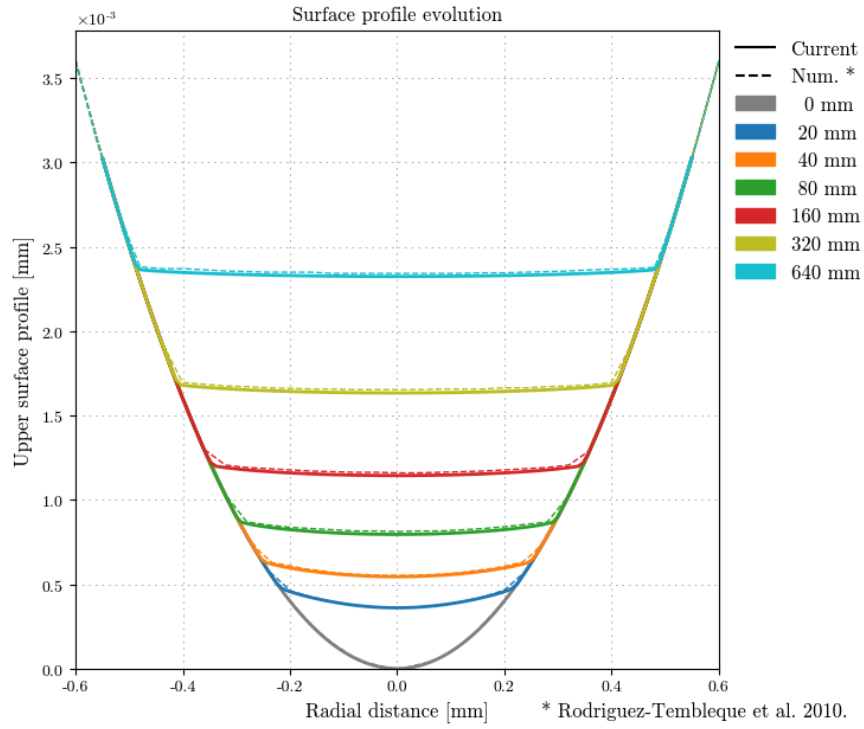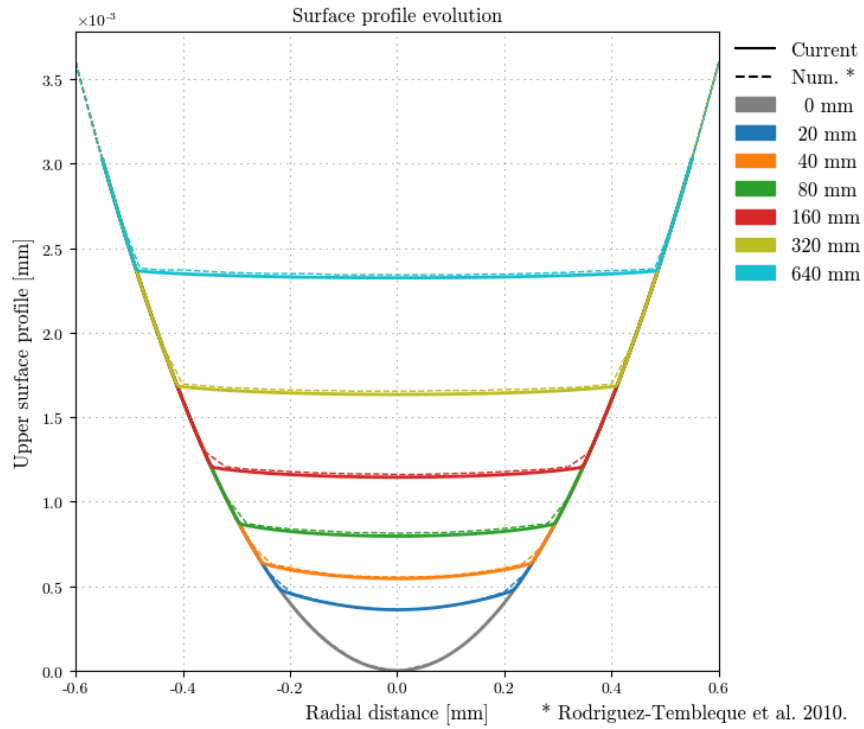
(a) 128×128 FA faces.

(b) 256×256 FA faces.

Figure 6.9: Pin surface evolution for the PoD case, 128×128 and 256×256 mesh densities.
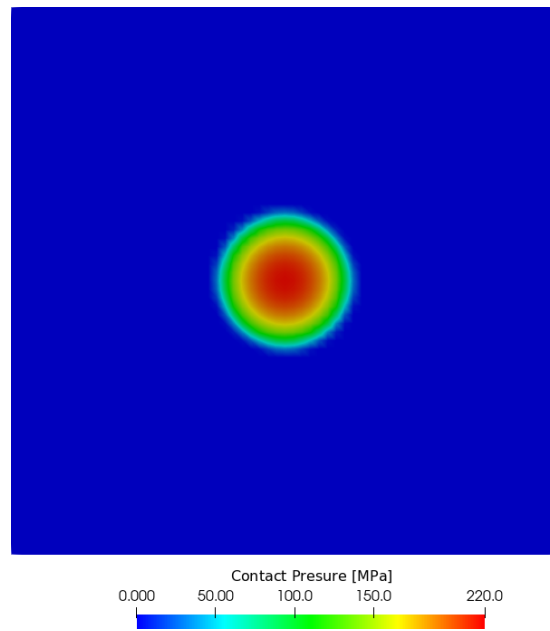
Figure 6.10: Contact pressure field at initial contact, PoD case, 64×64 FA faces.
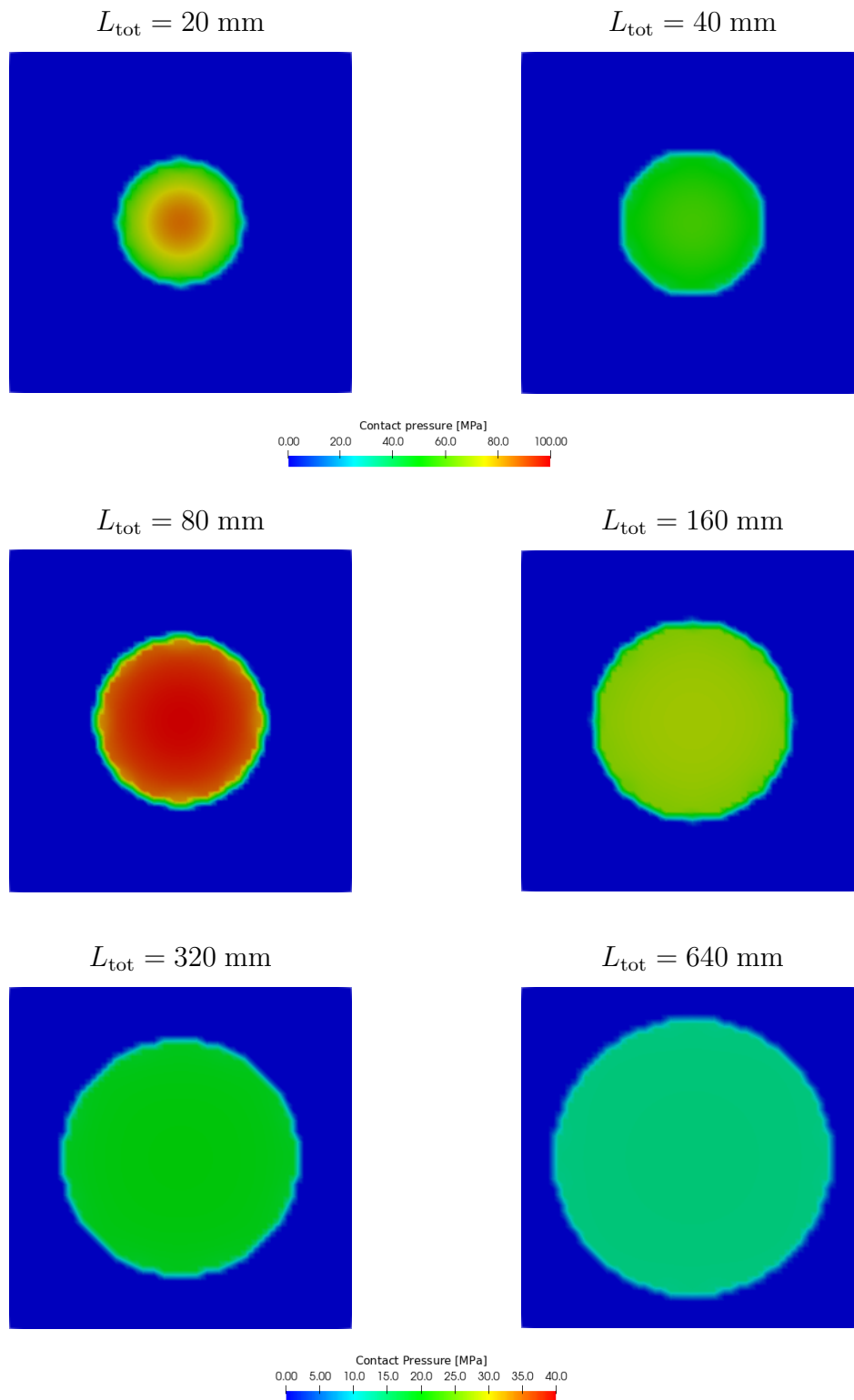
Figure 6.11: Contact pressure fields for the PoD case with 64×64 FA faces at different total sliding distances.
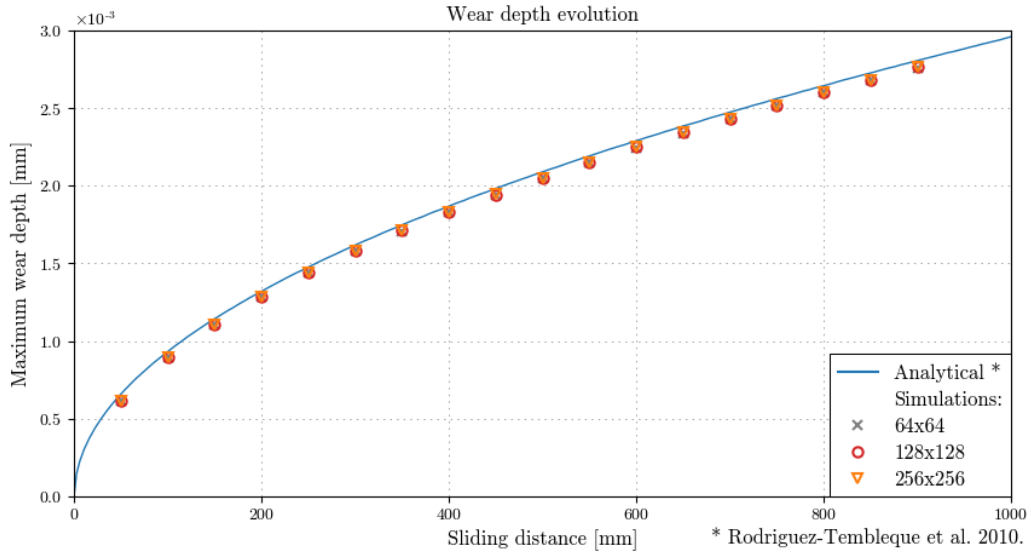
Figure 6.12: Maximum wear depth evolution: comparison with analytical data [2] for different mesh densities.
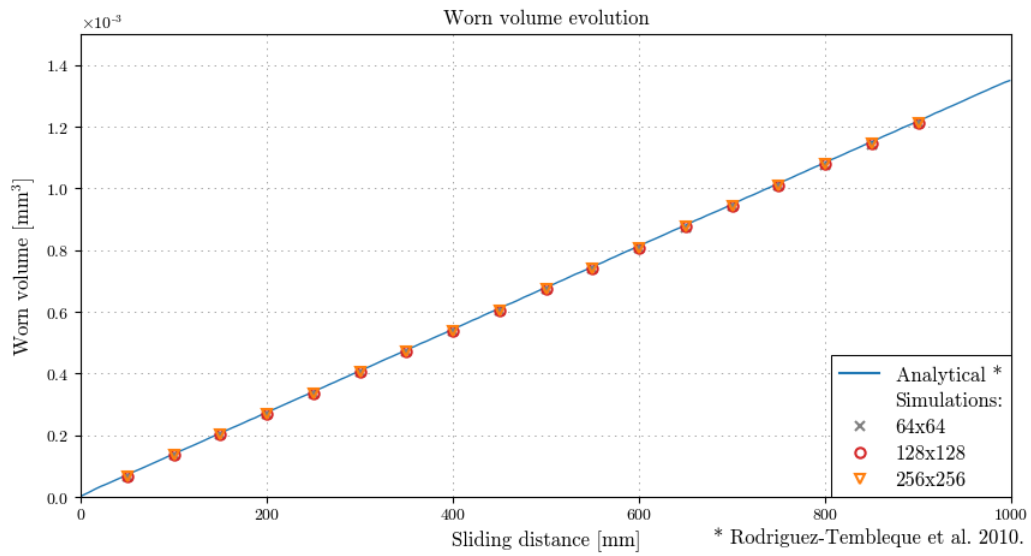
Figure 6.13: Worn volume evolution: comparison with analytical data [2] for different mesh densities.

6.2.2. Bilateral Surface Wear

Bilateral wear, i.e. wear and surface evolution of both surfaces, in the Pin–On–Disc case was investigated. The solver `2SurfRodriguezWearFoam` was developed for the purpose of bilateral surface wear analysis. The initial geometry of a spherically tipped pin sliding over a rotating disc was kept the same as in the unilateral wear case. The contact zone was discretised is the same way as shown in Fig. 6.3, with its length and width determined as being equal to twice the value of the Hertzian contact diameter, determined for the given load [153].

The material properties of the surface of the pin and the disc are the same, i.e. the elastic moduli are given as $E_\mathrm{p} = E_\mathrm{d} = 210$ GPa, while the Poisson's ratios are $\nu_\mathrm{p} = \nu_\mathrm{d} = 0.3$. The prescribed load is kept the same as in the unilateral wear case and is set to $F = 10.2$ N, while friction is neglected ($\mu = 0.0$). The simulation is performed using fixed sliding distance increments of $\Delta L = 1.0$ mm. The material properties and basic parameters for the case are shown in Table 6.2.

While the necessary contact parameters (E and ν) of the pin and disc surface are kept the same, separate dimensional wear coefficients are given for each of the two surfaces. Two case are analysed: a case where both surface have the same value of the dimensional wear coefficient, $K_\mathrm{D,p} = K_\mathrm{D,d} = 0.665 \times 10^{-13}$ Pa^{-1} and a case where the dimensional wear coefficient of the pin $k_\mathrm{D,p}$ is two times the value of dimensional the wear coefficient of the disc $k_\mathrm{D,d}$, i.e. $K_\mathrm{D,p} = 2\,K_\mathrm{D,d} = 0.887 \times 10^{-13}$ Pa^{-1} The values of the dimensional wear coefficients for both cases are summarised in Table 6.3.

Table 6.2: Bilateral wear PoD case parameters and material properties.

Parameter	Symbol	Value
Load	F	10.2 N
Elastic modulus of pin	E_p	210 GPa
Elastic modulus of disc	E_d	210 GPa
Poisson's ratio of pin	ν_p	0.3
Poisson's ratio of disc	ν_d	0.3
Radius of pin	R	50 mm
Sliding distance increment	ΔL	1.0 mm

Table 6.3: Bilateral wear PoD case wear coefficients.

Dimensional wear coefficient	Case 1	Case 2
Pin $(K_{\mathrm{D,p}})$	$0.6650 \times 10^{-13}\ \mathrm{Pa}^{-1}$	$0.8870 \times 10^{-13}\ \mathrm{Pa}^{-1}$
Disc $(K_{\mathrm{D,d}})$	$0.6650 \times 10^{-13}\ \mathrm{Pa}^{-1}$	$0.4435 \times 10^{-13}\ \mathrm{Pa}^{-1}$

An analysis of the influence of wear on the surface evolution of the pin and the disc was performed for both cases. The numerical results from the current research, calculated using the `2SurfRodriguezWearFoam` solver, were validated against numerical data provided by Rodríguez-Tembleque et al. [2]. Fig. 6.14 depicts the evolution of the surface of the pin and the disc for the first case, when the surfaces have equal dimensional wear coefficients. The figure shows the changes in surface heights from the initial moment ($L_{\mathrm{tot}} = 0$ mm) to the total sliding distance of $L_{\mathrm{tot}} = 500$ mm.
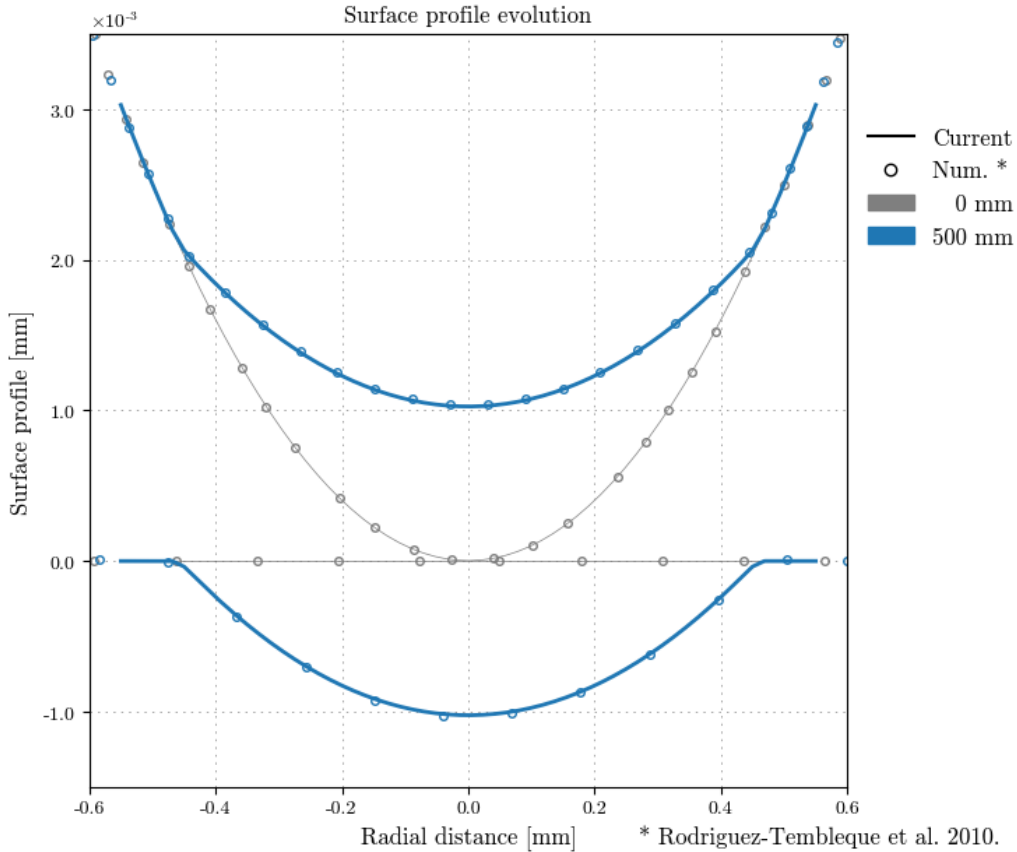
Figure 6.14: Bilateral surface wear PoD case with $K_{\mathrm{D,p}} = K_{\mathrm{D,d}}$

6. Numerical Results

The numerical results for the surface evolution from the current research are compared to the numerical results from the literature [2] in Fig. 6.14 and show very good agreement. The be more precise, the current numerical results (full lines) and the data from [2] (circles) show excellent agreement at he extremes of the radial distance, while only minor deviations may be noticed at the centre of contact. Generally, the results depict the evolution of the upper (pin) and lower (flat disc) surfaces from the initial point contact case. A representation of the two surfaces in their initial state is shown in Fig. 6.16a, while the final state of the surfaces after 500 mm of sliding is depicted in Fig. 6.16b. A scale factor of 30 was used for better visualisation of the surfaces.
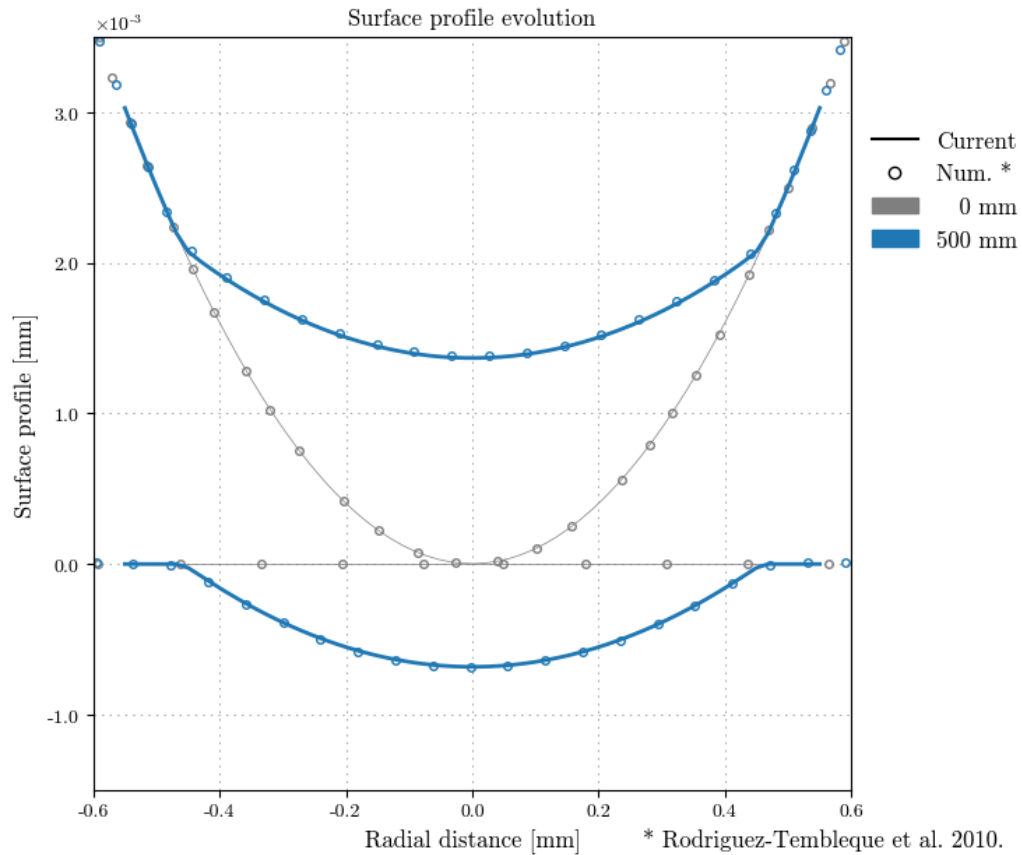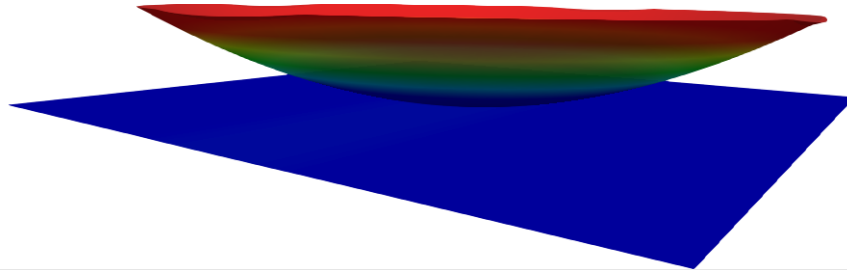

Figure 6.15: Bilateral surface wear PoD case with $K_{D,p} = 2\,K_{D,d}$

A similar comparison between numerical data from [2] and numerical data from the current research, regarding the surface evolution of the case in which the dimensional wear coefficient of the pin is twice that of the disc, i.e. $K_{D,p} = 2\,K_{D,d}$,

is given in Fig. 6.15. As in the previous case, the figure depicts the initial state of the surface of the pin and the disc ($\Delta L = 0.0$ mm) and the final state after 500 mm of sliding. The numerical results (depicted as full lines in Fig. 6.15) show very good agreement with the data from [2] (depicted as circles). A visualisation of the final state of the two surfaces is given in Fig. 6.16c, using a scale factor of 30 for better visualisation.

If the numerical results for the different dimensional wear coefficients (Table 6.3), which are shown in Figures 6.14 and 6.15, are compared, differences in the surface evolution for the two cases may be noted. In the second case, Fig. 6.15, the surface of the pin (upper surface) is worn at a faster rate than when compared to the first case, shown in Fig. 6.14. The exact opposite is true for the surface of the disc (lower surface), which is worn less in the second case. Such results are expected as the wear depth is determined by the wear coefficient. In the second case the surface of the pin has a higher wear coefficient than in the first case, thus is worn more. Again the opposite is true for the surface of the disc, which has a lower wear coefficient in the second case and is worn less than in the first case.
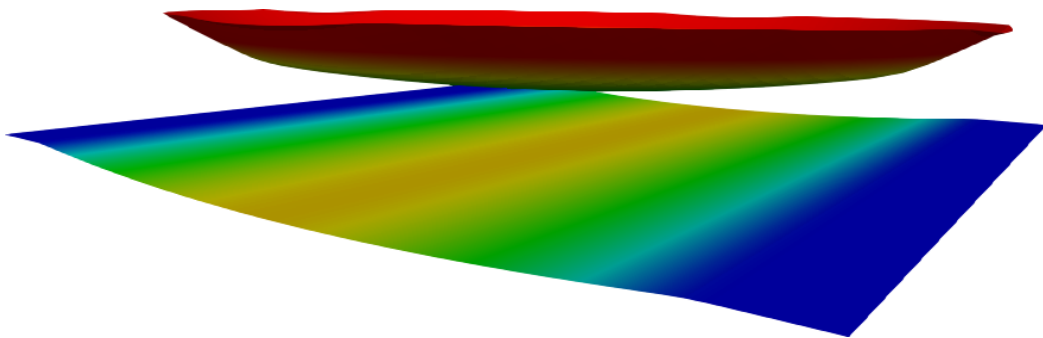
(a) Initial surface states.
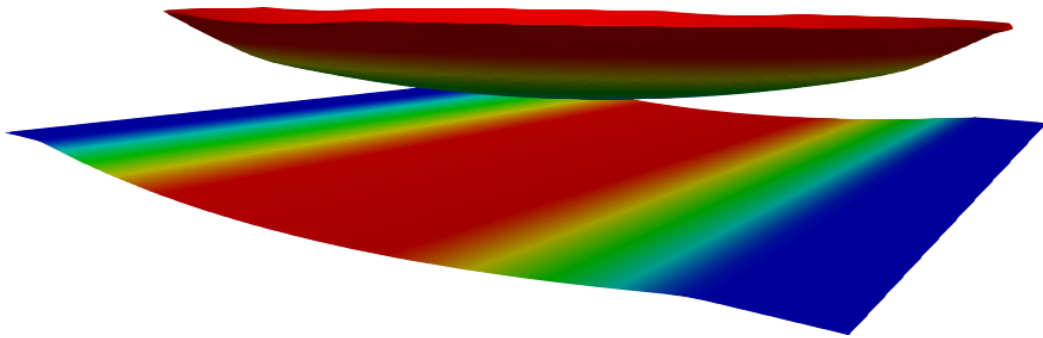
(b) Surfaces after 500 mm of sliding for $K_{\mathrm{D,p}} = K_{\mathrm{D,d}}$

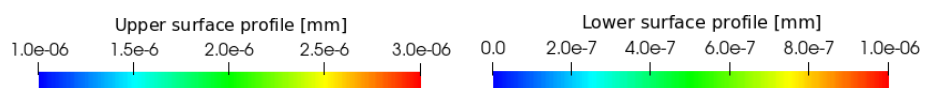(c) Surfaces after 500 mm of sliding for $K_{\mathrm{D,p}} = 2\,K_{\mathrm{D,d}}$

Figure 6.16: Initial and final surface states for bilateral wear in PoD case

6.3.   Ring–On–Block Sliding Wear

In Section 6.3., the wear algorithm was validated against numerical data from the literature for unilateral and bilateral wear of an initially point contact case. In this section, the solver `zhanLineContactWearFoam` is used to validate the results of the wear algorithm for an initially line contact case. The results are compared to numerical results and experimental data provided by Zhan and Huang. [34].
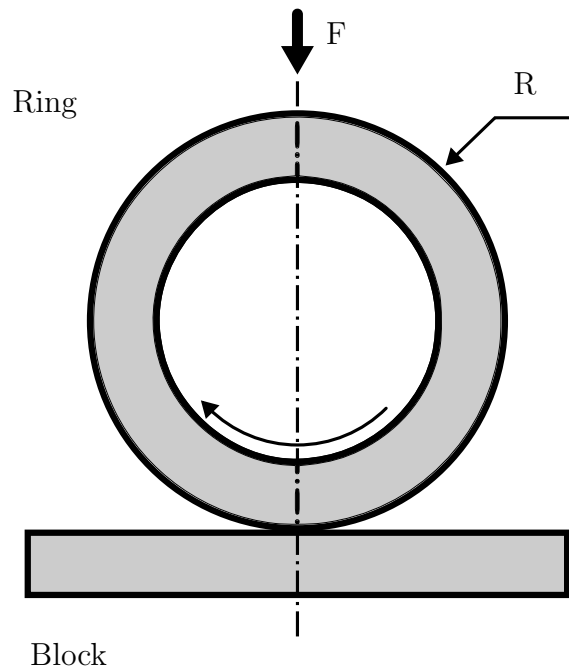

Figure 6.17: Representation of the Ring–On–Block setup.

The case considered here is the Ring–On–Block (RoB) case, show in Fig. 6.17. A ring with radius R is pressed against a block under the load F, while rotating at a fixed speed. The radius of the ring is $R = 24.61$ mm and its width is $W_r = 13.06$ mm. The width and length of the block are $W_b = 12.32$ mm and $L_b = 19.05$ mm. The load used to establish contact between the ring and the block is set to $F = 300$ kN/m. Zhan and Huang [34] concluded that friction may be neglected as it does not affect the shape distribution, it only shifts the contact region with respect to the initial contact region. The effect of such a shift can be disregarded for most engineering applications as these cases do not usually exceed $\mu = 1.0$. In this particular case, the friction coefficient would be $\mu = 0.13$,

making the shift of the contact region negligible.

The material properties of the ring and the block are given as follows: the elastic moduli of the ring and the block are $E_r = 209$ MPa and $E_b = 204$ MPa respectively, while Poisson's ratios are given as $\nu_r = 0.269$ and $\nu_b = 0.285$. In this particular setup, the ring would show uniform wear along its circumference, thus the wear depth on the surface of the ring can be considered negligible when compared to the wear on the block. Thus, for the numerical setup, only the block will be worn. The dimensional wear coefficient of the contact pair was determined experimentally by Zhan and Huang [34] as $K_D = 1.245 \times 10^{-9}$ MPa^{-1}. Plastic asperity deformation was not directly taken into account, but is considered indirectly through the experimentally determined wear coefficient [34]. The most important geometrical and material properties of the Ring–On–Block case are summarised in Table 6.4.

Table 6.4: Geometrical and material properties for the Ring–On–Block (RoB) case.

Parameter	Symbol	Value
Ring radius	R	24.61 mm
Ring width	W_r	13.06 mm
Block width	W_b	12.32 mm
Block length	L_b	19.05 mm
Applied load	F	300 kN/m
Friction coefficient	μ	0.13
Elastic modulus of the ring	E_r	209 MPa
Elastic modulus of the block	E_b	204 MPa
Poisson's ratio of the ring	ν_r	0.269
Poisson's ratio of the block	ν_b	0.285
Wear coefficient	K_D	1.245×10^{-9} MPa^{-1}

In contrast to the discretisation of the contact zone performed for the PoD case in Sec. 6.2., where the domain was discretised using an equal number of FA faces in both directions, the contact zone in the RoB case is discretised using strips. This is shown in Fig. 6.18. In the RoB case, the initial contact between the surfaces is a line contact. Thus, the shape of the contact pressure curve remains constant

in the direction parallel to the ring's axis of rotation. This, in turn, means that the contact zone needs only to be discretised in the direction perpendicular to the ring's axis of rotation. The discretisation can then be performed using N strips with a length equal to the length of the domain, instead of using $N \times N$ square elements. This requires the use of a modified deterministic contact model for line contact, which relies on strip elements and is based on Eq. 5.4. The use of only N strip elements in stead of $N \times N$ square elements, considerably reduces the computational requirements, even for 256 FA strips used for this case. Fig. 6.18 depicts the contact zone as discretised using 64 FA strips (faces) for better visualisation. In the actual simulation, the discretisation was performed using 256 FA faces along the width of the contact area.
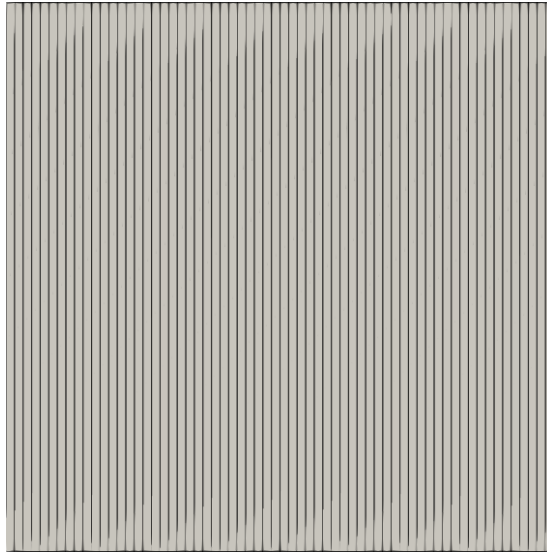

Figure 6.18: Contact zone discretised using 64 FA strips along the width of the contact zone.

The simulations were performed using the `zhanLineContactWearFoam`, which uses the incremental wear model with a fixed sliding distance increment ΔL. The sliding increment was chosen to balance computational efficiency with numerical stability. The fixed sliding increment used in the simulations was set to $\Delta L = 10.0$ mm

The numerical results from the current research showing the evolution of the contact pressure due to wear are show in Fig. 6.19. The results show how the contact pressure changes as the surface of the block is worn, and the total

6. Numerical Results

sliding distance changes from $L_{\text{tot}} = 0$ m to $L_{\text{tot}} = 300$ m. The results from the current study are validated against the numerical results from Zhan and Huang [34]. For small sliding distances (0 m, 0.5 m) the results are closely aligned with the numerical data from the literature, showing a sharp pressure peak at the centre of contact. A slight underestimation of the pressure peak at the centre of contact may be noted for the current results at 0.5 m. As the sliding distance increases, the pressure peaks become broader as the contact zone becomes larger due to wear and the pressure distribution flattens. At larger sliding distances, the current numerical results still closely follow the data from [34]. Overall, the current numerical results show very good agreement with the numerical data from Zhan and Huang [34], with only minor discrepancies seen at the sliding distances of 25 m and 75 m.
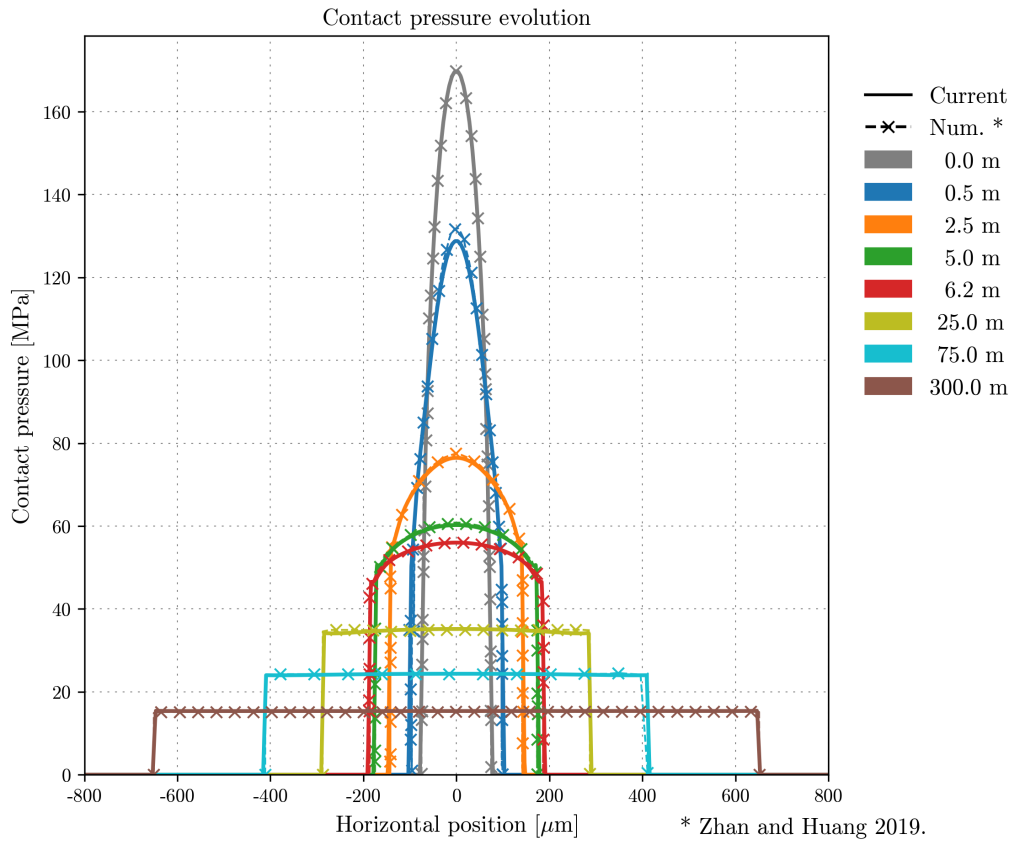

Figure 6.19: Contact pressure evolution for the Ring–On–Block case.

The surface evolution due to wear acting on the block is given in Fig. 6.20.

110

The figure presents numerical results, which show how the surface of the block is gradually worn as the total sliding distance increases. Initially represented by a straight horizontal line, the surface of the block evolves into a wear groove, which expands as the sliding distance increase form 0 m to 300 m. The numerical results from the current research are very closely aligned with the numerical data from the literature [34], showing very good agreement across all sliding distances, with little to no deviation. As expected, the current numerical results predict the changes in the surface of block, i.e. the trend of the wear groove becoming deeper and broader.
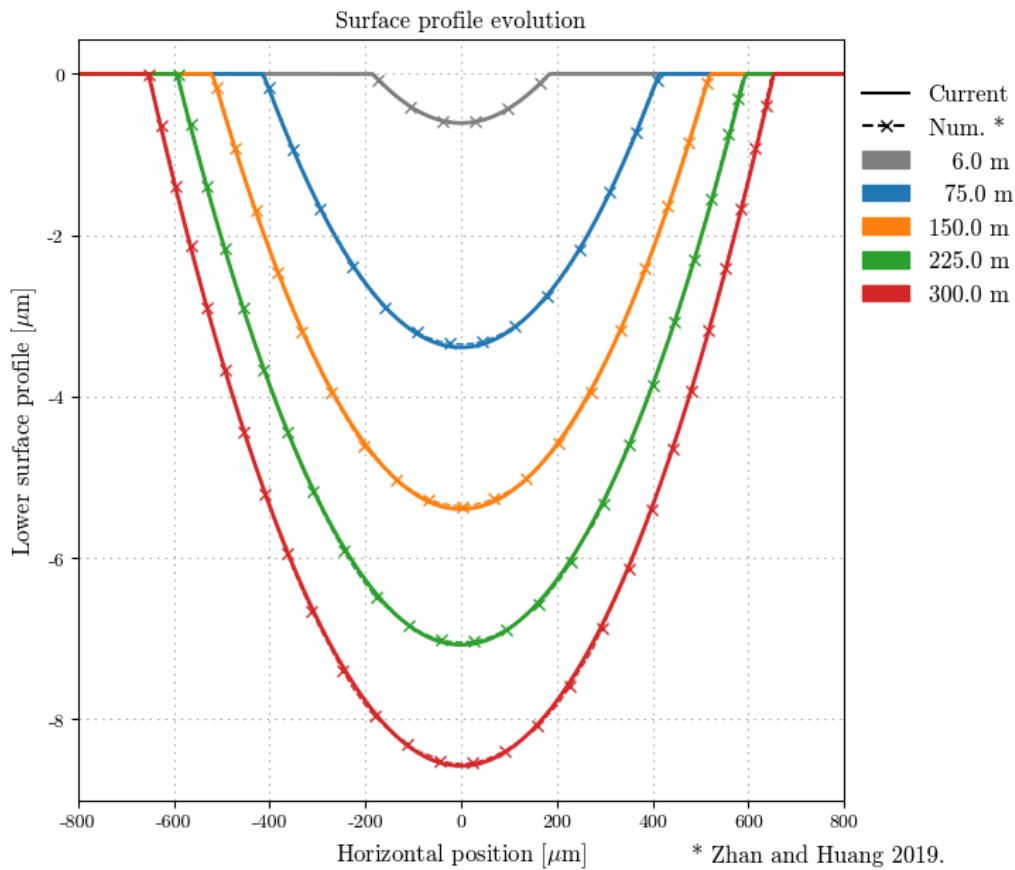

Figure 6.20: Surface evolution of the block for the Ring–On–Block case.

The numerical data resulting from the simulations using the `zhanLineContactWearFoam` solver is also validated against experimental data provided by Zhan and Huang [34]. Fig. 6.21, show the comparison between the experimentally determined values of the wear depth on the surface of the block, numerical

data from the literature and the numerical data from the current research. The values are provided for four different total sliding distances: 75 m, 150 m, 225 m and 300 m. As was determined earlier by examining Fig. 6.20, and confirmed by the results shown in Fig. 6.21, the current numerical results show very good agreement wiht the numerical data from Zhan and Huang [34], with little to no discrepancies. When the experimental data is considered, the current numerical results follow the general behaviour of the experimental data, i.e. both show the wear depth increasing symmetrically towards the centre, creating a parabolic distribution. At 75 m the numerical results accurately predict the depth of the wear groove, while underestimating the width of the wear groove. For the sliding distances of 150 m and 225 m, the current numerical results show an overestimation of the maximum wear depth, but with a better prediction of the width of the groove. For the last sliding distance of 300 m, the numerical and experimental results are in very good agreement for both the depth and width of the wear groove.

The results for the maximum wear depth and width of the wear groove were analysed for different total sliding distances, comparing the results from the current research with the experimental and numerical data from [34]. The comparison between the aforementioned results is given in Table 6.5 and Table 6.6. The same tables provide the relative error between the experimental data and the numerical results, both from the current research and from the literature [34]. The wear groove width results from the current model consistently shows improved values of the relative error, when compared to numerical results from [34], most noticeable for the lower sliding distance $L_{\text{tot}} = 75.0$ m. Looking at the results for the wear depth, the current numerical approach produces results which closely follow the trend of the numerical data from the literature, with a slight increase in the relative error. The general behaviour of the current results aligns with physical expectations, showing an increase of the maximum wear depth with an increase in L_{tot}. For the maximum wear depth at 75 m, the relative error of the current model is minimal, showing great agreement with the experimental data, while the relative error for the width of the wear groove is 15.18%. For 225 m, the relative error of the current model for the wear depth increase to 40.36% , while the relative error for the wear groove width decreases to 4.35%. For the
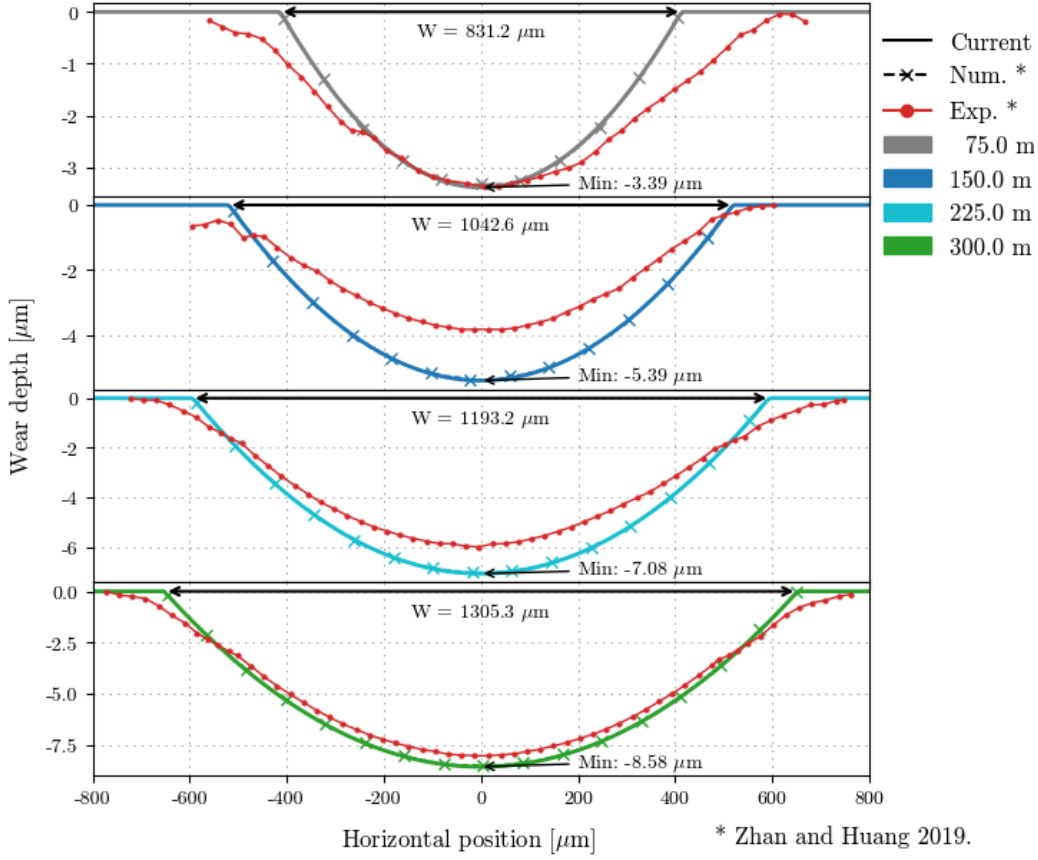
Figure 6.21: Wear groove analysis for the the Ring–On–Block case.

last two sliding distances (225 m and 300 m), the errors for the depth decrease to 18.99% and 6.72%, while the errors for the wear groove change to 2.99% and 4.72 %, respectively. The numerical data from the literature [34] closely follows the data from the current model, with similar values of the relative error. It should be noted that the measurement uncertainties for the experimental data are not known.

6.4. Reciprocating Ball–On–Flat Wear

In this section the numerical results of a wear analysis for a reciprocating Ball–On–Flat (BoF) setup are presented. The setup is analysed using the `anderssonWearFoam` solver developed as part of this research. The solver uses the wear algorithm presented in Sec. 5.4., more specifically, it relies on the quasi–steady–

6. Numerical Results

Table 6.5: Comparison of wear groove width values in the RoB case

L_{tot} (m)	Scar Width (µm)			Relative Error	
	Exp. [34]	Num. [34]	Current	Num. [34]	Current
75	980	822.97	831.2	16.02%	15.18%
150	1,090	1,034.78	1,042.6	5.07%	4.35%
225	1,230	1,183.72	1,193.2	3.76%	2.99%
300	1,370	1,302.41	1,305.3	4.93%	4.72%

Table 6.6: Comparison of maximum wear depth values in the RoB case

L_{tot} (m)	Maximum Wear Depth (µm)			Relative Error	
	Exp. [34]	Num. [34]	Current	Num. [34]	Current
75	3.34	3.35	3.39	0.30%	1.50%
150	3.84	5.35	5.39	39.32%	40.36%
225	5.95	7.03	7.08	18.15%	18.99%
300	8.04	8.53	8.58	6.09%	6.72%

state wear model discussed in Sec. 5.3.. The results from the current numerical analysis are validated against numerical data from Andersson et al. [27].

The reciprocating Ball–On–Flat case setup is depicted in Fig. 6.22. In the setup, a ball of radius $R = 5$ mm is pressed against a perfectly flat surface with a set load. Both the surface of the ball (upper surface) and the flat (lower surface) are made of the same material, i.e. AISI25100 steel, and have the same material properties: elastic moduli $E_b = E_f = 207$ GPa, Poisson's ratios $\nu_b = \nu_f = 0.3$ and hardness $H_b = H_f = 4$ GPa. The applied load is 100 N, which is much greater than in the previous cases. At high loads, the contact stress can exceed the yield strength of the material, thus elastic–perfectly plastic behaviour is assumed [27]. The wear coefficient for the surface pair was determined experimentally in [27], and is given as the total dimensional wear coefficient $K_D = 3.11 \times 10^{-16}$ Pa^{-1}. According to Andersson et al. [27], wear is assumed to be equal on both the ball and the flat, thus: $K_{D,b} = K_{D,f} = 1.555 \times 10^{-16}$ Pa^{-1}. A summary of the geometrical and material properties for the Ball–On–Flat case is given in Table 6.7.
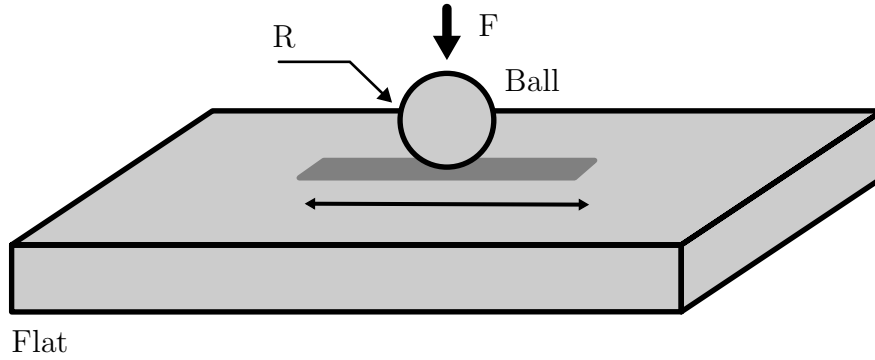
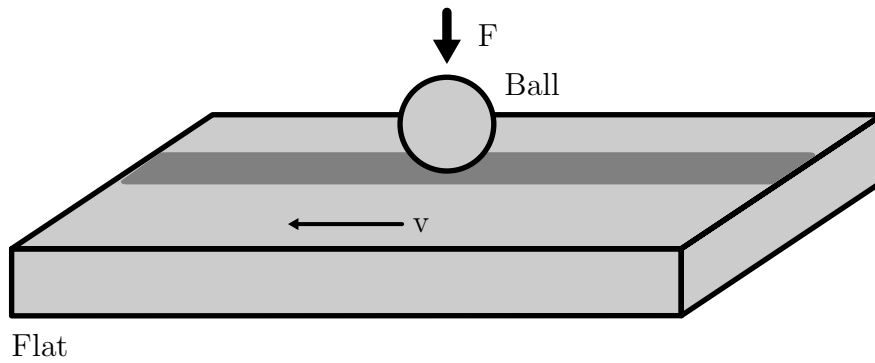Figure 6.22: Representation of the Reciprocating Ball–On–Flat setup.

Figure 6.23: Periodic Ball–On–Flat case.

The reciprocating Ball–On–Flat setup, depicted in Fig. 6.22, is used to analyse wear in an initially point contact case, undergoing reciprocating motion. As per Sec. 5.3., the quasi–steady–state wear model is applied, thus transforming the reciprocating motion into a sliding motion with a constant sliding velocity v. The total time of sliding is set to $T_{\text{tot}} = 3600$ s. The sliding time increment ΔT was set as $\Delta T = 0.25$ seconds, with a constant average velocity $v = 0.1$ m/s. According to Ilincic et al. [29], the sliding distance per cycle, denoted as the peal–to–peak stroke length S shown in Fig. 6.24, can be determined using the average sliding velocity v and stroke frequency f as follows:

$$v = 2\,S\,f \quad \rightarrow \quad S = \frac{v}{2\,f} \tag{6.1}$$

Using Eq. 6.1, the average sliding velocity $v = 0.1$ m/s and the stroke frequency $f = 25$ Hz, the stroke length was calculated as $S = 25$ mm. The stroke length is used as the sliding distance per cycle, discussed in Sec. 5.3., and is required for

Table 6.7: Geometrical and material properties for the Ball–On–Flat (BoF) case.

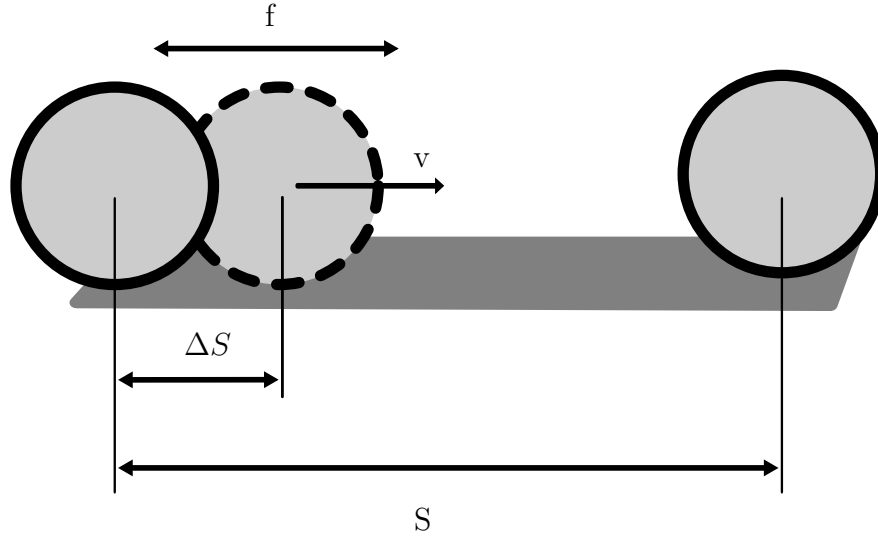| Parameter	Symbol	Value
Ball radius	R	$5\,\text{mm}$
Applied load	F	$100\,\text{N}$
Elastic modulus of ball	E_{b}	$207\,\text{GPa}$
Elastic modulus of flat	E_{f}	$207\,\text{GPa}$
Poisson's ratio of ball	ν_{b}	0.3
Poisson's ratio of flat	ν_{f}	0.3
Hardness of ball	H_{b}	$4\,\text{GPa}$
Hardness of flat	H_{f}	$4\,\text{GPa}$
Wear coefficient (total)	K_{D}	$3.11 \times 10^{-16}\,\text{Pa}^{-1}$
Wear coefficient of ball	$K_{\text{D,b}}$	$1.555 \times 10^{-16}\,\text{Pa}^{-1}$
Wear coefficient of flat	$K_{\text{D,f}}$	$1.555 \times 10^{-16}\,\text{Pa}^{-1}$

Figure 6.24: Peak–to–peak stroke in the BoF case.

the averaging procedure between the fast and slow time scale.

The computational domain used to describe contact zone is square, with its width and length determined as twice the value of the Hertzian contact diameter [153]. The domain was discretised using 128×128 FA faces.

The evolution of the contact pressure is shown in Fig. 6.25 for a cross–section at $y = 0$. The results show how the contact pressure evolves, reducing in magnitude, as the sliding time increase. This happens due to surface wear, which cause the contact area to increase. The load becomes supported by a larger surface area, thus reducing the contact pressure magnitude and causing a wider pressure distribution. It should be noted that the maximum value of the pressure was not high enough to cause plastic deformation. Furthermore, both the current data and the data from the literature show rapid flattening in the early stages of the simulation, caused by high wear rates brought on by high values of pressure at the beginning of the simulation. As the simulation time increases the wear rates decrease as the pressure curves flatten.

The same figure (Fig. 6.25) shows the comparison between the numerical results of the current research and the numerical data from the literature [27]. The current numerical data follows the trend of the numerical data from [27] consistently across all sliding times, decreasing the contact pressure peak and widening the contact area. The only noticeable difference between the current results and the ones from [27] can be seen at the edges of the contact zone. This is most noticeable at 500 s, where the pressure curve resulting from the current model shows a more gradual transition towards the end of the contact zone. Both the current data and the data from the literature show rapid flattening in the early stages of the simulation, cause by high wear rated brought on by high values of pressure, which stabilise as the simulation time increases and the wear rates decrease. Fig. 6.26 shows two contour plots of the contact pressure at 200 s. The plot in Fig. 6.26a shows the contour plot of the contact pressure from the current model, while Fig. 6.26b shows the same contour plot as reported by Andersson et al. [27]. The contour plots show very good agreement, with only slight differences which are attributed to the visualisation procedure.

An analysis of the surface evolution was performed and the results are shown in Fig. 6.27, where Fig. 6.27a shows the surface of the ball in the sliding direction at $y = 0$, as predicted by the current model. A depiction of the surface of the ball in the direction perpendicular to the sliding direction at $x = 0$ is shown in Fig. 6.27b. The results of the current model are compared to numerical data from [27], showing very good agreement across all sliding times and for both

the sliding direction and the direction perpendicular to the sliding direction. **The difference between the ball surface profile evolution in the two directions is attributed to the contact conditions in the BoF setup**. The numerical results from the current model show that surface wear is deeper and more pronounced in the sliding direction ($y = 0$), while the perpendicular ($x = 0$) direction shows a shallower and more symmetric surface profile.

The surface evolution of the flat (lower surface) is reported in Fig. 6.28, under the assumption of equal wear on both surfaces [27]. The figure shows the evolution of the wear groove in the direction perpendicular to the direction of sliding ($x = 0$). As expected, the wear groove becomes deeper and wider as the total sliding time increases and the effects of wear accumulate. It should be noted that the validation against the numerical data from [27] was not possible, as the required data was not available.

A visualisation of the surface height field for the surface of the ball (the upper surface) at different time steps is given, together with a three–dimensional visualisation of the aforementioned field, in Fig. 6.29. For better visualisation of the three–dimensional surface, a scaling factor of 10 was used. Similarly, the visualisation of the surface height field together with a three–dimensional view of the surface of the flat (the lower surface) was provided in Fig. 6.30, here a scaling factor of 30 was used for better visualisation. The two images clearly show how the wear affects the surfaces of the ball and the flat, increasing the area of contact. As discussed, the surface of the ball is being flattened, loosing its spherical shape, while a wear groove is being formed on the lower surface, increasing in width and depth.
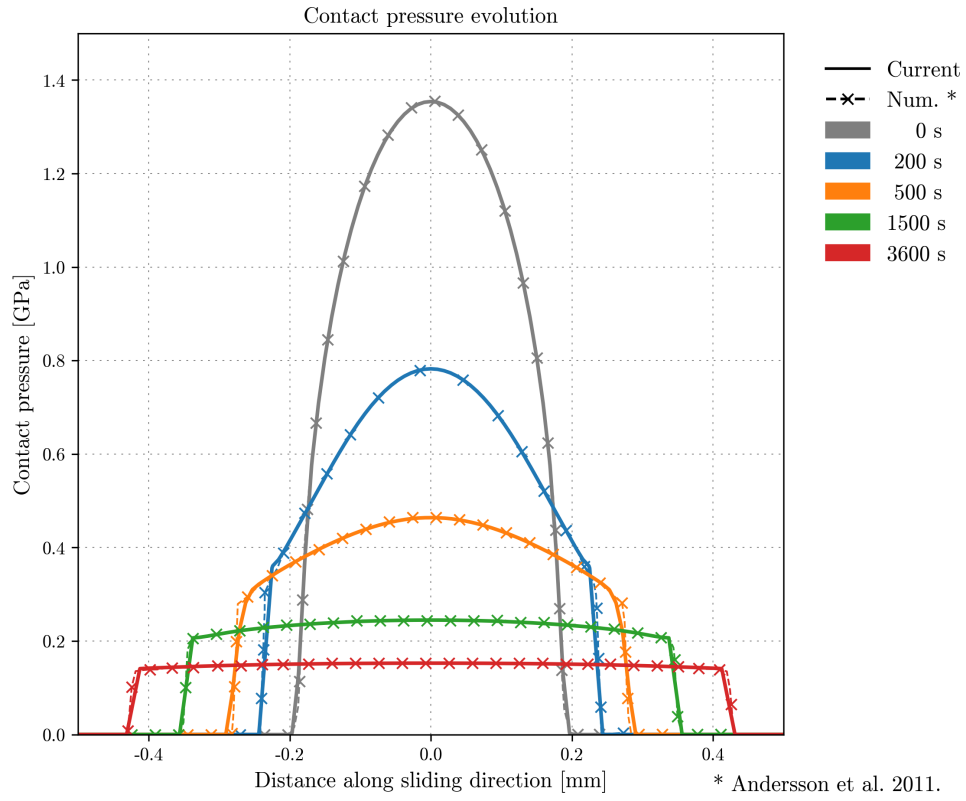
Figure 6.25: Contact pressure evolution for the Ball–On–Flat case at $y = 0$
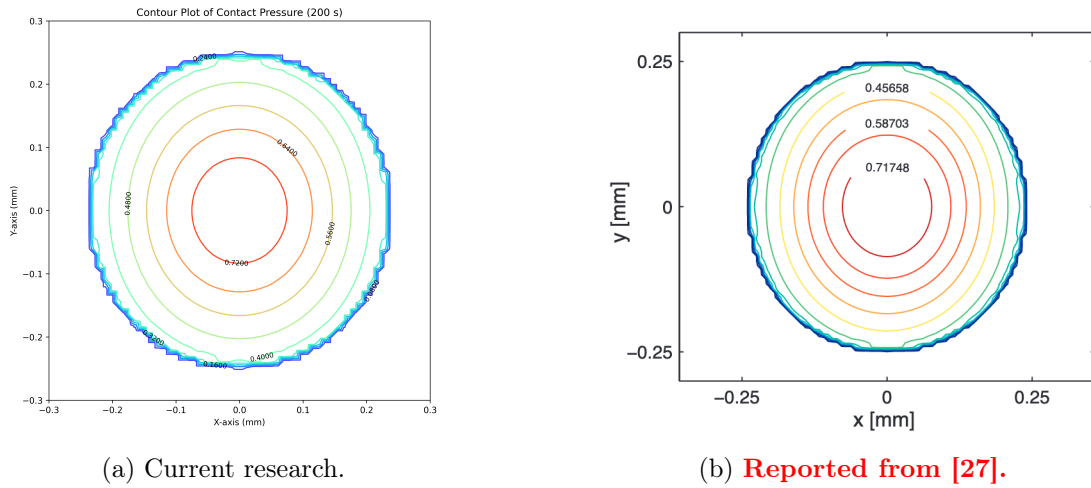

(a) Current research.

(b) **Reported from [27].**
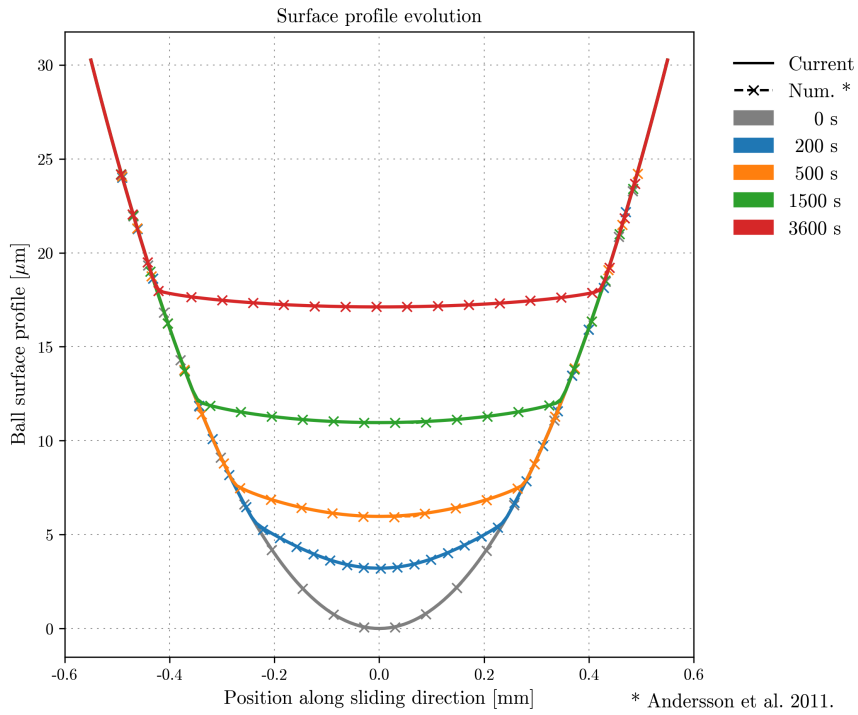
Figure 6.26: Contour plot for contact pressure at 200 s

119

(a) Evolution of the surface of the ball at $y = 0$, BoF case.
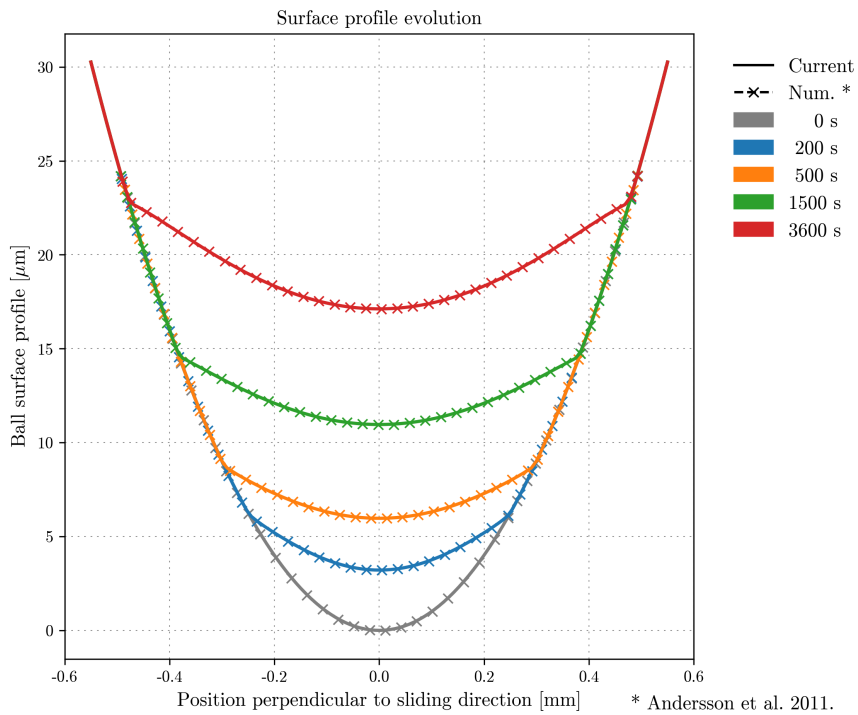
(b) Evolution of the surface of the ball at $x = 0$, BoF case.

Figure 6.27: Evolution of the surface of the ball for the BoF case.
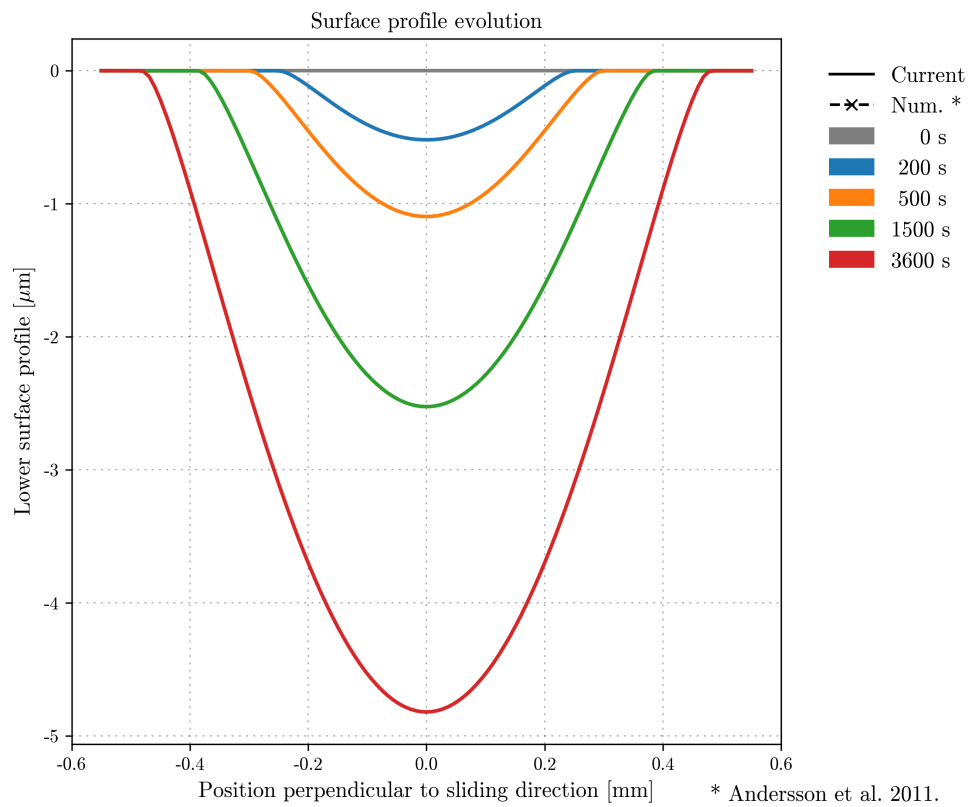
Figure 6.28: Evolution of the surface of the flat, direction perpendicular to the direction of sliding, BoF case.

$T_{\text{tot}} = 200$ s

$T_{\text{tot}} = 500$ s

$T_{\text{tot}} = 1500$ s

$T_{\text{tot}} = 3600$ s

Upper surface profile [μm]

0.00   5.00   10.0   15.0   20.0   25.0   30.0   35.0
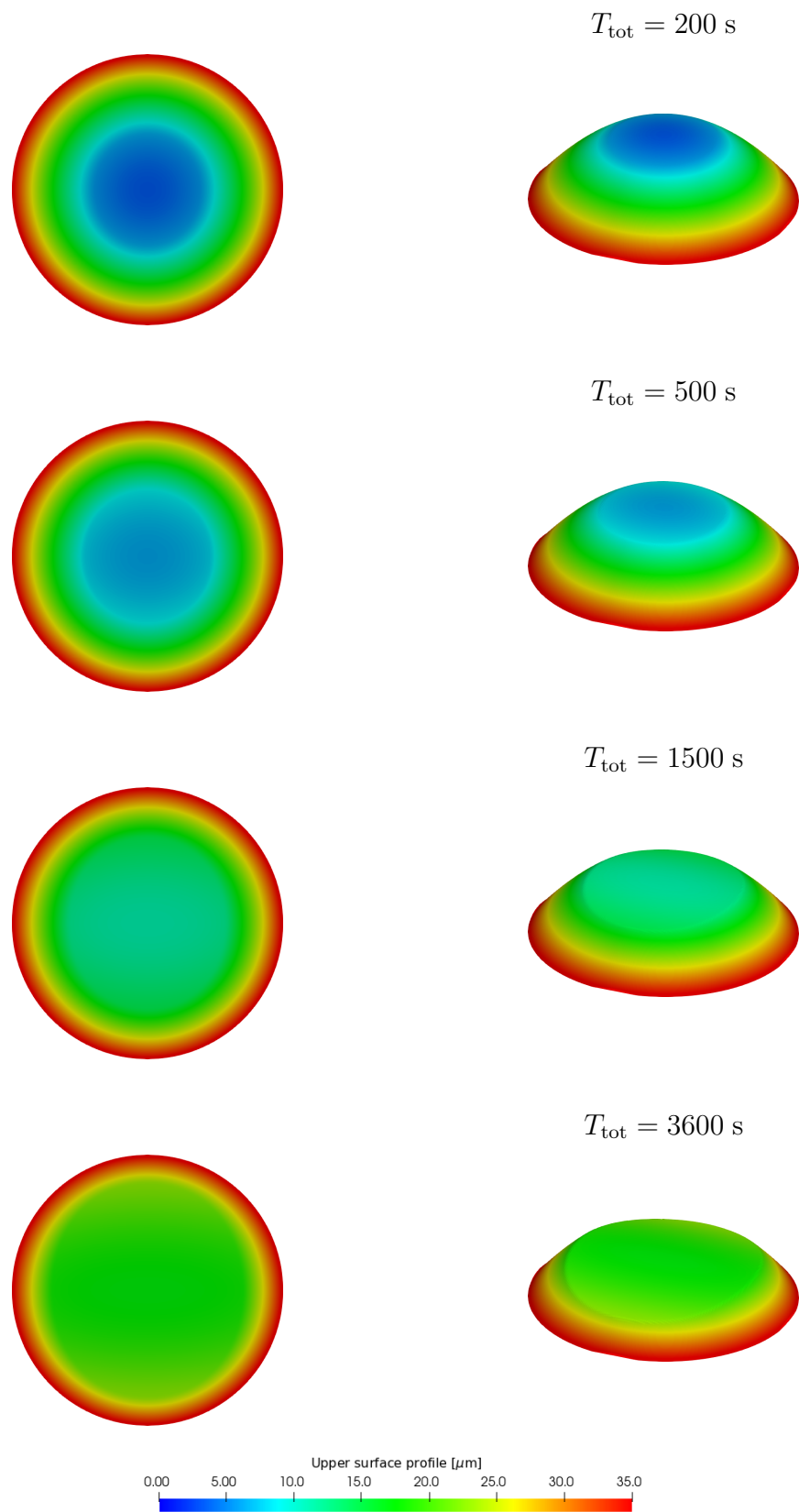
Figure 6.29: Ball surface evolution at 200 s, 500 s, 1500 s, 3600 s.

$T_\mathrm{tot} = 200$ s

$T_\mathrm{tot} = 500$ s

$T_\mathrm{tot} = 1500$ s

$T_\mathrm{tot} = 3600$ s

Lower surface profile [μm]

-4.00   -3.50   -3.00   -2.50   -2.00   -1.50   -1.00   -0.500   0.00

Figure 6.30: Flat surface evolution at 200 s, 500 s, 1500 s, 3600 s.

123

6.5.   Ring–On–Ring Rough Surface Wear

In this section, the wear algorithm is used to analyse wear on a real rough surface. A surface measurement was used to analyse part of a surface used in a Ring–On–Ring (RoR) tribological setup. The measured surface profile was directly used as input in the wear analysis simulation, using the `furustigWearFoam` solver developed for this research. The measured surface profile was obtained from the experimental data published by Furustig et al. [3, 154], the same authors also provided corresponding numerical data.
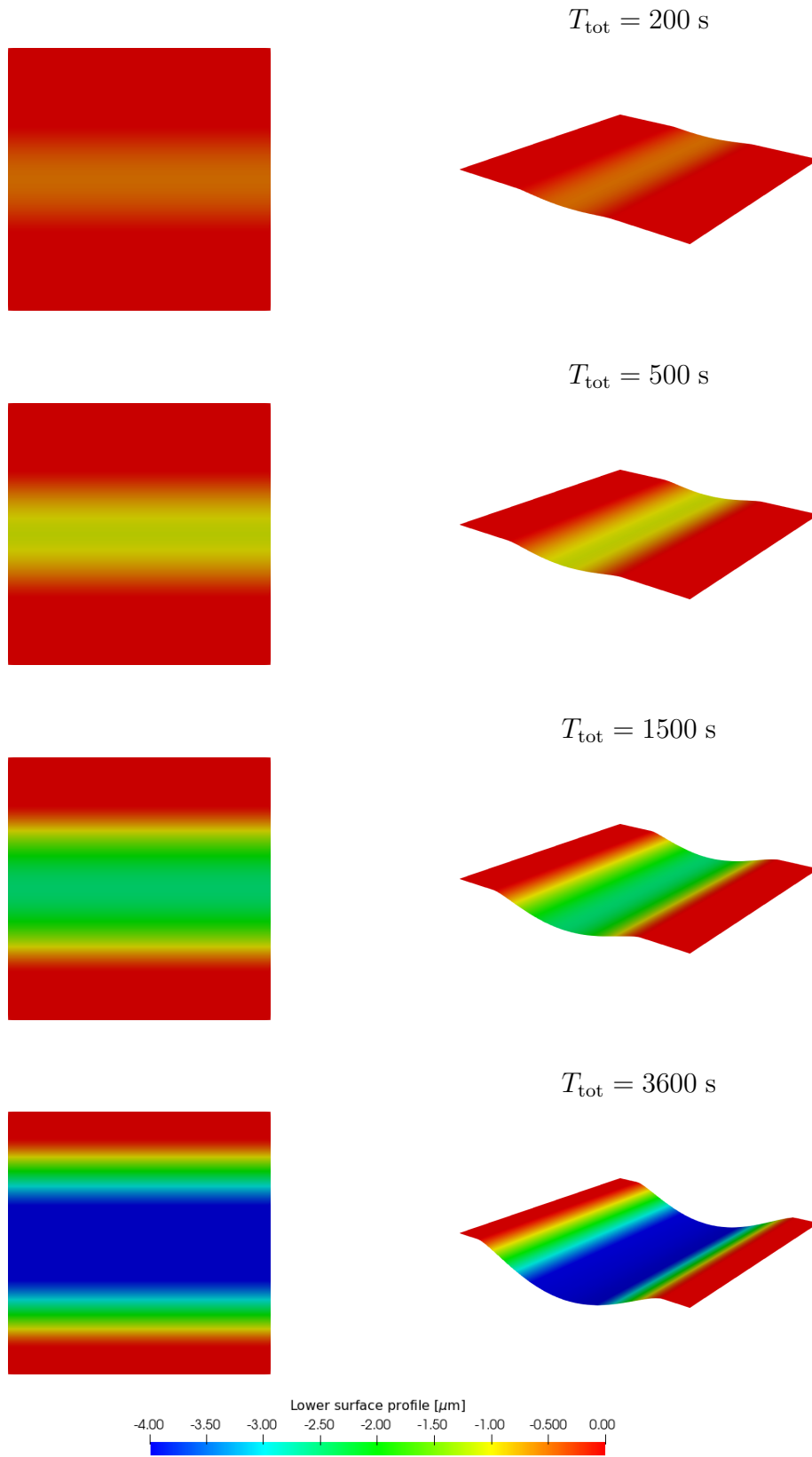
The Ring–On–Ring tribological setup is depicted in Fig. 6.31. The setup consist of two rings moving against each other. In most cases, one of the rings is stationary while the other ring rotates, resulting in sliding interaction between the contacting surfaces of the rings. The relative sliding motion between the two rings leads to the occurrence of wear between the surfaces [155]. In this particular setup, the surface of the upper ring is considered smooth while the lower ring has a rough surface.
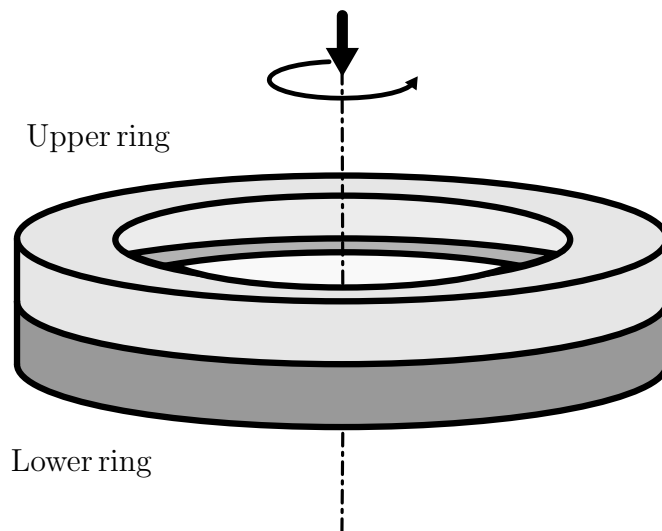

Figure 6.31: Representation of the Ring–On–Ring setup.

Fig. 6.32 shows the lower ring with a marked region which represents the measured area used in the simulation. Furustig et al. [3] performed high precision atomic force microscopy (AFM) to measure the height of the surface profile for a selected region of the surface of the ring. The measured surface, which was
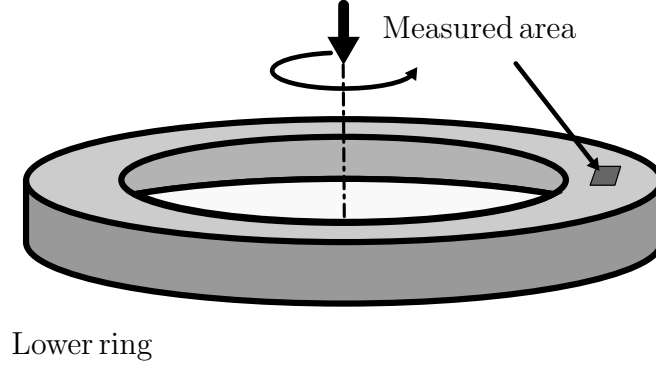
Figure 6.32: Measured area in the Ring–On–Ring case.

directly used as input for `furustigWearFoam` solver, is shown in Fig. 6.33. The dimensions of the surface are 50 μm × 50 μm. The two marks visible on the measured surface are indentation marks, which were used to help align the surface measurements before and after wear.

The simulated contact area is sufficiently small (50 μm × 50 μm) and sufficiently far away from the axis of rotation, thus all of the points in the contact zone cna be considered as having the same velocity and travel the same distance during one increment of the simulation. The upper disc rotates at a speed of 4 rpm, assuming a constant contact radius over the area of contact $R = 50$ mm, the sliding velocity may be determined as:

$$v = 2\pi R f = 2\pi R \frac{4}{60} \tag{6.2}$$

$$v = 0.021 \text{ m/s} \tag{6.3}$$

The simulation was run for 30 s, divided into 100 time increments, resulting in a sliding time increment $\Delta T = 0.3$ s or a slide increment of $\Delta L = 6.3$ mm. The total sliding distance in the simulation was set to 630 mm.

The elastic modulus was set to $E = 210$ GPa and the Poisson's ratio was set to $\nu = 0.29$, for both surfaces in contact. The dimensional wear coefficient for the contact pair was set to $K_{\text{D}} = 2.0 \times 10^{-15}\,\text{Pa}^{-1}$ [3]. Furustig et al. [3] reported localised values of the pressure for the surface area in Fig. 6.33, keeping surface dimensions in mind (50 μm × 50 μm), the load acting on the contact zone is calculated as $F = 2.75$ mN. The computational domain is a square domain with

dimensions corresponding to the dimensions of the measured surface area and was discretised using 256×256 FA faces. The geometrical and material properties used in the simulation are summarised in Table 6.8.

Table 6.8: Geometrical, material, and simulation parameters for the Ring–On–Ring (RoR) case.

Parameter	Symbol	Value
Surface dimensions	-	$50\,\mu\text{m} \times 50\,\mu\text{m}$
Contact radius	R	$50\,\text{mm}$
Rotational speed	f	$4\,\text{rpm}$
Sliding velocity	v	$0.021\,\text{m/s}$
Simulation time	T_{tot}	$30\,\text{s}$
Time increment	ΔT	$0.3\,\text{s}$
Slide increment	ΔL	$6.3\,\text{mm}$
Total sliding distance	L_{tot}	$630\,\text{mm}$
Applied load	F	$2.75\,\text{mN}$
Elastic modulus	E	$210\,\text{GPa}$
Poisson's ratio	ν	0.29
Dimensional wear coefficient	K_{D}	$2.0 \times 10^{-15}\,\text{Pa}^{-1}$
Computational domain	-	256×256 FA faces

The wear depth field, resulting from the numerical simulation performed in this study, is shown on the left–hand side of Fig. 6.34. The current numerical result are compared to the numerical data from Furustig et al. [3] shown on the right–hand side of Fig. 6.34. The data fields were given with their respective colourbars, with the current numerical results trying to mimic the colurmap used in [3] as closely as possible. Thus, both figures use a similar colormap to represent wear depth, making direct visual comparison possible. Furustig et al. [3] reported the wear depth values between -100 nm and 250 nm, which is also reported by the numerical data from the current research. This shows that the current numerical results follow the trend of the numerical data from [3]. Furthermore, both images show wear occurring near the edges of the indentation marks show in Fig. 6.33 and both show a localized region of higher wear near the upper–right edge of the lower indentation mark. The numerical data from [3] shows more localized

wear with a more concentrated wear region. On the other hand, the current wear model shows slightly less concentrated high wear regions. While there are slight differences in the extent and distribution of wear, the fundamental patterns appear to align well.

Furustig et al. [3] presented results from experimental measurements of the wear depth, performed on the same Ring–On–Ring setup as described earlier. The experimental results reported from [3] are given in Fig. 6.35. If compared to the numerical result from the current wear model (left–hand side of Fig. 6.34) we can notice that the wear model does not capture all of the wear patterns shown by the experimental values. The same is true for the numerical data provided by [3], shown on the right–hand side of Fig. 6.34. Both the numerical data from the current research and the experimental data display similar localized regions of higher wear depths near the edges of the indentation marks, while the experimental data shows a broader wear distribution and secondary wear zones not captured by the numerical models. Some of these secondary wear zones were captured by the current model, likely due to a finer resolution, but were not captured by the approach used in [3]. The current research shows wear depth magnitudes close to those shown by the experimental values, while correctly capturing the shape of the primary wear region.

The wear depths smaller than 100 nm are shown in the experimental measurements of the worn surface, but were not captured by the current model, nor the numerical data from Furustig et al. [3]. Wear depths larger than 100 nm, were captured by the current wear model, correctly representing wear trends on the larger scales. Numerical results accurately predict wear depth and distribution, showing good agreement with experimental measurements for contact pressure dominated regions. For regions more distant from the high pressure contact region, where wear is caused by different phenomena (third–body interactions, adhesive forces, molecular–scale interactions) to correctly capture nanoscale wear advanced modelling techniques, such as the molecular dynamics approach, are required.
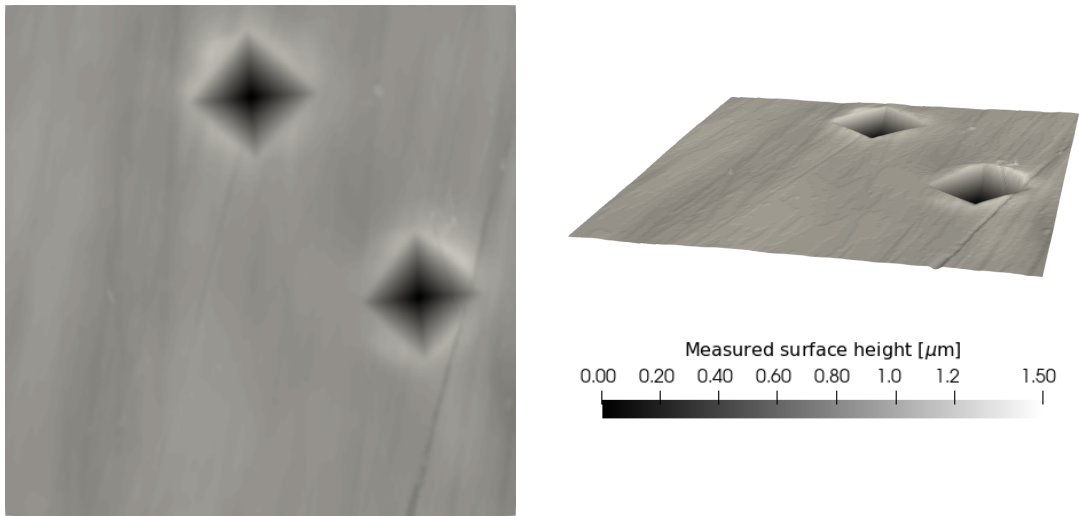
Figure 6.33: Measured surface used as input for numerical model.

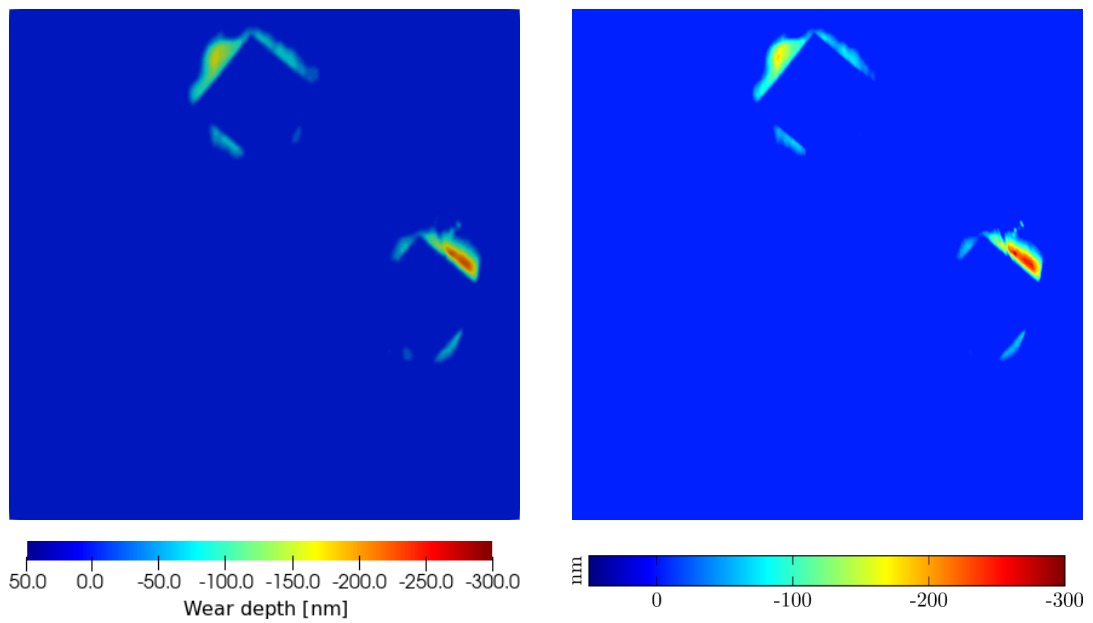Figure 6.34: Numerical wear depth from the current research (left) and as reported by Furustig et al. [3] (right).
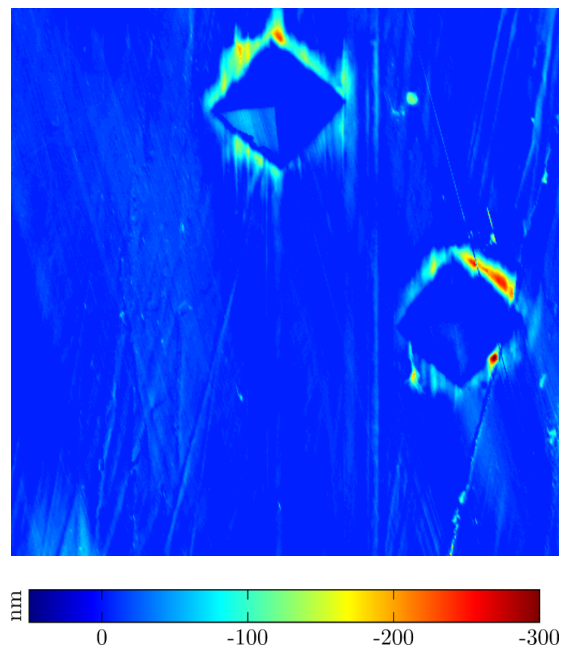
Figure 6.35: Experimentally measured wear depth reported by Furustig et al. [3].

6.6.   Lubricated Ball–On–Disc Wear

The previous sections offered validation of unlubricated (dry) wear against numerical and experimental data found in the literature, for several common tribological cases. The implemented lubricated contact models were based on the research done by Škurić [42], who provided validation for the lubrication model in contacts not considering wear. This section offers an overview of the results of wear analysis for the contact between a rough surface with measured surface roughness and a flat under lubricated conditions.
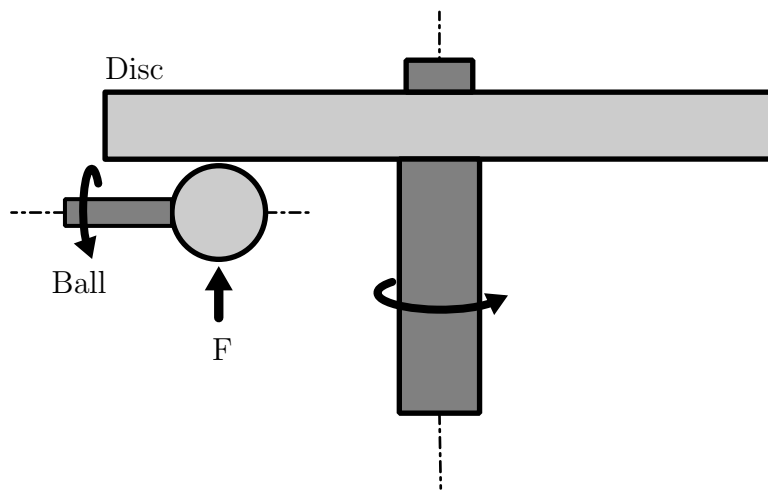
Figure 6.36: Representation of the Ball–On–Disc setup.

The numerical simulation was set up to mimic the condition of the Ball–On–Disc (BoD) tribological test case [149], as show in Fig. 6.36. The wear analysis was performed for the contact between a rough steel ball and a smooth disc using the developed solver `ballOnDiscT68WearFoam`. The ball is made out of ANSI52100 steel and has a radius of 19.05 mm, while the disc is made out of glass. The Young's moduli of the ball and the disc are 207 GPa and 75 GPa, respectively, while their Poisson's ratios are 0.3 and 0.22. The density of the steel of the ball is $\rho_b = 7860 \text{ kg/m}^3$, while the density of the disc is $\rho_d = 2600 \text{ kg/m}^3$. The dimensional wear coefficient for the contact pair was set to $K_D = 1.0 \times 10^{-14} \text{Pa}^{-1}$, assuming equal wear on both surfaces, the dimensional wear coefficients of the ball and the disc are $K_{D,b} = K_{D,d} = 0.5 \times 10^{-14} \text{Pa}^{-1}$ The geometrical and material properties of the two surfaces are given in Table 6.9.

Table 6.9: Geometrical and material properties for the Ball–On–Disc case.

Parameter	Symbol	Value
Ball radius	R_b	$19.05\,\mathrm{mm}$
Young's modulus of ball	E_b	$207\,\mathrm{GPa}$
Young's modulus of disc	E_d	$75\,\mathrm{GPa}$
Poisson's ratio of ball	ν_b	0.3
Poisson's ratio of disc	ν_d	0.22
Density of ball	ρ_b	$7860\,\mathrm{kg/m^3}$
Density of disc	ρ_d	$2600\,\mathrm{kg/m^3}$
Dimensional wear coefficient (total)	K_D	$1.0 \times 10^{-14}\,\mathrm{Pa^{-1}}$
Dimensional wear coefficient of ball	$K_\mathrm{D,b}$	$0.5 \times 10^{-14}\,\mathrm{Pa^{-1}}$
Dimensional wear coefficient of disc	$K_\mathrm{D,d}$	$0.5 \times 10^{-14}\,\mathrm{Pa^{-1}}$

Sveral roughness profiles were measured experimentally by Guegan et al. [149, 4] and were used by Škurić [42] to analyse lubricated contact for different slide–to–roll ratios SRR and different entrainment speeds. Škurić identified the roughness profile which showed the best agreement with the experimental data, thus the same profile was used for the wear analysis with the current model. The chosen roughness profile of the ball [4] is shown in Fig. 6.37 and the roughness parameters calculated using FFT analysis by Guegan et al. [149] are given in Tabel 6.10.
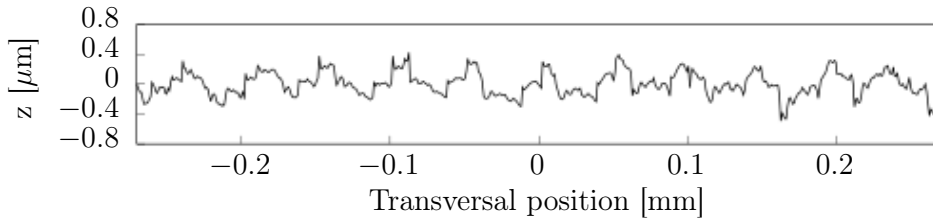

Figure 6.37: Roughness specimen [4] used in Ball–On–Disc simulations

The wear analysis is performed for lubricated contact conditions, using the Shell Turbo T68 oil as lubricant [149]. The Dowson–Higginson pressure–density relation (Eq. 5.29) was used, with the coefficients in [42] as $C_1 = 0.9228\,\mathrm{GPa}$

6. Numerical Results

Table 6.10: Roughness parameters for Specimen 1 used in Ball–On–Disc simulations.

Parameter	Value
Peak-to-valley height	$0.52\,\mu\mathrm{m}$
Wavelength	$45\,\mu\mathrm{m}$
RMS	$0.15\,\mu\mathrm{m}$

and $C_2 = 1.31$, and derived from the density and pressure values given by Dwyer–Joyce et al.[156]. The pressure and temperature dependence of viscosity is governed by the Improved Yasutomi model given by Eq. 5.30 and using the parameters provided in Table 5.1. The Ree–Eyring model (Eq. 5.31) was used to govern the shear dependence of viscosity, with the Ree–Eyring stress given as $\tau_{\mathrm{E}} = 4.70$ MPa for the Turbo T68 oil. The density of the lubricant at 15 °C was found in the literature [157] and is $\rho = 876$ kg/m^3.

The normal contact load between the ball and the disc used in the numerical simulation was set to 20 N. The entrainment speed, i.e. the relative velocity at which the lubricant is drawn into the contact zone between the two surfaces in relative motion, is varied to cover both the mixed and hydrodynamic lubrication regimes. The entrainment speed determines whether a sufficient lubricant film can be established, with higher entrainment speeds resulting in thicker lubricant films, thus reducing direct surface–to–surface contact and minimizing wear. **Two entrainment speeds were analysed in the current study: a low speed ($U_{\mathrm{e}} = 0.02$ m/s) which results in the near–boundary lubrication regime being established, with higher wear due to a more pronounced asperity contact and a higher speed ($U_{\mathrm{e}} = 0.1$ m/s) which promotes lubrication and places the contact in the mixed lubrication regime with reduced wear.** The relative motion between the two surfaces is determined by the slide–to–roll ratio SRR, which determines whether pure rolling (SRR = 0) or partial sliding (SRR > 0) conditions occurs. Generally, a higher SRR causes more friction and wear as sliding is more pronounced in the contact, while lower SRR promotes rolling motion, which is less prone to wear. **In the current simulation the slide–to–roll ratio is set to SRR = 1, meaning that the sliding motion is equal to the rolling motion, thus a significant amount of**

sliding motion occurs, potentially increasing the shear force on the lubricant, leading to a thinner lubricant film.

The computational domain is a square domain the size of 0.54 mm × 0.54mm, which is determined as two times the value of the Hertzian contact diameter [153]. The computational domain was discretised using 128×128 FA faces. This resolution provided sufficient accuracy while maintaining computational efficiency.
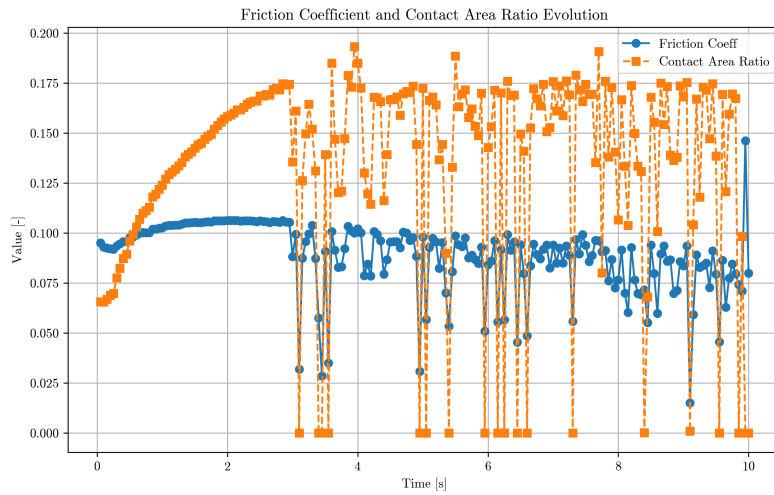

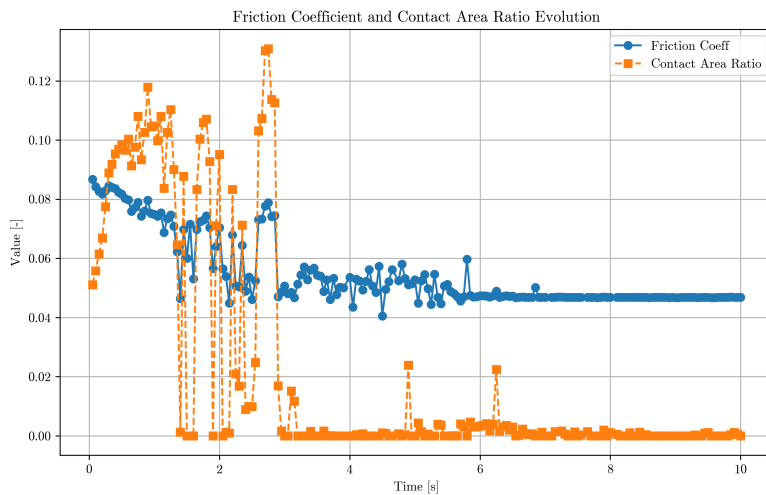Figure 6.38: Evolution of the coefficient of friction and contact area, $U_e = 0.02$ m/s.

Figure 6.39: Evolution of the coefficient of friction and contact area, $U_e = 0.1$ m/s.

6. Numerical Results

The same ball–on–disc setup was used by Škurić [42] to investigate the lubricated contact under different conditions, without considering the influence of wear. The author used the same surface roughness as depicted in Fig. 6.37 ans compared the values of the contact area and the coefficient of friction with the experimental data provided by Guegan et al. [149] for different entrainment speeds and different values of the SRR. The author concluded that the very good agreement with the values of the experimentally measured friction coefficient, particularly for higher values of the entrainment speed where hydrodynamic lubrication is more pronounced. This research expanded this investigation to include the effects of wear on the values of the contact area and the coefficient of friction. The `ballOnDiscT68WearFoam` solver was used to analyse how wear affects the values of the friction coefficient for two entrainment speeds: 0.02 m/s and 0.1 m/s. Fig. 6.38 depicts the evolution of the friction coefficient and the contact area due to wear for the 0.02 m/s case. The values of the friction coefficient show minor oscillations, which is expected for steady sliding wear under the specified considering The average value of the friction coefficient is between 0.075 and 0.1, and is in accordance with the values expected under a near–boundary lubrication regimes with pronounced asperity contact. The noticeable variations of the contact area ratio are attributed to the intermittent asperity contact in this regime. More specifically, as the surface is worn and the surface geometry changes, different parts of the surface come in and out of the contact with the surface of the disc. The average value of the contact area ratio was determined as being in the range of 0.12 to 0.15, which suggests significant solid–to–solid contact between the surfaces. This was also expected, as a low entrainment speed was chosen, placing the contact in the near–boundary region of the mixed lubrication regime, where the influence of the lubricant film is not pronounced. The oscillations in the friction coefficient are closely linked to the engagement and disengagement of the surface asperities, shown by the sudden oscillations in the contact area ratio.

A similar analysis was performed for a higher entrainment speed of 0.1 m/s, placing the contact in the mixed lubrication regime with a more pronounced effect of hydrodynamic lubrication. The results of the analysis are shown in Fig. 6.39. Looking at the results shown in the figure, a sharp increase in the friction coefficient may be noticed, with the value of the fiction coefficient stabil-

ising around the value of 0.45 after 3 seconds of sliding. Similarly, the contact area ratio shows significant fluctuations and high values at the initial phase of the simulation. Then, the values of the contact area start decreasing after the first 2 seconds of sliding, finally dropping to near–zero values around 3 seconds. The behaviour of the Friction coefficient is closely related to the evolution of the contact area at the beginning of the contact and the formation of the lubricant film. As the initial surface is worn, more asperities come into contact, while the lubricant film is still not fully formed, which is shown by the increase in the value of the contact area ratio during the initial phase. The initially higher values of the contact area ratio show more asperity interactions at the beginning of the wear process, while the reduction of the values as wear progresses shows a transition from the mixed lubrication regime into the hydrodynamic lubrication regimes. After the initial 2 seconds, direct surface–to–surface contact becomes minimal, which is also supported by the stabilisation of the values of the friction coefficient. The reduction of the contact area ratio and the stabilisation of the friction coefficient are both consequences of the contact transitioning from a mixed lubrication regime with high asperity interactions to a hydrodynamic lubrication regime, where friction is influenced by the formation of the lubricant film rather than direct surface–to–surface contact.

An analysis of the evolution of the surface profile of the ball was performed next. The results of the ball surface analysis in the direction perpendicular to the direction of sliding are shown in Fig. 6.40 for the $U_\mathrm{e} = 0.02$ m/s case and in Fig. 6.41 for the $U_\mathrm{e} = 0.02$ m/s case. Fig. 6.40 depicts the surface profile of the ball through different sliding times. At 0 s, the initial surface profile is shown. The surface profile changes due to pronounced wear in the near–boundary regime, leading to a reduction in the surface roughness. At such a low entrainment speed, the influence of the lubricant film is minimal, meaning that the load is mostly carried by the asperities and the surface changes are more pronounced. This is confirmed by the flattening of the surface profiles through different times shown in Fig. 6.40, where by 7.s s of sliding, the initial profile becomes much smoother with a noticeable reduction in the surface heights.

A similar analysis is given in Fig. 6.41, but for a higher entrainment speed. At higher entrainment speeds (0.1 m/s) the lubrication regime shifts from near–

Figure 6.40: Surface evolution of the ball in the direction perpendicular to sliding direction, $U_e = 0.02$ m/s.
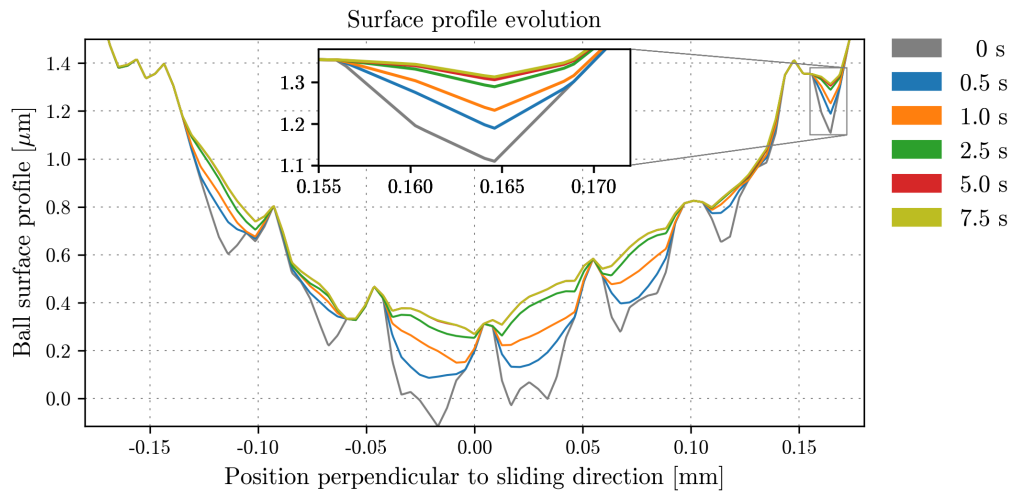
Figure 6.41: Surface evolution of the ball in the direction perpendicular to sliding direction, $U_e = 0.1$ m/s.

boundary lubrication to the mixed lubrication regime, but at the beginning of the sliding process, as the lubricant film is not fully developed, the asperity interactions are more pronounced and the calculated wear depth is higher for the same time increment due to higher relative motion between the surfaces. Fig. 6.41 depicts how the initial surface profile (0 s) evolves, becoming less smooth as the

surface is worn. The main difference, when compared to the lower entrainment speed case, is the fact that after 0.5 s of sliding, the changes to the surface profile become less pronounced and the intensity of wear is reduced. This happens as the contact conditions shift towards more pronounced hydrodynamic lubrications. As the lubricant film becomes more stable, the direct surface–to–surface contact is reduced and the changes to the surface profile become less pronounced. After 5 s of sliding, the contact transitions into a fully hydrodynamic lubrication regime where the load is mainly supported by the lubricant film and there is virtually no more wear. Thus, the lines denoting the ball surface profile at 5 s and 7.5 second are virtually aligned, with only minimal differences.
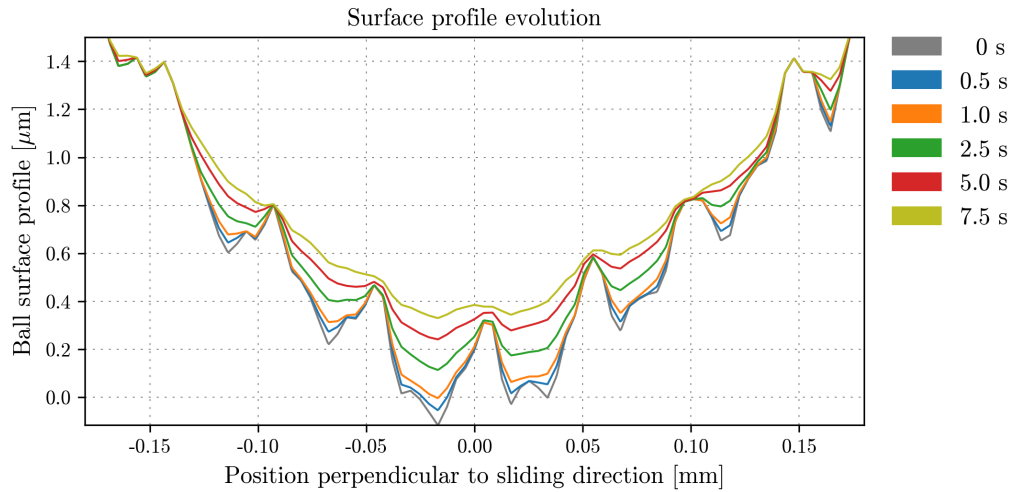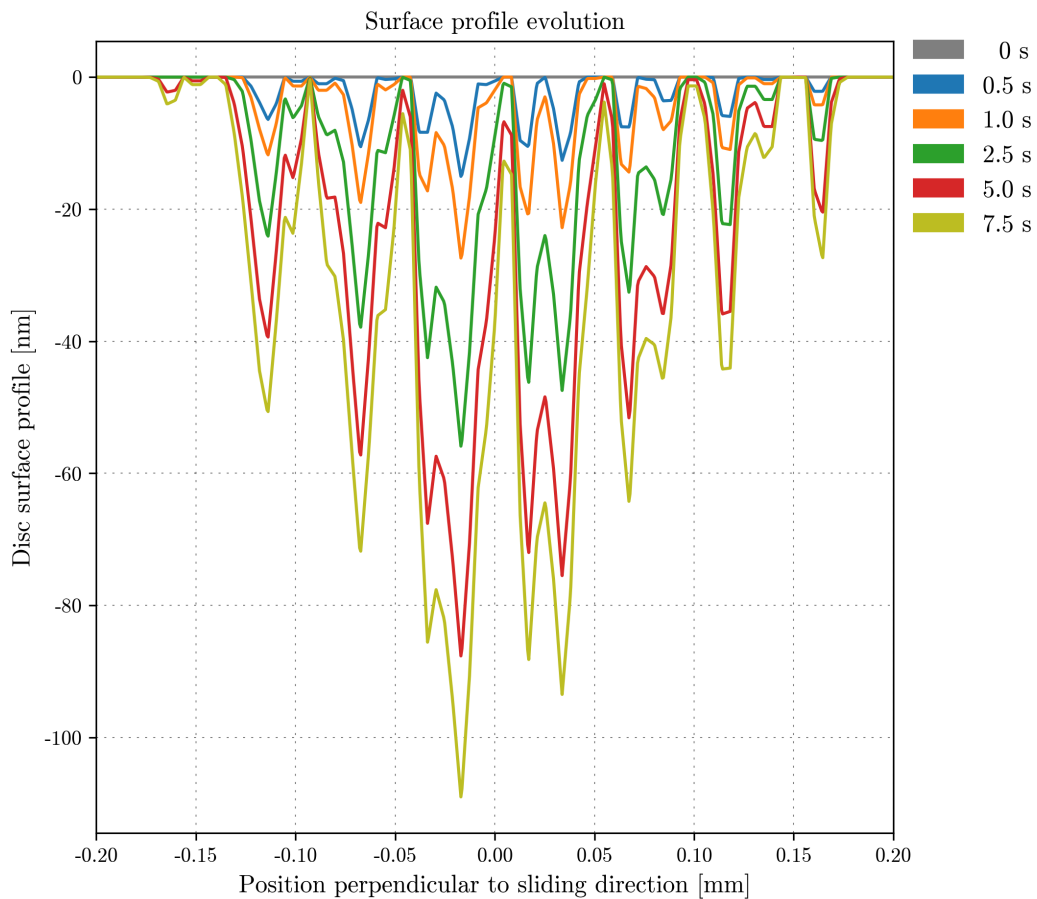

Figure 6.42: Surface evolution of the disc, direction perpendicular to sliding direction, $U_e = 0.02$ m/s.
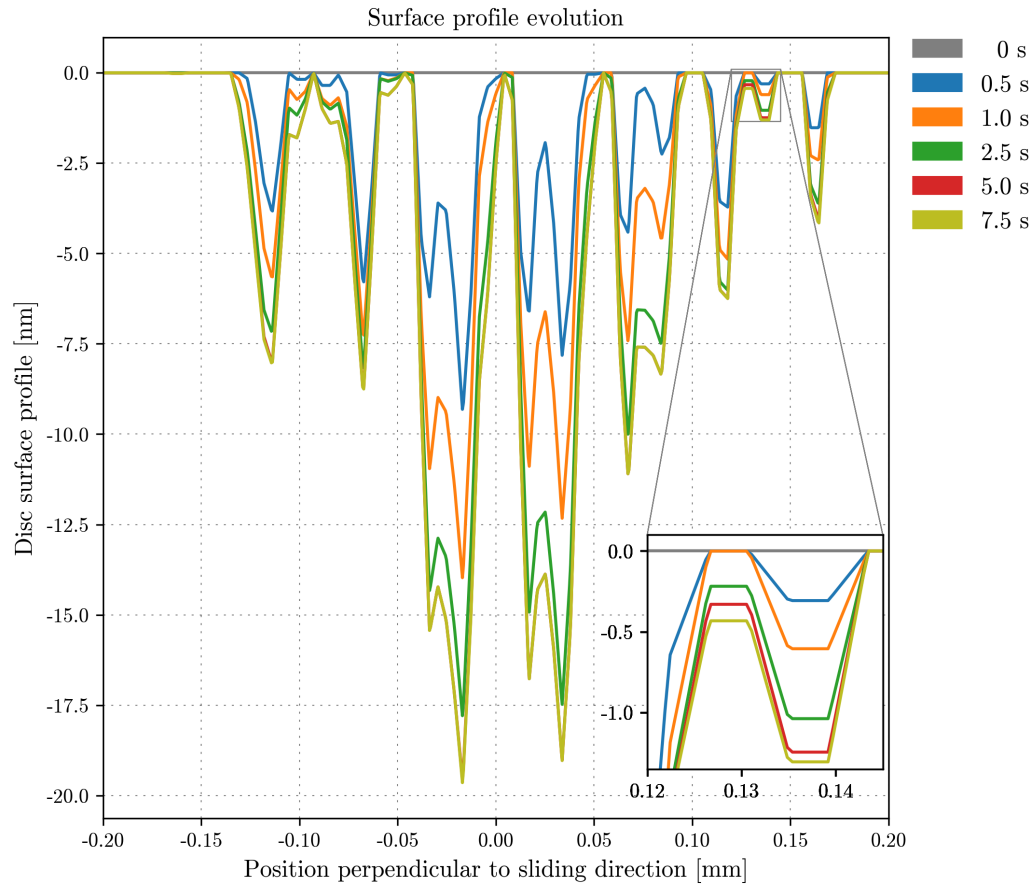
Figure 6.43: Surface evolution of the disc, direction perpendicular to sliding direction, $U_e = 0.1$ m/s.

The changes to the surface of the disc in the direction perpendicular to the sliding direction are reported in Figures 6.42 and 6.43. In both cases, the surface of the disc at the initial moment is depicted as a straight line, while the changes to the flat surface of the disc are depicted as negative values of the surface profile (wear depth) for different sliding times. In both cases, the initially flat surface of the disc evolves due to wear. At the points where the peaks of the surface profile of the ball come into direct contact with the flat disc, the flat surface of the disc is worn, creating valleys which increase in depth as the sliding continues. In both cases, the wear pattern is thus localized to the point of contact between the surfaces. Focusing on the low entrainment speed case (0.02 m/s) show in Fig. 6.42, it can be noticed that the lack of a thick lubricant film results with a more sig-

nificant removal of the material, leading to wear depths of over 100 nm. The disc surface evolves gradually, with more pronounced regions of localised wear, focused around areas of direct surface–to–surface contact. As no significant lubrication film is formed, the wear process does not stabilise and the surface continues to be worn. In the higher entrainment speed case (0.1 m/s), the behaviour of the disc surface profile differs from that of the lower speed case, as depicted in Fig. 6.43. The most noticeable difference can be noticed in the maximum wear depth. In the higher velocity case, the maximum values of the wear depth, i.e. the deepest valleys formed due to wear, do not exceed 20 nm. Generally, the valleys formed due to wear are much shallower in the higher speed case, which is attributed to lower wear caused by less asperity interactions because of a pronounced influence of the lubricant film. After 2.5 s of sliding the changes of the disc surface profile reduce significantly and become minimal after 5 s of sliding. This is attributed to the formation of a lubrication film which separates the two surface, reducing the direct surface–to–surface contact. The stabilisation of profile evolution after 2.5 s is thus associated with the transition towards hydrodynamic lubrication.

Results showing the contact pressure evolution for the lower entrainment speed case (0.02 m/s) and the higher entrainment speed case (0.1 m/s) are shown in Fig. 6.44 and Fig. 6.45 respectively. The results given in Fig. 6.44 show uneven pressures across the contact zone with high pressure peaks which exceed the values of 1.4 GPa at the initial moment of sliding. The high pressure peaks at the beginning of the sliding process are attributed to the dominance of direct surface–to–surface contact and insufficient lubrication. As the sliding continues, sharp asperities are removed and the surface profiles are evened out, causing a redistribution of the load and lowering of the intensity of the contact pressure peaks. Nevertheless, pressure peaks remain visible across different sliding times as they are caused by insufficient film thickness, which is unable to fully separate the two contacting surfaces. Looking at the contact pressure results for the higher entrainment speed case given in Fig. 6.45, similar high pressure peaks may be noticed at the beginning of the simulation as in the lower entrainment speed case. The faster relative motion between the surfaces facilitates faster wear during the initial phase of sliding, which can be seen as a pronounced reduction of the pressure peaks in the first 0.5 s of sliding. The higher relative speed promotes wear

during the initial asperity interaction, but it also leads to a faster formation of a lubricant film. This lubricant film separates the surfaces and leads to a reduction of direct surface–to–surface contact, seen as a sudden drop in contact pressure which is most noticeable after 2.5 s. After 2.5 s of sliding, the contact pressure drops drops, first to near–zero and then to zero values, as hydrodynamic lubrication is achieved. The lubricant separates the surfaces of the ball and the disc and reduces wear to minimal values, as also confirmed by the minimal changes in the surface profiles shown in Fig. 6.41 and Fig. 6.43.

The contact pressure field from the lower entrainment speed case (0.02 m/s) is given in Fig. 6.46 for several different time instances. In the initial phase ($T_{tot} = 0$ s) the contact pressure is localised in a narrow regions with high pressure peaks near the centre of the contact, indicating more concentrated asperity contact. Such an uneven distribution at the initial moment of contact is attributed to the surface profile of the ball. As the sliding continues ($T_{tot} = 0.5$ s to 1.0 s) the high pressure regions remain concentrated, but reduces in magnitude, which is attributed to wear and load redistribution over the worn contact area. As sliding continues, the lubricant is entrained in the contact zone, thus some of the load is carried by the lubricant film and not only the contacting asperities. In such conditions, the lubricant film reduces surface–to–surface contact, which contributes to the reduction of the contact pressure peaks. In the low entrainment speed case, a fully formed lubricant film is not present and mixed (near–boundary) contact conditions are retained, resulting in only a partial decrease in asperity interactions. The same trend is noticeable in through later phases of sliding ($T_{tot} = 2.5$ s to 7.5 s), where the pressure field becomes more evenly distributed due to wear smoothing the asperities. The load is distributed over a larger contact area are high pressure peaks are reduced to values which do not exceed 1 GPa. Again, the lower entrainment speed does not allow for the contact to transition into full hydrodynamic lubrication, remaining in the mixed lubrication regime the lubricant can only support a small portion of the load.

An analysis of the evolution of the contact area for the lower entrainment speed case is given in Fig. 6.47. The contact area behaviour is similar to that of the contact pressure fields. In the initial phase ($T_{tot} = 0$ s) the contact area consists of several thin and disconnected regions, meaning there are isolated areas

of asperity contact on which the load is concentrated. The initially small contact areas result in the high contact pressure regions visible in Fig. 6.46. In the early phase of sliding ($T_{\text{tot}} = 0.5$ s to 1.0 s), wear starts reducing the asperity heights, thus creating a larger contact area with more direct surface–to–surface contact. This expansion of the contact area continues through later stages of sliding ($T_{\text{tot}} = 2.5$ s to 7.5 s). The contact area increases significantly, becoming more continuous as the surface profiles becomes smoother due to wear. The expansion of the contact area reduces the localised contact pressure peaks as the load is distributed more uniformly over a larger area.

Fig. 6.48 depicts the contact pressure field at different time of sliding for the higher entrainment speed case (0.1 m/s). Initially ($T_{\text{tot}} = 0$ s) the contact pressure is localised, forming narrow bands with high pressure peaks. These localised areas of high pressure are attributed to direct surface asperity interactions, as the lubricant film has not yet developed. The at $T_{\text{tot}} = 0.5$ s the pressure peaks are still visible, but the distribution of the contact pressure becomes wider. The load is redistributed as wear flattens the asperities and the lubricant film starts to develop. Asperity interactions are still significant, which is shown by the still visible pressure peaks. At $T_{\text{tot}} = 1.0$ s the combined effect of wear and lubrication leads to a more efficient redistribution of load, resulting in a more uniform pressure field. The pressure peaks decrease noticeably as wear further smooths the surface asperities, which allows the lubricant film to spread more evenly. At $T_{\text{tot}} = 2.5$ s the high contact pressure zones are eliminated, showing only a few low contact pressure zones. As surface asperities were smoothed out by wear and a thicker lubricant film was established, the direct surface–to–surface contact was minimised, resulting in minimal contact pressures. After 2.5 s, the contact is fully supported by the lubricant film as fully hydrodynamic lubrication conditions were achieved.

The surface area evolution for the 0.1 m/s case is given in Fig. 6.49. The initially fragmented contact area is causes by the surface roughness of the ball. As sliding progresses, the contact area becomes larger, as the surface asperities are worn and more of the surface of the ball comes in direct contact with the surface of the disc. This expansion of the contact are through wear is visible at 0.5 s and 1.0 s of sliding. After that, the contact starts shifting into a more

pronounced hydrodynamic lubrication regime, and more of the load is supported by the lubricant film instead of the contacting surfaces, which is made clear by the severely reduced contact area at 2.5 s of sliding. After that, the contact fully shifts into the hydrodynamic lubrication regime and the direct surface–to–surface contact area is reduced to zero.
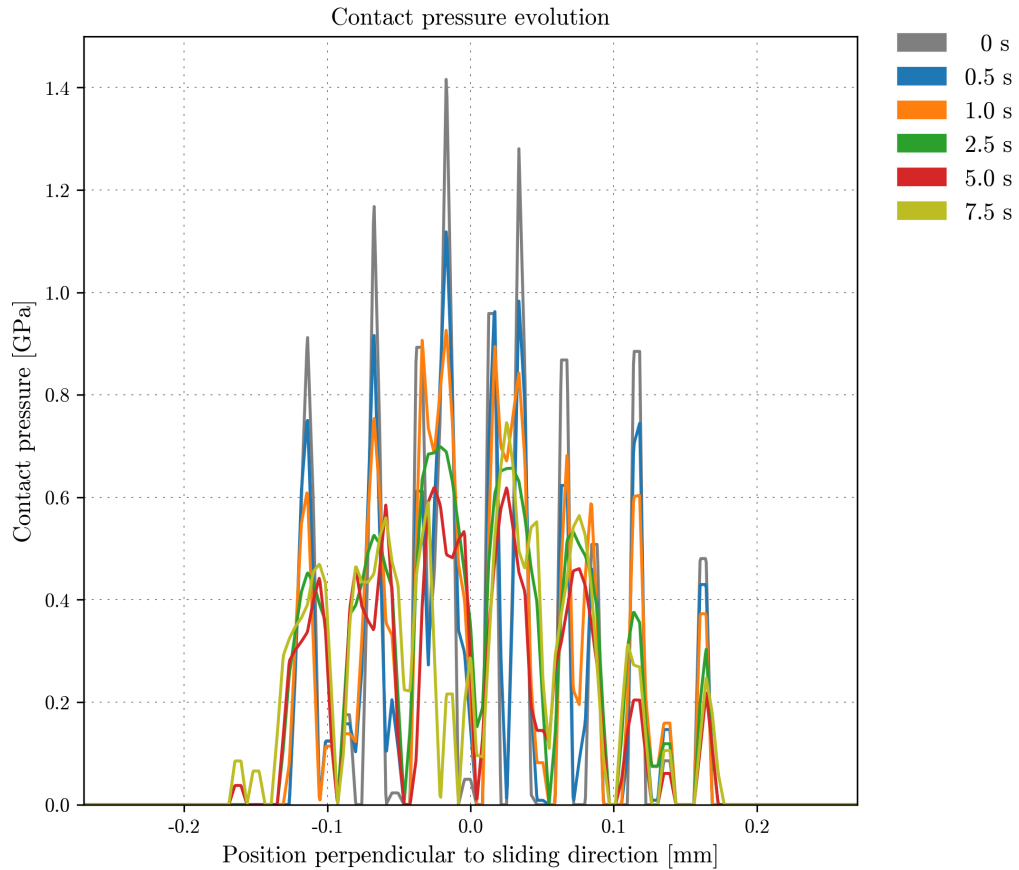
Figure 6.44: Pressure evolution in the direction perpendicular to sliding direction, $U_{e} = 0.02$ m/s.
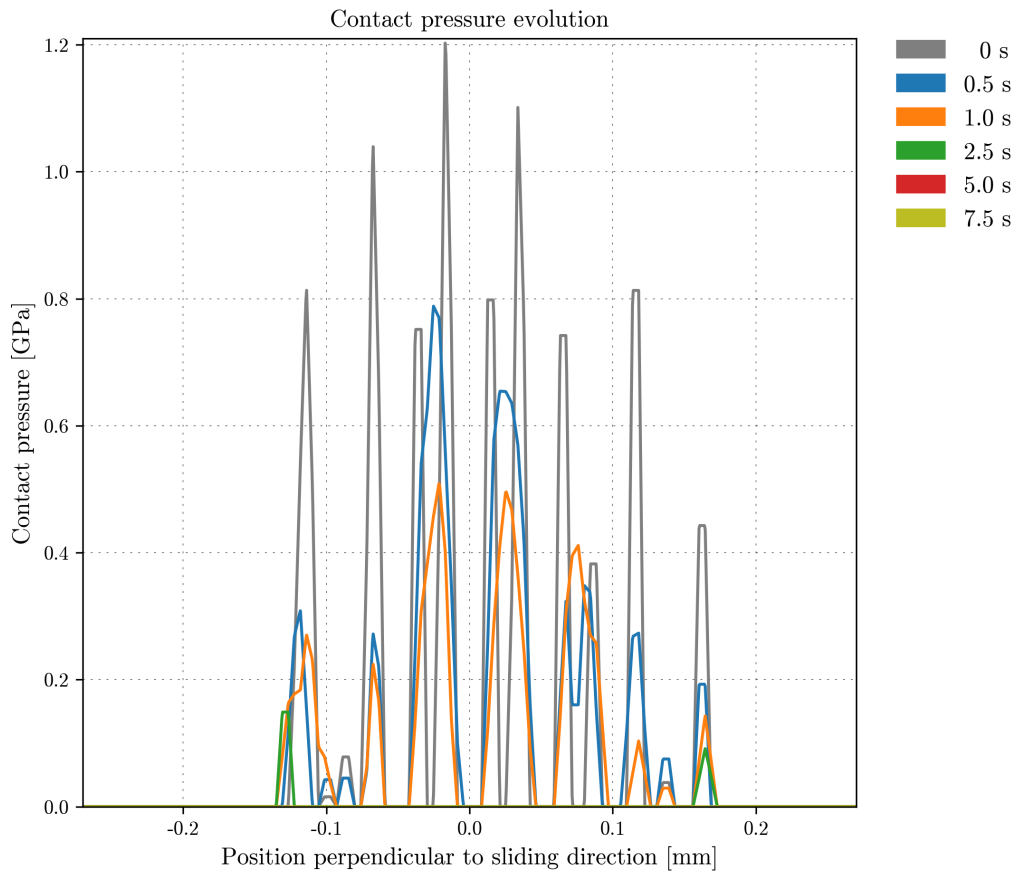
Figure 6.45: Pressure evolution in the direction perpendicular to sliding direction, $U_e = 0.1$ m/s.

$T_{\text{tot}} = 0$ s

$T_{\text{tot}} = 0.5$ s

$T_{\text{tot}} = 1.0$ s

$T_{\text{tot}} = 2.5$ s

$T_{\text{tot}} = 5.0$ s

$T_{\text{tot}} = 7.5$ s

Contact pressure [GPa]

0.00   0.20   0.40   0.60   0.80   1.0   1.2   1.44
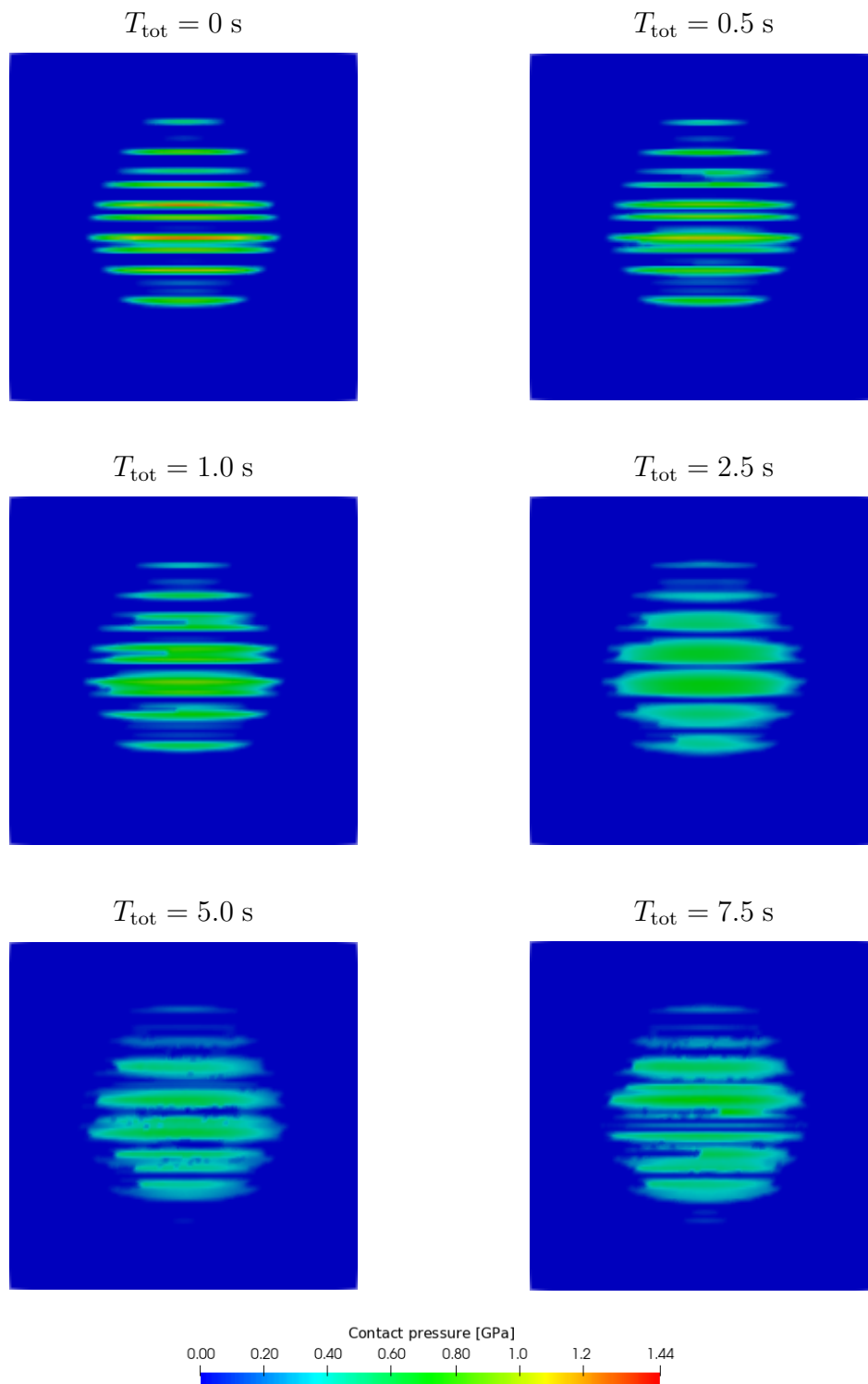
Figure 6.46: Contact pressure fields at different sliding times, $U_{\text{e}} = 0.02$ m/s.

$T_\text{tot} = 0$ s

$T_\text{tot} = 0.5$ s

$T_\text{tot} = 1.0$ s

$T_\text{tot} = 2.5$ s

$T_\text{tot} = 5.0$ s

$T_\text{tot} = 7.5$ s
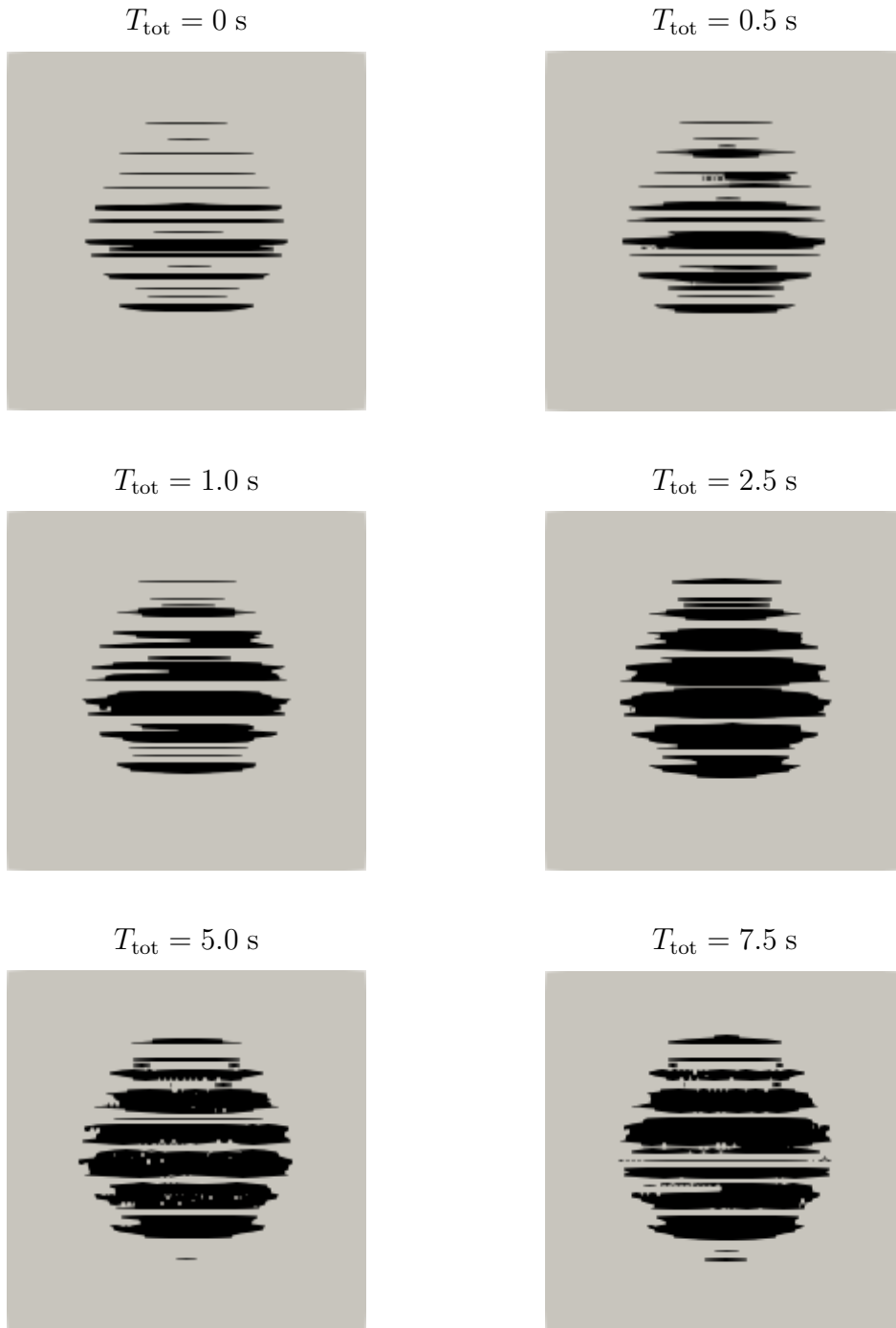
Figure 6.47: Contact area evolution at different sliding times, $U_\text{e} = 0.02$ m/s.

$T_\text{tot} = 0$ s

$T_\text{tot} = 0.5$ s

$T_\text{tot} = 1.0$ s

$T_\text{tot} = 2.5$ s
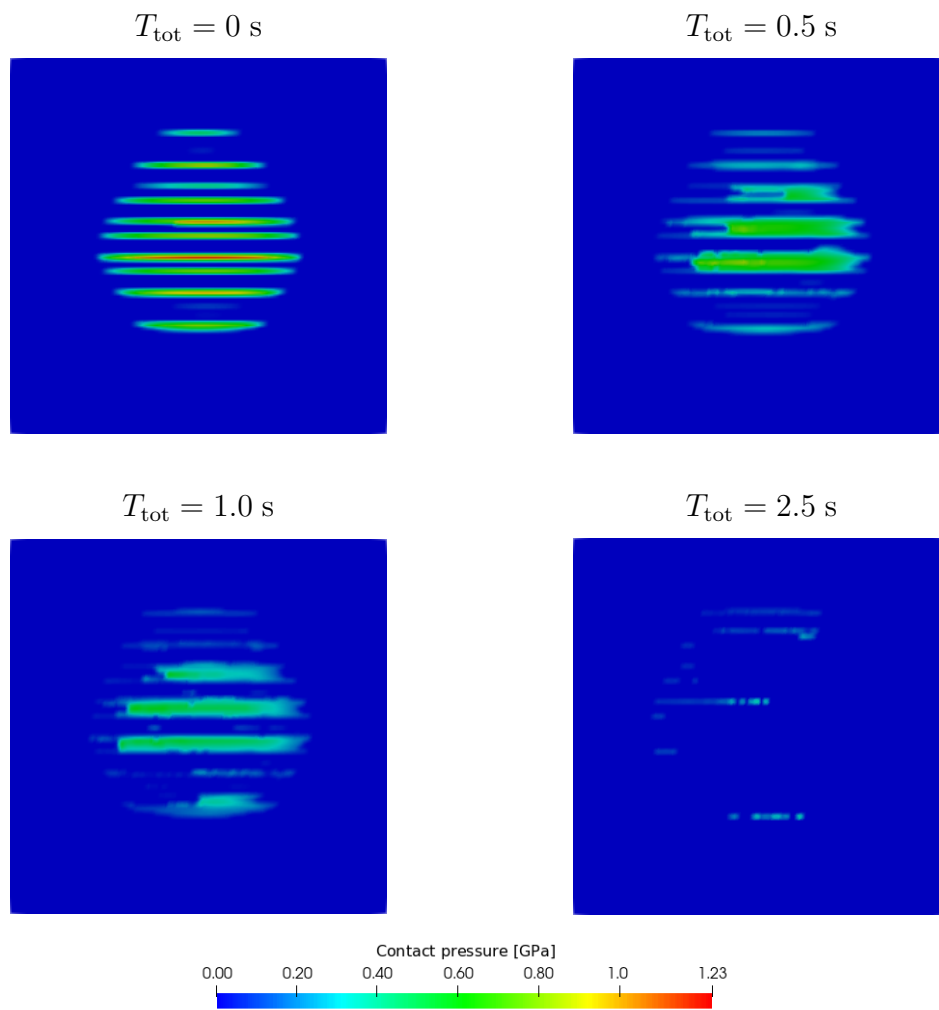
Figure 6.48: Contact pressure fields at different sliding times, $U_\text{e} = 0.1$ m/s.

$T_{\text{tot}} = 0$ s

$T_{\text{tot}} = 0.5$ s

$T_{\text{tot}} = 1.0$ s

$T_{\text{tot}} = 2.5$ s
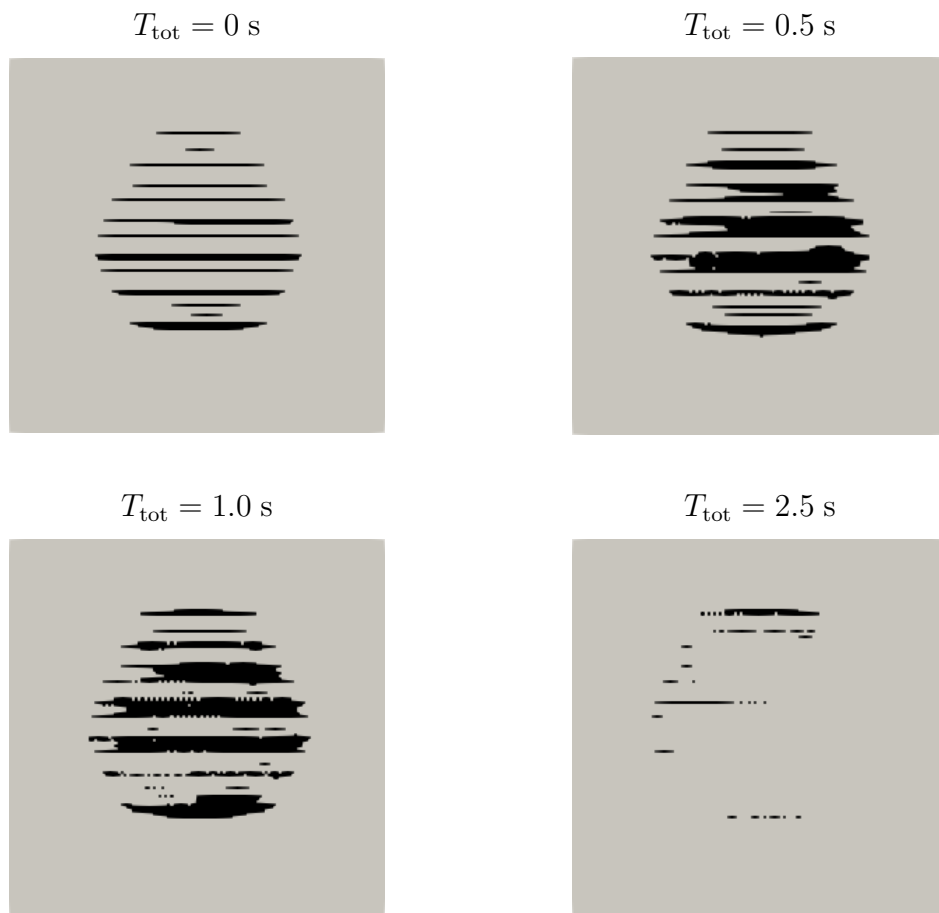
Figure 6.49: Contact area evolution at different sliding times, $U_{\text{e}} = 0.1$ m/s.

6.7.   Conclusion

This chapter presented a validation and verification of the wear algorithm using several different numerical cases. Each case was chosen to closely mimic one of the more common tribological systems with numerical, analytical or experimental data available for comparison.

The single–surface wear model was validate first. The validation of the unilateral (single–surface) wear model was performed using a Pin–On–Disc test case and the numerical results were compared with the numerical data provided by Rodríguez-Tembleque et al. [2]. The numerical results from the current research showed excellent agreement with the available numerical data from the literature, most notably for the contact pressure and surface profile evolution results. Slight deviations of the current results when compared with the numerical data from [2] were noticed in the low pressure region and were attributed to the methodological differences between the Boundary Element Method employed by Rodríguez-Tembleque et al. [2] and the Finite Area Method used in the current research. Simulations for different mesh densities were performed, revealing improved accuracy for finer meshes but at increased computational demands. Thus, the 64×64 finite area faces mesh was determined as being optimal for continuing with the validation of bilateral surface wear.

The bilateral surface wear model was validated next. Once again, the data from the current research was validated against numerical results provided by Rodríguez-Tembleque et al. [2]. The calculate numerical data describing the changes in surface profiles due to wear showed excellent agreement when compared with the data from the literature. The analysis was performed on two separate cases with different wear coefficient attributed to each surface. The numerical results showed the expected trends, such as higher wear on the surface of the pin for the case in which the pin had a higher wear coefficient than the disc. For both cases, the calculated surface heights (surface profiles) closely matched the data from the literature, thus validating the bilateral surface wear model.

The validation continued with a Ring–On–Block test case, used for validating the results of a wear model for initially line contact conditions. In this case, the computational domain was discretised using long strips instead of square finite

area faces. The numerical results were compared to numerical and experimental data from Zhan and Huang [34], following the trends seen in the experimental data and showing excellent agreement with the numerical data for both the contact pressure and surface profile evolution. The data showing the evolution of the surface profile, i.e. the formation of the wear groove, closely aligned with the trends seen in the experimental data from the literature, with some deviations in maximum wear depth and wear groove width noticeable for the intermediate phases of the experiment. For the final measurement of the wear groove at the end of the experiment, the numerical model showed very good agreement, thus demonstrating its ability to accurately predict surface wear even in cases with initially line contact conditions.

The reciprocating Ball–On–Flat test case was analysed next, validating the quasi–steady–state wear model implemented in the current research. The numerical results regarding the surface profile and contact pressure evolution were analysed and showed excellent agreement with the numerical data provided by Andersson et al. [27]. The analysis of the surface evolution showed the difference in wear intensity based on the sliding direction and confirmed the trend of higher wear rates occurring in the initial stages of contact, before the surface of the ball is flattened.

The Ring–On–Ring test case was used together with a surface scan of a real rough surface to validate the ability of the wear algorithm to simulate wear using direct surface measurements as input. The numerical results were compared to the numerical and experimental results provided by Furustig et al. [3]. The numerical results from the current research closely matched the numerical data from the literature. While both numerical results showed captured key trends seen in the experimental findings, such as localised regions of higher wear near the indentation marks on the scanned surface, secondary wear patterns seen in the experimental data were not captured by the numerical results. The model accurately predicted wear depths and higher wear regions, demonstrating the ability of the wear algorithm to calculate wear on real rough surfaces, but highlighted the need for a different approach for analysing nanoscale wear.

Finally, a lubricated Ball–On–Disc test case was used for a cumulative analysis of wear on a rough surface with a realistic surface profile under lubricated contact

conditions. Two different cases were analysed using the Shell Turbo T68 oil as lubricant and two different entrainment speeds, thus placing the initial contact in two different lubrication regimes: near–boundary and mixed lubrication. The results accurately predicted the expected trends regarding the contact pressure and surface profile evolution, while the contact area ratio and friction coefficient analyses showed the expected transition between the lubrication regimes.

In conclusion, the results given by the wear algorithm were validated against available numerical, analytical and experimental data for various numerical test cases, showing the applicability of the wear algorithm for wear analysis across different tribological scenarios.

7. Conclusions and Future Work

The research provided in this thesis aimed at advancing the understanding of wear and wear–related phenomena in rough surface contacts under lubricated contact conditions through the development and validation of a novel numerical framework used for wear prediction in various tribological scenarios. A unique method, combining wear calculation with lubricated contact calculations, was developed and implemented. The framework was developed as a unique implementation of three models: a wear model, a deterministic contact model and a lubrication model.

The thesis begins with an overview of the development of the field of tribology, highlighting the importance of wear in modern industry and the need to reduce friction and wear in modern energy systems. The shift of modern tribology from experimental procedures towards computational modelling, such as computational fluid dynamics, is discussed and an overview of previous studies focusing on using different numerical approaches to modelling wear is given, concluding that numerical approaches present a viable alternative to costly trial–and–error based methods.

The study continues by exploring the fundamental concepts behind friction and wear, focusing on adhesion and asperity deformation as the primary mechanisms causing wear. An overview of the four main types of wear was given, focusing on adhesive wear as the basis for this research. The work done by Archard on understanding wear was presented, culminating in the formation of Archard's Wear Law. An examination of Archard's assumptions is given together with the fundamental equations of the model. This sets the basis for the numerical implementation of the model.

For the wear model to be applicable for wear analysis of lubricated contact conditions and surfaces with realistic roughness profiles, the wear model needed to be coupled with a lubrication model and a contact model. Thus, the development of a modified Reynolds equation for modelling thin film flows was discussed. The aforementioned equation incorporates the effects of lubrication and surface

roughness through the use of flow factors, thus allowing for accurate prediction of hydrodynamics pressure and shear stress. The modified Reynolds equation was presented together with its derivation from the Navier–Stokes and continuity equations. The problem of including cavitation was discussed and the boundary conditions used for ensuring mass conservation for both the cavitating and full–film regions were introduced: the zero–gradient pressure boundary condition at the rupture boundary and the non–zero pressure gradient at the formation boundary. To include the effects of surface roughness on thin film flows, the averaged form of the Reynolds equation was introduced. The equation uses flow factors (the pressure flow factor and the shear flow factor) to account for the influence of surface asperities without creating an additional strain on computational resources, as the required flow factors are calculated analytically based on surface parameters. A discussion on asperity contact models was given. In contrast to statistical models, deterministic contact models use surface topography data to calculate the contact parameters required for the wear and lubrication models (contact pressure, area, deformations), providing higher accuracy with an acceptable increase in computational requirements. A review of relations describing the changes in density and rheological properties of lubricant due to variations in pressure, temperature and shear stress was performed.

A numerical implementation of a deterministic asperity contact model based on the Fast Fourier Transform was presented together with an implementation of the lubricant flow model, incorporating cavitation effects via a modified Reynolds equation. By coupling the Reynolds equation with a deterministic asperity contact model, precise calculation of contact pressures, deformations and other input parameters needed for the wear model became possible across different lubrication regimes. The implementation of the wear model based Archard's Wear Law was presented. The model employs an incremental and a quasi–steady–state approach to predict wear for a single or both surfaces in contact. For cases where the behaviour of the surface contact follows a cyclic pattern (rotation, periodic sliding, etc.), separation of the time scales is performed. By decoupling the calculation of wear on the fast time scale (single rotation in a pin–on–disc setup) and the slow time scale (several rotations) the surface geometry and pressure evolution due to the transient wear process can be captured effectively. The Finite

152

Area Method was used for spatial and temporal discretization of the implemented models, ensuring computational efficiency while maintaining accuracy.

Furthermore, the study offers an overview of the integration of the previously described models into a wear algorithm, thus providing an effective approach, developed for simulating wear under different lubrication regimes. The algorithm uses an iterative approach to update surface geometries based on wear parameters and variables provided by the lubrication and deterministic contact models. Validation of the wear algorithm against available experimental and numerical data from the literature, demonstrated the applicability of the framework across different tribologcal scenarios, e.g. Pin–On–Disc, Ring–On–Block, and Ball–On–Flat setups. The single–surface wear model was validated against numerical data from literature in a Pin–On–Disc test case showing excellent agreement, particularly for contact pressure and surface profile evolution. The bilateral surface wear model was validated using the same test case, with the numerical results closely matching the numerical data from the literature and correctly capturing the evolution of surface profiles, thus demonstrating the capability of the model to calculate wear for different surfaces based on their respective wear coefficients. Modelling wear for initially line contacts was validated on a Ring–On–Block case, where the domain was discretised using long strips instead of square finite area faces. The numerical results for this case showed excellent agreement with numerical data from the literature while correctly following the trends seen in the experiments. The quasi–steady–state wear model was validated on a reciprocating Ball–On–Flat case, accurately predicting the surface profile and contact pressure evolution, which was confirmed by comparison with numerical data from the literature.

The study also investigates the effects of different lubrication regimes, such as near–boundary and mixed lubrication conditions, on surface profile and contact pressure evolution caused by surface wear. This, together with the ability of the algorithm to use measured surface profiles as input for simulation of real rough surfaces, enhances the applicability of the framework to real–world applications. More specifically, a Ring–On–Ring test case was used in combination with surface scans of a real rough surface, validating the ability of the algorithm to preform wear simulations using direct surface measurements. The numerical results accu-

rately predicted the trends seen in the experimental data, but were not able to capture secondary wear patterns on the nano scale. Finally, the cumulative testing of the applicability of the wear algorithm for wear analysis of rough surfaces under lubricated contact conditions was performed on a lubricated Ball–On–Disc test case using the Shell Turbo T68 oil as lubricant. The results were analysed for two cases under mixed and near-boundary lubrication regimes, confirming the ability of the algorithm to predict contact pressure and surface profile evolution due to wear throughout lubrication regime transitions.

In conclusion, the implemented wear algorithm was validated against available numerical, analytical and experimental data for different tribological test cases, confirming the robustness and applicability of the developed framework for wear analysis across various tribological scenarios.

In future studies, the developed framework will be validated on a more complex test case, closely based on an industrial application. As an example, the framework could be used to study wear between the casing and the vanes of a vane pump. Nevertheless, one of the biggest challenges during this research was lack of adequate experimental data regarding the surface profiles and lubricant properties. Thus, for such a complex validation case, surface scans of the contacting surfaces before and after the wear process would need to be available together with detailed specification of the exact properties of the lubricant used in the experiment.

Furthermore, in a continuation of this work, the wear model would need to be expanded to consider more complex relations between the applied load and the calculated wear, moving beyond the relatively simple linear relation described by the Archard model. Additionally, the wear modelling framework should be expanded to consider the thermodynamics of friction and wear, allowing for the calculation of the temperature increase due to sliding contact and the effect of the temperature changes on the wear coefficient. The wear calculation framework could be further expanded to consider the interaction of the worn material and the lubricant resulting in the formation of a tribofilm. Such a model would need to consider both tribofilm formation due to chemical reactions and tribofilm removal due to mechanical rubbing.

Lastly, the wear framework was used to analyse wear in different tribological

scenarios directly connected to industrial applications or experimental setups. While this done to validate the framework and showcase its applicability to industrial problems, the same framework may be used to investigate tribological problems found in medical applications, such as friction and wear investigation in hip implants, knee replacements and dental implants. Using the developed wear framework to predict wear in medical devices, implants and tissue, could provide invaluable information for the further development of medical devices and procedures.

7. Conclusions and Future Work

Appendices

A Discretisation of Cavitation Boundaries

Both the modified (Eq. 5.15) and the averaged (Eq. 5.18) forms of the Reynolds equation, given in Sec. 5.2.2. were discretised within the framework of the Finite Area Method, which was presented in Chapter 4.. The discretisation procedure needed for the implementation of the modified and averaged Reynolds equation in `foam-extend` was presented by Škurić [42] and is reiterated here for the sake of completeness.

Eq. 5.15 is discretised on an orthogonal finite area mesh, following the procedure outlined in [42]. The discretisation procedure needs to take into account the cavitation boundaries. A depiction of a finite area face P is given in Fig. A1, together with four neighbouring faces denoted as N, S, E and W. Finite area faces which are in the cavitating region are shown in blue, while those in the active region are shown in grey.
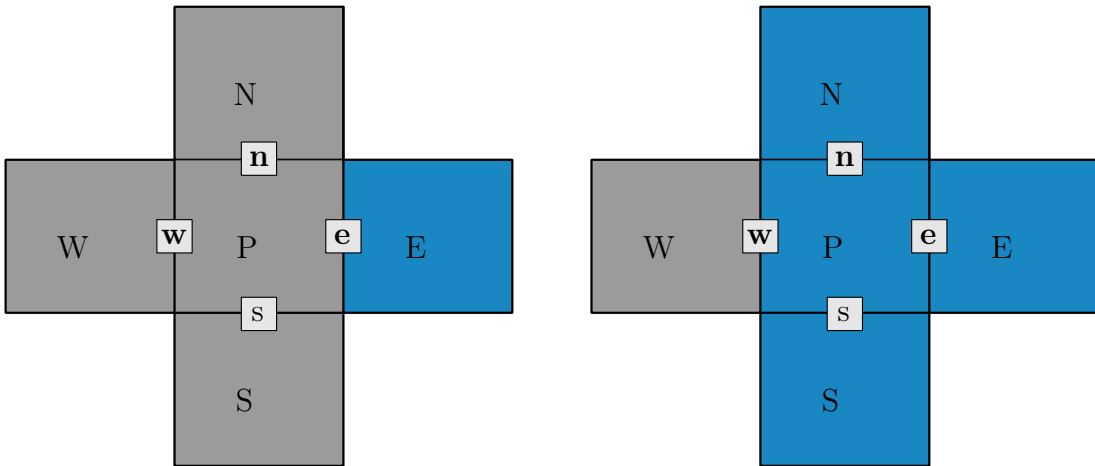
Figure A1: Representation of the active (grey) and cavitating regions (blue).

As discussed in Sec. 5.2.2., the rupture and formation boundaries separate the active and cavitating regions. Eq. 5.15 represents a density–based form of the Reynolds equation and is solved for the values of density ρ. In the cavitating region ρ represents the density of the liquid–gas mixture, while for the active region, it represents the density of the liquid. For the cavitating region, the

switch function evaluates to zero ($\alpha = 0$) and the left–hand term of Eq. 5.15 (the Poiseuille term) becomes zero. The first term on the right–hand side, i.e. the Couette term, and the second term, i.e. the squeeze and local expansion term, remain as the only active terms. In the full–film region, the switch function evaluates to unity ($\alpha = 1$), thus all of the terms in Eq. 5.15 remain active. Special care must be taken to satisfy the condition for mass conservation between the cavitating and full–film regions, i.e. to satisfy the boundary conditions specified by Eqs. 5.16 and 5.17.

According to [42] different treatment of the Poiseuille and Couette terms is required, depending whether a finite area face P is completely in the active region, completely in the cavitating region or at the rupture or fromation boundary. If the finite area face P is in the **active region** (non–cavitating) and all of the surrounding faces (N, S, E, W) are also **active** (non–cavitating) faces, the face P is considered completely in the **ative region** (Fig. A1). The Poiseuille coefficient, the Couette coefficient and the squeeze and local expansion terms are discretised as follows:

- Poiseuille coefficient (discretised using Eq. 4.16 and 4.18):

$$
\begin{aligned}
\oint_{\partial S_P} \nabla_s \bullet (\Gamma \nabla_s \rho) \, \mathrm{d}L &= \oint_{\partial S_P} \mathbf{m} \bullet (\Gamma \nabla_s \rho) \, \mathrm{d}L \\
&= \Gamma_e L_e \frac{\rho_E - \rho_P}{L_{PE}} + \Gamma_w L_w \frac{\rho_W - \rho_P}{L_{PW}} \\
&\quad + \Gamma_n L_n \frac{\rho_N - \rho_P}{L_{PN}} + \Gamma_s L_s \frac{\rho_S - \rho_P}{L_{PS}},
\end{aligned}
\tag{A1}
$$

where $\alpha = 1$ and $\Gamma = \frac{\alpha \beta h^3}{12\eta}$.

- Couette coefficient (discretised using Eq. 4.12 and 4.13):

$$
\begin{aligned}
\oint_{\partial S_P} \nabla_s \bullet (h \overline{\mathbf{U}}) \rho \, \mathrm{d}L &= \oint_{\partial S_P} \mathbf{m} \bullet (h \overline{\mathbf{U}}) \rho \, \mathrm{d}L \\
&= \mathbf{m}_e \bullet (h \overline{\mathbf{U}})_e L_e \rho_e + \mathbf{m}_w \bullet (h \overline{\mathbf{U}})_w L_w \rho_w \\
&\quad + \mathbf{m}_n \bullet (h \overline{\mathbf{U}})_n L_n \rho_n + \mathbf{m}_s \bullet (h \overline{\mathbf{U}})_s L_s \rho_s \\
&= \dot{s}_e \rho_e + \dot{s}_w \rho_w + \dot{s}_n \rho_n + \dot{s}_s \rho_s,
\end{aligned}
\tag{A2}
$$

where the mean velocity of the contacting surfaces a and b is calculated as $\overline{\mathbf{U}} = \frac{\mathbf{U_a}+\mathbf{U_b}}{2}$, while the edge values of density ρ are determined using the central differencing scheme, i.e. Eq. 4.13.

- Temporal derivative, i.e. squeeze and local expansion term (discretised using the implicit Euler method, Eq. 4.25):

$$\frac{\partial (h\rho)}{\partial t} = \frac{\mathrm{d}\,(h\rho)}{\mathrm{d}t} = \frac{h_P^n \rho_P^n S_P^n - h_P^o \rho_P^o S_P^o}{\Delta t}, \tag{A3}$$

where the temporal derivative equals zero, if a steady–state case is considered.

The finite area face P is considered to be completely in the **cavitating region** if both the face P and its neighbouring faces (N,S,E,W) are cavitating faces, Fig. A1. The Couette term and the temporal derivative are calculated in the same way as for the active region, resulting in Eqs. A2 and A3, respectively. The only difference being, that the values of density ρ in Eq. A2 are calculated using the upwind differencing scheme [85]. As per the method proposed by Elord and Adams, the switch function α (Eqs. 5.14 and 5.15) evaluates to zero, making the Poiseuille term equal to zero:

$$\oint_{\partial S_P} \nabla_s \bullet (\Gamma \nabla_s \rho)\,\mathrm{d}L = \oint_{\partial S_P} \mathbf{m} \bullet (\Gamma \nabla_s \rho)\,\mathrm{d}L = 0, \tag{A4}$$

where $\alpha = 0$ and $\Gamma = \frac{\alpha \beta h^3}{12\eta}$.

Special treatment is needed to satisfy the cavitation boundary conditions given by Eqs. 5.16 and 5.17. If the finite area face P, depicted on the left side of Fig. A2, is an **active** face, while the face located downstream from face P, denoted as E, is a **cavitating** face, the Poiseuille coefficient is given as:

$$\begin{aligned}
\oint_{\partial S_P} \nabla_s \bullet (\Gamma \nabla_s \rho)\,\mathrm{d}L &= \oint_{\partial S_P} \mathbf{m} \bullet (\Gamma \nabla_s \rho)\,\mathrm{d}L \\
&= \Gamma_e L_e \frac{\rho_{\mathrm{cav}} - \rho_P}{L_{PE}} + \Gamma_w L_w \frac{\rho_W - \rho_P}{L_{PW}} \\
&\quad + \Gamma_n L_n \frac{\rho_N - \rho_P}{L_{PN}} + \Gamma_\mathrm{s} L_\mathrm{s} \frac{\rho_S - \rho_P}{L_{PS}},
\end{aligned} \tag{A5}$$

where $\alpha_e = 1$ and $\Gamma = \frac{\alpha \beta h^3}{12\eta}$.

Alternatively, if the finite area face P is a **cavitating**, depicted on the right side of Fig. A2, while the face located upwind from face P, denoted as W, is an **active** face, an additional source term needs to be added to face P:

$$S_P = \Gamma_w L_w \frac{\rho_{\text{cav}} - \rho_P}{L_{PW}}, \tag{A6}$$

where $\alpha_w = 1$ and $\Gamma_w = \left(\frac{\alpha \beta h^3}{12\eta} \right)_w$.

Lastly, according to [42], the discretisation of the averaged Reynolds equation, Eq. 5.18, follows the same principles as the discretisation of the modified Reynolds equation, Eq. 5.15.
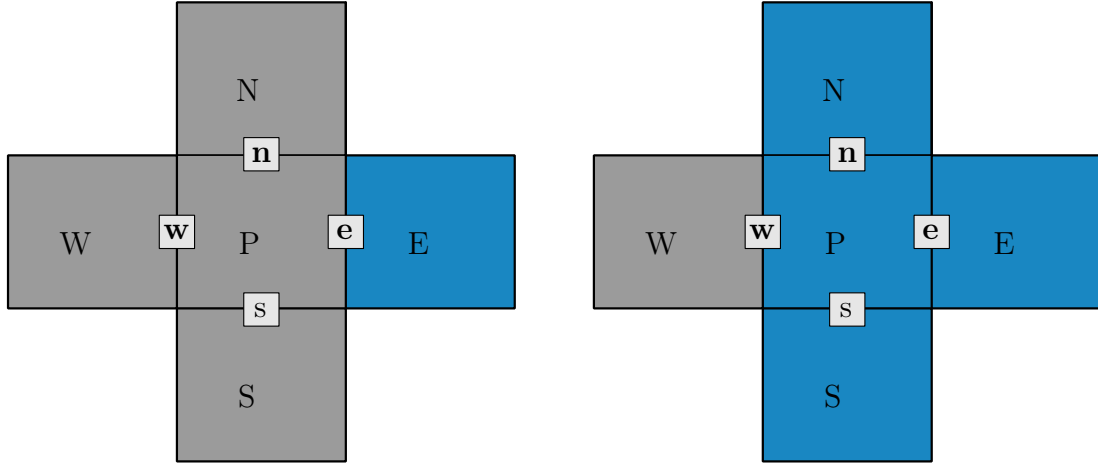
Figure A2: Representation of the cavitation boundaries.

B Flow Factors

Flow Factors by Wilson and Marsault

In Sec. 5.2.2., the flow factors derived by Wilson and Marsault [106] were introduced through Eqs. 5.20 and 5.21, which will be repeated here:

$$\text{Pressure}\,(H < 3): \qquad \phi_x = \left[a_2(H - H_c)^2 + a_3(H - H_c)^3\right]/H^3, \qquad (\text{B1})$$

$$\text{Shear}\,(H < 5): \qquad \phi_s = b_0 + b_1 H + b_2 H^2 + b_3 H^3 + b_4 H^4 + b_5 H^5, \qquad (\text{B2})$$

where H_c denotes the non–dimensional film thickness calculated as $H = h/R_q$, while the value of H at the percolation threshold H_c can be calculated as:

$$H_c = 3\left[1 - (0.47476/\gamma + 1)^{-0.25007}\right]. \qquad (\text{B3})$$

The expression for determining H_c, i.e. Eq. B3 relies on the Peklenik surface parameter γ, i.e. the correction length ratio [158], which is expressed as:

$$\gamma = \frac{\lambda_{0.5_x}}{\lambda_{0.5_y}}, \qquad (\text{B4})$$

and represents the ratio of the half–correlation lengths for each orthogonal direction x and y of a rough surface measurement [105]. According to Bodschwinna and Seewig [159], the the autocorrelation function determines how surface heights at a certain point of the surface are related to another point, expressed as a function of the distance between the two points. Thus, the correlation length can be defined as the distance at which the value of the autocorrelation function drops to zero (or a value close to zero) as the distance increases [160]. Furthermore, the value of the correlation length gives insight on how quickly the surface roughness changes spatially. In a similar manner, the half–correlation length $\lambda_{0.5}$ defines the distance at which the value of the autocorrelation function drops to half of

its maximum value [160]. If the surface roughness of two surfaces needs to be considered, the combined correlation length may be expressed as [161]:

$$\frac{1}{\lambda_{ab}} = \frac{1}{\lambda_a} + \frac{1}{\lambda_b}. \tag{B5}$$

The functions a_2 and a_3 in Eq. B1 (or Eq. 5.20 in Sec. 5.2.2.), are functions of the correlation function γ and can be expressed through semi–empirical expressions:

$$a_2 = 0.051375 \ln^3(9\gamma) - 0.0071901 \ln^4(9\gamma), \tag{B6}$$

$$a_3 = 1.0019 - 0.17927 \ln(\gamma) + 0.047583 \ln^2 - 0.016417 \ln^3(\gamma). \tag{B7}$$

On the other hand, Eq. B2 (or Eq. 5.21 in Sec. 5.2.2.) depends on the coefficients b_0, b_1, b_2, b_3, b_4, b_5 and on H. Wilson and Marsault provided expressions for these coefficients [106]:

$$b_0 = 0.12667\gamma^{-0.6508},$$
$$b_1 = \exp\left(-0.38768 - 0.44160 \ln(\gamma) - 0.12679 \ln^2(\gamma) + 0.042414 \ln^3(\gamma)\right),$$
$$b_2 = -\exp\left(-1.1748 - 0.39916 \ln(\gamma) - 0.11041 \ln^2(\gamma) + 0.031775 \ln^3(\gamma)\right),$$
$$b_3 = \exp\left(-2.8843 - 0.36712 \ln(\gamma) - 0.10676 \ln^2(\gamma) + 0.028039 \ln^3(\gamma)\right), \tag{B8}$$
$$b_4 = -0.004706 + 0.0014493 \ln(\gamma) + 0.00033124 \ln^2(\gamma) - 0.00017147 \ln^3(\gamma),$$
$$b_5 = 0.00014734 - 4.255 \times 10^{-5} \ln(\gamma) - 1.057 \times 10^{-5} \ln^2(\gamma) + 5.0292 \times 10^{-6} \ln^3(\gamma).$$

Škurić [42] analysed the shear flow factors provided by Wilson and Marsault [106] and noticed that Eq. B2 (Eq. 5.21) provides inconsistent results for some values of γ: under–prediction for $\gamma = 1/9$, over–prediction for $\gamma = 1/3$ and notable deviation from [106] for $\gamma = 1/6$. In order to provide better agreement between shear flow factors, Škurić [42] introduced a new analytical equation derived by curve–fitting:

$$\begin{aligned}
\phi_\mathrm{s} =\; & p_{00} + H\left\{p_{10} + H\left[p_{20} + H\left(p_{30} + H\left(p_{40} + p_{50}H\right)\right)\right]\right\} \\
& + H\gamma\{ \\
& \qquad\quad p_{11} + H\left[p_{21} + H\left(p_{31} + p_{41}H\right)\right] \\
& \qquad\quad + \gamma\left[p_{12} + \gamma\left(p_{13} + p_{14}\gamma\right)\right] \\
& \qquad\quad + H\gamma\left(p_{22} + p_{32}H + p_{23}\gamma\right) \\
& \qquad\} \\
& + \gamma\left\{p_{01} + \gamma\left[p_{02} + \gamma\left(p_{03} + \gamma\left(p_{04} + p_{05}\gamma\right)\right)\right]\right\},
\end{aligned} \tag{B9}$$

where if $\gamma < 1$, the constants p_{xy} are defined as:

$$\begin{aligned}
p_{00} &= 1.0360000 \\
p_{10} &= 0.3781000 & p_{01} &= -4.05000 \\
p_{20} &= -0.1298000 & p_{02} &= 9.71100 \\
p_{30} &= -0.0147700 & p_{03} &= -13.49000 \\
p_{40} &= 0.0073650 & p_{04} &= 10.21000 \\
p_{50} &= -0.0005668 & p_{05} &= -3.19400 \\
p_{11} &= 0.6817000 \\
p_{21} &= 0.0030600 & p_{12} &= -1.20400 \\
p_{31} &= -0.0128900 & p_{13} &= 0.66320 \\
p_{41} &= 0.0005116 & p_{14} &= -0.10980 \\
p_{22} &= 0.0900800 \\
p_{32} &= 0.0033670 & p_{23} &= -0.04641,
\end{aligned} \tag{B10}$$

while for $\gamma \geq 1$ as

$$
\begin{aligned}
p_{00} &= 0.14030000 \\
p_{10} &= 0.74480000 \qquad\qquad p_{01} = 0.10980000 \\
p_{20} &= -0.27440000 \qquad\qquad p_{02} = -0.10420000 \\
p_{30} &= 0.03141000 \qquad\qquad p_{03} = 0.02828000 \\
p_{40} &= -0.00059320 \qquad\qquad p_{04} = -0.00310500 \\
p_{50} &= -0.00007039 \qquad\qquad p_{05} = 0.00012030 \\
p_{11} &= -0.20300000 \\
p_{21} &= 0.05916000 \qquad\qquad p_{12} = 0.02689000 \\
p_{31} &= -0.00483300 \qquad\qquad p_{13} = -0.00141300 \\
p_{41} &= 0.00010060 \qquad\qquad p_{14} = 0.00002183 \\
p_{22} &= -0.00596800 \\
p_{32} &= 0.00026560 \qquad\qquad p_{23} = 0.00019160.
\end{aligned}
\tag{B11}
$$

Flow Factors by Patir and Cheng

Flow factors, which were derived by Patir and Cheng [104, 105], were introduced in Sec. 5.2.2. by Eqs. 5.23 to 5.27, which will be repeated here:

Pressure $(H \geq 3)$:

$$\phi_x = 1 - C \exp(-rH) \qquad \text{for} \qquad \gamma \leq 1, \tag{B12}$$

$$\phi_x = 1 - CH \exp(-r) \qquad \text{for} \qquad \gamma > 1, \tag{B13}$$

Shear :

$$\phi_s = V_{r_a} \Phi_s \left(H, \gamma_a \right) - V_{r_b} \Phi_s \left(H, \gamma_b \right) \quad \text{with:} \tag{B14}$$

$$\Phi_s = A_1 H^{\alpha_1} \exp \left(-\alpha_2 H + \alpha_3 H^2 \right) \qquad\qquad \text{for} \quad H \leq 5, \tag{B15}$$

$$\Phi_s = A_2 \exp \left(-0.25H \right) \qquad\qquad \text{for} \quad H > 5. \tag{B16}$$

Eqs. B12 and B13 (or Eq. 5.23 and 5.24 in Sec. 5.2.2.) require the constants C and r, which are provided in Table B1. In Eq. B14 (or Eq. 5.25), the variables V_{r_a} and V_{r_b} are the variance ratios of surfaces a and b, and are determined as:

$$V_{r_a} = \left(\frac{R_{q_a}}{R_q}\right)^2, \qquad V_{r_b} = \left(\frac{R_{q_b}}{R_q}\right)^2 = 1 - V_{r_a}. \qquad (B17)$$

Lastly, Eqs. B15 and B16 (or Eqs. 5.26 and 5.27) in Sec 5.2.2., require the coefficients A_1, A_2, α_1, α_2, α_3 as functions of the Peklenik parameter γ, which are given in Table B2.

Table B1: Coefficients C and r used in Eqs. B12 and B13.

γ	C	r	Range
1/9	1.480	0.42	$H > 1$
1/6	1.380	0.42	$H > 1$
1/3	1.180	0.42	$H > 0.75$
1	0.900	0.56	$H > 0.5$
3	0.225	1.50	$H > 0.5$
6	0.520	1.50	$H > 0.5$
9	0.870	1.50	$H > 0.5$

Table B2: Shear flow factor coefficients for Eqs. B15 and B16.

γ	A_1	α_1	α_2	α_3	A_2
1/9	2.046	1.12	0.78	0.03	1.856
1/6	1.962	1.08	0.77	0.03	1.754
1/3	1.858	1.01	0.76	0.03	1.561
1	1.899	0.98	0.92	0.05	1.126
3	1.560	0.85	1.13	0.08	0.556
6	1.290	0.62	1.09	0.08	0.388
9	1.011	0.54	1.07	0.08	0.295

Bibliography

[1] Ž. Tuković, Metoda kontrolnih volumena na domenama promjenjivog oblika, Ph.D. thesis, Chair of Turbomachinery, Faculty of Mechanical Engineering and Naval Architecture, University of Zagreb (2005).

[2] L. Rodríguez-Tembleque, R. Abascal, M. Aliabadi, A boundary element formulation for wear modeling on 3D contact and rolling-contact problems, International Journal of Solids and Structures 47 (18-19) (2010) 2600–2612. `doi:10.1016/j.ijsolstr.2010.05.021`.

[3] J. Furustig, I. Dobryden, A. Almqvist, N. Almqvist, R. Larsson, The measurement of wear using AFM and wear interpretation using a contact mechanics coupled wear model, Wear 350–351 (2016) 74–81. `doi:10.1016/j.wear.2016.01.002`.

[4] J. Guegan, Experimental Investigation into the Influence of Roughness on Friction and Film Thickness in EHD Contacts, Ph.D. thesis (2015).

[5] S. Bair, Comment on "The Relationship Between Friction and Film Thickness in EHD Point Contacts in the Presence of Longitudinal Roughness" by Guegan, Kadiric, Gabelli, & Spikes, Tribology Letters 65 (3) (2017) 83. `doi:10.1007/s11249-017-0867-z`.

[6] J. Williams, The Invention of Tribology: Peter Jost's Contribution, Lubricants 12 (3) (2024) 65. `doi:10.3390/lubricants12030065`.

[7] E. Ciulli, Tribology and Industry: From the Origins to 4.0, Frontiers in Mechanical Engineering 5 (2019) 55. `doi:10.3389/fmech.2019.00055`.

[8] O. Reynolds, On the theory of lubrication and its application to Mr. Beauchamp tower's experiments, including an experimental determination of the viscosity of olive oil, Philosophical Transactions of the Royal Society of London 177 (1886) 157–234. `doi:10.1098/rstl.1886.0005`.

[9] D. Dowson, G. R. Higginson, Elasto-Hydrodynamic Lubrication the Fundamentals of Roller and Gear Lubrication, [1st ed.] Edition, Commonwealth and International Library, Pergamon Press, Oxford, 1966.

[10] E. Ciulli, Vastness of Tribology Research Fields and Their Contribution to Sustainable Development, Lubricants 12 (2) (2024) 33. `doi:10.3390/lubricants12020033`.

[11] R. Gohar, H. Rahnejat, Fundamentals of Tribology, third edition Edition, World Scientific, Hackensack, New Jersey London Singapore Beijing, 2018.

[12] M. Nosonovsky, B. Bhushan, Green tribology: Principles, research areas and challenges, Philosophical Transactions of the Royal Society A: Mathematical, Physical and Engineering Sciences 368 (1929) (2010) 4677–4694. `doi:10.1098/rsta.2010.0200`.

[13] L. J. Hernández-Mora, L. A. De La Vega Ibarra, G. Urriolagoitia-Sosa, B. Romero-Ángeles, G. M. Urriolagoitia-Calderón, Numerical modelling of mechanical contact between dissimilar materials, Journal of Physics: Conference Series 1221 (1) (2019) 012040. `doi:10.1088/1742-6596/1221/1/012040`.

[14] Y. Meng, J. Xu, Z. Jin, B. Prakash, Y. Hu, A review of recent advances in tribology, Friction 8 (2) (2020) 221–300. `doi:10.1007/s40544-020-0367-2`.

[15] E. Boukas, J. Yang, G. Yin, Q. Zhang, Manufacturing systems: Wear modeling and numerical procedures, Stochastic Analysis and Applications 15 (3) (1997) 269–293. `doi:10.1080/07362999708809476`.

[16] N. Stalin-Muller, K. Dang Van, Numerical simulation of the sliding wear test in relation to material properties, Wear 203–204 (1997) 180–186. `doi:10.1016/S0043-1648(96)07417-0`.

[17] S. Rice, F. Moslehy, Modeling friction and wear phenomena, Wear 206 (1-2) (1997) 136–146. `doi:10.1016/S0043-1648(96)07360-7`.

[18] H. Meng, K. Ludema, Wear models and predictive equations: Their form and content, Wear 181–183 (1995) 443–457. `doi:10.1016/0043-1648(95)90158-2`.

[19] J. F. Archard, Contact and Rubbing of Flat Surfaces, Journal of Applied Physics 24 (8) (1953) 981–988. `doi:10.1063/1.1721448`.

[20] P. P~odra, S. Andersson, Simulating sliding wear with finite element method, Tribology International 32 (2) (1999) 71–81. `doi:10.1016/S0301-679X(99)00012-2`.

[21] J. Williams, Wear modelling: Analytical, computational and mapping: A continuum mechanics approach, Wear 225–229 (1999) 1–17. `doi:10.1016/S0043-1648(99)00060-5`.

[22] M. Öqvist, Numerical simulations of mild wear using updated geometry with different step size approaches, Wear 249 (1-2) (2001) 6–11. `doi:10.1016/S0043-1648(00)00548-2`.

[23] J. Molinari, M. Ortiz, R. Radovitzky, E. Repetto, Finite-element modeling of dry sliding wear in metals, Engineering Computations 18 (3/4) (2001) 592–610. `doi:10.1108/00368790110407257`.

[24] V. Hegadekatte, S. Kurzenhäuser, N. Huber, O. Kraft, A predictive modeling scheme for wear in tribometers, Tribology International 41 (11) (2008) 1020–1031. `doi:10.1016/j.triboint.2008.02.020`.

[25] C. R. Á. Da Silva, G. Pintaude, Uncertainty analysis on the wear coefficient of Archard model, Tribology International 41 (6) (2008) 473–481. `doi:10.1016/j.triboint.2007.10.007`.

[26] A. Vakis, V. Yastrebov, J. Scheibert, L. Nicola, D. Dini, C. Minfray, A. Almqvist, M. Paggi, S. Lee, G. Limbert, J. Molinari, G. Anciaux, R. Aghababaei, S. Echeverri Restrepo, A. Papangelo, A. Cammarata, P. Nicolini, C. Putignano, G. Carbone, S. Stupkiewicz, J. Lengiewicz, G. Costagliola, F. Bosia, R. Guarino, N. Pugno, M. Müser, M. Ciavarella,

Modeling and simulation in tribology across scales: An overview, Tribology International 125 (2018) 169–199. `doi:10.1016/j.triboint.2018.02.005`.

[27] J. Andersson, Numerical simulation of a wear experiment (2011) 6.

[28] E. Bortoleto, A. Rovani, V. Seriacopi, F. Profito, D. Zachariadis, I. Machado, A. Sinatora, R. Souza, Experimental and numerical analysis of dry contact in the pin on disc test, Wear 301 (1-2) (2013) 19–26. `doi:10.1016/j.wear.2012.12.005`.

[29] S. Ilincic, A. Vernes, G. Vorlaufer, H. Hunger, N. Dörr, F. Franek, Numerical estimation of wear in reciprocating tribological experiments, Proceedings of the Institution of Mechanical Engineers, Part J: Journal of Engineering Tribology 227 (5) (2013) 510–519. `doi:10.1177/1350650113476606`.

[30] J. Lengiewicz, S. Stupkiewicz, Efficient model of evolution of wear in quasi-steady-state sliding contacts, Wear 303 (1-2) (2013) 611–621. `doi:10.1016/j.wear.2013.03.051`.

[31] K. K. Bose, P. Ramkumar, Finite element method based sliding wear prediction of steel-on-steel contacts using extrapolation techniques, Proceedings of the Institution of Mechanical Engineers, Part J: Journal of Engineering Tribology 233 (10) (2019) 1446–1463. `doi:10.1177/1350650119836813`.

[32] C. Curreli, F. Di Puccio, L. Mattei, Application of the finite element submodeling technique in a single point contact and wear problem, International Journal for Numerical Methods in Engineering 116 (10-11) (2018) 708–722. `doi:10.1002/nme.5940`.

[33] C. Curreli, M. Viceconti, F. Di Puccio, Submodeling in wear predictive finite element models with multipoint contacts, International Journal for Numerical Methods in Engineering 122 (15) (2021) 3812–3823. `doi:10.1002/nme.6682`.

[34] W. Zhan, P. Huang, Numerical analysis of time-varying wear with elastic deformation in line contact, Friction 7 (2) (2019) 143–152. `doi:10.1007/s40544-017-0195-1`.

[35] A. Winkler, M. Marian, S. Tremmel, S. Wartzack, Numerical Modeling of Wear in a Thrust Roller Bearing under Mixed Elastohydrodynamic Lubrication, Lubricants 8 (5) (2020) 58. `doi:10.3390/lubricants8050058`.

[36] M. Maier, M. Pusterhofer, F. Grün, Multiscale Wear Simulation in Textured, Lubricated Contacts, Coatings 13 (4) (2023) 697. `doi:10.3390/coatings13040697`.

[37] A. Ghanbarzadeh, M. Wilson, A. Morina, D. Dowson, A. Neville, Development of a new mechano-chemical model in boundary lubrication, Tribology International 93 (2016) 573–582. `doi:10.1016/j.triboint.2014.12.018`.

[38] A. Ghanbarzadeh, P. Parsaeian, A. Morina, M. C. T. Wilson, M. C. P. Van Eijk, I. Nedelcu, D. Dowson, A. Neville, A Semi-deterministic Wear Model Considering the Effect of Zinc Dialkyl Dithiophosphate Tribofilm, Tribology Letters 61 (1) (2016) 12. `doi:10.1007/s11249-015-0629-8`.

[39] A. Azam, A. Ghanbarzadeh, A. Neville, A. Morina, M. C. Wilson, Modelling tribochemistry in the mixed lubrication regime, Tribology International 132 (2019) 265–274. `doi:10.1016/j.triboint.2018.12.024`.

[40] E. Georgiou, L. Lopes, M. De Bilde, D. Drees, How can we measure sliding wear in an efficient way?, Wear 458–459 (2020) 203414. `doi:10.1016/j.wear.2020.203414`.

[41] M. Ciavarella, A. Papangelo, J. R. Barber, Effect of Wear on the Evolution of Contact Pressure at a Bimaterial Sliding Interface, Tribology Letters 68 (1) (2020) 27. `doi:10.1007/s11249-020-1269-1`.

[42] V. Škurić, Numerical simulation of lubricated wire rolling and drawing, Ph.D. thesis, Zagreb (2019).

[43] H. M. Stanley, T. Kato, An FFT-Based Method for Rough Surface Contact, Journal of Tribology 119 (3) (1997) 481–485. `doi:10.1115/1.2833523`.

[44] F. Sahlin, R. Larsson, A. Almqvist, P. M. Lugt, P. Marklund, A mixed lubrication model incorporating measured surface topography. Part 1: Theory

of flow factors, Proceedings of the Institution of Mechanical Engineers, Part J: Journal of Engineering Tribology 224 (4) (2010) 335–351. `doi:10.1243/13506501JET658`.

[45] F. Sahlin, R. Larsson, P. Marklund, A. Almqvist, P. M. Lugt, A mixed lubrication model incorporating measured surface topography. Part 2: Roughness treatment, model validation, and simulation, Proceedings of the Institution of Mechanical Engineers, Part J: Journal of Engineering Tribology 224 (4) (2010) 353–365. `doi:10.1243/13506501JET659`.

[46] V. Škurić, P. D. Jaeger, H. Jasak, Lubricated elastoplastic contact model for metal forming processes in OpenFOAM, Computers & Fluids 172 (2018) 226–240. `doi:10.1016/j.compfluid.2018.06.011`.

[47] V. Škurić, P. De Jaeger, H. Jasak, Lubricated Contact Model for Cold Metal Rolling Processes, in: J. M. Nóbrega, H. Jasak (Eds.), OpenFOAM®, Springer International Publishing, Cham, 2019, pp. 309–323. `doi:10.1007/978-3-319-60846-4_23`.

[48] L. Balatinec, T. Uroić, V. Škurić, H. Jasak, Numerical analysis of lubricated point contacts using the Finite Area Method, International Journal of Non-Linear Mechanics 149 (2023) 104314. `doi:10.1016/j.ijnonlinmec.2022.104314`.

[49] H. Jasak, OpenFOAM: Open source CFD in research and industry, International Journal of Naval Architecture and Ocean Engineering 1 (2) (2009) 89–94. `doi:10.2478/IJNAOE-2013-0011`.

[50] R. Gohar, H. Rahnejat, Fundamentals of Tribology, third edition Edition, World Scientific, New Jersey, 2019.

[51] F. P. Bowden, D. Tabor, The Friction and Lubrication of Solids, Oxford University Press, Oxford, 2023.

[52] B. Bhushan, Tribology: Friction, wear, and lubrication, in: R. C. Dorf (Ed.), The Engineering Handbook on CD-ROM, CRC Press, Boca Raton, FL, 1997, Ch. 21.

Bibliography

[53] D. Stepanov, V. Beregun, O. Harmash, Y. Chvertko, I. Novikov, Analysis of the Influence of non-Metallic Inclusions on the Wear Resistance of the Weld Metal, in: 2020 IEEE 40th International Conference on Electronics and Nanotechnology (ELNANO), IEEE, Kyiv, Ukraine, 2020, pp. 302–306. `doi:10.1109/ELNANO50318.2020.9088780`.

[54] A. Abdelbary, Friction and Wear of Polymer and Polymer Composites, in: H. Jena, J. K. Katiyar, A. Patnaik (Eds.), Tribology of Polymer and Polymer Composites for Industry 4.0, Springer Singapore, Singapore, 2021, pp. 33–54. `doi:10.1007/978-981-16-3903-6_3`.

[55] A. Abdelbary, Wear of Polymers and Composites, Elsevier Science & Technology, Cambridge, 2015.

[56] J. Zhang, H. Li, Y. Zhou, S. Chen, Q. Rong, An Analysis of Trabecular Bone Structure Based on Principal Stress Trajectory, Bioengineering 10 (10) (2023) 1224. `doi:10.3390/bioengineering10101224`.

[57] M. M. Khonsari, E. R. Booser, Applied Tribology: Bearing Design and Lubrication, third edition Edition, John Wiley & Sons Inc, Hoboken, NJ, 2017.

[58] P. Villaggio, Wear of an Elastic Block, Meccanica 36 (3) (2001) 243–250. `doi:10.1023/A:1013986416527`.

[59] T. Reye, Zur theorie der zapfenreibung, Der Civilingenieur 4 (1860) 235–255.

[60] M. M. Khrushchov, M. A. Babichev, Investigation of Wear of Metals, Russian Academy of Sciences, Moscow, 1960.

[61] V. L. Popov, Analytic solution for the limiting shape of profiles due to fretting wear, Scientific Reports 4 (1) (2014) 3749. `doi:10.1038/srep03749`.

[62] J. F. Archard, W. Hirst, The Wear of Metals under Unlubricated Conditions, Proceedings of the Royal Society of London. Series A, Mathematical and Physical Sciences 236 (1206) (1956) 397–410. `arXiv:99967`.

[63] J. F. Archard, Wear Theory and Mechanisms, ASME, New York, 1980, pp. 35–80.

[64] L. Mattei, F. Di Puccio, Influence of the wear partition factor on wear evolution modelling of sliding surfaces, International Journal of Mechanical Sciences 99 (2015) 72–88. `doi:10.1016/j.ijmecsci.2015.03.022`.

[65] Q. J. Wang, Y. Qian, Encyclopedia of Tribology, Springer, New York, 2013.

[66] A. Cameron, W. L. Wood, The full journal bearing`doi:10.1243/PIME_PROC_1949_161_010_02`.

[67] W. A. Gross, Gas bearings: Journal and thrust 182 (1) (1967) 116–150. `doi:10.1243/PIME_CONF_1967_182_012_02`.

[68] L. E. C. Ruskell, Reynolds equation and elastohydrodynamic lubrication in metal seals, Proceedings of The Royal Society A: Mathematical, Physical and Engineering Sciences`doi:10.1098/RSPA.1976.0080`.

[69] T. F. Conry, S. Wang, C. Cusano, A Reynolds-Eyring Equation for Elastohydrodynamic Lubrication in Line Contacts, Journal of Tribology 109 (4) (1987) 648–654. `doi:10.1115/1.3261526`.

[70] W. Shapiro, Impact on Reynolds theory on bearing and seal design, Journal of Tribology-transactions of The Asme`doi:10.1115/1.3261325`.

[71] S. R. Brown, H. W. Stockman, S. J. Reeves, Applicability of the Reynolds Equation for modeling fluid flow between rough surfaces, Geophysical Research Letters 22 (18) (1995) 2537–2540. `doi:10.1029/95GL02666`.

[72] L. Bertocchi, D. Dini, M. Giacopini, M. T. Fowell, A. Baldini, Fluid film lubrication in the presence of cavitation: A mass-conserving two-dimensional formulation for compressible, piezoviscous and non-Newtonian fluids, Tribology International 67 (2013) 61–71. `doi:10.1016/j.triboint.2013.05.018`.

[73] G. Bayada, L. Chupin, Compressible Fluid Model for Hydrodynamic Lubrication Cavitation, Journal of Tribology 135 (4) (2013) 041702. `doi:10.1115/1.4024298`.

[74] Y. Liu, Q. J. Wang, S. Bair, P. Vergne, A Quantitative Solution for the Full Shear-Thinning EHL Point Contact Problem Including Traction, Tribology Letters 28 (2) (2007) 171–181. `doi:10.1007/s11249-007-9262-5`.

[75] X. Wang, Y. Liu, D. Zhu, Numerical Solution of Mixed Thermal Elastohydrodynamic Lubrication in Point Contacts With Three-Dimensional Surface Roughness, Journal of Tribology 139 (1) (2017) 011501. `doi:10.1115/1.4032963`.

[76] W. Habchi, P. Vergne, S. Bair, O. Andersson, D. Eyheramendy, G. Morales-Espejel, Influence of pressure and temperature dependence of thermal properties of a lubricant on the behaviour of circular TEHD contacts, Tribology International 43 (10) (2010) 1842–1850. `doi:10.1016/j.triboint.2009.10.002`.

[77] X. Liu, M. Jiang, P. Yang, M. Kaneta, Non-Newtonian Thermal Analyses of Point EHL Contacts Using the Eyring Model, Journal of Tribology 127 (1) (2005) 70–81. `doi:10.1115/1.1843161`.

[78] H. J. Kim, P. Ehret, D. Dowson, C. M. Taylor, Thermal elastohydrodynamic analysis of circular contacts Part 1: Newtonian model, Proceedings of the Institution of Mechanical Engineers, Part J: Journal of Engineering Tribology 215 (4) (2001) 339–352. `doi:10.1243/1350650011543583`.

[79] H. J. Kim, P. Ehret, D. Dowson, C. M. Taylor, Thermal elastohydrodynamic analysis of circular contacts Part 2: Non-Newtonian model, Proceedings of the Institution of Mechanical Engineers, Part J: Journal of Engineering Tribology 215 (4) (2001) 353–362. `doi:10.1243/1350650011543592`.

[80] H. Zhang, Q. Yang, W. Zhao, F. Jiang, Study on Solution Algorithm of Reynolds Equation of Self-acting Gas Journal Bearings Based on Finite Difference Method, in: F. Chu, Z. Qin (Eds.), Proceedings of the 11th IFToMM International Conference on Rotordynamics, Vol. 139, Springer International Publishing, Cham, 2024, pp. 236–244. `doi:10.1007/978-3-031-40455-9_19`.

[81] D. Skaltsas, G. N. Rossopoulos, C. I. Papadopoulos, A comparative study of the Reynolds equation solution for slider and journal bearings with stochastic roughness on the stator and the rotor, Tribology International 167 (2022) 107410. `doi:10.1016/j.triboint.2021.107410`.

[82] M. M. Gogazeh, H. A. Al Dabbas, N. W. Musa, Mathematical Model and Theoretical Investigation of the Performance of Journal Bearing using a discretized Reynolds Lubrication Equation with Finite Width, WSEAS TRANSACTIONS ON APPLIED AND THEORETICAL MECHANICS 18 (2023) 327–335. `doi:10.37394/232011.2023.18.31`.

[83] Y. Xi, J. Deng, Y. Li, A solution for finite journal bearings by using physics-informed neural networks with both soft and hard constrains, Industrial Lubrication and Tribology 75 (5) (2023) 560–567. `doi:10.1108/ILT-02-2023-0045`.

[84] A. Almqvist, E. Burtseva, K. Rajagopal, P. Wall, On lower-dimensional models in lubrication, Part B: Derivation of a Reynolds type of equation for incompressible piezo-viscous fluids, Proceedings of the Institution of Mechanical Engineers, Part J: Journal of Engineering Tribology 235 (8) (2021) 1703–1718. `doi:10.1177/1350650120973800`.

[85] H. Jasak, Error Analysis and Estimation for the Finite Volume Method with Applications to Fluid Flows, Ph.D. thesis, Imperial College London, London (1996).

[86] B. J. Hamrock, S. R. Schmid, B. O. Jacobson, Fundamentals of Fluid Film Lubrication, Dekker Mechanical Engineering, CRC Press, 2004.

[87] D. Gropper, L. Wang, T. J. Harvey, Hydrodynamic lubrication of textured surfaces: A review of modeling techniques and key findings, Tribology International 94 (2016) 509–529. `doi:10.1016/j.triboint.2015.10.009`.

[88] H. W. Swift, The Stability of Lubricating Films in Journal Bearings, Minutes of the Proceedings of the Institution of Civil Engineers 233 (1932) (1932) 267–288. `doi:10.1680/imotp.1932.13239`.

[89] W. Stieber, Das Schwimmlager: Hydrodynamische Theorie Des Gleitlagers, VDI-Verlag, Berlin, 1933.

[90] B. Jakobsson, L. Floberg, The finite journal bearing considering vaporization, Transactions of Chalmers University of Technology 190 (1957) 1–116.

[91] K.-o. Olsson, Cavitation in dynamically loaded bearings, 1965.

[92] H. Elrod, M. Adams, A Computer Program for Cavitation and Starvation Problems, in: Cavitation and Related Phenomena in Lubrication, Vol. 37, 1974, pp. 37–41.

[93] D. Vijayaraghavan, T. G. Keith, An Efficient, Robust, and Time Accurate Numerical Scheme Applied to a Cavitation Algorithm, Journal of Tribology 112 (1) (1990) 44–51. `doi:10.1115/1.2920229`.

[94] Y. Qiu, M. M. Khonsari, On the Prediction of Cavitation in Dimples Using a Mass-Conservative Algorithm, Journal of Tribology 131 (4) (2009) 041702. `doi:10.1115/1.3176994`.

[95] M. Fesanghary, M. M. Khonsari, A Modification of the Switch Function in the Elrod Cavitation Algorithm, Journal of Tribology 133 (2) (2011) 024501. `doi:10.1115/1.4003484`.

[96] M. Giacopini, M. T. Fowell, D. Dini, A. Strozzi, A Mass-Conserving Complementarity Formulation to Study Lubricant Films in the Presence of Cavitation, Journal of Tribology 132 (4) (2010) 041702. `doi:10.1115/1.4002215`.

[97] A. Almqvist, J. Fabricius, R. Larsson, P. Wall, A New Approach for Studying Cavitation in Lubrication, Journal of Tribology 136 (1) (2014) 011706. `doi:10.1115/1.4025875`.

[98] T. Woloszynski, P. Podsiadlo, G. W. Stachowiak, Efficient Solution to the Cavitation Problem in Hydrodynamic Lubrication, Tribology Letters 58 (1) (2015) 18. `doi:10.1007/s11249-015-0487-4`.

[99] F. Sahlin, A. Almqvist, R. Larsson, S. Glavatskih, A cavitation algorithm for arbitrary lubricant compressibility, Tribology International 40 (8) (2007) 1294–1300. `doi:10.1016/j.triboint.2007.02.009`.

[100] A. Almqvist, P. Wall, Modelling Cavitation in (Elasto)Hydrodynamic Lubrication, in: P. H. Darji (Ed.), Advances in Tribology, InTech, 2016. `doi:10.5772/63533`.

[101] W. R. D. Wilson, Friction and lubrication in bulk metal-forming processes, Journal of Applied Metalworking 1 (1) (1978) 7–19. `doi:10.1007/BF02833955`.

[102] F. Cyriac, A. Akchurin, Thin film lubrication, lubricants and additives, Springer, Cham, 2020, pp. 33–75. `doi:10.1007/978-3-030-47451-5_3`.

[103] A. Almqvist, On the effects of surface roughness in lubrication, Ph.D. thesis, Luleå University of Technology, Luleå, Sweden (2006).

[104] N. Patir, H. S. Cheng, An Average Flow Model for Determining Effects of Three-Dimensional Roughness on Partial Hydrodynamic Lubrication, Journal of Lubrication Technology 100 (1) (1978) 12–17. `doi:10.1115/1.3453103`.

[105] N. Patir, H. S. Cheng, Application of Average Flow Model to Lubrication Between Rough Sliding Surfaces, Journal of Lubrication Technology 101 (2) (1979) 220–229. `doi:10.1115/1.3453329`.

[106] W. R. D. Wilson, N. Marsault, Partial Hydrodynamic Lubrication With Large Fractional Contact Areas, Journal of Tribology 120 (1) (1998) 16–20. `doi:10.1115/1.2834180`.

[107] J. A. Greenwood, J. B. P. Williamson, Contact of Nominally Flat Surfaces, Proceedings of the Royal Society A: Mathematical, Physical and Engineering Sciences 295 (1442) (1966) 300–319. `doi:10.1098/rspa.1966.0242`.

[108] A. Megalingam, K. S. H. Ramji, A Comparison on Deterministic, Statistical and Statistical with Asperity Interaction Rough Surface Contact Models, Journal of Bio- and Tribo-Corrosion 7 (3) (2021) 95. `doi:10.1007/s40735-021-00526-3`.

[109] R. L. Jackson, I. Green, On the Modeling of Elastic Contact between Rough Surfaces, Tribology Transactions 54 (2) (2011) 300–314. `doi:10.1080/10402004.2010.542277`.

[110] T. Hisakado, Effect of surface roughness on contact between solid surfaces, Wear 28 (2) (1974) 217–234. `doi:10.1016/0043-1648(74)90163-X`.

[111] J. A. Greenwood, J. H. Tripp, The Elastic Contact of Rough Spheres, Journal of Applied Mechanics 34 (1) (1967) 153–159. `doi:10.1115/1.3607616`.

[112] J. I. McCool, Predicting Microfracture in Ceramics Via a Microcontact Model, Journal of Tribology 108 (3) (1986) 380–385. `doi:10.1115/1.3261209`.

[113] J. A. Greenwood, J. H. Tripp, The Contact of Two Nominally Flat Rough Surfaces, Proceedings of the Institution of Mechanical Engineers 185 (1) (1970) 625–633. `doi:10.1243/PIME_PROC_1970_185_069_02`.

[114] J. Pullen, J. B. P. Williamson, On the plastic contact of rough surfaces, Proceedings of the Royal Society of London. A. Mathematical and Physical Sciences 327 (1569) (1972) 159–173. `doi:10.1098/rspa.1972.0038`.

[115] W. R. Chang, I. Etsion, D. B. Bogy, An Elastic-Plastic Model for the Contact of Rough Surfaces, Journal of Tribology 109 (2) (1987) 257–263. `doi:10.1115/1.3261348`.

[116] Y. Zhao, D. M. Maietta, L. Chang, An asperity micro contact model incorporating the transition from elastic deformation to fully plastic flow, Transactions of the ASME Journal of Tribology 122 (2000) 86–93.

[117] R. L. Jackson, I. Green, A Finite Element Study of Elasto-Plastic Hemispherical Contact Against a Rigid Flat, Journal of Tribology 127 (2) (2005) 343–354. `doi:10.1115/1.1866166`.

[118] R. L. Jackson, I. Green, A statistical model of elasto-plastic asperity contact between rough surfaces, Tribology International 39 (9) (2006) 906–914. `doi:10.1016/j.triboint.2005.09.001`.

[119] S. S. Wadwalkar, R. L. Jackson, L. Kogut, A study of the elastic—plastic deformation of heavily deformed spherical contacts, Proceedings of the Institution of Mechanical Engineers, Part J: Journal of Engineering Tribology 224 (10) (2010) 1091–1102. `doi:10.1243/13506501JET763`.

[120] H. Peng, Z. Liu, F. Huang, R. Ma, A study of elastic–plastic contact of statistical rough surfaces, Proceedings of the Institution of Mechanical Engineers, Part J: Journal of Engineering Tribology 227 (10) (2013) 1076–1089. `doi:10.1177/1350650112474399`.

[121] V. A. Yastrebov, J. Durand, H. Proudhon, G. Cailletaud, Rough surface contact analysis by means of the Finite Element Method and of a new reduced model, Comptes Rendus. Mécanique 339 (7-8) (2011) 473–490. `doi:10.1016/j.crme.2011.05.006`.

[122] H. M. Westergaard, Bearing Pressures and Cracks, Journal of Applied Mechanics 6 (1939) A49–A53.

[123] K. Johnson, J. Greenwood, J. Higginson, The contact of elastic regular wavy surfaces, International Journal of Mechanical Sciences 27 (6) (1985) 383–396. `doi:10.1016/0020-7403(85)90029-3`.

[124] A. Almqvist, F. Sahlin, R. Larsson, S. Glavatskih, On the dry elasto-plastic contact of nominally flat surfaces, Tribology International 40 (4) (2007) 574–579. `doi:10.1016/j.triboint.2005.11.008`.

[125] W. Habchi, A Full-System Finite Element Approach to Elastohydrodynamic Lubrication Problems: Application to Ultra-Low-Viscosity Fluids, Ph.D. thesis, Institut National des Sciences Appliquées de Lyon, Lyon, France (2008).

[126] C. J. A. Roelands, W. O. Winer, W. A. Wright, Correlational Aspects of the Viscosity-Temperature-Pressure Relationship of Lubricating Oils (Dr In dissertation at Technical University of Delft, 1966), Journal of Lubrication Technology 93 (1) (1971) 209–210. `doi:10.1115/1.3451519`.

[127] L. Houpert, New Results of Traction Force Calculations in Elastohydrodynamic Contacts, Journal of Tribology 107 (2) (1985) 241–245. `doi:10.1115/1.3261033`.

Bibliography

[128] S. Bair, A Note on the Use of Roelands Equation to Describe Viscosity for EHD Hertzian Zone Calculations, Journal of Tribology 115 (2) (1993) 333–334. `doi:10.1115/1.2921011`.

[129] S. Bair, The Variation of Viscosity With Temperature and Pressure for Various Real Lubricants, Journal of Tribology 123 (2) (2001) 433–436. `doi:10.1115/1.1308024`.

[130] A. K. Doolittle, Studies in Newtonian Flow. II. The Dependence of the Viscosity of Liquids on Free-Space, Journal of Applied Physics 22 (12) (1951) 1471–1475. `doi:10.1063/1.1699894`.

[131] A. Hajishafiee, Finite-volume CFD modelling of fluid-solid interaction in EHL contacts`doi:10.25560/32100`.

[132] M. Hartinger, D. Gosman, S. Ioannides, H. A. Spikes, CFD Modelling of Elastohydrodynamic Lubrication, in: World Tribology Congress III, Volume 1, ASMEDC, Washington, D.C., USA, 2005, pp. 531–532. `doi:10.1115/WTC2005-63840`.

[133] K. L. Johnson, J. L. Tevaarwerk, Shear behaviour of elastohydrodynamic oil films, Proceedings of the Royal Society of London. A. Mathematical and Physical Sciences 356 (1685) (1977) 215–236. `doi:10.1098/rspa.1977.0129`.

[134] K. Sharif, S. Morris, H. Evans, R. Snidle, Comparison of non-Newtonian EHL models in high sliding applications, in: Tribology Series, Vol. 39, Elsevier, 2001, pp. 787–796. `doi:10.1016/S0167-8922(01)80159-0`.

[135] P. J. Carreau, Rheological Equations from Molecular Network Theories, Transactions of the Society of Rheology 16 (1) (1972) 99–127. `doi:10.1122/1.549276`.

[136] S. Bair, M. Khonsari, An EHD Inlet Zone Analysis Incorporating the Second Newtonian, Journal of Tribology 118 (2) (1996) 341–343. `doi:10.1115/1.2831306`.

[137] S. Bair, P. Vergne, M. Querry, A unified shear-thinning treatment of both film thickness and traction in EHD, Tribology Letters 18 (2) (2005) 145–152. `doi:10.1007/s11249-004-1770-y`.

[138] S. Bair, A Rough Shear-Thinning Correction for EHD Film Thickness, Tribology Transactions 47 (3) (2004) 361–365. `doi:10.1080/05698190490455519`.

[139] D. Dowson, G. R. Higginson, Elasto-Hydrodynamic Lubrication: International Series on Materials Science and Technology, Pergamon, Oxford, 2014.

[140] J. R. Macdonald, Some Simple Isothermal Equations of State, Reviews of Modern Physics 38 (4) (1966) 669–679. `doi:10.1103/RevModPhys.38.669`.

[141] D. Zhu, On the Thermo–Elastohydrodynamic Problem in Elliptical Contacts, Ph.D. thesis, Tsinghua University, PR China (1984).

[142] P. Yang, On the Transient Thermal Elastohydrodynamic Lubrication, Ph.D. thesis, Tsinghua University, PR China (1989).

[143] X.-L. Yan, Y.-Y. Zhang, G.-X. Xie, X.-Q. Du, F. Qin, Effects of Texture Orientation on the Mixed Thermal Elastohydrodynamic Lubrication and Fatigue Life in Point Contacts, Journal of Tribology 141 (1) (2019) 011501. `doi:10.1115/1.4040474`.

[144] J. I. McCool, Relating Profile Instrument Measurements to the Functional Performance of Rough Surfaces, Journal of Tribology 109 (2) (1987) 264–270. `doi:10.1115/1.3261349`.

[145] A. E. H. Love, A Treatise on the Mathematical Theory of Elasticity, Cambridge university press, 2013.

[146] R. Gohar, Elastohydrodynamics, 2nd Edition, Imperial College Press, London, 2001.

[147] W. W. Chen, S. Liu, Q. J. Wang, Fast Fourier Transform Based Numerical Methods for Elasto-Plastic Contacts of Nominally Flat Surfaces, Journal of Applied Mechanics 75 (1) (2008) 011022. `doi:10.1115/1.2755158`.

[148] D. Bonneau, A. Fatu, D. Souchet, Hydrodynamic Bearings, 1st Edition, Wiley, 2014. `doi:10.1002/9781119004769`.

[149] J. Guegan, A. Kadiric, A. Gabelli, H. Spikes, The Relationship Between Friction and Film Thickness in EHD Point Contacts in the Presence of Longitudinal Roughness, Tribology Letters 64 (3) (2016) 33. `doi:10.1007/s11249-016-0768-6`.

[150] S. Bair, C. Mary, N. Bouscharain, P. Vergne, An improved Yasutomi correlation for viscosity at high pressure, Proceedings of the Institution of Mechanical Engineers, Part J: Journal of Engineering Tribology 227 (9) (2013) 1056–1060. `doi:10.1177/1350650112474394`.

[151] P. Ehret, D. Dowson, C. M. Taylor, On lubricant transport conditions in elastohydrodynamic conjuctions, Proceedings of the Royal Society of London. Series A: Mathematical, Physical and Engineering Sciences 454 (1971) (1998) 763–787. `doi:10.1098/rspa.1998.0185`.

[152] V. Hegadekatte, N. Huber, O. Kraft, Finite element based simulation of dry sliding wear, Modelling and Simulation in Materials Science and Engineering 13 (1) (2005) 57–75. `doi:10.1088/0965-0393/13/1/005`.

[153] C. Wu, L. Zhang, P. Qu, S. Li, Z. Jiang, W. Liu, Characterization of interface stresses and lubrication of rough elastic surfaces under ball-on-disc rolling, Proceedings of the Institution of Mechanical Engineers, Part J: Journal of Engineering Tribology 231 (12) (2017) 1552–1573. `doi:10.1177/1350650117700793`.

[154] J. Furustig, Semi-Deterministic Numerical Simulations of Wear on Various Scales 178.

[155] N. Fatima, P. Marklund, R. Larsson, Water contamination effect in wet clutch system, Proceedings of the Institution of Mechanical Engineers, Part D: Journal of Automobile Engineering 227 (3) (2013) 376–389. `doi:10.1177/0954407012455145`.

[156] R. S. Dwyer-Joyce, B. W. Drinkwater, C. J. Donohoe, The measurement of lubricant–film thickness using ultrasound, Proceedings of the Royal Society of London. Series A: Mathematical, Physical and Engineering Sciences 459 (2032) (2003) 957–976. `doi:10.1098/rspa.2002.1018`.

[157] W. ten Napel, P. Klein Meuleman, T. Lubrecht, R. Bosma, L. Houpert, Traction in Elastohydrodynamic Lubrication at Very High Contact Pressures, in: Eurotrib '85, 4th European Tribology Congress, Elsevier, Ecully, France, 1985-09-09/1985-09-12.

[158] J. Peklenik, Paper 24: New Developments in Surface Characterization and Measurements by Means of Random Process Analysis, Proceedings of the Institution of Mechanical Engineers, Conference Proceedings 182 (11) (1967) 108–126. `doi:10.1243/PIME_CONF_1967_182_309_02`.

[159] H. Bodschwinna, J. Seewig, Frequency and Autocorrelation Function, in: Q. J. Wang, Y.-W. Chung (Eds.), Encyclopedia of Tribology, Springer US, Boston, MA, 2013, pp. 1270–1272. `doi:10.1007/978-0-387-92897-5_307`.

[160] P. Podulka, Resolving Selected Problems in Surface Topography Analysis by Application of the Autocorrelation Function, Coatings 13 (1) (2022) 74. `doi:10.3390/coatings13010074`.

[161] B. Bhushan, Modern Tribology Handbook, Two Volume Set, 0th Edition, CRC Press, 2000. `doi:10.1201/9780849377877`.

Abbreviations

AFM Atomic Force Microscopy. 124

BEM Boundary Element Method. 6

BoD Ball–On–Disc. 130

BoF Ball–On–Flat. v, 113, 116, 118, 120, 121

CFD Computational Fluid Dynamics. 2, 3

DFT Discrete Fourier Transform. 60

EHL Elastohydrodynamic Lubrication. 2, 6

FA Finite Area. iv, v, 88–91, 94, 99, 100, 108, 109, 116, 126, 133

FAM Finite Area Method. 7, 9, 31, 46, 57, 59, 60, 63

FEA Finite Element Analysis. 2, 4, 5

FEM Finite Element Method. 5–7, 9, 34, 40

FFT Fast Fourier Transform. 6, 40, 57, 60, 61, 131

FVM Finite Volume Method. 7, 9, 34, 46

GW Greenwood–Williamson. 38, 39

JFO Jakobsson–Floberg–Olson. 32, 33

JG Jackson–Green. 39

MD Molecular Dynamics. 2

PoD Pin–On–Disc. iv, v, vii, 86, 88, 91, 92, 95–100, 102–104, 106, 108

Abbreviations

RMS Root Mean Squared. 37, 39, 66, 67

RoB Ring–On–Block. vii, 107, 108, 114

RoR Ring–On–Ring. 124

SRR Slide–to–Roll Ratio. 131, 132, 134

WLF Williams–Landel–Ferry. 70

Curriculum Vitae

Luka Balatinec, born in Zagreb on November 15th, 1993, completed high school in his hometown. He pursued a degree in Mechanical Engineering at the Faculty of Mechanical Engineering and Naval Architecture, University of Zagreb. His undergraduate studies focused on Power Engineering, leading to a thesis on the Mathematical Model of Block K in TETO Zagreb.

For his master's degree, he specialized in Computational Fluid Dynamics (CFD) under the mentorship of Professor Hrvoje Jasak, PhD. He worked on the Atlas of Nasal Flows project, receiving the Rector's Award, and wrote his master's thesis on Rotor-Stator Interfaces for CFD Simulations in Turbomachinery. He graduated Magna Cum Laude in 2019, starting his PhD studies after graduation

Since 2020, he has been a research assistant at the Faculty, focusing on CFD simulations in turbomachinery, biological flows, naval hydrodynamics, combustion, and heat transfer. He has co-authored several scientific publications and presented at international conferences.

Declaration

Parts of the work presented in this thesis have been published in publications listed below.

Selected Publications

[1] L. Balatinec, T. Uroić, V. Škurić, H. Jasak, Numerical analysis of lubricated point contacts using the finite area method, International Journal of Non-Linear Mechanics 149 (2023) 18. `doi:10.1016/j.ijnonlinmec.2022.104314`.

[2] L. Balatinec, T. Uroić, H. Jasak, Towards a lubricated wear model using the finite area method, in: The 19th OpenFOAM Workshop, Beijing, China, 2024, 25.06.2024-28.06.2024.

[3] L. Balatinec, T. Uroić, H. Jasak, Development of a wear model using the finite area method, in: 18th OpenFOAM Workshop 2023, Genova, Italy, 2023, 11.07.2023-14.07.2023. `doi:10.6084/m9.figshare.24081426`.

[4] L. Balatinec, Lubricated contact analysis using the finite area method (poster), in: 17th OpenFOAM Workshop, Cambridge, United Kingdom, 2022.

[5] L. Balatinec, T. Uroić, H. Jasak, Sliding wear simulations in foam-extend, in: M. Horvat, H. Jasak (Eds.), 17th OpenFOAM Workshop, Cambridge, United Kingdom, 2022, pp. 203–203.

[6] V. Škurić, L. Balatinec, H. Jasak, Analysis of lubricated point contacts using the finite area method, in: 16th OpenFOAM Workshop, Dublin, Ireland, 2021, pp. 5–5.